# Vortices in the Subarctic Seas and their interactions with bottom topography

**Marta Trodahl**


Dissertation for the degree of Philosophiae Doctor (PhD)

Section for Meteorology and Oceanography

Department of Geosciences

University of Oslo

May 2022

To my beloved farfar

*Series of dissertations submitted to the*
*Faculty of Mathematics and Natural Sciences, University of Oslo*
*No. 2540*

ISSN 1501-7710



Cover: Hanne Baadsgaard Utigard.
Print production: Graphics Center, University of Oslo.

# :Preface

This synthesis and collection of papers are submitted for the degree of pilosophiae doctor (PhD) in Oceanography at the Section for Meteorology and Oceanography (MetOs), Department of Geosciences, University of Oslo. The thesis consists of an introduction, a summary of findings, a future outlook and lastly the papers. The author contributions to each paper are specified in Chapter 4.

**Paper I:** **Marta Trodahl** and Pål Erik Isachsen, (2018), "Topographic influence on baroclinic instability and the mesoscale eddy field in the northern North Atlantic Ocean and the Nordic Seas", Journal of Physical Oceanography doi: 10.1175/JPO-D-17-0220.1, 2018

**Paper II:** **Marta Trodahl**, Pål Erik Isachsen, Jonathan M. Lilly, Johan Nilsson, and Nils Melsom Kristensen, (2020), "The regeneration of the Lofoten Vortex through vertical alignment", Journal of Physical Oceanography doi:10.1175/JPO-D-20-0029.1

**Paper III:** **Marta Trodahl**, LaCasce, J. H, (submitted: May 2022), "Stable surface anticyclones in basins", Journal of Physical Oceanography

Other publications from the PhD period that are not included in the thesis:

**I** Johannes Sandang Dugstad, Ilker Fer, Joseph Henry Lacasce, Marta Sanchez de la Lama, **Marta Trodahl**, (2019), "Lateral Heat Transport in the Lofoten Basin: Near-Surface Pathways and Subsurface Exchange", Journal of Geophysical Research doi:10.1029/2018JC014774

# :Acknowledgments

Firstly, I would like to thank to my supervisors Prof. Joseph Henry LaCasce and Prof. Pål Erik Isachsen. I am very grateful for all the knowledge you shared with me over the years, and for always keeping the door open for discussions.

Thanks also to Jan Erik Weber who presented me with the fruits of doing a PhD, and who encouraged me to go for it! Thanks to Lars Petter Røed, I have learnt so much from you, and your enthusiasm for the field has been an inspiration! Thanks to Nils Melsom Christensen who (patiently) taught me all the pitfalls of ROMS modeling. I benefited greatly from this throughout my PhD.

To the people in the METOS hallway : it has been great to share both office-time and spare-time with you! A special thanks to Ada and Eli for all your support and the feedback on this thesis. You have such been a blessing and an inspiration through these years! I have really appreciated our friendships, and I most certainly couldn't have done this without the two of you!

Dear all girls in the "Dreamteam", Kine Merete, Benedicte, Jeanette, Åse Marie and Stina, and also Silja, Maria, Malin, Marie, Vivian and many more, for your wonderful friendships and good times during these years!

Thanks to all in the Trodahl family for your care and support! Thanks mom and dad who always encouraged me to pursue my passion. And Ester: I am so grateful for all the encouragement you have given, and also for wonderful hikes and numerous activities.

I want to thank my dear belated Farfar, Kåre Trodahl, who made it to 101 years old this year. This thesis is dedicated to him. He introduced me to the joy of mathematics before starting school, and cheered me on throughout this degree.

Last, but not least: Mein Liebling Viktor - Thank you for being there for me, for making me laugh when I wanted to cry, and for reminding me to take one step at a time. You light up my life with so much joy and fun, and I can't wait to share the post-PhD life with you!

Marta Trodahl
Oslo, May 2022

# Contents

# Part I

# Thesis

# Chapter 1

# :Motivation and objectives

> One can marvel at this manifestation of 'order within disorder ' and be fascinated both by the beauty of the patterns and by the challenge such a phenomenon presents to dynamical theory.
>
> *Mcwilliams 1989*

Despite major leaps in oceanographic research and technology the past decades, several aspects of the general circulation are not fully described. An essential part of the circulation are coherent swirling bodies of water; mesoscale (10-100 km) vortices, also called eddies. Mesoscale vortices are abundant everywhere in the World Ocean and are vital in upholding equilibrium balances that govern the global circulation and thus also the climate (*McWilliams*, 2008). The integrated effect of mesoscale vortices plays an important role for how momentum, heat, salt, and other tracers are transported in the ocean. More insight into vortex life cycles and impacts is needed, such as their formation, spatial structure, distribution, interactions with neighboring vortices and with the ambient environment is necessary to obtain a better understanding of the general circulation in the global ocean.

Gaining more knowledge of the mesoscale vortex field is not only essential for our present-day understanding of the general circulation, but also for future predictions of climate. However, due to their small spatial extent, mesoscale vortices are seldom resolved in climate models. Instead, the effects of mesoscale vortices are parameterized by the imprint they leave on the larger scale dynamics. These effects are typically included in models through *eddy parameterization schemes*. These schemes provide the parameterized eddy transport of momentum, heat, salt, and tracers in the models. Some schemes are based on the notion that mesoscale vortices (eddies) originate through baroclinic instability, which again rely on simplified models of baroclinic instability (*Charney*, 1947; *Eady*, 1949; *Phillips*, 1954). Such simplified models are often based on an unrealistic oceanic setting. For example, the Eady model (*Eady*, 1949), which is widely used to infer vortex characteristics in climate model parameterizations (*Eden et al.*, 2009; *Uchida et al.*, 2017), assumes that the ocean bottom is flat. An assumption that is highly inaccurate, particularly along the ocean margins where the eddy

activity typically is largest (*Chelton et al.*, 2007, 2011). This thesis does not focus on climate model parameterization, but it addresses issues arising from making this flat-bottom assumption. Topography can significantly impact the growth of an instability and its spatial characteristics. A flat-bottom assumption is potentially most detrimental at high latitudes, where the influence of bottom topography on the flow is stronger than at lower latitudes. In the polar regions, topography directs the time mean currents to flow along the continental slopes (*Isachsen et al.*, 2003; *Nøst and Isachsen*, 2003). A description of the circulation therefore needs to account for the effects that topography has on both the larger scale and the mesoscale flow field. This thesis will focus on topographic effects on the mesoscale flow field.

Studying the mesoscale vortex field is especially challenging in the polar regions since vortex length scales significantly decrease with latitude. The small length scales make them both harder to observe and to model. While satellite observations have played an important role in our understanding of the ocean circulation and current variability, the resolution of satellite altimetry is often too coarse to fully capture mesoscale features at high latitudes. Moreover, satellite data can only provide a view of the sea surface, whereas vortices can be located at different ocean depths and extend vertically up to order 1000 m. It is therefore important to be able to describe their full three-dimensional structure and behavior. A tool to investigate and represent the three-dimensional flow fields is through regional numerical modeling, which are able to resolve the mesoscale and sub-mesoscale dynamics. Such models allow for detailed investigations of vortex evolution and propagation. While theoretical and idealized modeling of mesoscale vortices have a long tradition, they often only offer a 2D spatial perspective, and are based on a simplified representation of the flow field. However, when utilized together with an ocean model with a full representation of the flow field, the combination can bridge the gap between simplified theoretical understanding and realistic complex models. In this thesis we combine simplified theory and idealized and realistic high-resolution modeling, to gain insight the mesoscale vortex field in a climate-sensitive high latitude region with prominent bottom topography, namely the Subarctic Seas.

The Subarctic Seas encompass the Barents Sea, the Nordic Seas and the Labrador Sea. This thesis primarily focus on the the Nordic Seas, a marginal sea located between Greenland and Norway that play an essential role in the global climate. Most of the waters transported in and out of the Arctic Ocean pass through this region. Due to a large heat exchange with the atmosphere, the Nordic Seas act as an important transitional zone for the waters migrating through. The route entails complex bottom topography and high mesoscale vortex activity. The strong topographically-guided currents in the region are initially swift and narrow, which limits the air-sea heat fluxes and water transformations due to short exposure time to cooling and a small surface area where the cooling can occur. However, the presence of mesoscale vortices significantly alters the heat loss by increasing both the lateral spreading of the warm saline Atlantic Water (AW) emerging from the south, as well as the transit time through the region. In fact, mesoscale vortices are key drivers to the lateral heat transport that aids regulating the heat loss taking place over the basins.

The eddy activity and spreading of AW is especially evident in the Lofoten Basin,

which is a focus region of this thesis. The Lofoten basin is a deep bowl-shaped basin off the coast of Northern Norway, and a hot spot for mesoscale vortex activity, and literally a hotspot in terms of heat content. The warm AW extends deeper and occupies a larger area than in the adjacent basins, making it the primary resovoir of heat in the Nordic Seas (*Orvik and Niiler*, 2002). The production of mesoscale vortices delay the northbound flow, and therefore assists in controlling the transit time of the AW through these Seas. The vortices also contribute to spread the warm water (*Spall*, 2011). When the AW broadens, it produces a larger area subject to surface cooling and buoyancy loss. Serving as the main heat source to the Arctic Ocean, the prolonged residence time and further cooling of the AW are important processes for maintaining the climate. Mesoscale vortices located in this region are thus of a global significance. but how these vortices are formed, and what sets their characteristics is still not clear. This thesis focuses on these questions. While eddy heat transport is not the focus of this thesis, general knowledge of vortex distribution and characteristics can however shed light to this issue.

The Lofoten Basin is dominated by large buoyant anticyclones, believed to emerge from the unstable mean slope current. Once the vortices form, they break free from the slope current and propagate into the basin. One of these, the Lofoten Vortex (LV), exhibits remarkable behavior. The LV is exceptionally robust, with a lifetime that could extend decades. The LV is topographically locked to the center of the basin, and enclosed by a time mean cyclonic slope circulation. Located in the midst of a highly turbulent field, the dynamics behind such a persistence is baffling. The vortex's long lifetime offers a unique opportunity to study a vortex life cycle in detail. Two main processes have been suggested for the persistence of the LV; wintertime convection and vortex mergers (*Ivanov and Korablev*, 1995; *Köhl*, 2007). Due to the coarse resolution of model data and observations used in earlier studies, a direct link between these processes and vortex longevity has not yet been made. The work in this thesis represents the first study that show such a direct link. Moreover, observations suggest that the existence of stable anticyclones located over topographic bowls or troughs could be a general feature. But, there is presently no theory that can explain their longevity or formation. Theory predicts that turbulent flow over topography generates a steady state cyclonic circulation over a basin, but the theory does not account for the anticyclonic circulation. This thesis aims to contribute to resolve this disparity.

## 1.1 Objectives

The goal of this thesis is to gain insight into the mesoscale vortex field at high latitudes, with a particular emphasis on the influence of bottom topography. The main objectives are:

- Investigate topographic control on unstable growth in the Subarctic seas using linear theory and a realistic numerical model
- Investigate vortex merging as a process for maintaining the Lofoten Vortex using a realistic numerical model

- Investigate the formation of long lived basin-trapped anticyclones using theory and idealized modeling

# Chapter 2

# :Background

> It came as a shock in the 1960's that the ocean, like the atmosphere, has an active weather at all depths with a scale of order 100 km (the mesoscale) which had slipped through the coarse grid of traditional sampling.
>
> *Walter Munk*
> *1997*

This chapter covers some basic background information for the work contained in this thesis, and a further discussion of topics briefly mentioned in the previous chapter. The first four sections contain general information, beneficial for a reader outside the field. The following sections contain more a specific introduction to the thesis' objectives.

## 2.1 The revolutionary discovery

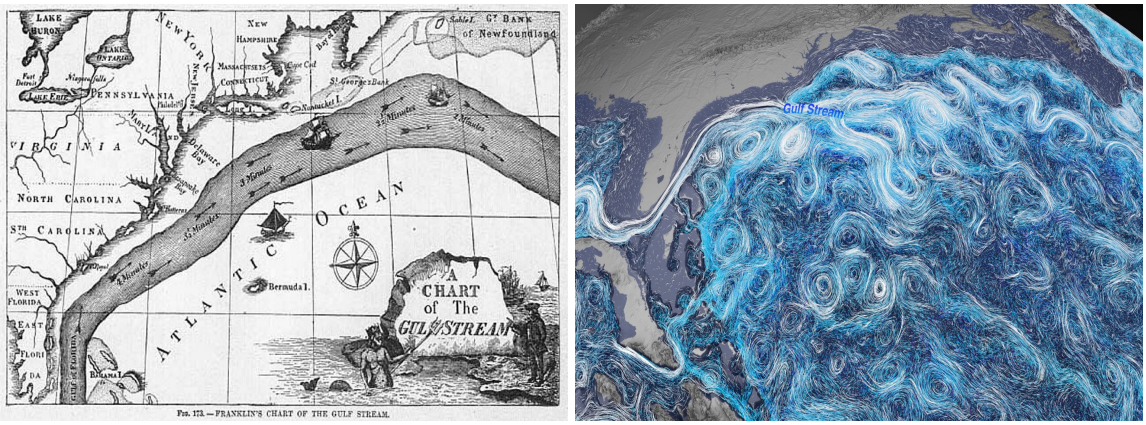


Fig. 173.—FRANKLIN'S CHART OF THE GULF STREAM.

***Figure 2.1:*** *a) Benjamin Franklin's map of the Gulf Stream, drafted in 1769 (Oceanic and Administration, 2021). b) Ocean currents obtained from the ECCO-2 model (Shirah, 2020)*

Our current perception of the ocean has developed substantially during the last century. In fact, many of the greatest discoveries in oceanography date back only 60 years. Prior to the 1960s, a common conception was that the ocean was dominated by steady mean

surface currents and a slow deep circulation. It took considerable time after the Gulf Stream was first charted in the 1700s (figure 2.1a), before the current was depicted as dynamically active as it is. Figure 2.1b shows surface currents from a numerical ocean model simulation, where a plethora of so-called Gulf Stream rings is evident. The first Gulf Stream ring was detected in the 1950s using neutrally buoyant floats (*MODE Group*, 1978). With sparsely distributed research vessels, and a tradition to not repeat measurements at the same location, attaining a comprehensive picture of the global circulation had not yet been feasible (*Hasselmann*, 2010). The first hundred years of oceanography was *a century of undersampling*, according to the well known oceanographer Walter Munk (*L. Vere*, 1997). But this changed with the *mesoscale revolution* (*Hasselmann*, 2010). Novel advanced technology made ocean exploration on a grander scale possible. Measurements successively uncovered an abundance of rings, or mesoscale vortices, throughout the World's Ocean.

Mesoscale vortices are isolated, coherent features rotating clockwise (high pressure) or anticlockwise (low pressure) in the northern hemisphere, referred to as anticyclones and cyclones respectively. They are dynamically equivalent to the high and low synoptic pressure systems in the atmosphere. Atmospheric weather systems was well-studied at the time such systems were first discovered in the ocean (*Charney*, 1947; *Eady*, 1949). But in part due to the ocean's vast scale and inaccessibility, ocean vortices are harder to capture in real-time observations. Observing these structures is also more challenging due to their significantly smaller size. In both fluids, the vortex size is governed by the Rossby deformation radius, $L_d$, which depends on the fluid's stratification, and is inversely proportional to the latitude (*Vallis*, 2006). In the atmosphere, both $L_d$ and weather systems occur on length scales of 100-1000 km. In the ocean, typical length scales are 10-100 km, with the smallest scales occuring at high latitudes.

The discovery that the ocean also contained weather sparked intense research activity on the topic. Mesoscale vortices became the prime focus of many of the regional measurement programs in the 1970s and onward, and increasingly acknowledged as an important part of the general circulation (*MODE Group*, 1978). The research was given yet another boost with the emergence of satellite observations (*Le Traon*, 2013). Since vortices often are characterized by a density anomaly, they are visible in satellite images of sea surface temperature. Furthermore anticyclones and cyclones cause closed contours of high and low sea surface height (SSH), and are manifested as bumps and valleys in satellite altimeter maps, as shown in figure 2.2 (*Robinson*, 2010). In the early 1990s, satellite observations provided for the first time global maps of the sea surface. These observations not only confirmed that mesoscale vortices exist in some locations, but revealed that the ocean is practically full of them.

In the next section we look at the implications of an ocean full of mesoscale vortices and why they are important to study.

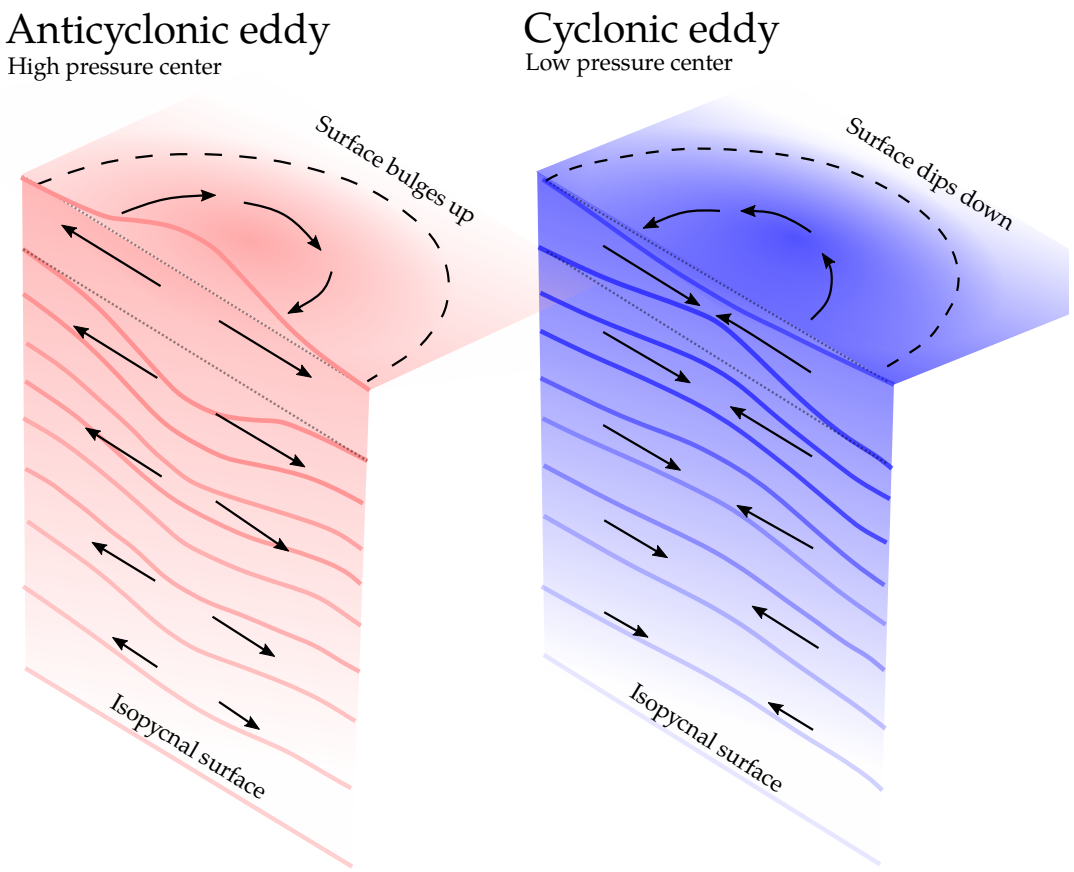


***Figure 2.2:*** *Idealized illustration of a surface intensified warm core anticyclone and a cold core cyclone, in the northern hemisphere. The most basic balance for mesoscale vortices is between the horizontal pressure gradient force (shown by black arrows) and the Coriolis force directed perpendicular to the right of the flow. The pressure gradient is upheld by the sea surface slope that bulge (dip) toward the anticyclonic (cyclonic) vortex center. The anomaly requires deviations in the isopycnals at depth, which compensate by dipping down (bulging up). The sea surface anomalies make ocean vortices detectable from space. The illustration is an amended version of figure 3.7 in Robinson (2010).*

## 2.2 Why study ocean vortices?

Mesoscale vortices are highly energetic features. Vortices typically account for the majority of the oceanic kinetic energy (*Chelton et al.*, 2007; *McWilliams*, 2008), with approximately 50 times the kinetic energy of the mean circulation (*Stammer*, 1997; *Tulloch et al.*, 2011). In the oceanic energy cycle, vortices are important for the conversion of energy, transferring energy from the general circulation to the mesoscale, which will be discussed further in the section 2.4. Through this transfer, vortices can act to constrain the strength of the larger scale currents. On the contrary, they may also feed back into the mean currents which helps maintain them. When the energy has been transferred to the mesoscale, vortices further transport and redistribute momentum laterally, vertically and across scales. 3D turbulence theory predicts that the energy that goes into the vortex field is passed downscale to smaller and smaller scales, where eventually it dissipates into thermal energy (*Vallis*, 2006). In geostrophic turbulence theory, the energy absorbed around $L_d$ is believed to be passed upscale via vortex mergers in an inverse cascade (*Fjørtoft*, 1953; *Kraichnan*, 1967; *Scott and Arbic*, 2007; *Tulloch et al.*,

2011). As the vortices coalesce and grow horizontally, they also attain a deeper structure and undergo a so-called barotropization. The barotropization process involves a vertical transfer of energy and momentum, which eventually leads to large scale energy dissipation, via bottom friction (*Larichev and Held*, 1995). Observational evidence of the presence of an active inverse cascade in the ocean was first presented by *Scott and Wang* (2005).

Furthermore, vortices largely influence the distribution of both active and passive tracers (*Griffies*, 2004). Active tracers, such as temperature and salinity, are tracers that can impact the ocean's density, and thereby also affect the circulation. Passive tracers, such as nutrients and oxygen, do not affect the circulation. In a stably stratified interior ocean, mesoscale vortices act to stir and mix tracers adiabatically, along isopycnals (*Griffies*, 2004). The mixing is an irreversible process that tend to homogenize the tracer distribution.

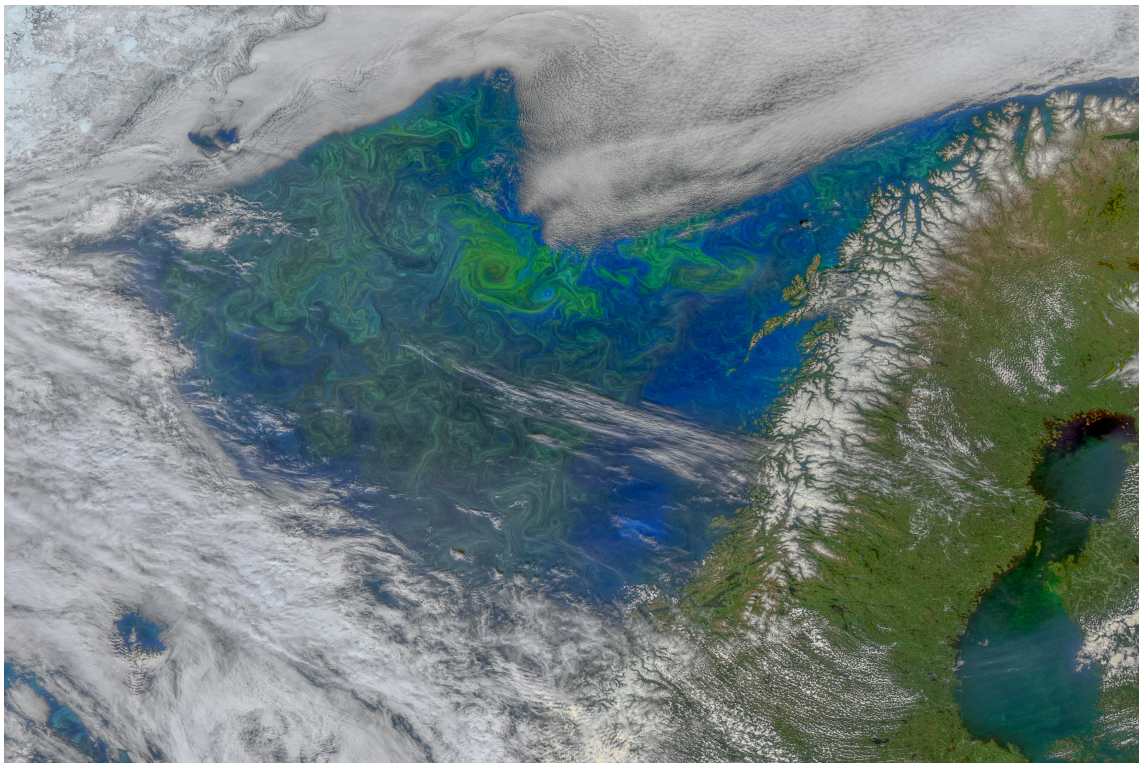

***Figure 2.3:*** *Aqua Ocean Color Data revealing a spring plankton bloom outside the Lofoten Islands. The observations are made by a Moderate-resolution Imaging Spectroradiometer (MODIS).*

Moreover, vortices are important for the offshore transport of coastal waters. Coastal water contains both naturally occurring material and introduced material. Nonlinear vortices (with a higher rotational than translation speed) can trap and transport material (*Chelton et al.*, 2011), such as nutrients, and aid biological activity in offshore waters and the open oceans (*Waite et al.*, 2016). Vortices also support primary biological activity through stirring and vertical mixing in the upper ocean, and are amongst the main causes for the variance of phytoplankton (*Glover et al.*, 2018). In figure 2.3 a distinct anticyclone in the midst of a rich turbulent field is visible off the Lofoten Islands in Northern Norway, during a phytoplankton bloom in June 2020 (*NASA*, 2020).

Near-surface anticyclones and cyclones affect the stratification locally by either lifting or depressing the pycnocline. Cyclones lift the pycnocline, and may provide additional nutrients to the euphotic zone (*Hernández-Hernández et al.*, 2020). Studies have suggested that, by this *eddy-pumping* effect, cyclones may cause an increase in productivity for months at a time. Heightened levels of productivity might have broader impacts than purely on the local biological activity. For instance, the Norwegian Sea actually represents a sink of $CO_2$ due to its high phytoplankton productivity (*Ezat et al.*, 2017).

In the atmosphere, mid-latitude vortices are instrumental for poleward heat transport, and thus reduce the temperature difference between north and south (*Vallis*, 2006). Oceanic vortices are responsible for the major poleward heat transport across the Antarctic Circumpolar Current (*Farneti et al.*, 2010), however their global contribution is uncertain. The mesoscale contribution to the meridional heat transport is regionally dependent, and is largest near boundary currents (*Delman and Lee*, 2021). In our study region, vortices *indirectly* affect the poleward heat transport by spreading out warm Atlantic Water, and by extracting energy from the northbound, fast moving Norwegian Atlantic Current (NwAC).

## 2.3 The research area and oceanographic setting

The major currents in the region are displayed in figure 3.1. The Nordic Seas consist of the Iceland Sea, the Greenland Sea, the Norwegian Sea and the Lofoten Basin. These regions share the same large scale circulation pattern; cyclonic gyres tied to the local topography. The warm waters in the east and cold waters in the west are separated by the North Polar Frontal Zone (*Rodionov et al.*, 2004). The North Polar Frontal Zone aligns with a subsurface ridge system that extends from Iceland to Svalbard. The Norwegian Atlantic Current (NwAC) flows north along the topography in two branches (figure 3.1) (*Orvik and Niiler*, 2002). The outer branch follows approximately the 2000 m isobath, and the inner branch follows the Norwegian continental slope. A third northward flowing current, the Norwegian Coastal Current, flows along the coast. The Norwegian Coastal Current transports fresh and nutrient rich waters from river runoff and outflow from the Baltic Sea. Interactions with the saline slope current dilutes its signature on its journey north. In the west, the East Greenland Current flows southward alongside Greenland, merges with the Irminger Current south of Iceland, and flows into the Labrador Sea (*Le Bras et al.*, 2018).

As mentioned in the previous chapter, the Nordic Seas is an important region for the global climate. This region hosts the upper and lower limb of the meridional overturning circulation, connecting the North Atlantic and the Arctic ocean in two ways. The upper limb, a major poleward inflow of warm, saline Atlantic Water (AW) is located in the east. Air-sea interactions cool the AW during its transit, releasing a substantial amount of heat to the atmosphere before entering the Arctic Ocean. Although the maximum air-sea heat flux can reach much higher values, the average heat flux for the Nordic Seas region is about 160-180$W/m^2$ (*Walczowski*, 2014). These values are comparable to the amount of heat the ocean absorbs in the tropics (*Walczowski*, 2014). The

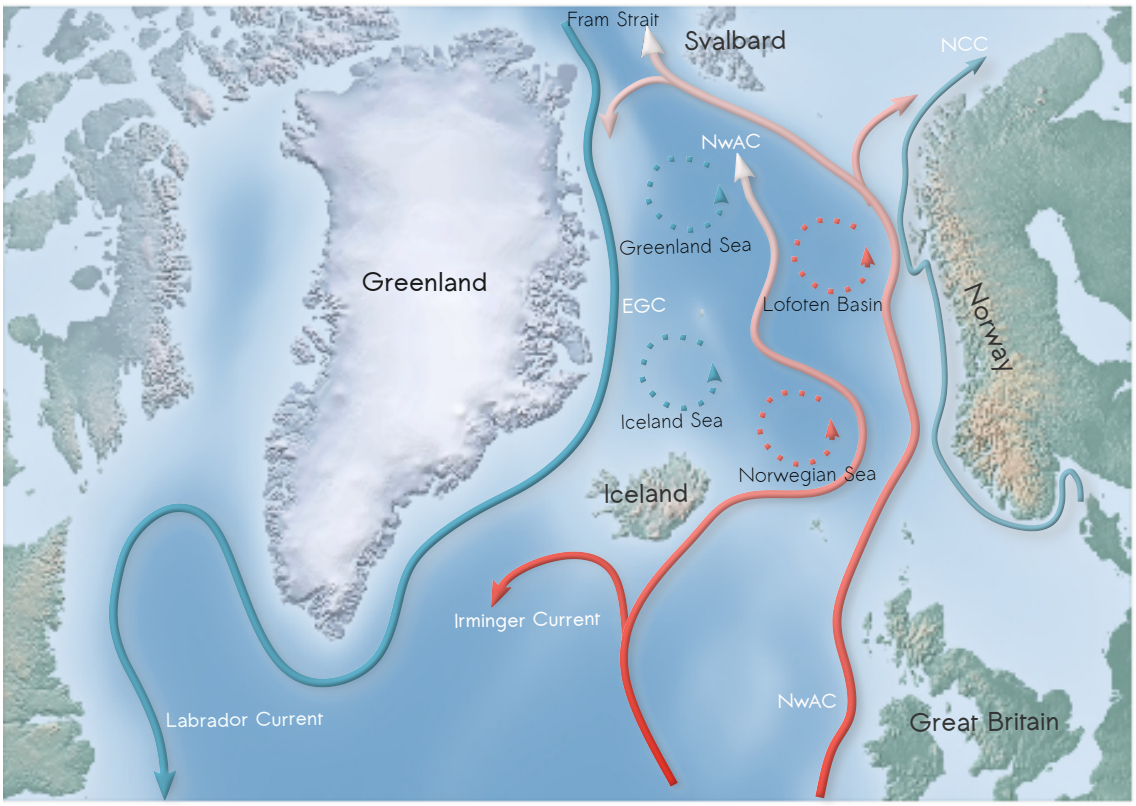


***Figure 2.4:*** *A sketch of the time-mean, large-scale surface circulation in the region of the Subarctic Seas investigated in this thesis. The two branches of the Norwegian Atlantic Current are shown in red, denoting warmer waters. These waters successively cool poleward. The Norwegian Coastal Current, hugging the coast of Norway, is shown in green. Water from the Arctic Ocean is imported to the region through the Fram Strait by the East Greenland Current, and exported in the upper layers by the Labrador Current, both shown in blue denoting colder waters.*

AW heat content has major implications for the sea ice cover near Svalbard and in the Barents Sea. The cooling and densification of AW in the Nordic Seas creates modified water masses that feed the lower limb of the overturning circulation. Cold and fresh Polar Water as well as transformed dense AW fills the western part of the Nordic Seas. These waters enter the region at the Fram Strait, and are exported to the North-Atlantic in the south.

Research activity in the Nordic Seas led to a detailed description of the general circulation as early as in 1909. The map of *Helland-Hansen and Hjalmar* (1909) captures the major features of the large-scale circulation (figure 2.5). *Blindheim and Østerhus* (2005) writes: *"their work described the sea in such detail and to such precision that investigations during succeeding years could add little to their findings"*. Their description of the surface circulation is largely accepted still today. *Helland-Hansen and Hjalmar* (1909) were the first to suggest that topography excerted a steering effect on the currents in this region. In their thorough investigations, they even observed mesoscale features. Waves on scales of about 10 km seen in hydrographic sections

were attributed to either gravity waves or vortex movements. Early in recognizing the importance of such phenomena, they stated: *"The knowledge of the exact nature and causes of these "waves" and their movements would, in our opinion, be of signal importance to Oceanography, and as far as we can see, it is one of its greatest problems that most urgently calls for a solution."*. However, the spatial resolution of their data was too low to chart the full mesoscale circulation. Even to this day, a full picture of the mesoscale circulation has not been attained. In fact, most existing numerical model simulations spanning the entire region, are merely eddy permitting, which means that mesoscale features are only partly resolved.

***Figure 2.5:*** *Map of the surface circulation by Helland Hansen and Nansen in 1909.*

The Nordic Seas features vortices in many locations. Being an area where widely distinct water masses meet and cohabit, the energy contained in the fronts separating the water masses can support vigorous boundary currents and an intense eddy kinetic energy field. Amid the branches of the NwAC there is a broad band of vastly variable flow. This band is typically densely populated by mesoscale vortices (*Rodionov et al.*, 2004). The most eddy active location is however the Lofoten Basin. The rich vortex field is evident in the sea surface height field shown in figure 2.6.

The latter part of this thesis focuses on the mesoscale vortex field in the Lofoten Basin, with a particular focus on the long-lived Lofoten Vortex (LV). The first part of this thesis asks more generally what the root cause of the mesoscale vortices in the Nordic Seas is.

## 2.4 What generates ocean vortices?

Maintaining the abundance of mesoscale vortices globally requires a steady energy source. Several mechanisms generate ocean vortices, ranging from instabilities of the

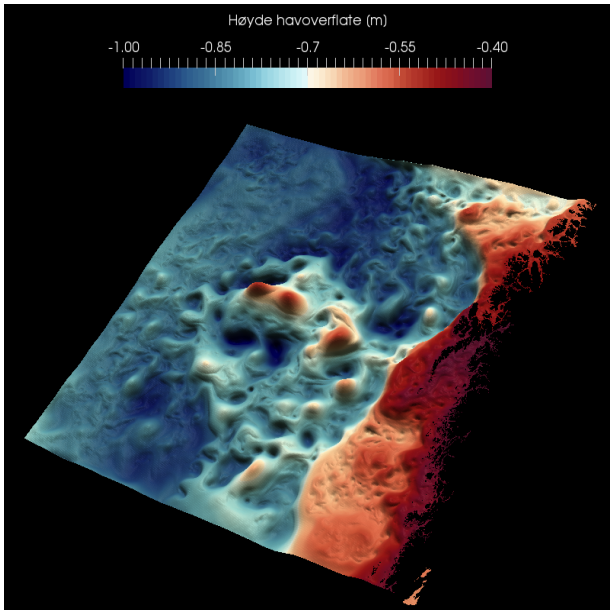


***Figure 2.6:*** *Snapshot of sea surface height from the high resolution model simulation of the Lofoten Basin, used in PaperII. The ocean surface is warped to illustrate the multitude of bumps and valleys imprinted on the sea surface by mesoscale ocean vortices. Anticyclones are revealed by the bumps and cyclones by the valleys. The most intense structures are the tallest (deepest).*

ambient, large scale circulation, flow passing intricate bottom topography and atmospheric forcing. This thesis focuses on baroclinic instability; a vertical shear instability. This type of instability is believed to be the dominant formation mechanism for oceanic mesoscale vortices, and also for atmospheric synoptic scale vortices (*Vallis*, 2006). It serves as an efficient pathway for energy to feed a perturbation that amplifies and grows into a vortex. The source of the energy is the available potential energy (APE) of a mean flow. In baroclinic instability, a perturbation grows by drawing APE from the background state and converting it to EKE (*Vallis*, 2006). The APE is proportional to the lateral temperature gradient. In the atmosphere, the equator-to-pole temperature gradient maintains a vertically sheared zonal mean flow, the jet stream. The weather in the atmosphere, originates as baroclinically unstable waves on the jet stream. In the ocean, zonal mean currents are not common due to the physical barrier of the continents. The mean currents are deflected by land and forced to rather flow along the continental slopes. The density difference between coastal waters and open ocean yields a vertically sheared current, with strongly sloping isopycnals. The slope of the isopycnals reflects a pool of APE.

Figure 2.7 illustrates the process of baroclinic instability. Panel 2.7a displays meanders on an unstable mean flow. The meanders pinch off when they reach finite amplitude, i.e are fully developed. Panel 2.7b show a vertical transect across the current. Water is exchanged across the sloping isopycnals (black contours), light water is moved up into a lighter environment and dense water is moved down into a denser environment. In this configuration, the exchange can lead to the perturbation amplifying. A vertical exchange on the other hand, represents a stable scenario. When light water is moved down into a denser environment and dense water moved up into a lighter environment, buoyancy and gravity will counteract the motion. Without such restoring forces, the

initial motion can amplify. The shaded, wedged area between the horizontal plane and the isopycnal denote the area of unstable exchange. Panel 2.7c illustrates that the energy conversion leaves the mean state altered. The tilt of the isopycnals are relaxed, reflecting a lower level of APE. In the process, the vertical gradient (stratification) is enhanced, while the lateral gradient is reduced.

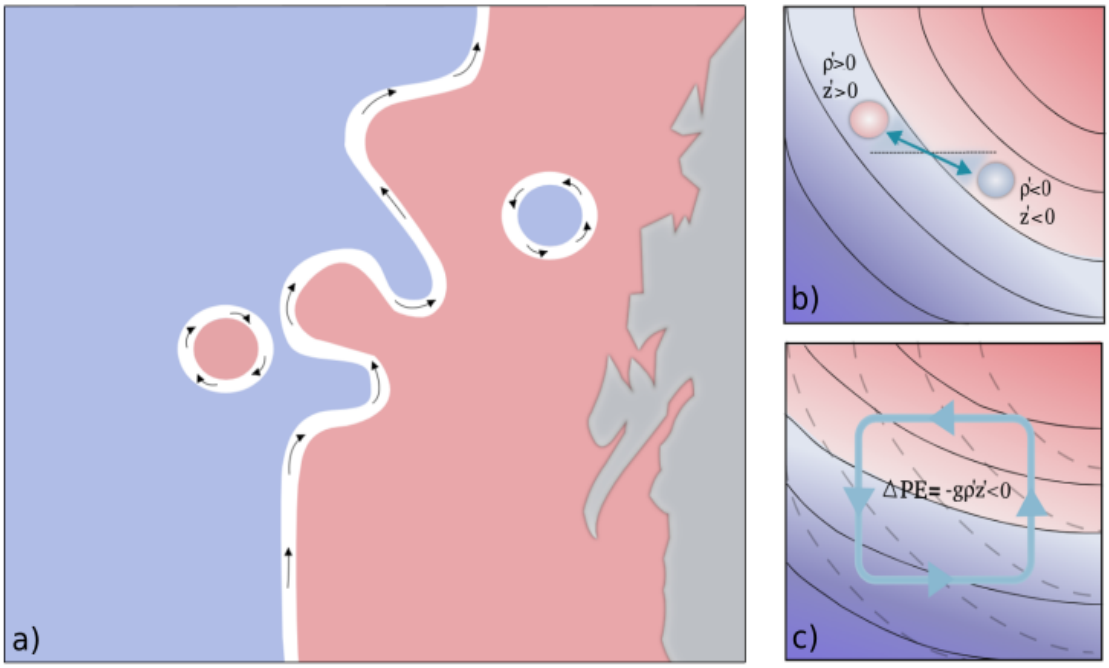


***Figure 2.7:*** *Idealized illustration of baroclinic instability. a) Horizontal overview of an unstable current with warm (light) waters to the left, and colder waters to right. A buoyant anticyclone and a denser cyclone have shed from the current. b) Vertical transect across the current showing slantwise convection. Light water is moved up ($z' > 0$) into a denser environment, $\rho' > 0$, and dense water is moved down ($z' < 0$) into a lighter environment ($\rho' < 0$). The original motions of the water parcels experience no restoring force, and the motions thus amplify. c) The end product of the process where the isopycnal slopes have relaxed. The available potential energy (APE) has been lowered, seen by the negative change in the APE ($g\rho' z'$). The APE has been converted into KE assisting the perturbation to continue its trajectory and grow. Dashed lines show the initial isopycnals. The restratifying effect of the vortices can be thought of as an overturning circulation, illustrated by the cyan arrows.*

The mean kinetic energy (KE) of the mean flow can also supply energy to a growing perturbation via barotropic instability; a lateral shear instability. However, baroclinic instability is considered to be the main cause for generating oceanic mesoscale vortices (*Gill et al.*, 1974; *Pedlosky*, 1987). The reason for this is related to the ocean's supply of available KE compared to APE. *Gill et al.* (1974) observed that vortices are especially abundant in regions of high baroclinicity, where the isopycnals are steep. They demonstrated with an energy analysis, that the bulk of APE contained in the sloping isopycnals is 1000 times larger than the bulk of KE contained in the large-scale circulation. Thus, they suggested that baroclinic instability is likely the primary source of mesoscale oceanic vortices. Later studies have supported their findings (*Smith*, 2007; *Tulloch et al.*, 2011; *Vollmer and Eden*, 2013). The mesoscale turbulence observed in satellite altimetry have shown to be highly correlated with local baroclinicity (*Smith*,

2007). Additionally, linear stability calculations performed globally up to 60° latitude, indicates that virtually the entire ocean is baroclinically unstable (*Smith*, 2007; *Stammer*, 1997). On the basis of satellite altimetry data, *Chelton et al.* (2007, 2011) identified origins of mescoscale vortices in all parts of the global ocean.

## 2.5 Baroclinic instability and the role of topography in the Subarctic Seas

Mesoscale vortices have been identified in all parts of the Subarctic Seas, in observations and numerical model simulations (*Rodionov et al.*, 2004). However, questions still remain regarding where the vortices originate, and how they are formed. Along the frontal zones and boundary currents there is typically high eddy activity (*Rossby et al.*, 2009). Vortices in such locations are believed to be locally generated, either from one form of instability (barotropic, baroclinic or frontal) or from a mixed instability (*Fossum*, 2006; *Jakobsen et al.*, 2003; *Sherwin et al.*, 2006; *Shi and Røed*, 1999). The central Lofoten basin and Labrador Sea off the west coast of Greenland are also areas known to be particularly rich in eddy activity. In these regions, vortices are believed to originate from an instability of the slope current and to primarily be advected into the basins (*Köhl*, 2007; *Lilly et al.*, 2003; *Prater*, 2002). This thesis aims to investigate whether baroclinic instability can account for the majority of the observed mesoscale eddy variability in the study region. Specifically, a core question in this thesis is how bottom topography affects the stability of the large-scale currents.

The dynamics governing the flow is likely strongly impacted by topography in this high latitude region, where both the planetary vorticity gradient and the density stratification is weak. In the Nordic Seas, the deep currents are in essence assumed to be governed by f/H theory and thus mostly follow f/H contours, where f is the Coriolis parameter and H is the bottom depth (*Isachsen et al.*, 2003; *Nøst and Isachsen*, 2003). A topographic steering of the currents is however also evident at the sea surface, indicating that the topographic control extends throughout the water column. Studies from some isolated regions have suggested that bottom topography may have a leading-order effect on baroclinic instability of the currents. To offer a complete view, this thesis aims to extend the existing studies to cover the entire region.

A linear stability analysis (LSA) can shed light on vortex origins and topographic impacts. The analysis provides the geographical distribution of growth locations and typical properties of the growing perturbations, such as length scales and growth rates. The growth rate indicates the time from a perturbation emerges until it reaches finite amplitude. The linear predictions can then be compared to the observed or modeled vortex field, to give an indication of a plausible generation mechanism. This thesis employs fields from a numerical ocean model for such a comparison, to address whether baroclinic instability is sufficient to explain both the spatial distribution and scales of the observed vortex field. A limitation of the LSA is that the analysis is linear, while vortex evolution is typically highly nonlinear after the growth stage. An inverse cascade, in

which like-signed vortices merge, will likely change the initial vortex size distribution. An LSA determines only the initial scales of the unstable waves (*Manley and Hunkins*, 1985). In addition to neglecting nonlinear interactions, the analysis neglects non-local effects. Vortices may propagate or be advected away from their source region. Thus, a full agreement between the linear predictions and the fully developed field is not expected.

As mentioned earlier, former studies of the stability of large-scale currents and on mesoscale dynamics in the Subarctic Seas have mostly focused on isolated areas. *Mysak and Schott* (1977) studied the stability of the NwAC around 63°N using idealized barotropic and baroclinic models and observations. The observed variability in the NwAC could not be explained in the barotropic model experiments, because barotropic instability did not produce growth rates near those inferred from observations. They then performed an LSA utilizing an two layer channel model with a uniform, cross-channel bottom topography. Properties of unstable growth arising from baroclinic instability yielded a better agreement with observations. In addition, adjusting the topographic slope to realistic values had a positive impact on the results.

*Ikeda et al.* (1989) investigated mesoscale variability in the frontal zone between the NwAC and the NCC off the south western part of Norway. An energy analysis showed that only 1% of the energy transfer in the current were associated with barotropic instability, and that the corresponding wavelengths were significantly larger than the observed eddy sizes. They concluded that baroclinic instability is primarily responsible for the variability of the NwAC in this area. They also found that an across-channel slope suppressed unstable growth, whereas an along channel slope enhanced the growth.

*Haugan et al.* (1991) studied the stability of the NwAC and the NCC between 61-64°N, using a $2\frac{1}{2}$-layered idealized model with a cross-shore topography. The effect of the topography on the NwAC stability were investigated in four model experiments. The current was placed in varying distances from the shelf-slope. One experiment with the entire current core located off the shelf-slope (over a flat bottom topography) produced a very stable current. Strong instabilities were however generated when most of the current core was located over the slope, in contrast to the findings of *Ikeda et al.* (1989).

Stability of the West Spitsbergen Current (WSC), the northernmost continuation of the NwAC, has been examined in several studies (*Hanzlick*, 1983; *Teigen et al.*, 2010, 2011). *Hanzlick* (1983) applied the model of *Mysak and Schott* (1977) and found evidence of baroclinic instability. Reduced growth rates in the WSC compared to the NwAC further south were attributed to the effect of steeper bottom slopes near Svalbard. He noted that a less steep slope promotes instability. *Teigen et al.* (2010, 2011) found that the easternmost part of the WSC to be both barotropically and baroclinically unstable.

*Thomsen et al.* (2014) performed a linear stability analysis of the Labrador Current on the western side of the basin to find an explanation for enhanced eddy kinetic energy observed in winter. They neglected topography in these calculations due to the focus on

seasonal effects. The analysis uncovered three dominant types of unstable modes. The largest was a so-called balanced, interior mode, originating from baroclinic instability. The Labrador Current off the west coast of Greenland has been thoroughly investigated using both idealized and realistic models (*Bracco and Pedlosky*, 2003; *Bracco et al.*, 2008; *Chanut et al.*, 2008; *Eden and Böning*, 2002; *Gelderloos et al.*, 2011). The realistic studies have argued that barotropic and baroclinic, or a mixed instability, is necessary to produce the observed vortex field. The more idealized studies suggest that primarily baroclinic instability can explain the observed vortex characteristics. *Bracco et al.* (2008) found that a topographic slope generally inhibits instability, but also that intense growth occurred in a region with a very steep slope. They proposed that the steep slope acts as a vertical wall, and that the current core is mostly over flat bottom and thus is governed by flat bottom dynamics.

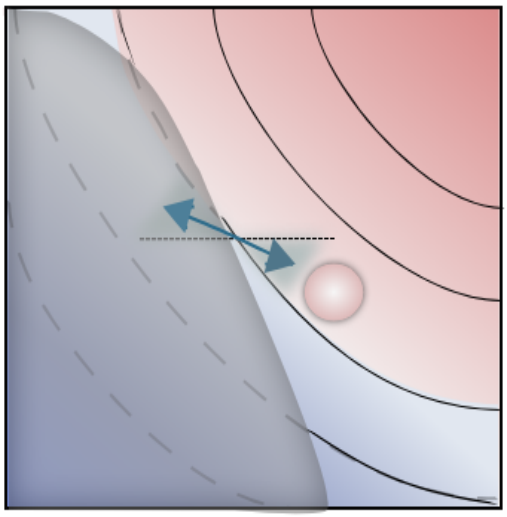

***Figure 2.8:*** *A scenario with the slope of the topogaphy (b) is greater than the isopycnal slope (a), i.e $b > a$. Unstable water mass exchange is prevented by the presence of steep topography. Red colors indicate a lighter environment and blue colors denser environment. Isopycnals are shown as black contours.*

In most of these studies, the impact of bottom topography on mesoscale dynamics is demonstrated in various ways. But diagnosing this impact is still subject to controversy. Additional studies have argued a topographic slope tends to stabilize the system, others have argued that it can act to destabilize the current (*Charney*, 1947; *Orlanski and Cox*, 1973; *Pedlosky*, 1964). A central question is thus; How is the stability of the large scale currents in the Subarctic Seas impacted by the presence of topography? A stabilizing effect of a bottom slope on baroclinic instability can be somewhat intuitive. When the bottom slope, $b$, lies between the horizontal plane and the isopycnal slope, $a$, it reduces the wedged area of unstable exchange (e.g. figure 2.7). If $b$ exceeds $a$, the bottom slope blocks the water mass exchanges that can lead to an APE release (figure 2.8). However, the bottom slope could also act to enhance the instability in another configuration, by forcing water parcels to move along an optimal route for energy conversion. In theory, a maximum conversion of APE into kinetic energy occurs at an angle $a/2$. Horizontal motion onto the slope induces a vertical motion, and topography can promote a motion proportional to this angle. The perturbed waves will then encounter a maximum

unstable plane, which can lead to intense eddy velocities. Possible outcomes are less intuitive when the isopycnal slope is oriented opposite of the topographic slope. This issue is highly relevant in the Subarctic region, where the boundary currents are flowing along the topography with light water to the right. Dramatic variations in the sea bed occur along the entire margin of the region (figure 2.9), and some of the most intense eddy activity occur along the steepest parts of the topography.

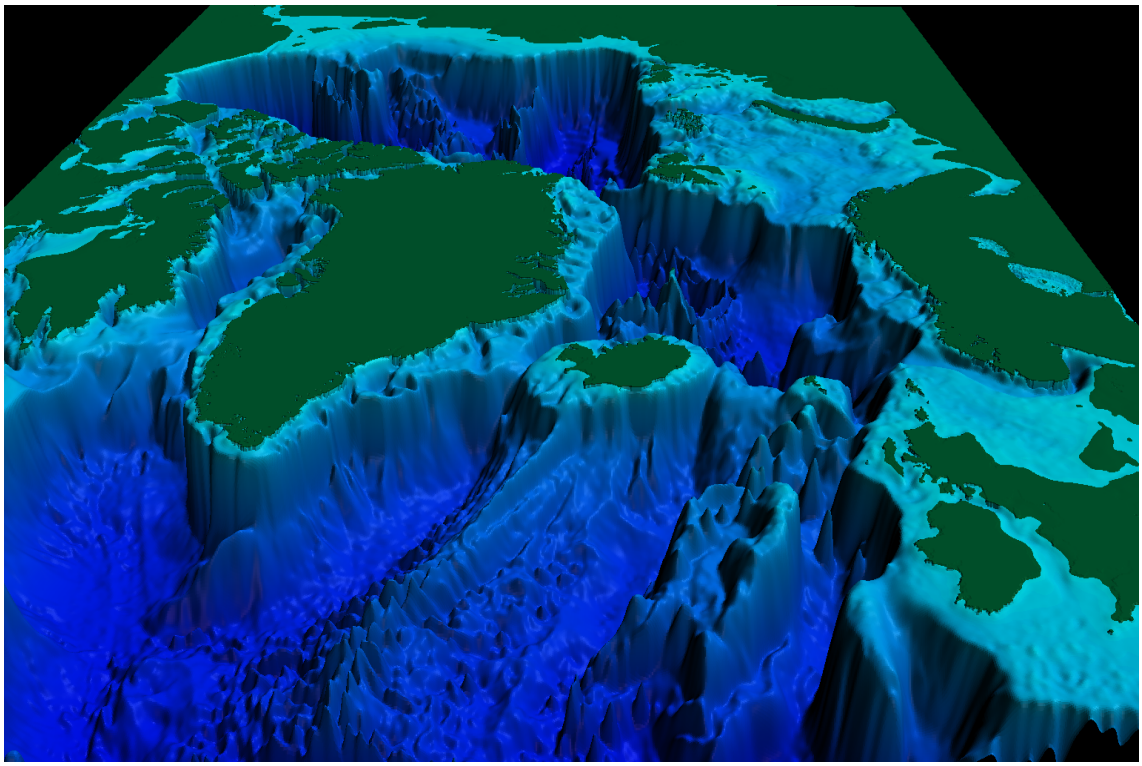

***Figure 2.9:*** *Topography from the 4 km model used in PaperII. Note that the aspects ratios are exaggerated.*

In a study of the stability of the NwAC round the Lofoten basin, *Isachsen* (2015) focused on the effects of topography. He performed a linear stability analysis based on a numerical model simulation, and compared the predictions with flat bottom Eady theory[1]. *Isachsen* (2015) showed that the current is most unstable over the steepest bottom slopes, in agreement with observed mesoscale variability. This is not apparent from extended Eady theory, which predicts suppressed growth.

The Eady model has been generalized to include a sloping bottom (*Blumsack and Gierasch*, 1972; *Mechoso*, 1980). In this model, stability is controlled by a slope parameter, $\delta = b/a$. A sketch of the growth rates' dependency on $\delta$ and wave numbers,

[1]The relatively simple Eady model captures the essence of baroclinic instability (*Eady*, 1949). The Eady model contains a zonal mean flow in thermal wind balance, a flat bottom channel with constant stratification, and no planetary beta. The Eady model supports waves trapped on each boundary. If these waves couple, they can act to mutually amplify and thus give rise to a growing disturbance. Waves that are larger, and thus deeper, can under the right conditions interact. The fastest growing wave is the wave that extracts the maximum APE from the background state. In the Eady model, the fastest growing wave has a horizontal scale near the Rossby deformation Radius, $L_d$. This is why $L_d$ is considered the canonical horizontal length scale for weather systems in the atmosphere and ocean.

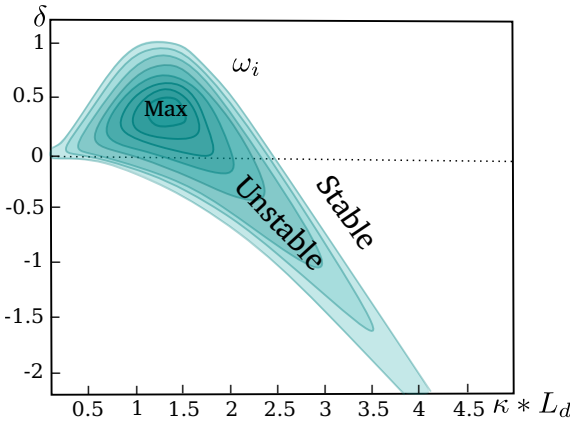


***Figure 2.10:*** *Simplified sketch of computed growth rates, $\omega_i$ (colored contours), versus $\delta$ for different slope configurations and wave numbers normalized by the Rossby deformation radius, $\kappa L_d$. $\delta$ is positive when the slopes are oriented the same way. High wave numbers reflect small length scales. The white areas signify a stable configuration. Maximum growth occur around $\delta \approx 0.5$ and $\kappa L_d \approx 1.3$*

is shown in figure 2.10. Waves are stabilized for $\delta > 1$ (such as seen in the example figure 2.8). For positive $\delta$ values, the growth rates are enhanced compared to a flat bottom, $\delta = 0$. Maximum growth occur close to $\delta = 0.5$. For negative $\delta$ values, a narrow band of successively shorter waves are unstable, with lower growth rates than generic Eady waves. Thus, in a setting with very steep topography, this theory predicts reduced growth rates relative to flat bottom theory. *Isachsen* (2015) remarks that the areas where maximum growth occur show such a reduction relative to a flat bottom.

However, the vertical structure of the wave amplitude differed from the Eady model. Due to the contribution of the bottom topography, the unstable growth is not typically associated with interacting edge waves, such as in the Eady model. Instead, it is associated with the interaction between an edge and an interior Rossby wave, or solely between interior Rossby waves (see section 3.3.4 for further details). *Tulloch et al.* (2011) suggests that this type of instability is prevalent in the global ocean. The Eady model cannot support such waves in the interior due to it simplification of constant isopycnal slopes, whereas typical oceanic conditions are commonly surface intensified. The findings of *Isachsen* (2015) thus indicates that a more complex model is needed to explain the dynamics in this region.

This thesis extends the analysis of *Isachsen* (2015) with the aim to test the applicability of the Eady model as a leading-order model for the entire subarctic region. Besides attaining a better understanding of the dynamics in a negative $\delta$-regime, diagnosing the applicability is also of interest since some eddy transport parameterizations rely on flat bottom Eady growth rates and length scales.

## 2.6 The regeneration of the Lofoten Vortex

The latter part of this thesis focuses on the longevity and evolution of the Lofoten Vortex. Studying this vortex in detail can lead to a broader understanding of the longevity of anticyclones in general. With a core depth centered at about 700–900m, and a typical

radius of 2-4$L_d$, the LV share similarities with sub- or intra-thermocline anticyclonic vortices found in other oceanic regions. These vortices have a lens-like core, located in or below the main thermocline, and are also known to be long-lived (*Prater and Sanford*, 1994). An example are Mediterranean Water eddies (Meddies) that can stay coherent for multiple years (*Richardson et al.*, 2000). Meddies typically propagate over longer distances and complex topography, and their lifetimes are strongly affected by seamount encounters. The LV on the other hand, is topographically locked within the 3000-m isobath in the Lofoten Basin, and thus resides in a limited region without such encounters (*Fer et al.*, 2018; *Rossby et al.*, 2009; *Søiland and Rossby*, 2013). However, the environment the LV is located in is strongly turbulent. Figure 2.11 shows a model example of the intense mesoscale variability in the basin. High deformation rates, vortex instability and dissipation from bottom friction are some processes that can act to terminate the LV long before its potentially decadal long lifetime. The observed relative vorticity in the vortex core is typically around $-0.5f$ but the maximum can approach the theoretical limit for anticyclones, $-f$ (*Fer et al.*, 2018). In order to sustain such high levels of intensity, a regeneration mechanism seems necessary. Previous studies have suggested two mechanisms that rejuvenate the vortex; wintertime convection and vortex merging. This thesis investigates the influence of vortex merging.

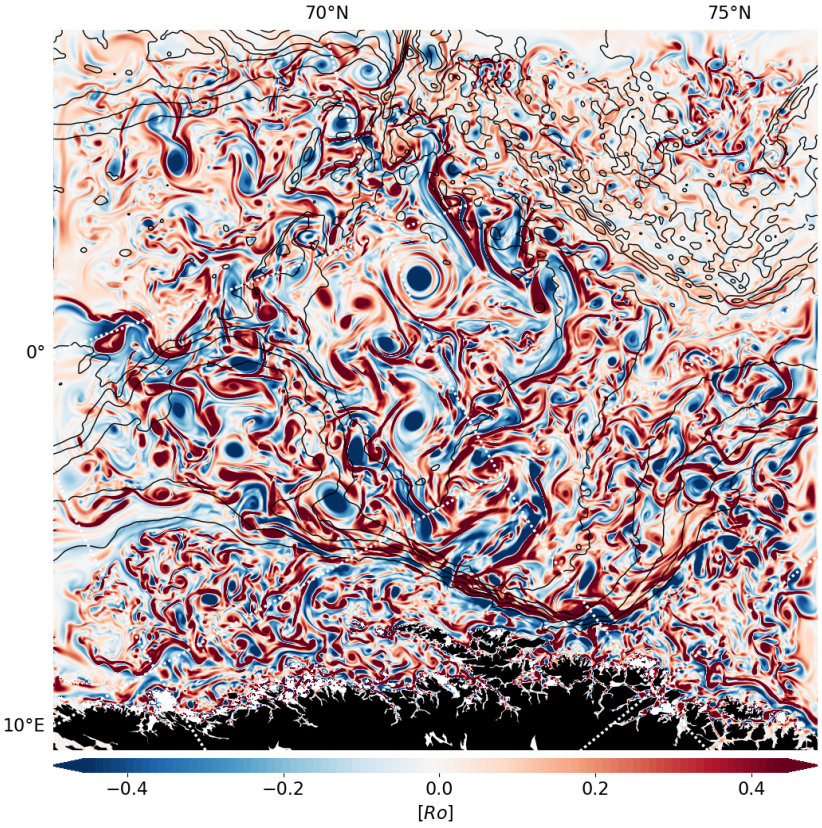


***Figure 2.11:*** *The Rossby number (the relative vorticity field normalized by f) in the Lofoten Basin during wintertime, from a high resolution model simulation used in this thesis. The Lofoten Vortex is indicated by LV in the basin.*

Vortex merging is a complex and nonlinear process that plays a key role in the transfer of energy across multiple scales. A simplified example of the process is the coalescence

of two same-signed symmetric (equal in size and strength) vortices with cores located at the same vertical level. The merger is initiated when the ratio between the vortex core radius and the separation distance is below a certain threshold. The co-rotating vortices then quickly deform due to mutually imparted strain, generate intrusions or filaments that connect the cores, and finally merge to form one larger, single structure. This type of vortex interaction leads to horizontal growth of vortex size, and is a possible channel for the inverse energy cascade predicted in geostrophic turbulence. The physical mechanism behind vortex mergers has been described in various ways (*Brandt and Nomura*, 2007; *Cerretelli and Williamson*, 2003; *Dritschel*, 1985; *Huang*, 2005; *Melander et al.*, 1988; *Meunier and Leweke*, 2001; *Meunier et al.*, 2002), but is perhaps most easily illustrated by decomposing the vorticity into symmetric and anti-symmetric parts. *Cerretelli and Williamson* (2003) show that the anti-symmetric contribution generate two counter-rotating vortex pairs that push the cores toward each other (see figure 2.12). This idealized case is without a background flow, stratification, straining field, and the influence of surrounding vortices, which could all impact the vortex interaction. For example, opposite-signed vortices may couple with the approaching vortices, and act to inhibit or assist in the merger, by affecting the separation distance through mutual-advection. An example of this is shown in figure 2.13, where a cyclone is entrained in the merger between the LV and another anticyclone. The other anticyclone formed a dipole with the cyclone, and the resulting advection was seen to accelerate the anticyclone toward the LV.

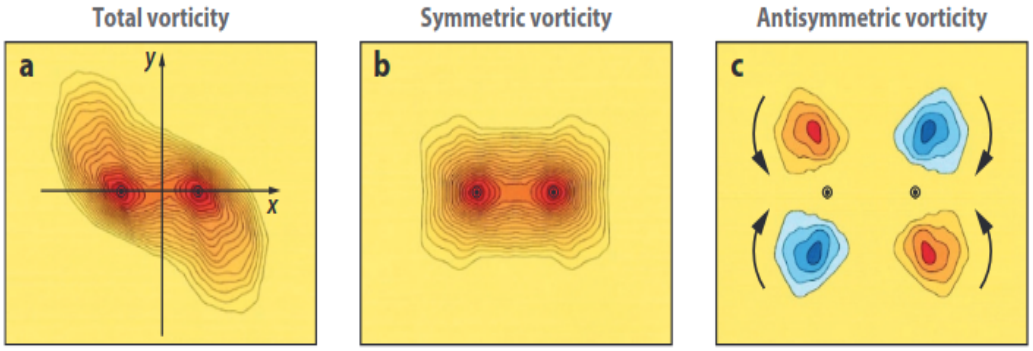


***Figure 2.12:*** *The decomposed relative vorticity field at the initial stage of a vortex merger (figure10 in Leweke et al. (2016), which was adapted from Cerretelli and Williamson (2003)). a) Total, b) symmetric and (c) anti-symmetric vorticity field.*

Due to the complexity of the process, investigations of vortex mergers have mostly been conducted in theoretical settings. Some theoretical works consider asymmetric vortex pairs (*Brandt et al.*, 2010; *Melander et al.*, 1987; *Ozugurlu et al.*, 2008) or symmetric vortex interactions with external influences (*Brandt and Nomura*, 2007; *Carton et al.*, 2002; *Dritschel*, 2002; *Perrot and Carton*, 2008, 2010). However, most works consider interactions of identical vortices in an isolated, quiet environment (*Carton*, 1992; *Griffiths and Hopfinger*, 1987; *Melander et al.*, 1988; *Sutyrin and Yushina*, 1989; *Velasco Fuentes and Velázquez Muñoz*, 2003; *von Hardenberg et al.*, 2000; *Waugh*, 1992). This is a highly idealized case and real oceanic vortices are seldom identical. A more realistic scenario is where the vortices differ in size and strength, which is also the case

in the Lofoten basin. In addition to complete merger events, as described above, the merger process can then also be partially completed, and other processes, such as partial straining out and complete straining out, can occur (*Brandt et al.*, 2010; *Dritschel*, 1995; *Dritschel and Waugh*, 1992; *Yasuda and Flierl*, 1995). In a partial merger, parts of the vorticity of the weaker vortex is absorbed by the stronger vortex (*Yasuda and Flierl*, 1995). In a straining out event, the weaker vortex is drained out into a thin filament that wrap around the stronger vortex. Moreover, interacting vortex cores may not have the same density, and thus be located at different depths. An interaction fulfilling some required conditions, such as horizontal and vertical separation distance, will then lead to a vertical alignment of the cores (*Reinaud and Dritschel*, 2002).

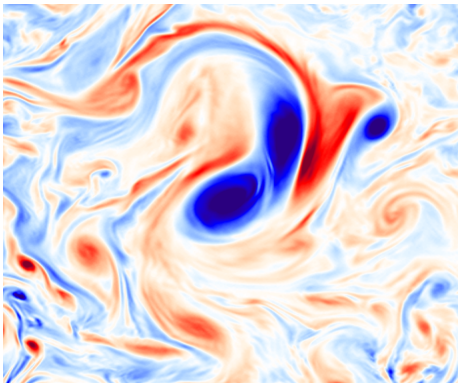

***Figure 2.13:*** *An example of a merger event between the LV and another anticyclone. Red colors indicate positive relative vorticity, blue colors indicate negative vorticity). A cyclone assists in the merger.*

The notion of vertical alignment was introduced by *McWilliams* (1989). He observed that vortices stacked on top of each other in numerical experiments of decaying, stratified quasi-geostrophic turbulence. The end state was dominated by tall vertical structures, arising from a combination of vortex cores. Studying the process analytically using a two-layer quasi-geostrophic system, *Polvani* (1991) found that vertical alignment occur for larger vortices, with radii on the order of, or larger than, $L_d$. A vertical alignment thus leads to deeper structures once they have grown to $L_d$, and is connected to the barotropization of energy in the inverse cascade. Motivated by this, several more studies have considered the vertical alignment process (*Corréard and Carton*, 1999; *Martinsen-Burrell et al.*, 2006; *Perrot et al.*, 2010; *Reinaud and Carton*, 2019, 2020; *Reinaud and Dritschel*, 2002; *Sutyrin et al.*, 1998). However, none of these works consider the process in fully realistic oceanic conditions. This thesis aims to contribute to the existing literature by documenting the process for a vortex in a realistic ocean model.

In situ observations of vortex interactions in fully realistic conditions are scarce, since obtaining observations of such a swift process is challenging, and requires high temporal and spatial resolution. One of the first records of a vortex merger was made in the East Australian Current (*Cresswell*, 1982). The observations were taken before and after the merger event, and show-cased the alignment of two vertically offset vortices. Based on these observations, *Nof and Dewar* (1994) studied the coalescence of

two anticyclonic lenses with different densities, utilizing laboratory and numerical experiments. They found that the anticyclonic lenses tend to vertically align rather than undergo a horizontal merger. The lighter vortex stacks on top of the denser vortex, resulting in a double core vertical structure.

The number of observational records of double core anticyclones has increased in recent years (*Armi et al.*, 1989; *Baird and Ridgway*, 2012; *Barceló-Llull et al.*, 2017; *Belkin and Mikhailitchenko*, 1986; *Belkin et al.*, 2020; *Bogdanov et al.*, 1985; *Brundage and Dugan*, 1986; *Carton et al.*, 2010; *Cresswell*, 1982; *Dmitrenko et al.*, 2008; *Garreau et al.*, 2018; *Itoh and Yasuda*, 2010; *Lilly et al.*, 2003; *Prater and Sanford*, 1994; *Rogachev et al.*, 2007; *Schultz Tokos et al.*, 1994), but whether these have formed from an alignment has not directly been documented. In the Labrador Sea, *Lilly et al.* (2003) found that both Irminger rings and convective lenses exhibit vertically aligned cores. They argued that the cores stem from two distinct vortices, rather than forming from wintertime convection. In the Algerian Basin *Garreau et al.* (2018) observed an anticyclone with two cores stacked in the vertical. The two lens-like cores contained water masses from different origins, suggesting that the vertical structure is the outcome of a vertical alignment of the two cores. In the North Atlantic, *Belkin et al.* (2020) documented the alignment of two Gulf Stream rings. They observed a double core anticyclone in in situ measurements and examined its evolution using satellite maps of sea surface temperature and sea surface height. The satellite observations suggests that the anticyclone was formed by an interaction between two warm-core anticyclonic rings. There also exists records of double core anticyclones in the Arctic Ocean (*Zhao and Timmermans*, 2015). Some of these studies refer to this type of anticyclones as *unusual*. However, the growing number of such observations suggests that it might instead be common. The observations from the Labrador Sea indicates that the majority of the anticyclones have a double core rather than a single core. It is on the other hand not known what impact this process has on the resulting combined vortex. If this type of vortex interaction is typical for long-lived anticyclones, investigating this impact can contribute to understanding their evolution.

In some observations from the Lofoten Basin (Figure 2.14), the LV also consist of two cores in the vertical (*Fer et al.*, 2018; *Yu et al.*, 2017). This feature has previously been attributed to seasonal changes of the stratification. However, this thesis shows that it is a result of a vertical alignment. Revisiting the hypothesis of *Köhl* (2007), this work investigates the role of vortex mergers in regenerating the LV. Horizontal vortex mergers, complete and partial, are examined, but a key aspect of this work is to specifically examine the impacts of vertical alignments.

## 2.7 The formation of stable surface anticyclones

Observations from the North-Atlantic and the Pacific suggest an occurrence of several long lived anticyclonic mesoscale vortices trapped above topographic depressions. The anticyclones are near-surface features and typically have a vertical extent of $1000 - 1500$ m, although a deep velocity component may exist. At several locations, the anticyclonic vortices are embedded within a time mean cyclonic flow that is locked

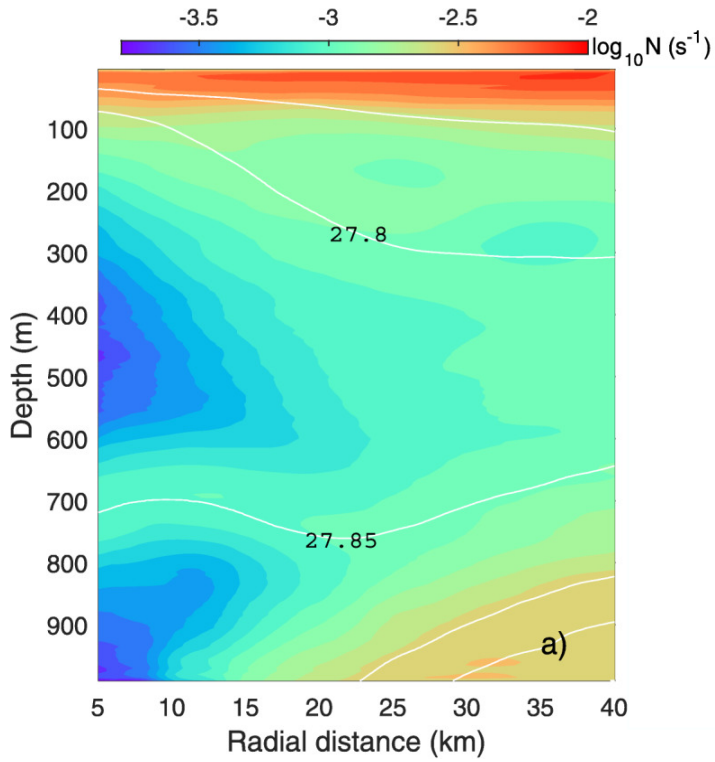


***Figure 2.14:*** *Figure 6a in Yu et al. (2017) showing the radial profile of N (log10) in the Lofoten Vortex core. The white lines are density contours, every* $0.05 kgm^3$.

to the topography. Anticyclonic recirculations in the North Atlantic considered to be quasi-permanent features are the Rockall Trough Eddy and the Mann Eddy. The persistence of both vortices are evidenced by their sea surface signature observed in altimetry climatologies (figure 2.15). Records also exists of long lived anticyclones clustering in the Iceland Basin (*Zhao et al.*, 2018a). In the Pacific, robust anticyclones have been observed along the Kuril-Kamchatka trench and near the deep Bussol Strait off the Kuril Islands (*L'Her et al.*, 2021; *Prants et al.*, 2020). In addition, mean dynamic height data have revealed two semi-permanent anticyclonic eddies off the north-east coast of New Zealand, the Wairarapa and Hikurangi eddies. They are found over the Hikurangi Trough, a 3750 m deep bathymetric feature (*Chiswell*, 2005). The most studied location is the Lofoten Basin, a bowl-shaped basin, with a time mean cyclonic slope circulation. As noted, the LV is a quasi-permanent anticyclonic vortex situated in the center of the basin. This thesis focuses on the LV. (*Belonenko et al.*, 2017; *Bosse et al.*, 2019; *Fer et al.*, 2018; *Köhl*, 2007; *Raj et al.*, 2015; *Søiland and Rossby*, 2013; *Søiland et al.*, 2016; *Straneo and Fiammeta*, 2015; *Yu et al.*, 2017).

The recurring observations of long lived anticyclones over topographic depressions are intriguing. The vortices are typically significantly larger than the internal deformation radius, and thus prone to baroclinic instability. It is perplexing why vortices of this size, submerged in a highly turbulent field, should not decay faster nor break up, but rather exhibits life times that extends far beyond an expected time span. Dissipation from e.g. bottom friction would alone act to spin down the vortex over the course of months. The mechanism behind such a resilience is still not clear.

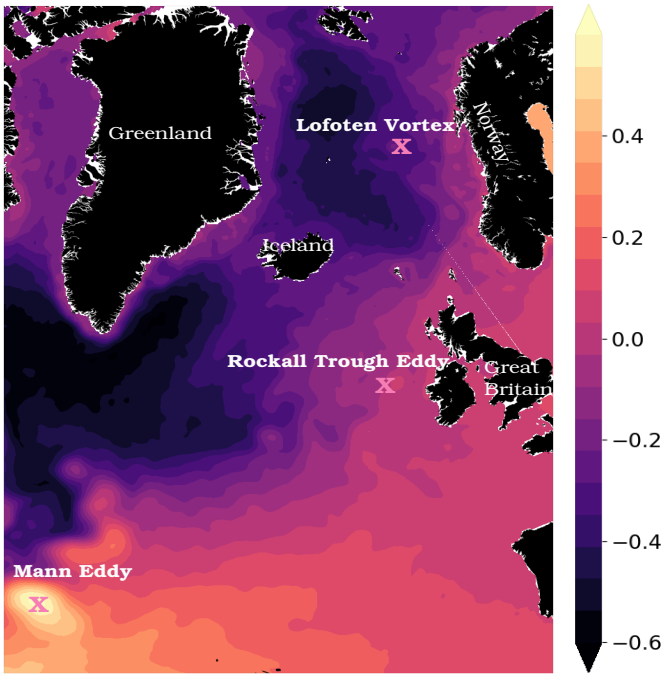


***Figure 2.15:*** *Mean dynamic topography [m] from AVISO. Indicated by the crosses are the Lofoten Vortex in the Lofoten Basin, the Mann Eddy in the Newfoundland Basin, and the Rockall Trough Eddy in the Rockall Trough.*

Understanding how the LV is maintained has been the subject of considerable scientific attention over the past few decades, and its extreme persistence is well-documented. How such a vortex can stay stable is not obvious and remains an open question. With a lifetime that extends over several decades, it raises the question whether the vortex could be considered part the *steady* circulation, rather than being a transient feature.

A determining factor for the formation of the Lofoten vortex is evidently topography. An indication of this was found by *Belonenko et al.* (2021). They conducted model simulations with varying topography over the Norwegian and the Lofoten Basins. The model was initialized from a state with no preexisting mesoscale vortex field. The Lofoten basin topography was removed (flattened) in two experiments and retained in two others. Without the Lofoten Basin topography, no LV formation occurred in the basin. Rather, a persistent anticyclone formed in the Norwegian Basin, indicating that a topographic depression is essential in obtaining the observed circulation pattern.

*Solodoch et al.* (2021) examined the topographic influence on the formation of bowl-trapped anticyclones in idealized spin down experiments over a bowl-shaped basin. They utilized a primitive equation model with one and two isopycnal layers. Both a bowl-trapped surface intensified anticyclone and a bottom intensified cyclonic slope circulation emerged from a broad spectrum of random initial relative vorticity distributions and a variety of different basin configurations. Solodoch notes that if the anticyclone is transient, this could explain why it does not show up in topographic turbulence theory predictions. On the other side, he also remarks that the anticyclone in their simulations show no significant decay over a long period ($>$ 10 years).

*Shchepetkin* (1995) studied vortex-topography interactions using barotropic shallow water model experiments. Both relative vorticity and potential vorticity initial states were used, composed of randomly oriented dipoles in a square basin. The flow organized into a cyclonic boundary current over the topography. Additionally, a large anticyclone emerged in the domain center in experiments on an f-plane or with a weak planetary $\beta-$effect. With a stronger planetary $\beta$, the anticyclonic vortex decayed due to planetary wave radiation.

So, model simulations reproduce the pattern of a long lived anticyclone enclosed by a cyclonic circulation. Theory for turbulent barotropic flows over topography however only predicts a cyclonic circulation in a basin (*Bretherton and Haidvogel*, 1976; *Salmon et al.*, 1976) and anti-cyclonic flow over seamounts (*Nycander and Lacasce*, 2004). This work has led to parameterizations of eddy-topography interactions (*Cummins and Holloway*, 1994; *Holloway*, 1992; *Merryfield et al.*, 2001; *Zou and Holloway*, 1994). While the widely utilized *Gent and Mcwilliams* (1990) (GM) parameterization would, for decaying turbulence, bring the ocean to a state of rest under the impact of eddies. *Holloway* (1992) suggested rather that unresolved eddies should drive the ocean toward a state with mean currents aligned with topography. The GM parameterization is based on eddy-induced transport of isopycnal layer depth, and the notion that eddies act to remove APE from the mean flow and level out isopycnals (as discussed in 2.4). Instead of providing a damping effect, *Holloway* (1992) in contrast argues that the eddies act as a driving force to the ocean circulation.

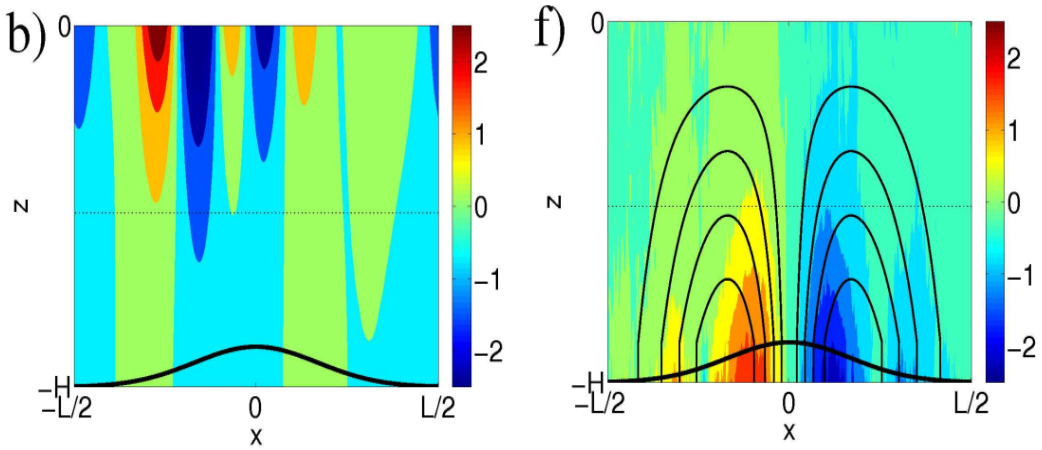


***Figure 2.16:*** *Figure 2b,f in Venaille (2012). Topographic bump is shown in a thick black contour. Left: Vertical transect of the PV field at t=0. Right: The final state. The meridional velocity field taken in the center of the domain (thinner black contours).*

The theory assume a barotropic ocean, but the ocean is not a homogeneous fluid. A question is whether the predictions are valid also in a stratified setting. Aiming at improving the parameterizations of *Holloway* (1992), *Merryfield* (1998) expanded to a continuously stratified setting building on the procedures of *Salmon et al.* (1976). His calculations indicated that the barotropic findings are generally consistent with the stratified case, yielding anticyclonic flow over bumps. A difference however is that stratification introduces a vertical structure of the mean flow. In the stratified predic-

tions, the topographically locked flow is bottom intensified. Increased stratification leads to further bottom intensification of the flow. Also using statistical mechanics, *Venaille* (2012) similarly found that a surface-intensified random initial field tend toward a bottom intensified flow correlated with topography. These theoretical predictions corresponded well with their numerical model simulations of freely evolving stratified QG turbulence over a bump, shown in figure 2.16.

So, studies that extended to stratified turbulence over variable topography have found that the solutions keep the sense of rotation, cyclonic flow over a bowl, but attains a vertical structure that is bottom-intensified. This offers an explanation for the bottom-intensified cyclonic slope circulation. But the predictions cannot explain an anticyclonic circulation enclosed in the cyclonic circulation anticipated over a bowl. In calculations of two-layer QG turbulence over topography, *Merryfield and Holloway* (1999) did derive solutions of a bottom intensified mean flow with some cases of a reversed upper layer mean flow, stronger than the lower layer flow. However, this occurs when applying strong friction and cannot account for bowl-trapped anticyclones produced in inviscid model simulations nor in observations from settings with realistic bottom friction. There is presently no formal description of how the two circulation patterns can coexist. Nevertheless, such patterns are found in observations and in numerical model simulations as described earlier. This thesis revisits the theory to seek a better understanding of this discrepancy. A minimum enstrophy solution for a two layer flow over topography is derived and the solution examined in light of numerical model experiments of fully turbulent flow over topography.

# Chapter 3

# :Research tools

> The subject of geostrophic turbulence is a wondrous one, giving rise to phenomena that are both beautiful and important — the jets and eddies on Jupiter and the weather on Earth are but two examples.
>
> *V*allis (2006)

This chapter contains an overview of the various models and methods applied in this thesis. The individual papers provide additional details on the methods, and the following overview is therefore meant to complement the information already covered in the papers. This thesis' research topics are explored in various degrees of complexity. In order to understand ocean dynamics, one approach is to utilize a numerical ocean with its full complexity. The results may however be influenced by numerical choices of how to represent various processes. Moreover, it can be hard to distinguish the effect of single processes when the model simulations include a myriad of different kinds of interactions. Furthermore, the model output alone do not explain the simulated phenomena. In tandem, it is beneficial to utilize a simplified model in order to study the role of a few processes in greater detail. In fact, the foundation of vortex dynamics has its core nearly exclusively in simplified theory using approximate models. This thesis therefore make use of a combination of realistic numerical and idealized numerical model simulations, and analytical analysis based on simplified models.

## 3.1 Numerical model simulations

The model tool in all the papers in this thesis is the Regional Ocean Modeling System (ROMS; *Haidvogel et al.*, 2008; *Shchepetkin and McWilliams*, 2005). ROMS is a hydrostatic, primitive equation model formulated with a horizontal near-orthogonal staggered C grid and a generalized sigma coordinate system in the vertical, the s-coordinate (*Shchepetkin and McWilliams*, 2005). The model layers follow the variations of the seabed terrain and can support a weighted distribution of the layers with depth. An increase in vertical resolution can be gained either near the free sea surface, ocean floor or both. This allows for a more detailed description of the processes occurring in the

region(s) of enhanced resolution. The stretching is controlled by the parameters $\sigma_t$ and $\sigma_b$, with values from 0-1, and a higher number signifies larger amount of stretching. In all model simulations, the resolution is increased near the sea surface which allows for a well represented pycnocline profile. Minor stretching is applied near the bottom. Stretching parameters along with other simulation details are listed in table 3.1. In the following sections we describe the various model setups in more detail.

| MODEL RUN | SUBARCTIC | LOFOTEN BASIN | IDEALIZED BOWL |
|---|---|---|---|
| LATERAL RESOLUTION | 4 km | 0.8 km | 5 km |
| VERTICAL LAYERS | 35 | 60 | 30 |
| VERTICAL RESOLUTION(MAX, MIN) | 0.3-80 m | 0.3-80 m | 1.7-160 m |
| DURATION | 1993-2005 | 1995-2002 | 5-7 years |
| MODEL OUTPUT | 24 hours | 6-24 hours | 24 hours |

***Table 3.1:*** *The model setups used in this thesis.*

### 3.1.1 Realistic model runs

The model experiment for Paper I spans a broad region containing the entire Subarctic Seas and the Arctic Ocean. This thesis focuses on the Nordic Seas (model domain is shown in figure 3.1). The model has a 4 km lateral resolution and 35 vertical levels. This model gives the basis for performing a stability analysis on the mean flow field and to examine the statistics of the vortex field. The model experiment for Paper II covers a smaller area (model domain is indicated by the black line in figure 3.1). The model spans the Lofoten Basin, with a lateral resolution of 800 m and with 60 vertical levels. A higher spatial as well as temporal resolution in this model allows for a more detailed analysis of stages in a vortex life cycle and vortex interactions.

At a resolution of 4 km and 800 m, mesoscale vortices are partly to fully resolved on the model grids. With an internal Rossby deformation radius on the order of 10 km over the basin, the Lofoten Basin simulation is considered a so-called eddy-resolving model. This implies that mesoscale variability, i.e. oceanic weather, is to a large extent represented in the model, as opposed to being parameterized. The Lofoten basin run thus includes more variability than the eddy-permitting Arctic model run, and even supports some sub-mesoscale($< 10$ km) features. To ensure that the internal model dynamics are consistent with the boundary conditions the first five years in the 4 km run and the first two years in the 800 m run are considered model spinup and omitted from the analysis. The two models are otherwise set up and run with similar parameters and forced identically.

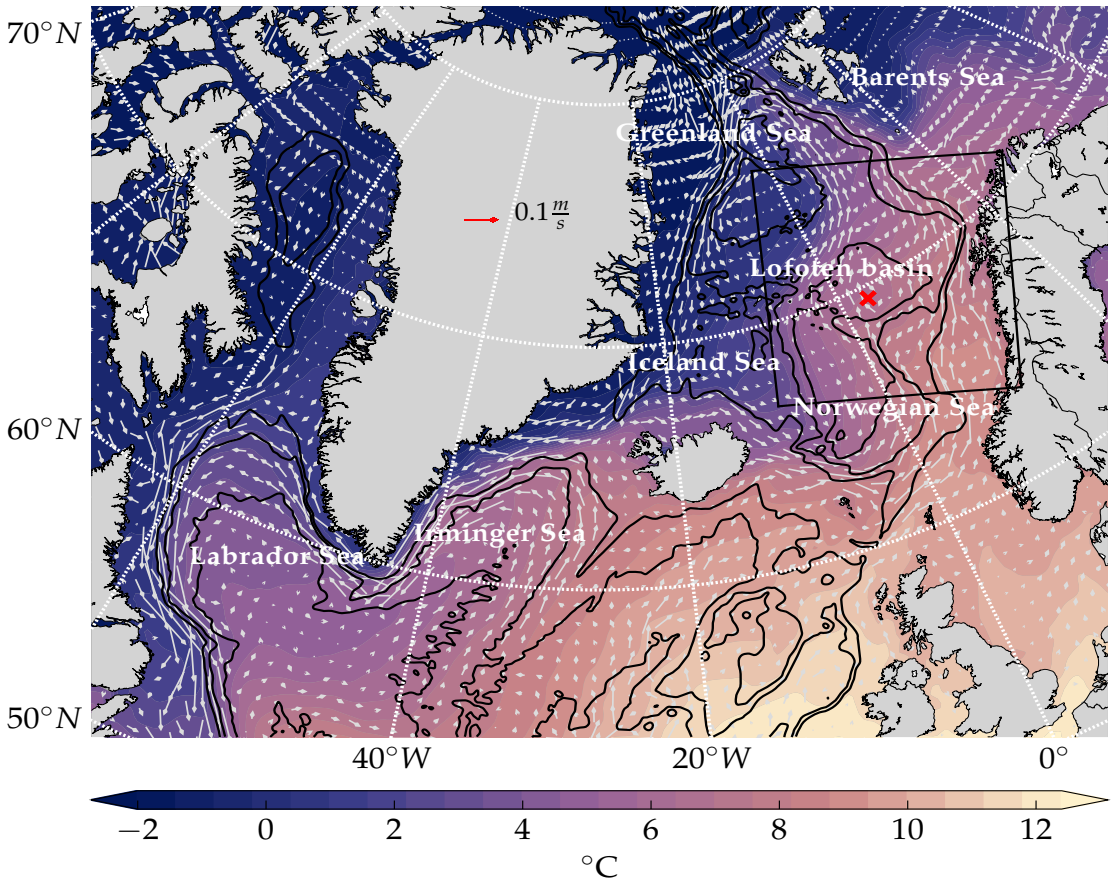


***Figure 3.1:*** *Time-mean SST from the OSTIA reanalysis. The time-mean surface geostrophic currents are shown by the vectors (AVISO). The Lofoten Basin model domain is marked by the black box, and the observed time-mean position of the Lofoten vortex by the red cross. Topography is shown in black contours for every 1000 m.*

The initial model states utilize fields from the global Forecast Ocean Assimilation Model (FOAM) (*MacLachlan et al.*, 2015). FOAM has a resolution of 25 km, and thus no mesoscale eddy field at these latitudes is supported. A fourth-order centered scheme is used for vertical advection, and a third-order upwind scheme is used for horizontal advection. No explicit horizontal eddy viscosity or diffusion is applied, but the upwind advection scheme includes some implicit biharmonic diffusion. The k–$\varepsilon$ version of the general length scale (GLS) scheme is chosen to represent the net effects of small-scale vertical mixing (*Umlauf and Burchard*, 2003; *Warner et al.*, 2005). The open lateral boundaries are relaxed toward FOAM with a 15-day relaxation time scale, and atmospheric forcing from the ERA-interim atmospheric reanalysis (*Uppala et al.*, 2005) is applied every 6 hours. Runoff from major rivers are supplied by monthly climatologies from a river discharge model from the Norwegian Water Resources and Energy Directorate (*Beldring et al.*, 2003).

### 3.1.2 Idealized model run

The idealized model runs are carried out to investigate how a turbulent flow on its own evolve over topography, without the added complexity of other factors, such as applied forcing. Model simulations are initialized with a random velocity field freely evolving over a bowl-shaped basin and over random topography. The random topography includes both topographic depressions and elevations. To evaluate the behavior of isolated anticyclones and cyclones over a bowl, some runs are initialized with single monopoles over the basin.

The model geometry is a doubly periodic square box with sides of length $L$ =1205 km. The model's lateral grid spacing is 5000 m, with 30 vertical levels. A 5th order upwind scheme is used for horizontal advection. A fourth-ordered centered scheme is used for vertical advection and vertical mixing is parameterized by K profile (KPP) scheme (*Large et al.*, 1994).

The bottom topography (H) employed has the form

$$H = D + h_0 \cdot e^{-(\frac{(x-xc)}{a}^2 + \frac{(y-yc)}{b}^2)},$$

where $D$ =1500 m is the depth outside the bowl, $h_0$ =600 m is the bowl depth, xc and yc are the center points of the model domain, a and b, are the e-folding widths in the x and y directions. We use a slightly elliptical bowl with $b/a \approx 0.8$.

Density is solely determined by temperature using the 1980 equation of state (EOS-80), with salinity set to a constant, $S = 35$ PSU. The temperature stratification is given by $T = T_s e^{\frac{z}{h_e}}$, where $T_s$ is the sea surface temperature and $h_e$ the stratification depth. This profile is used as a horizontally homogeneous background field in both the turbulence and monopole simulations. For the turbulence simulations, grid-scale Gaussian noise is added to the temperature field at each model layer. The noise is surface intensified and decays exponentially with an e-folding scale equal to the stratification depth, which amounts to $h_e \approx (1/4)D$. With no flow at the bottom, the initial velocity field in geostrophic balance is given by integrating the thermal wind relation upward:

$$u = \int_{-H}^{z} \frac{g}{\rho_0 f} \frac{\delta \rho}{\delta y} dz,$$
$$v = \int_{-H}^{z} -\frac{g}{\rho_0 f} \frac{\delta \rho}{\delta x} dz.$$

Here $g = 9.81 ms^{-2}$ is the gravitational constant, $\rho_0$ is a reference density, $\rho$ is the density, and $dz$ is the vertical grid spacing. All simulations are run on an f-plane with the Coriolis parameter set to $f = 1.37 \cdot 10^{-4} s^{-1}$, to represent a high latitude basin. The internal Rossby radius, using the approximation $L_d = \int_{-H}^{0} N dz / f\pi$, is about 20 km. $N$ is the ambient buoyancy frequency.

Spin down experiments are run for 7 years. A quadratic bottom drag with low, intermediate and high values of drag-coefficients is added in some simulations. The bottom

stress is given by the function $\tau_b = C_d \|\mathbf{u_b}\| \mathbf{u_b}$ , where $C_d$ is a drag coefficient and $\mathbf{u_b}$ is the bottom velocity. Intermediate friction ($C_d = 10^-3$) is most fitting to a realistic setting, and we chose to focus on comparing these runs to the inviscid case.

To generate the random bottom topography, Gaussian noise is subtracted from the depth, D. The amplitude of the Gaussian noise is set to 100 m and the width of the perturbations to approximately 3-5$L_d$. The generated fields consist not only of closed contour topographic features, but also of open troughs and ridges.

In the monopole simulations we construct a vortex with the following relative vorticity profile $\zeta = \pm\zeta_0 e^{-(\frac{r}{R_e})^\sigma}$. Vortex polarity is given by the sign, r is the radial distance to the center of the vortex, and $\sigma$ denotes the radial vorticity gradient which the controls the radial steepness of the profile. $\zeta_0 = V_0/R_e$ is set by the maximum azimuthal velocity, $V_0 = 0.6$ m/s, and the vortex e-folding radius, $R_e = 40$ km, prescribed at initialization. The ratio of vortex size to $L_d$ is adjusted according to typical observed values of $R_e/L_d \approx$ 2-4. The azimuthal velocity at the surface is determined from $v(0,r) = \frac{1}{r}\int \zeta r dr$. The vortex is surface intensified and decays exponentially with depth with the product $e^{\frac{-z}{H_e}}$, where $H_e = 500$ m denotes the vertical e-folding scale of the vortex. We study how the monopoles behave from initial positions on the slope and in the bowl center. The experiments are run for 5 years with no bottom friction.

## 3.2 Vortex detection and tracking

In all papers of this thesis, mescoscale coherent vortices are detected and tracked from daily fields in the realistic numerical models. Vortices are identified by the hybrid method of *Penven et al.* (2005). The method involves locating closed contours of SSH and the Okubo–Weiss (OW) parameter. Closed contours of SSH represents streamlines for the surface geostrophic flow when the Rossby number is small. The OW parameter reflects the relative strength of vorticity versus deformation:

$$OW = S_n^2 + S_s^2 - \zeta_z^2.$$

The normal strain, $S_n = \partial_x u - \partial_y v$, and the tangential stretching, $S_s = \partial_x v + \partial_y u$, represent the total deformation, and the vertical component of the relative vorticity, $\zeta_z = \partial_x v - \partial_y u$, represents the rotation. The eddy core is expected to be dominated by rotation, and thus have negative values of the OW parameter.

The detection routine consists of three steps:

1. Local extrema are identified in daily model SSH field. Each local extremum represents a potential vortex center.
2. The largest closed SSH contour surrounding the extremum is located.
3. Within the closed SSH region, the OW$=0$ contour is extracted. The center of the vortex core is defined as the geographical mean position of all the points inside this $OW = 0$ contour.

Figure 3.2 shows an example of a detected eddy where all three criteria are met. Considering the finite resolution of the models, a minimum eddy effective radius is set to 2 $dx$, where $dx$ is the model resolution. Features smaller than this are rejected. A maximum eddy radius is also set to 100 km to prevent gyre-scale flows to be identified as vortices. Additionally, an SSH-extremum has to exceed the value of all neighboring grid points within a square box of $20 \times 20$ km surrounding the extrema. This ensures a lower limit on the separation distance between two adjacent eddies, and smaller-scale variations in the SSH field are ignored.

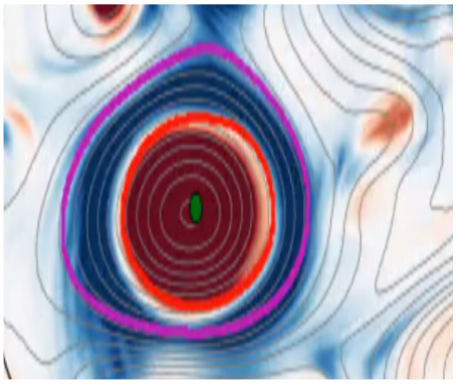

***Figure 3.2:*** *An example of the fulfillment of the vortex detection criteria. Colors show the Okubo Weiss parameter, red colors denote negative values and blue colors denote positive values. The grey contours are SSH contours. The purple contour is the largest closed sea surface height contour around the estimated vortex center (green dot). The OW* $= 0$ *contour is shown in red.*

To trace the vortices in time, the tracking algorithm developed by *Penven et al.* (2005) is used. This algorithm utilizes a similarity condition. Eddies, e1 and e2, detected in two following days, are the same if the generalized distance $\mathrm{X}_{e1,e2} = \sqrt{\frac{\delta D^2}{D_0} + \frac{\delta R^2}{R_0} + \frac{\partial \zeta^2}{\zeta_0}}$ is minimal. The terms are the normalized differences in separation distance, radius, and vorticity. The normalization factor $X_e 1, e2$ is invalid if the two vortices does not share the same polarity (*Halo et al.*, 2014). Additionally, the propagation distance between the two vortices cannot exceed twice the average of their size.

## 3.3 Linear stability analysis for flow over topography

In Paper I we investigate the generation mechanism and characteristics of the mesoscale eddy field in the Subarctic model domain. We perform a linear stability analysis (LSA) on the mean fields in a quasi-geostrophic (QG) framework. The QG framework provides an approximate model, based on a simplified set of equations. The model is suitable to describe the evolution of motions on the time and spatial scales of weather systems, while faster, smaller-scale motions (such gravity waves) are eliminated.

The stability analysis yields characteristics of baroclinically unstable waves. Essential quantities to draw from the stability analysis are growth rates, vertical structures, and length scales of the most unstable modes. The most unstable wave will be the wave emerging first in an unstable mean state, and is believed to continue to dominate at the

early stages of a vortex life cycle. The analysis can also help identifying regions of pronounced growth along the mean current. Below is a summary of the three main points in the procedure, following *Smith* (2007):

1. The quasi-geostrophic potential vorticity (QGPV) equation and the boundary equations are linearized about a specified mean state, and perturbation solutions are sought.

2. A plane-wave solution is inserted into the linearized set of equations, which forms a generalized eigenvalue problem. The eigenvalue problem is further discretized vertically and solved numerically.

3. Eigenvalues and eigenvectors are extracted from eigenvalue solution. The growth rates and length scales of the prominent wave are obtained by these, respectively.

To give the full context of the problem, a description of the first step is first given below. Then follows some other complementary aspects of the analysis which is not covered in Paper I.

### 3.3.1 The QG setting

The approximated model is based on three major assumptions[1]. First, in addition to being in hydrostatic balance in the vertical, the motions (with a characteristic horizontal velocity and length scale, U and L) are in near geostrophic balance in the horizontal. The motions are thus characterized by a small Rossby number, $R_o = U/fL << 1$. Second, the variations in $f = f_0 + \beta y$ are small, and are on the order of $R_o$, $\frac{|\beta y|}{f_0} \propto R_o$. Third, the bottom topography is not too intrusive on the fluid depth. The fraction of the bottom elevation to the full ocean depth is required to also be on the order of $R_o$. In essence, the equations strictly account for motions with small departures from purely hydrostatic and geostrophic conditions, with modest latitudinal extent, and with limited bottom elevations.

In the inviscid interior, in the absence of forcing and dissipative effects, QG potential vorticity (QGPV) is materially conserved (invariant or constant on a fluid particle) when following the geostrophic flow.

$$\frac{D_g q}{Dt} = (\partial t + \mathbf{u_g} \cdot \bigtriangledown) q = 0, \; -H < z < 0, \tag{3.1}$$

Here $q$ is the QGPV, and $\mathbf{u_g} = u_g \mathbf{i} + v_g \mathbf{j}$ the lateral geostrophic velocities. The subscript denoting geostrophic terms is omitted hereafter. The tendency equation can be expressed in terms of a stream function, $\psi$, leading to one equation with only one unknown quantity. By definition $\psi = \frac{p}{\rho_0 f_0}$, which under geostrophy gives $u = -\frac{\partial \psi}{\partial y}$ and

[2]The theory in this section is based on notes from the compendium found at https://folk.universitetetioslo.no/josepl/papers/geo4901a.pdf

$v = \frac{\partial \psi}{\partial y}$. Expressed in terms of a stream function, the QGPV is:

$$q = \bigtriangledown^2 \psi + \beta y + \frac{\partial}{\partial z}(\frac{f_0^2}{N^2}\frac{\partial \psi}{\partial z}),$$

On the RHS, the first term is the vertical component of the relative vorticity, $\beta y$ is the variable part of the planetary vorticity, and the final term is a stretching term (or perturbation layer thickness in a layered formulation) (*Vallis*, 2006).

The interior connects with the boundaries through the top ($z = 0$) and bottom ($z = -H$) buoyancy equations,

$$(\partial_t + \mathbf{u} \cdot \bigtriangledown) b = 0, \; z = 0$$
$$(\partial_t + \mathbf{u} \cdot \bigtriangledown) b + N^2 \mathbf{u} \cdot \bigtriangledown \mathbf{h} = 0, \; z = -H$$

where $b = f_0 \frac{\partial \psi}{\partial z}$, is the buoyancy. At the lower boundary, $N^2 = -\frac{\rho}{g}\frac{\partial \rho}{\partial z}$ is the buoyancy frequency and $h$ is the topography.

The stream function is divided into a background time mean and a transient eddying state, $\psi = \Psi + \psi'$, and the PV terms then become

$$q = Q + q', \text{ where}$$
$$Q = \bigtriangledown^2 \Psi + \beta y + \frac{\partial}{\partial z}\frac{f_0^2}{N^2}\frac{\partial \Psi}{\partial z},$$
$$q' = \bigtriangledown^2 \psi' + \frac{\partial}{\partial z}\frac{f_0^2}{N^2}\frac{\partial \psi'}{\partial z}.$$

The buoyancy, topography and velocities is also separated into a mean state and a deviation from the mean state, $b = B + b'$, $h = H + h'$ and $\mathbf{u} = \mathbf{U} + \mathbf{u}'$ respectively.

The background state is furthermore assumed to not vary across the lateral scale of the waves; a so-called homogeneous or local approximation. The local approximation entails that strong variations in the background flow does not occur at grid resolution. In this thesis, this means that each grid point is considered a $4 \times 4$ km box with doubly periodic boundaries. The assumption that the mean state is invariant at such scales could be a significant violation. Narrow jets and narrow lateral gradients could occur at, or below, grid resolution in our study domain. Nevertheless, smoothing out these features could also significantly affect the results. Making the approximation leaves only a depth-dependence in the mean lateral flow $\mathbf{U} = U(z)\mathbf{i} + V(z)\mathbf{j}$ and the stratification $N^2 = N^2(z)$. Moreover, this leads to setting the mean relative vorticity $\bigtriangledown^2 \Psi = 0$. The QGPV-equations and the boundary equations linearized around the mean state becomes:

$$\begin{aligned} (\partial_t + \mathbf{U} \cdot \bigtriangledown) q + \mathbf{u} \cdot \bigtriangledown Q = 0, \; -H < z < 0 \\ (\partial_t + \mathbf{U} \cdot \bigtriangledown) b + \mathbf{u} \cdot \bigtriangledown B = 0, \; z = 0 \\ (\partial_t + \mathbf{U} \cdot \bigtriangledown) b + \mathbf{u} \cdot (\bigtriangledown B + N^2 \bigtriangledown h) = 0, \; z = -H, \end{aligned} \tag{3.2}$$

Unstable wave characteristics are attained by inserting plane wave solutions to equations 3.2 and solving the resulting eigenvalue problem.

### 3.3.2 The eigenvalue problem

Seeking wavelike perturbations amounts to searching for normal-mode solutions on the form

$$\psi = Re\{\hat{\psi}(z)e^{i(kx+ly-i\omega t)}\},$$

where $\hat{\psi}(z)$ represents the perturbation's vertical structure, $\omega$ represents the wave frequency, and $k$, $l$ are the lateral wave numbers (*Vallis*, 2006). Note that both the amplitude and the frequency can become complex.

Substituting the solution into the QGPV equation and the equations valid at the boundary leads to a generalized eigenvalue problem

$$\omega B\hat{\psi} = A\hat{\psi}$$

where A and B triagonal matrices of size $N \times N$ when discretized on a vertical grid with $N$ layers. The boundary conditions are incorporated into the QGPV equation (see 3.3.3) and thus represented in A and B (*Smith*, 2007).

The problem is solved numerically at every horizontal model grid point for $200 \times 200$ wave numbers. The solution yields $N$ eigenvectors and $N$ eigenvalues, providing the vertical structure of the unstable waves $\hat{\psi}(z)$ and their frequencies $\omega = \omega_r + i\omega_i$, respectively (*Smith*, 2007). For an unstable wave, $\omega$ will have a positive imaginary part. The term $e^{\omega_i t}$ amplifies the amplitude $\hat{\psi}$ exponentially in time, as seen below when inserted into 3.3:

$$\psi(x,y,z,t) = Re\{\psi(z)e^{\omega_i t}e^{i(kx+ly-\omega_r t)}\}.$$

Here the vertical structure of the wave, $\psi(z)$, is complex.

At every grid point, there can be several growing waves for each wave number pair, (k,l). The largest, positive imaginary frequency, $\omega_i$, and the associated wave numbers are selected. The spatial and time scales of the most unstable wave are compared to the estimates from the Eady model.

Section 2c in Paper I provides more details on the analysis. In the next section, I discuss how the boundary conditions are treated, and how this treatment provides a useful view on the instability mechanism.

### 3.3.3 Generalized QGPV

In the discretization of the eigenvalue problem, the boundary conditions are incorporated into the interior equations. This results in solving one prognostic equation, $\frac{D\hat{q}}{dt} = 0$, where $\hat{q}$ is a generalized QGPV (*Lappa*, 2012). The procedure allows for a consolidated view of baroclinic instability solely in terms of PV. This is also highly useful when diagnosing the results attained from the LSA, which we will discuss further in the next section.

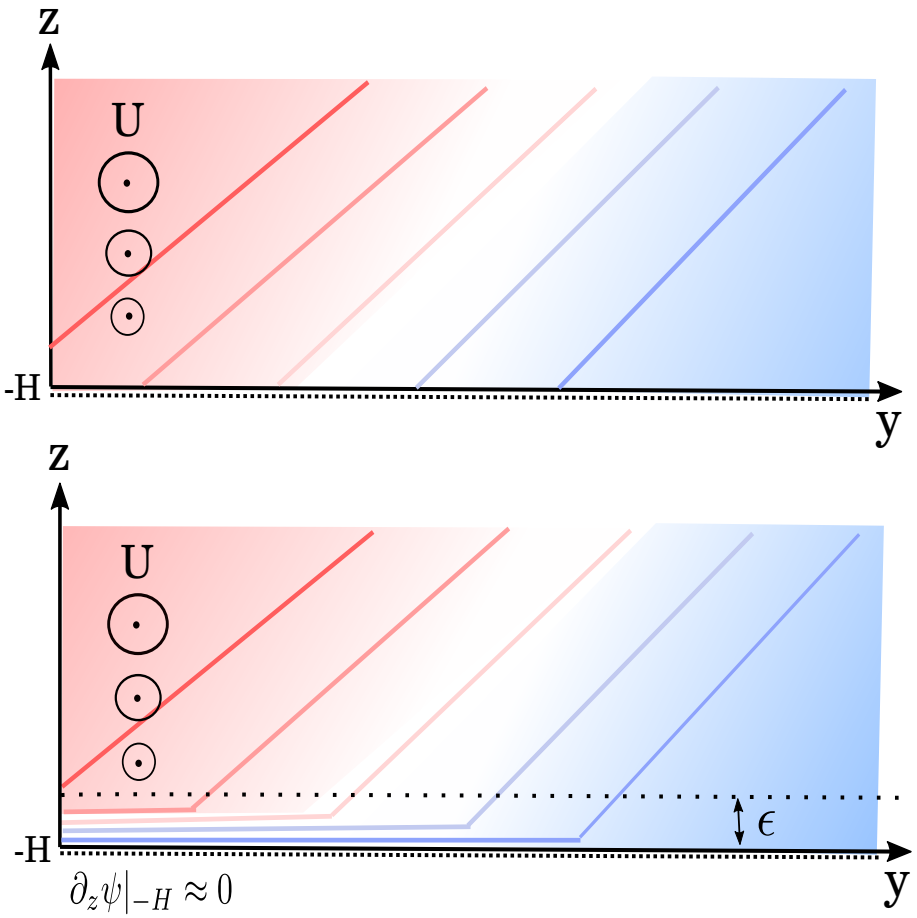


***Figure 3.3:*** *Illustration of Bretherton's potential vorticity sheet. Uniformly sloping isopycnals(contours), with lighter waters to the left. Zonal current with vertical shear supported by the lateral buoyancy gradient. Upper panel: Inhomogenous conditions at the boundaries. Lower panel: Isopycnals turn horizontal near the lower boundary, causing a homogeneous condition at this boundary. The figure is ammended from figure 2.1 in Smith (2003)*

The generalized form was first presented by *Bretherton* (1966). The concept revolves in adding boundary contributions as Dirac delta-functions to the interior PV. *Bretherton* (1966) demonstrated that by adding a thin layer of PV adjacent to the boundary, the presence of a lateral temperature (buoyancy) gradient on the boundary can be represented as a flow with a homogeneous temperature (buoyancy), albeit with a PV gradient, on that boundary (*Lappa*, 2012). This idea is valid for all baroclinic flows. To give an example, consider the illustration in figure 3.3a (*Smith*, 2003). A zonal flow, U, near the ocean bottom, $z = -H$, is flowing with light waters to the right. The flow has a uniform vertical shear due to the constant lateral buoyancy gradient. Sloping isopycnals (colored lines) are intersecting the lower boundary. Figure 3.3b shows another case with the same configuration, except there is no buoyancy gradient on the boundary (*Smith*, 2003). Instead, the isopycnals are leveled out near the boundary in a thin sheet with thickness $\varepsilon$. This case can be shown to be analogous the former. Consider integrating $q$ over the sheet (*Lappa*, 2012):

$$\int_{-H}^{-H+\varepsilon} q dz = \int_{-H}^{-H+\varepsilon} \left(f + \nabla^2 \psi\right) dz + \frac{f^2}{N^2} \frac{\partial \psi}{\partial z}\bigg|_{-H}^{-H+\varepsilon}$$

In the continuous limit as $\varepsilon$ goes to zero, the integral goes to zero. However, by applying a constant temperature at the boundary, i.e. setting $\frac{\partial \psi}{\partial z}_{-H} = 0$, we get

$$\int_{-H}^{-H+\varepsilon} q dz = \frac{f^2}{N^2} \frac{\partial \psi}{\partial z} \Bigg|^{-H+\varepsilon} = q_b$$

Thus, when implementing a homogeneous boundary condition, the sheet adjacent the boundary operate as a Dirac-delta sheet (*Lappa*, 2012). The same applies for the upper boundary. With this, the QGPV equation can be expressed in a generalized form

$$\frac{Dq}{dt} = \frac{D}{dt}\Big[q + q_b \delta(z-H) + q_t \delta(z)\Big]. \tag{3.3}$$

In the continuous case, the delta-sheet is infinitesimally thin. When discretized, the layer has to be finite. In this thesis' analysis, this finite thickness is the (variable) thickness of the lower model layer. As a consequence, the discretization involves an error of the order of this thickness (*Smith*, 2007).

### 3.3.4 Diagnosing stability

Solving the eigenvalue problem provides an overview over various locations where the background state is unstable. It may be challenging to decipher why the instabilities occur where they do. In order to understand the results, it is useful to examine the background conditions at these specific locations. *Charney and Stern* (1962) and *Pedlosky* (1964) derived necessary conditions for instability, the Charney-Stern-Pedlosky (CSP) criterion, which requires that the lateral background PV gradient combined with the boundary velocity-shear, change sign in the vertical.

Over a flat bottom, the mean flow stability is thus related to the structure of $\nabla Q$, and the sign of the velocity shears at the top and bottom boundaries. Whether the CSP criteria is met can readily be demonstrated in the condensed form of PV discussed above (*Lappa*, 2012). With the PV-sheets close to the boundaries included, the mean PV-gradient is

$$Q_y = Q_y^{int} + \gamma U_z^{top} \delta(z) - \gamma U_z^{bot} \delta(z-H), \quad \gamma = \frac{f_0^2}{N^2}.$$

The gradient needs to change sign in the vertical for the flow to potentially be unstable. This is for an idealized case with a purely zonal flow ($V = 0$) (*Lappa*, 2012). In the analysis in this thesis, the mean PV gradient can be examined in a rotated reference frame, where the flow is rotated to align with the most unstable wave. This produces a related expression, now with the addition of a topographic slope:

$$Q_y = Q_y^{int} + \gamma U_z^{top} \delta(z) - \gamma U_z^{bot} \delta(z-H) - f h_y$$

where $\partial_y Q_{int} = \beta - f \partial_z \mathbf{s}$. $\partial_z \mathbf{s}$ is the vertical gradient of the isopycnal slope. Thus factors that can impact the stability of the mean flow is $\beta$, $\partial_z \mathbf{s}$, $U_z$ and $h_y$. By considering

the composition of each term, this can help to estimate the type of instability at play. The contribution of each term may be induced from this. At high latitudes, the value of $\beta$ is on the order of $10^{-12}$, and is likely negligible compared to the other terms. The isopycnal and topographic slopes are presumably dominant terms. The type of instabilities found in the LSA can be related to those of the three central idealized models of baroclinic instability, the Charney, Phillips and Eady model (*Charney*, 1947; *Eady*, 1949; *Phillips*, 1951). Such a classification is useful to get an indication of the relevance of the simplified models, and to better understand the dynamics.

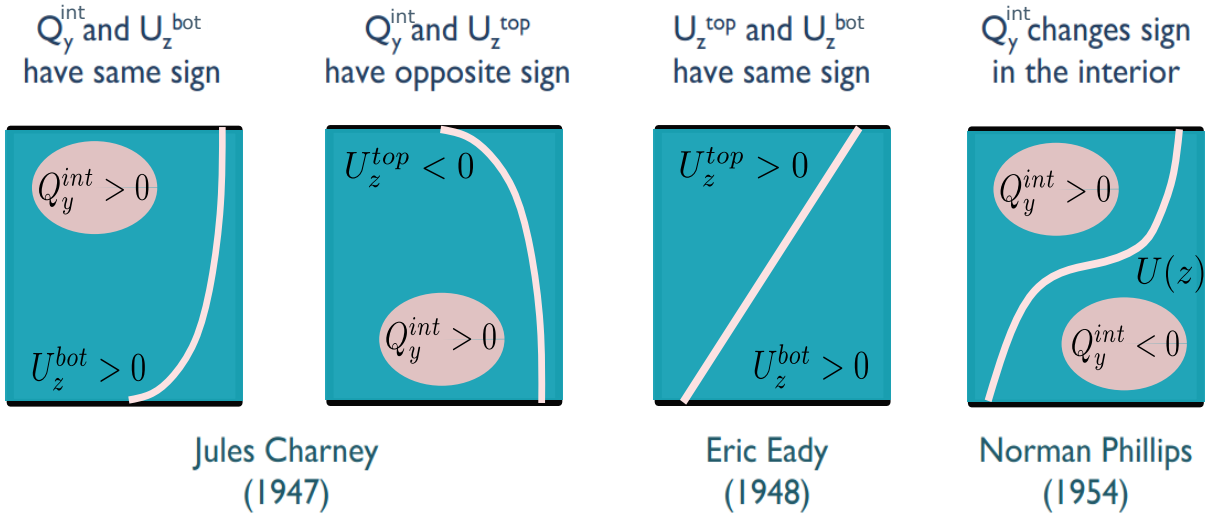


***Figure 3.4:*** *Sketch over different scenarios where the Charney-Stern-Pedlosky criteria is met, i.e where 3.4 may add to zero. The pink line illustrated the wave amplitude. The two left boxes illustrate necessary conditions for instability in the Charney model. The interior potential vorticity (PV) gradient need to have the same (opposite) sign as the bottom (top) contribution, resulting in a maximum wave amplitude at the lower (upper) boundary. For potential instability in the Eady model (third box), the interior mean PV is zero, and the upper and lower contribution have the same sign. This leads to maximum wave amplitude at both boundaries. In the Philips model (fourth box), the shear at the boundaries are absent, and the interior mean PV gradient has to change sign in the vertical. The figure is amended from slide 13 in Keating (2014).*

Figure 3.4 shows the necessary CSP-criteria for the three models (*Keating*, 2014). The pink line show the unstable wave amplitude. In the simple Eady case, the interior PV gradient is zero and instability is only possible with sheared velocities at the boundaries. This results in a maximum wave amplitude at the upper and lower boundary. On the other hand, the other models predict vertical structures that are amplified at one of the ocean boundaries. To fulfill the CSP criteria in the Philips model, the tilt of the isopycnal slopes need to reverse, to allow $\partial_y Q$ to change sign in the vertical. Phillips-type instabilities supports interacting interior (thickness) waves, which produce maximum amplitudes at the upper boundary and a weaker decay with depth. Charney-type instabilities support interactions between edge and Rossby waves, and have maximum wave amplitudes at either boundary with a sharp decay at depth. If the LSA exhibit similar types of instabilities, this gives an indication that the dynamics in these simple models can account for the growth. *Tulloch et al.* (2011) suggests that Philips-type instabilities are prevalent in the ocean.

## 3.4 Nonlinear analysis for flow over topography

In Paper III, we examine the nonlinearly stable steady state of unforced turbulence in two layers. The question we ask is; what does the end state of equilibrating turbulence look like in the presence of a bowl-shaped basin? Can theory predict a dual circulation pattern comprised of a cyclonic slope current and a surface intensified anticyclone? Below follows some background to the analysis performed in this thesis[2].

Several studies have investigated the stability and stationary statistics of turbulent flow over topography. The studies were motivated by the emergence of coherent vortices in unforced and forced 2D turbulent flows, a question which relates to the cascade of energy mentioned in section 2.2. In geostrophic turbulence, the up-scale cascade of energy can be regarded as a consequence of mergers between like-signed vortices, and a down-scale enstrophy cascade (the stretching of PV contours) (*Rhines*, 1979). The cascades can lead to a flow concentrated into a few, sparse vortices. During this self-organization of the flow, energy is shifted to larger scales as eddies merge and grow into taller, and broader structures. At the same time, enstrophy is shifted toward smaller scales, and will dissipate at the smallest scales if dissipation is present in the system. In these opposing cascades, the patterns related to the pressure ($\psi$) will exhibit successively larger scales. Energy is the measure of the velocity variance, and thus emulated by these larger scale structures. Meanwhile, below the length scales of these patterns, vorticity filaments will be teased out into even thinner filaments by the chaotic flow. Enstrophy is a measure of the variance of the vorticity, and thus strongly influenced by this filamentation. In this system, the total area averaged energy (E) and enstrophy ($Q$) is conserved. However, topography represents a source term for relative enstrophy, $|\bigtriangledown^2\psi|^2$. This carries an implication for an expected correlation between the mean field PV and the vorticity (*Rhines*, 1979).

*Bretherton and Haidvogel* (1976) explored the idea that topography alters the cascade and that, for a given energy, the cascade would bring the flow to a state where the potential enstrophy is minimized. In their study, they used calculus of variations to find solutions corresponding to this principle. The method comprises of finding where the variation of potential enstrophy, $\delta Q$, vanishes, while keeping the energy fixed. We briefly discuss the procedure here since the analysis in Paper III, albeit in two layers, builds on it.

The QGPV equation for an inviscid, homogeneous (1 layer) ocean with $\beta = 0$ is

$$\frac{Dq}{dt} = 0, \tag{3.4}$$

[3]The theory in this section is based on notes from the compendium found at https://folk.universitetetioslo.no/josepl/papers/gef4520jhl7.pdf, in addition to the cited studies

where $q = \bigtriangledown^2\psi + h$. $h = f\frac{h'}{H}$ and $h'$ is the deviation from the mean depth, H. The total enstrophy is $Q = \frac{1}{2}\int\int q^2 dA$ and the energy is $E = \frac{1}{2}\int\int |\bigtriangledown \psi|^2 dA$. Boundary conditions are either periodic or homogeneous ($\psi = 0$). The variational problem involves using a Lagrange multiplier technique. This is a method for minimizing (or maximizing) a function, $f_1$, while imposing a constraint on another function, $f_2$ (*Bertsekas*, 1996). The constraint might be that the function is equal to a constant, $c$. A variable called a Lagrange multiplier, $\mu_e$, is introduced, and a new functional $F = f_1 + \mu_e(f_2 - c)$ is defined. To find critical points of F, the variation of F is set to zero. In the case of minimizing the enstrophy, $f_1 = Q$, $f_2 = E$, and the constant c is a fixed value of the total energy. $\mu_e$ is determined by imposing that the energy matches the initial energy. This then amounts to

$$\delta F = \delta Q + \mu_e \delta E = \frac{1}{2}\int\int \bigtriangledown^2(\bigtriangledown^2\psi + h' - \mu_e\psi)\delta\psi dA = 0. \tag{3.5}$$

For the expression to be valid for all variations of $\delta\psi$, it requires that

$$\bigtriangledown^2\psi + h' - \mu_e\psi = 0. \tag{3.6}$$

Inserting a Fourier transform, $\sum_{k,l}\hat{A}e^{ikx+ily}$, for both the topography and stream function ($\hat{A} = \hat{\psi}, \hat{h}$) yields the solution

$$\hat{\psi} = \frac{\hat{h}}{\mu_e + \kappa^2}, \qquad \kappa^2 = k^2 + l^2. \tag{3.7}$$

This reflects a minimum critical point of the functional F. The minimum is found by evaluating the second variation of F. 3.7 is a unique and nonlinearly stable solution. The stability of the steady state is proven by nonlinear stability theory (*Arnol'd*, 1965). The solution entails a correlation between the stream function and the topography. How strongly the two fields correlate depends on the scale, $\kappa^2$, compared to $\mu_e$. As we see from 3.7, the Lagrange multiplier represents a length scale $L_0 = \mu_e^{-1/2}$. At small scales (high wave numbers) compared to $L_0$, $q = \bigtriangledown^2\psi + h' \approx 0$, and the relative vorticity responds to bottom-induced stretching. At large scales ($\kappa^2 << \mu_e$), $\hat{\psi} \approx \frac{\hat{h}}{\mu_e}$, and the flow almost aligns with the topographic contours. $\psi$ acts as a low pass filtered image of the topography, and mirrors a smooth version of the topography. This is illustrated in the numerical results of *Bretherton and Haidvogel* (1976), that agree with their analytical prediction (figure 3.5). The numerical experiments included some viscosity that acts to dissipate the enstrophy at small scales. In the case of a seamount (basin) the solution yields anticyclonic (cyclonic) circulation.

Using statistical mechanics, *Salmon et al.* (1976) also studied the decay of 2D turbulence over topography, in the absence of friction and dissipation. They demonstrated that the end states of such a decay, tend toward the most probable steady states given by canonical equilibrium theory. The theory is based on energy and enstrophy conservation, and predicts a steady solution on the form

$$\mu_s < \psi > = < q >, \tag{3.8}$$

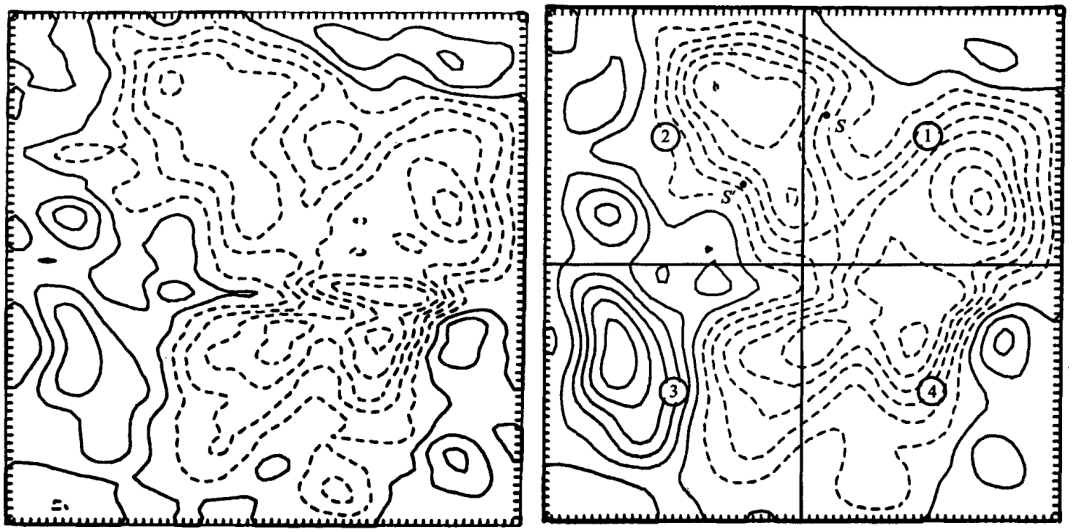


***Figure 3.5:*** *Figure 2a,c in Bretherton and Haidvogel (1976). Left: Bottom topography. Right: The final stream function. The stream function is proportional to and positively correlated with the topography, but contains less small scale features due to the low-pass filtering effect described in the text.*

where $<>$ denotes an ensemble average over a range of wave numbers of finite resolution, thus relating the coarse-grained PV field to its associated stream function. $\mu_s$ is the ratio of the Lagrange multipliers of the energy and the enstrophy, and is in general not equal to $\mu_e$. This solution also yields prograde flow around topographic features, which is flow keeping shallow waters to its right (in the northern hemisphere). *Carnevale and Frederiksen* (1987) showed that in the limit of infinite resolution, i.e where the highest wave number of the topography goes to infinity, 3.8 also reflects a minimum enstrophy state and is identical to 3.7. In this case $\mu_s \to \mu_e$.

This thesis revisits the theory and seeks a minimum enstrophy solution for two-layer QG flow over topography. The analysis follows the minimum enstrophy principle of *Bretherton and Haidvogel* (1976), described above, but now we have PV in two layers. Nondimensionalized PV in layer 1 and layer 2 are:

$$q_1 = (\bigtriangledown^2 - F_1)\psi_1 + F_1\psi_2 \tag{3.9}$$

$$q_2 = (\bigtriangledown^2 - F_2)\psi_2 + F_2\psi_1 + h, \tag{3.10}$$

with $F_i = \frac{f^2L^2}{g'H_i}$, $H_i$ is the mean layer thickness and $h = f_0 h_b/H_2$ is the bottom elevation.

We utilize the Lagrange multiplier technique to find where the total enstrophy, $Q = \int\int(q_1^2 + q_2^2)/2dA$, is minimized. The analysis given in Paper III is not repeated here, but the steps taken are rather summarized, to provide an algorithm for the procedure:

1. Define the functional $F = \int\int((q_1^2 + q_2^2)/2 + \mu E)dA$
2. Find the critical point of F by setting the first variation of F to zero; $\delta F = \int\int(q_1\delta q_1 + q_2\delta q_2 + \mu\delta E)dA = 0$.
3. Collect the terms involving first $\delta\psi_1$ and then $\delta\psi_2$, and require that $\delta F = 0$ for any $\delta\psi_i, i = 1,2$

4. Fourier transform the stream function and topography, and substitute into the coupled Euler-Lagrange equations resulting from the requirement above.

5. Solve the equations using the Cramer's rule[3].

6. Separate out the surface portion of the topographic mode and compare the residual with the surface mode, $\psi_{s1} = \psi_1 - \psi_{1t}$. The surface portion of the topographic mode is obtained by setting $q_1 = 0$, yielding $\psi_{1t} = F_1\psi_2/K^2 + F_1$. $F_1 = L^2/L_d^2$ is the ratio between the scale of topography and the Rossby deformation radius.

The two layered setting allows for a solution that contain both a surface and a topographic mode.

[3]Cramer's rule: For a linear system, $Ax = B$ (equation 10 in Paper III of this thesis)

$$\begin{bmatrix} a & b \\ c & d \end{bmatrix} \begin{bmatrix} \hat{\psi}_1 \\ \hat{\psi}_2 \end{bmatrix} = \begin{bmatrix} e \\ f \end{bmatrix},$$

assuming the determinant is non-vanishing, solutions for $\psi_1$ and $\psi_2$ is found from the division of the determinants of the square coefficient matrix, A, and a new matrix (*Kyrchei*, 2018). The new matrix is obtained by substituting one column in the matrix, A, by the solution vector, B. Thus,

$$\psi_1 = \frac{\begin{bmatrix} e & b \\ f & d \end{bmatrix}}{\begin{bmatrix} a & b \\ c & d \end{bmatrix}} = \frac{ed - bf}{ad - bc}, \quad \psi_2 = \frac{\begin{bmatrix} a & e \\ c & f \end{bmatrix}}{\begin{bmatrix} a & b \\ c & d \end{bmatrix}} = \frac{af - ec}{ad - bc}$$

# Chapter 4

# :Presentation of findings

This chapter presents the research accomplished in this thesis. The three sections summarize each paper with its main findings and main conclusions.

## 4.1 Paper summary

### 4.1.1 Paper I: Topographic influence on baroclinic instability and the mesoscale eddy field in the northern North Atlantic Ocean and the Nordic Seas

#### Objective

To investigate topographic control on unstable growth in the Subarctic seas, and relate the linear predictions to the statistics of the fully-developed eddy field and to the predictions from flat-bottom theory.

#### Summary

In this paper the role of baroclinic instability in generating the observed mesoscale eddy field in the Subarctic is studied using a linear stability analysis. The linear stability analysis unveil locations of instability and yield predictions of preferred characteristics of mesoscale vortices at early stages of their evolution. An eddy census is conducted from a ten year model simulation. Coherent vorticies are identified in daily model fields, providing vortex length scale and the eddy kinetic energy contained in the vortex field. The characteristics and geographical distribution of the equilibrated eddy field is compared to projections from linear stability calculations. Spatial scales and growth rates of the unstable waves are also contrasted to the estimates of the simplified flat-bottom model of baroclinic instability, the Eady model. The impact topography have on the stability of the background current and on structure of the gravest modes is investigated, and viewed in context of Eady theory.

**Main findings**

- The linear stability analysis shows large growth rates along the slopes corresponding to locations of high eddy activity.
- Topographic PV gradients have a significant impact on the growth rates.
- Over topography, the vertical structure of the gravest unstable modes do not correspond to maximum wave amplitudes at the surface and bottom as predicted by flat-bottom Eady theory.
- The fastest growing modes typically resemble a Charney- or Philips type instability with largest amplitude near the surface, and exponential decay at depth.
- Eady modes are found in the rare regions of nearly flat bottom topography.
- Suppressed length scales are observed over steep slopes, related to the decreased vertical scale of the unstable wave amplitude.
- Energy conversion rates strongly indicate that the major source for mesoscale eddies in the study region is baroclinic instability.

**Main conclusion**

This study suggests that the eddy field largely originates from baroclinic instability. Pure Eady theory, as well as modified Eady theory allowing for a bottom slope, is not sufficient as a lowest order model for the mesoscale dynamics in this region.

**Author contribution**

I set up and ran the ROMS hindcast simulation, produced and ran the code for the linear stability analysis and the eddy detection. The text was written with guidance from the coauthor.

### 4.1.2 Paper II: The regeneration of the Lofoten Vortex through vertical alignment

**Objective**

To analyze the role of vortex mergers in maintaining the Lofoten Vortex.

**Summary**

This paper studies the evolution of a long lived anticyclone, the Lofoten Vortex. The question of the vortex' rejuvenation is raised, and the potential contribution of vortex mergers explored. We run a ten year simulation using a very high resolution model. All anticyclones appearing over the simulation period are identified and tracked. In order to see how the basin is supplied with vortices, we map the pathways of anticyclones into the basin. The interaction between other anticyclones and the Lofoten vortex are investigated both laterally and vertically. The impact of merger events on the Lofoten vortex is examined in time series of integrated core properties over the entire simulation period.

**Main findings**

- Anticyclones are frequently shed from the Norwegian Atlantic Current, and spiral cyclonically into the basin center.
- The Lofoten Vortex forms and settles in the basin center during the first simulation year and the vortex does not break up throughout the model simulation.
- Basin anticyclones often have unequal densities, and tend to align vertically when they coalesce to form a taller column.
- The Lofoten Vortex core is always denser than the surrounding vortices. Under a vertical alignment, the Lofoten Vortex squeezes when it dives under a lighter vortex.
- The Lofoten Vortex undergoes 1-2 vertical alignments each year, and the spin up of the vortex can be linked to the squeezing under the tendency of PV conservation.

**Main conclusion**

Vertical alignment is key to regenerating the Lofoten Vortex. Wintertime convection does not contribute significantly to the vortex spin up. The longevity of other oceanic anticyclones might be impacted by vertical alignment.

**Author contribution**

I set up the ROMS model and ran the initial hindcast simulations. I conducted the analysis, produced and ran the eddy detection. I wrote the paper with guidance from the co-authors.

### 4.1.3 Paper III: Stable surface anticyclones in basins

**Objective**

To examine the formation of long lived bowl-trapped anticyclones using theory based on the minimum enstrophy principle and idealized modeling.

**Summary**

This paper investigates turbulent flows over a bow-shaped basin. A minimum enstrophy solution in two layers over topography is derived, to seek an explanation for the observed circulation which typically contains both a cyclonic bottom intensified slope circulation, and a surface intensified anticyclone. Current theoretical predictions accounts only for the cyclonic slope circulation. Aiming to assess the applicability of the predicted state beyond a two-layer quasi-geostrophic system, idealized primitive equation turbulence experiments over a bowl-shaped basin are conducted. The minimum enstrophy solution is examined in light of the numerical results. Experiments of monopoles initialized in isolation over the basin are run. Our findings are viewed in the context of a realistic eddy-resolving model simulation of the Lofoten Basin.

**Author contribution**

I ran the numerical model simulations, and the co-author worked out the analytical solutions. The text was written together with the co-author.

**Main findings**

- The minimum enstrophy solution predicts an anticyclonic circulation in the top layer and a cyclonic circulation in the lower layer over the basin.
- The numerical simulations supports the analytical solution, with the formation of a stable surface intensified anticyclone and a bottom intensified slope current.
- In the numerical simulation, bottom topography induces an anticyclone-cyclone asymmetry over the basin
- The flow in the realistic model experiment corresponds well to the idealized model experiments
- In idealized model experiments where bottom friction is applied, the bowl-trapped anticyclone exhibit deeper flow than in the inviscid case, and its vertical structure corresponds better to the observed structure of the Lofoten Vortex.

**Main conclusion**

Our findings show that two steady circulation patterns, a bottom intensified cyclone and a surface intensified anticyclone, can coexist over a basin. The minimum enstrophy solution explains how surface anticyclones can persist for so long over a basin, despite being larger than the deformation radius.

# Chapter 5

# :Summary and future perspectives

The first part of this chapter gives a synthesized summary of this thesis and its contributions, and the second part discusses some possible extensions to the work in this thesis.

## 5.1 Summary

A precondition for investigating oceanic vortices in polar regions is high resolution spatial data. As already mentioned, investigations of this kind have over the years suffered from a lack of resolution, both in observations and in models. This work offers new insights to the field with analysis based on unprecedented high resolution models for this region.

As a first step, we seek to understand how and where the vortices in the Subarctic region originate. In Paper I we therefore examined the initial stage of vortex evolution, by investigating unstable growth of perturbations stemming from baroclinic instability. In Paper I, we are concerned with selecting the fastest-growing waves in an unstable ambient flow. From a linear stability analysis, we attain linear predictions of the waves' length scales, vertical structure and growth regions. We furthermore conduct an eddy census built on 10 years of model data. A large number of studies have been devoted to quantifying the role of eddies in specific parts of the Nordic Seas, but no previous eddy census for the entire region exists. We compare the predicted characteristics of the fastest-growing waves to the characteristics of the equilibrated mesoscale eddy field in the numerical simulation. Furthermore, we investigate the impact topography has on the unstable growth, and look at the potential caveats of making a flat bottom assumption. From this we consider what relevance the canonical Eady model has in our study region. While there exist several studies on the stability of some of the currents in the study region, these investigations have addressed isolated sub-regions. Paper I is the first study to look at the general geographical distribution of baroclinic instability and how it relates to the macroturbulent flow field in the entire Subarctic region. The study offers a comprehensive view on the stability of the currents in this region. The analysis implies that the currents are baroclinically unstable all along the ocean margins, and that locations with the steepest topography typically both have the largest levels of EKE and the fastest conversion of APE. The paper thus argues that baroclinic instability of the slope current is the primary source for mesoscale vortices in the Nordic Seas.

Furthermore, the findings of this study suggests that the Eady model is not sufficient for explaining the dynamics taking place in the region.

The linear stability analysis in Paper I gives an estimation of the early development of waves giving rise to vortices. In Paper II, we look at later stages in a vortex life cycle. We hone in on one of the vortices in the region, and examine the evolution of the long-lived anticyclone, the Lofoten Vortex. We examine the daily evolution of the vortex and investigate whether vortex merger is a process responsible for maintaining it. With a very high spatial (800 m) and temporal (6 hours) resolution model, we acquire a nearly uninterrupted view of the merger process between anticyclonic vortices, specifically, between anticyclones with cores that lie on different depth levels. This is to the authors knowledge the first such investigation within a realistic ocean setting. Our data allow us to explore details of the coalescence which are otherwise hard to capture in sparse observational data or coarser models, owing to the swiftness of the process and the need for a high spatial resolution. Moreover, with the aim of better understanding the three-dimensional vortex evolution and interactions, we study the vertical development of the Lofoten Vortex at times before, during and after vortex mergers. In addition, an eddy census is conducted from 8 years of model data. Identified anticyclonic vortices are traced from their formation area into the basin. The Lofoten Vortex forms around half a year after the simulation spinup. It is seeded by anticyclones that originate from the boundary current. Three to four mergers (partial and complete) and one vertical alignment take place each year. No seasonal bias in the merger frequency nor in the instensity of the Lofoten Vortex is found. The relative vorticity and azimuthal velocity of the Lofoten Vortex is mainly affected by vertical alignments that regenerate the vortex. This reinforcement is related to the squeezing of the vortex core through the tendency of PV conservation. The resulting dual-core structure is not unique for the Loften Vortex, but it seems to be a general feature amongst the basin anticyclones. Our findings thus offer a new perspective on the regeneration of oceanic anticyclones; the regenerating impact of vertical alignment.

The motivation behind the third study was largely based on the findings in Paper II, where we observed that the Lofoten Vortex is remarkably stable. We therefore aimed to investigate more generally whether basin-anticyclones can be part of a steady solution. Even though linear theory is seemingly adequate to describe several of the features of the observed flow, the final equilibrated state is certainly dependent on nonlinear effects, exemplified in the violent vortex interactions studied in Paper II. To search for a probable end state, we therefore conduct a nonlinear analysis of turbulent flow over topography, using the minimum enstrophy principle, in Paper III. To assess the relevance of the predictions attained from two-layer QG equations, we also conduct turbulence experiments using a primitive equation numerical model, providing a more complex environment. In agreement with the numerical simulations, the minimum enstrophy solution predicts a cyclonic flow that is bottom-intensified, as well as a surface anticyclonic circulation. The sign of the circulation is reversed for elevated bottom topography. The bathymetry thus breaks the vortex symmetry expected in QG flows. The minimum enstrophy solution provides an explanation for the persistence of anticyclones observed over topographic depressions, and the results in this study thus offer a complementary view on anticyclone formation over a basin.

## 5.2 Future perspectives

### 5.2.1 Linking the Nordic Seas and the Arctic Ocean

In Paper I, the Arctic Ocean was excluded from the analysis, to focus on the Subarctic Seas. However, the Arctic Ocean region is a dynamically distinct region and immensely important in a global context. Despite this, basic aspects of the Arctic ocean circulation lack comprehensive descriptions (*Woodgate et al.*, 2001). Though dynamically distinct, with relatively weak stratification, a cyclonic boundary current and closed cyclonic gyres, the Arctic Ocean also bears some resemblance to the Subarctic Seas. The analysis and findings of this work also can be applied to investigate the dynamics of the Arctic Ocean. The Arctic Ocean is undergoing a so-called Atlantification, in which the area of warm and saline Atlantic Water is gradually expanding (*Asbjørnsen et al.*, 2020; *Tesi et al.*, 2021). The summer ice in the Arctic is rapidly decreasing (*Perovich et al.*, 2019), and potential future scenarios from climate models project an ice-free interior Arctic by around 2050 (*Collins et al.*, 2013). Moreover, the melting rates are generally underestimated in these model (*Manucharyan and Thompson*, 2022). The similarities between these regions could thus increase additionally in the coming years.

Much like the western part of the Subarctic Seas, the Arctic Ocean stratification is conceptually a three-layer system, comprised of the Arctic surface layer, the Atlantic Water at intermediate depth and the Arctic Deep Water. The intermediate layer consist of the Atlantic watermass, which enters the Arctic primarily from the Nordic Seas. The forcing mechanisms and the continuing pathway of the Atlantic Water (AW) into the Arctic ocean are only partially understood and an active research area (*Lique et al.*, 2015; *Spall*, 2013). Like in the Nordic Seas, the AW is guided by the topography in a cyclonic loop along the shelf slope as the Arctic Ocean Boundary Current. The mid-depth to deep circulation in the basins in the eastern Arctic Ocean is characterized by closed cyclonic gyres. Eddies are believed to be present all along the AW pathway. The present-day descriptions of their generation, propagation, and decay are however fragmented. Studies have found a strong seasonal signal in upper-ocean mesoscale variability (*Meneghello et al.*, 2021; *Wang et al.*, 2020). The EKE is highest in summer, and lowest in winter, presumably due to the differences in sea ice cover. As the sea ice is declining, *Manucharyan and Thompson* (2022) suggest that the reduced dissipation in the upper layers will cause more energetic eddies, and increased heat exchange between the atmosphere and ice. It is therefore relevant to map and understand the existing vortex field.

One important question is; What is the main source of mesoscale variability in the Arctic Ocean? A worthwhile undertaking is to investigate the stability of the Arctic Ocean Boundary Current. Observational studies have indicated that the major eddy generation sites are situated along the shelf slope in the vicinity of Barrow Canyon, and the Transpolar Drift Stream (*Spall et al.*, 2008; *Zhao and Timmermans*, 2015). A QG linear stability analysis computed (by this author) from a time mean field from the FOAM model gives indications that the unstable growth indeed is highest in these regions. Due to the approximate three-layer structure, a linear stability analysis in a simplified three layered configuration could be performed in comparison with full QG calculations.

The results in Paper 1 show that length scales of the unstable growth are in general suppressed over sloping topography, and that the unstable waves have a zero amplitude at the bottom. This implies that Eady dynamics cannot describe the growth, as it relies on the interaction between surface and bottom edge waves. A valid question is therefore: How much does a leading-order 3-layer analytic QG-model explain of the dominant stability characteristics in the Arctic Ocean? In particular, investigating this might provide some more insight into how bottom topography affects stability properties.

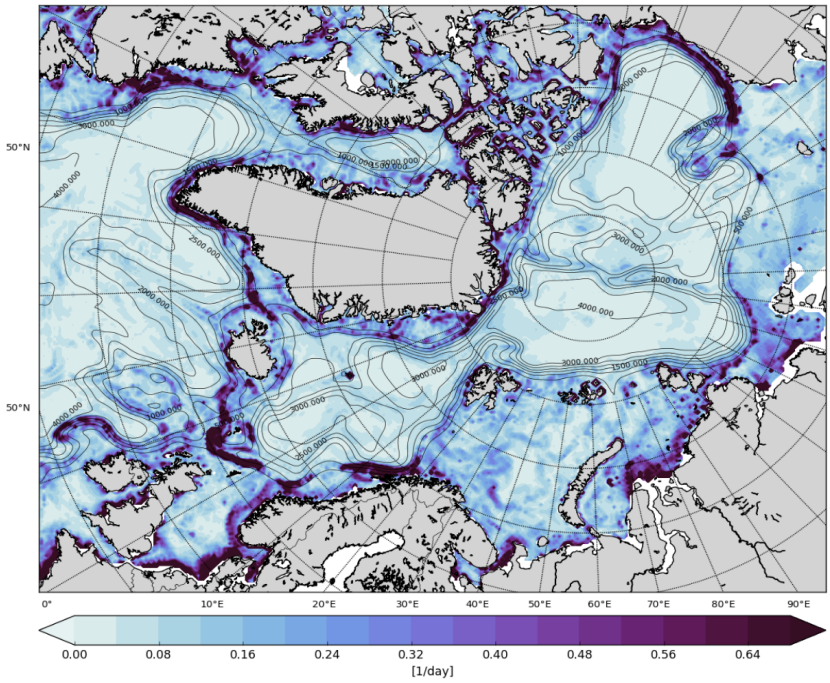


***Figure 5.1:*** *Growth rates* $(1/day)$ *computed from time-mean (1993-2003) FOAM reanalysis fields.*

Furthermore, a general view of the vortex distributions and characteristics in the Arctic Ocean could be attained by conducting an eddy census in a high-resolution model, such as done for the Nordic Seas and the Lofoten Basin in this thesis. The eddy census in Paper I showed that vortex scales are suppressed over steep topography, in agreement with predicted scales from the LSA. In addition, a clear asymmetry in vortex scales over the Lofoten basin is also seen in Paper III. The detected anticyclones are significantly larger than the cyclones. This could occur because the anticyclones are more capable of staying coherent over the basin and thus able to merge and grow, whereas the cyclones are easily strained out. A distinct difference can be seen when comparing the OW-parameter averaged over the detected vortex volumes (figure 5.2a,b). Over the basin, anticyclones have a stronger rotation versus deformation compared to the cyclones, indicating that anticyclones are more robust to strain-induced deformation. Furthermore, it is clear from the model simulations in Paper II and Paper III that anticyclones congregate over the basins. By tracing vortex pathways, anticyclones move in cyclonic loops toward the basin centre, as indicated in figure 5.2c,d. On the other hand, the cyclones appears to be expelled from the basin. A large portion of the cyclones are swept along with the boundary current, and their trajectories do not have a strong connection to the basin. This suggests that the basin cyclones may not have the

same origins as the anticyclones.

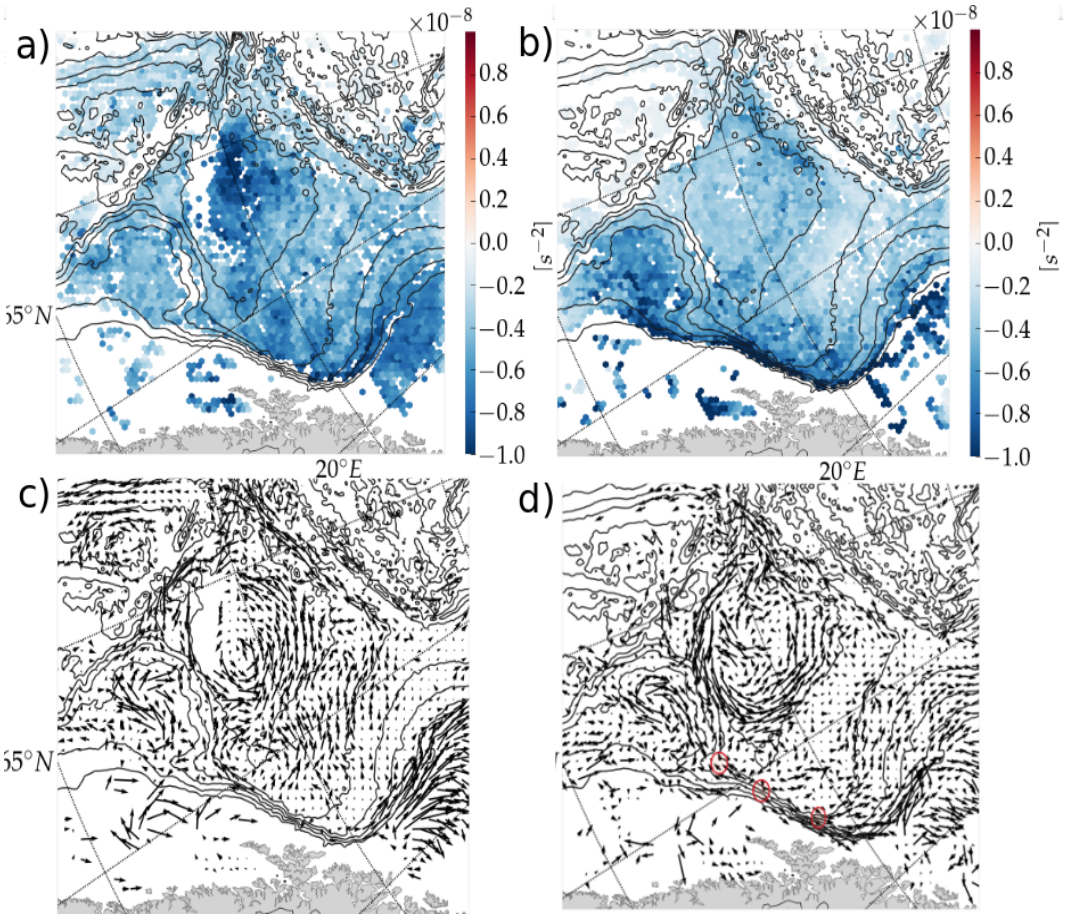


***Figure 5.2:*** *Volume averaged OW parameter over the detected vortex cores and propagation vectors for a,c) anticyclones and b,d) cyclones. There appears to be three specific locations along the continental slope (indicated in red circles in d) where vortices are preferably shed from the boundary current. This could be related to topographic features, but a closer examination is needed.*

Similar to the Lofoten basin, we may expect to have a similar accumulation of anticyclones over the Arctic basins. In an early observational eddy census, (*Manley and Hunkins*, 1985) found that vortices occupy 25 % of the surface area in the Canada basin. In a more recent observational census from the Canada basin, up to 98% of detected vortices were anticyclones (*Zhao et al.*, 2014). A question is whether there exist an anticyclone-cyclone asymmetry in the basin vortex fields also in these basins? And whether an asymmetry arises due to topography as suggested in Paper III, or due to other factors unique for the Arctic Ocean? Some studies have suggested that since cyclones tend to lie closer to the surface they are more affected by the frictional sea ice cover and spin down (*Chao and Shaw*, 1996). Also, vortices are mostly identified through their signature in the density field, i.e by isopycnal displacements. Anticyclones might be easier to observe due to their geometry, causing a blob in the density field contra merely causing an increase in stratification. The larger challenge of detecting cyclones may thus cause an observational bias. Also, if basin cyclones are smaller in scale, as suggested in this thesis, they are less detectable. Nevertheless, it is highly likely that the vortex behavior observed in the Lofoten basin may be general for other

high-latitude basins (that are connected source generating vortices), and worth looking into.

Understanding the evolution and origins of Lofoten Basin cyclones could also be of relevance to cyclones in the Arctic Ocean. The LV is often observed to be encircled by cyclonic vortices, but the origins of these cyclones have not been studied. It appears that some might be locally generated or they could originate from the Mohn ridge. The surrounding vortices may have an implication on the evolution of the anticyclonic vortices. In this study, quantitative implications of the effects of surrounding vortices during several vortex interaction events were seen, both during horizontal mergers and vertical alignments. External influences seems to both contribute in bringing the vortices closer and, in some cases, disrupt the interaction. Cyclones can lock onto one of the interacting anticyclones creating a dipole effect. This occurs in some of the partial merger events in Paper II. A dipole preventing mergers was described by *Ciani et al.* (2016). They studied mergers of shielded subsurface anticyclones. A similar dipolar effect was described by *Valcke and Verron* (1997) who studied the merger of shielded baroclinic quasi-geostrophic vortices. In both studies the two vortices exist in isolation, and the dipoles arise from the vortex PV structure alone. This mechanicm was not directly observed in this work, but similar opposite-signed PVa attachments might be possible when a surrounding vortex field exist. A question is whether some of the basin cyclones might be debris from the anticyclones positive PV lobes.

Another key issue is understanding the Beaufort Gyre. In contrast to the circulation in the Eurasian Basin and the basins in the Nordic Seas, driven by cyclonic wind stress, an atmospheric high pressure system commonly resides over the Beaufort gyre. This 'Beaufort high' drives anticyclonic flow in the interior of the Canada basin, whereas the flow pattern in the Eurasian basin is cyclonic. The wind causes convergence and Ekman pumping in center of the gyre, and a deepening of the fresh surface layer, creating a vast repository of freshwater there (*Manucharyan et al.*, 2016). The gyre have periods of weaker or even a reversed circulation, resulting in a release of fresh water into the North Atlantic. Eddies play an active part in balancing the Ekman pumping in the Beaufort gyre (*Manucharyan et al.*, 2016) and may contribute to the stabilization of the gyre. A lot of attention is given the Fresh Water Content of the gyre and potential scenarios which would lead to a fresh water release (*Mcphee et al.*, 2009; *Solomon et al.*, 2021). A different take on the ongoing studies is what sets the stability of the gyre. Whereas the Arctic Ocean Boundary Current flows cyclonically around the gyre, observations have implied that the deep gyre flow share the same anticyclonic circulation as the surface (*Dosser and Timmermans*, 2018). Is the large-scale anticyclonic forcing a particular source of instability and variability?

*Nøst et al.* (2008) examined the stability of barotropic flow over two connected bowl shaped basins in an idealized model domain. Wind forcing (anticyclonic and cyclonic wind stress) was applied in only one basin. When the Rossby number, $Ro$, and the Ekman number, $Ek$, is comparable (constituting weak nonlinearity), forcing of either sign produces an isobath-following circulation of the same sign in both basins. However, when $Ek << Ro$ (constituting strong nonlinearity), the anticyclonic circulation exhibit regions of cross-isobath flow, while the cyclonic case remains strictly isobath-

following. The authors suggest that there is a difference in the steady solutions and that, for weak bottom friction, only cyclonic circulation is stable over a basin. *LaCasce et al.* (2008) examined the steady state solutions from statistical mechanics(*Carnevale and Frederiksen*, 1987) for inviscid barotropic quasi-geostrophic flow over an elliptical basin, for various values of $\mu$. They found a similar asymmetry in the solutions, the cyclonic circulation mostly follow the isobaths, while the anticyclonic circulation is cross-isobath and breaks up into small scale vortices. The chaotic flow at smaller scales arise due to arrested topographic waves that, due to their prograde propagation, become stationary in the presence of an anticyclonic mean flow. While forced flows may exhibit both sense of rotation as shown in (*Nøst et al.*, 2008), their results indicate how the flow responds without forcing. If the forcing is turned off, the cyclonic cirulation would remain steady and simply spin down, while the anticyclonic circulation would evolve and break up. This could be relevant for periods of weaker flow in the Beaufort Gyre, and perhaps even more so for an intermediate period in the case of a flow-reversal.

A continuation of these studies could look further into nonlinear stability of wind-driven flow over asymmetric topography, but extend to a stratified flow. As noted by (*LaCasce et al.*, 2008), one could expect to find similar solutions, since the propagation direction of the topographic waves would still be prograde. However, following the arguments from *Nøst et al.* (2008), the circulation in the Eurasian basin should be more aligned with the isobaths than in the Canada basin, where more cross isobath flow might occur. To quantify the degree of topographic alignment of the flow in the Beaufort gyre, the existing Arctic Ocean observations could be examined, and compared to realistic model output. The effect of including a subsurface ridge in the northernmost basin, which could represent the Chucki Plateau, could also be tested.

Figure 5.3 shows two such simulations including a subsurface ridge (conducted by this author). Figure 5.3a (b) display the streamlines when strong anticyclonic (cyclonic) wind stress and weak bottom friction is applied, and the simulation has reached a steady state. In a) the resulting flow not only exhibit strong cross isobath flow, but the presence of a ridge makes the anticyclonic solution break up into smaller scale features. This is not seen in simulations without this ridge. The cyclonic solution looks similar to a stable state with streamlines aligned with the topography.

### 5.2.2 Three dimensional view of vortices

A lot of the observational database of vortices is derived from satellite observations, displaying their sea surface signatures. However, vortices are three-dimensional structures, so gaining knowledge of the full-depth dynamices of mesoscale vortices is important. In addition, vortices exist at different depths and may not be visible in surface observations. In the Arctic Ocean, the EKE is maximum below the surface, and the sub-surface EKE does not exhibit the aforementioned the seasonality with lower levels in wintertime (*Meneghello et al.*, 2021; *Zhao et al.*, 2018b).

Moreover, vortex studies have often been conducted in two-dimensions, in reduced-gravity models with one active layer, or in QG models with two or more layers. Sim-

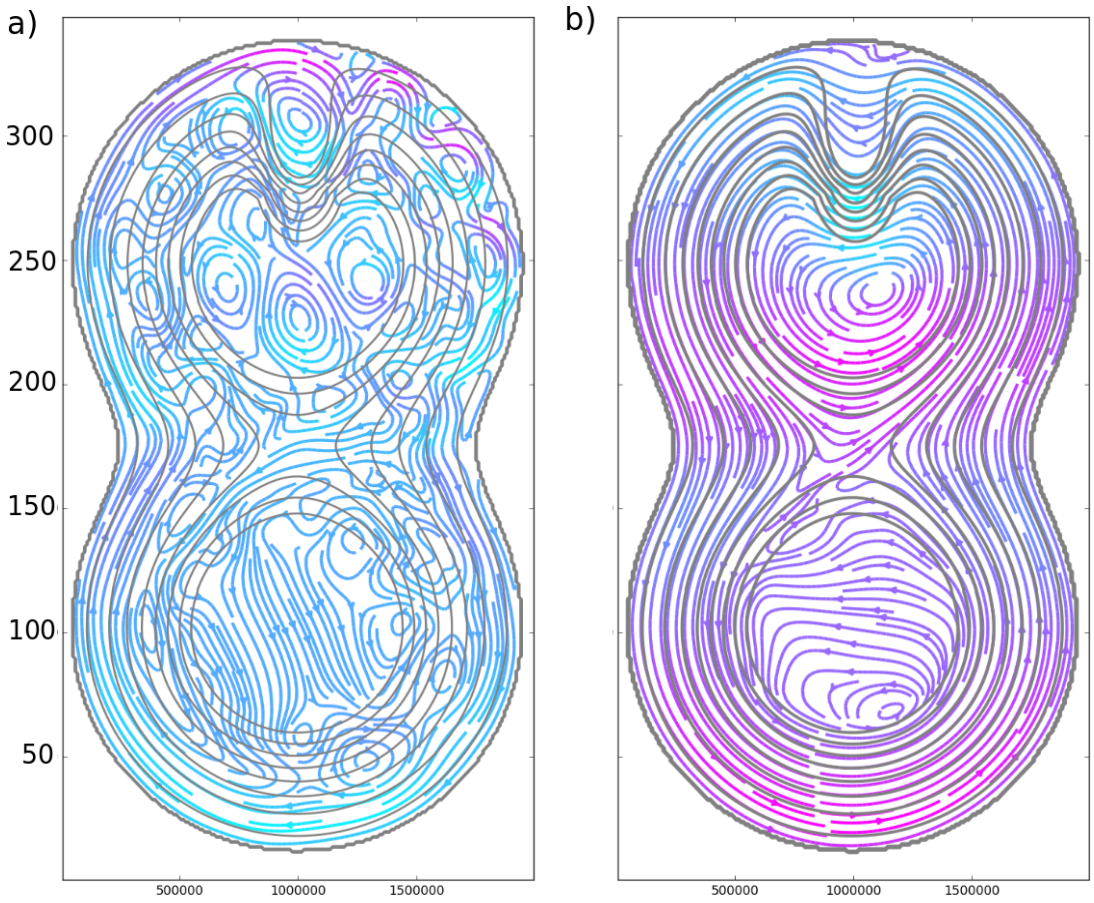


***Figure 5.3:*** *Steady state streamlines arising from a) strong anticyclonic wind forcing b) strong cyclonic wind forcing in barotropic model experiments using MITgcm.*

plified models are useful tools for examining complex vortex evolution, but the models might lack important processes. It is therefore valuable to also study vortex evolution in primitive equation models and in realistic oceanic settings. Several details about their evolution, especially those related to the sub-surface, are not fully understood.

One key question is how vortices obtain their vertical structure. Their vertical extent reflects how they are impacted by and how they impact the larger-scale currents and their surroundings. Some studies point to wintertime convection as a possible process that deepen anticyclones (*Ivanov and Korablev*, 1995; *Yu et al.*, 2017). Paper 2 showed that the vertical alignment is also a mechanism that cause a substantial and efficient deepening of anticyclonic vortices. Through this process, anticyclones could abruptly double in vertical extent, while wintertime convection was seen to cause minor deepening. The anticyclones in the Lofoten Basin are carriers of warm AW, and vertical alignment may contribute to deepen the overall AW extent in the basin. Furthermore, this deepening could connect the vortices to the bottom and possibly to large-scale energy dissipation.

To investigate whether this is the case, a study using the Lofoten Basin simulation could look into the degeneration of the basin anticyclones. Some studies address the decay of the LV (*Belonenko et al.*, 2017; *Fer et al.*, 2018). *Belonenko et al.* (2017) sug-

gest that either baroclinic instability or a mixed baroclinic–barotropic instability cause a gradual decay of the LV. They studied the vortex' stability in a two- and three-layer QG model with a flat and a sloping bottom. The flat-bottom analysis showed rapid decay, in disagreement with primitive equation realistic model simulations. Including a sloping bottom in the analysis reduced the decay-rates, more in agreement with the simulated decay. The last study of this thesis argues that the basin itself is central to the LV formation. The role of bottom friction is however not clear. The lower portion of the anticyclone forming in the idealized experiments in Paper III is of significant strength when friction is applied. This is in accordance with the realistic simulation in Paper II (which includes bottom friction) and observations, where the Lofoten Vortex maintains significant bottom velocities. Analysis is needed to clarify why the bottom portion is not just simply dissipated.

Furthermore, the Arctic Ocean is the most similar to the Lofoten Basin of the observed sites of double core structures. Vortices are found in the Canada Basin and the Eurasian basin, in all parts of the water column (*Manucharyan and Timmermans*, 2013; *Spall et al.*, 2008; *Timmermans*, 2008; *Watanabe*, 2011; *Zhao et al.*, 2014). As mentioned above, more than 90% of the observed eddies in the Arctic Ocean are anticyclonic. In Paper 2 we found that vertical alignment was key to the LV. The investigations also showed that the process is not unique for the LV, several anticyclones had double cores. Thus, vertical alignment could also contribute to the longevity of the Arctic anticyclones.

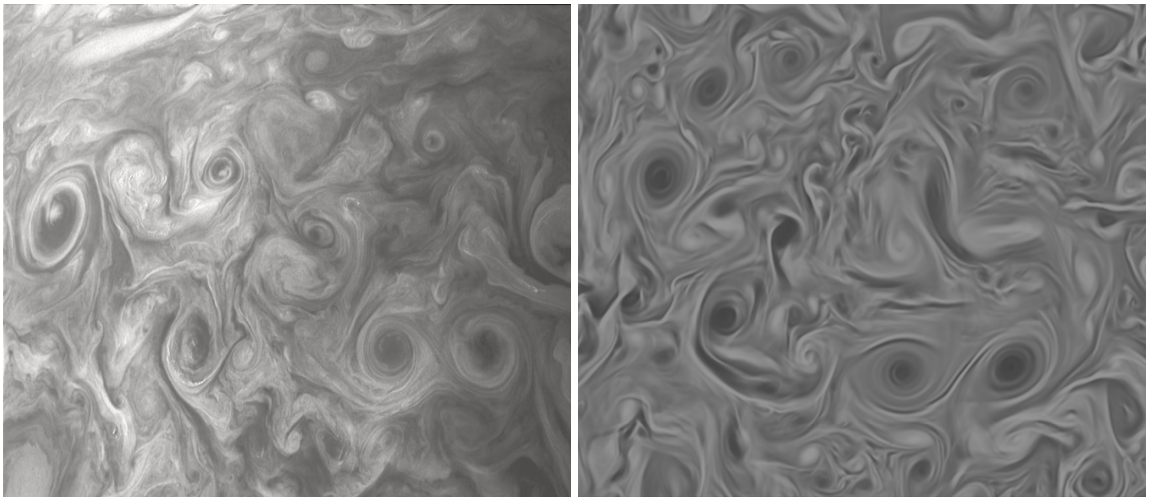

***Figure 5.4:*** *The vortex field on a) Jupiter and b) Lofoten Basin. The colors have been ammended in the figure from Jupiter (NASA/JPL/SwRI/MSSS/GeraldEichstädt/AlexisTranchandon/Solaris, 2017).*

Besides the long-lived anticyclones in the ocean, another long-lived anticylonic vortex is the Great Red Spot (GRS) on Jupiter. The GRS has stayed coherent since first observed 300 years ago (*Parisi et al.*, 2021), and its formation and longevity is somewhat of a mystery. Paper 2 showed that stable anticyclones can form over topographic depressions. Some studies has hypothesized that the GRS is attached to a topographic bump, however *Golitsyn* (1970) was the first of many who proposed that this is not the case. Jupiter has a rich vortex field. Figure 5.4 shows an example of similarities be-

tween the vortex field on Jupiter (a) compared to the Lofoten Basin (b). Some studies have suggested that vortex mergers could be important to the GRS (*Sánchez-Lavega et al.*, 2021), but from model experiments, there do not seem to be enough mergers to sustain it (*ScienceDaily*, 2013). As shown in this thesis, approximately one vertical alignment per year appears to be sufficient to rejuvenate the LV. Could vertical alignment also be relevant for the GRS?

### 5.2.3 The use of novel tools

High-resolution numerical models, such as used in this thesis, provide a complementary tool for detailed theoretical investigations of vortex evolution and propagation. However more observations are needed to document vortex interactions in the ocean. A tool that potentially could be useful is seismic imaging, which provides higher resolution (up to O(10 m)) than many other measurements. The reflections in seismic images from the water column are 100-1000 times weaker than below the ocean floor, but can however reveal the ocean stratification (*Zou et al.*, 2021). *Biescas et al.* (2008) observed double core vortices in seismic data. *Yang et al.* (2022) observed a lens-like mesoscale eddy in the Northwind Basin in the Arctic ocean using seismic sections. *Gula et al.* (2019) investigated submesoscale lens-shaped vortices in the Gulf Stream using seismic images in combination with glider data.

Because of high oil activity, Norway has a lot of seismic data, especially outside the Lofoten Islands. Some of these surveys even extend into the basin. None of the signals from the ocean has been utilized, and there exist a large catalogue of data that could be very interesting to investigate. Paper 2 showed that the double core structure lasted for months in summertime, whereas the core was rapidly homogenized in wintertime. Thus, vertical alignments may be easier to observe in summertime.

Lastly, investigations of three-dimensional ocean processes could benefit from advanced visualization tools. In Paper 2, the visualization tool Paraview was utilized to investigate what happened below the surface during a merger event. The details of the merger were hard to decipher in conventional two-dimentional transects, and might have been overlooked without three-dimensional animations. A clear lesson from this thesis is that Paraview or other similar programs could be valuable as complementary tools in studies of ocean vortices and dynamics.

### 5.2.4 Linking the mesoscale and the submesoscale

Some existing global climate models are approaching an eddy-resolving regime globally, in which mesoscale vortices are represented on the grid. This necessitates more investigations of processes occurring below the mesoscale, namely the submesoscale. Submesoscales are motions, such as fronts, filaments and vortices, with spatial scales of O(1-10) km and temporal scales O(1) day. The finer submesoscale motions are important for kinetic energy exchanges to small-scale dissipation, particularly in the upper ocean. The transfer of kinetic energy at small scales is presently not very well understood. The findings of *Scott and Wang* (2005) imply that $1/3$ of the KE at $L_d$ is passed

downscale, and $2/3$ is passed upscale. However, these findings are somewhat uncertain due to smoothing of the altimeter dataset used. Also, this division leaves boundary friction as the main dissipation route for the mesoscale kinetic energy. However, boundary friction might be responsible for merely 10% of the energy injected into the ocean (*Balwada et al.*, 2022), raising a question of how to close the budget.

Down-scale energy transfers via the submesoscales, leading to small-scale dissipation, may play an important role in closing the energy budget. Recent obvervational studies show evidence of both an inverse and forward cascade occuring in the upper 1000 m of the ocean (*Balwada et al.*, 2022; *Yu et al.*, 2021). The inverse cascade is present year-round, but the forward cascade exhibits a strong seasonal signal, infusing and draining the mesoscale kinetic energy in winter and summer, respectively. This seasonality only exist in ocean models with high spatial resolution. While findings in this thesis (Paper I) point to baroclinic instability as the main source of EKE in the region, other studies suggest that a significant portion of the conversion of APE to KE is rather triggered through an inverse cascade of submesoscale KE (*Dong et al.*, 2020; *Klein et al.*, 2019; *Yu et al.*, 2021). More studies are needed to provide a clearer picture of the distribution and transfer of energy.

One inherent limitation of the linear stability analysis in Paper I is that it neglects nonlinear interactions, which is likely important in setting the observed finite amplitude mesoscale vortex features. Due to the suppressed length scales of mesoscale vortices at high latitudes, there exists a strong overlap between the mesoscales and submesoscales. This might make interactions more frequent in such regions. Thus, the Nordic Seas might be a particularly interesting region for investigations of cross-scale interactions. The model utilized in Paper II is eddy-permitting in the submesocale range. While this thesis focused on studying mesoscale eddies, the model simulation, or another simulation with an even higher spatial resolution, could be utilized to study submesoscale features. A further analysis focusing particularly on multiscale interactions could be both feasible and relevant.

## 5.3 A concluding remark

Defining the ocean's role in the global climate demands an understanding of the dynamics of the ocean circulation. While it is important in itself to better understand the present-day circulation, it is crucial to understand the present-day circulation to know how the circulation will be impacted if the rapid climatic changes occurring in the high-latitude regions persist. Without such understanding, it is hard to interpret and predict how the high-latitude oceans and the Global Ocean responds to future climate scenarios. As noted in the introduction, mesoscale vortices contribute to setting the ocean state, and it is therefore essential to study their dynamics, such as vortex formation, interactions, instabilities, and external influences.

# Bibliography


Armi, L., D. Hebert, N. Oakey, J. F. Price, P. L. Richardson, H. T. Rossby, and B. Ruddick (1989), Two years in the life of a Mediterranean salt lens, *Journal of Physical Oceanography*, *19*(3), 354–370, doi:10.1175/1520-0485(1989)019<0354:TYITLO>2.0.CO;2. 2.6

Arnol'd, V. (1965), Variational principle for three-dimensional steady-state flows of an ideal fluid, *Journal of Applied Mathematics and Mechanics*, *29*(5), 1002–1008, doi:https://doi.org/10.1016/0021-8928(65)90119-X. 3.4

Asbjørnsen, H., M. Årthun, Skagseth, and T. Eldevik (2020), Mechanisms underlying recent arctic atlantification, *Geophysical Research Letters*, *47*(15), e2020GL088,036, doi:https://doi.org/10.1029/2020GL088036. 5.2.1

Baird, M. E., and K. R. Ridgway (2012), The southward transport of sub-mesoscale lenses of Bass Strait Water in the centre of anti-cyclonic mesoscale eddies, *Geophysical Research Letters*, *39*(2), doi:10.1029/2011GL050643. 2.6

Balwada, D., J.-H. Xie, R. Marino, and F. Feraco (2022), Direct observational evidence of an oceanic dual kinetic energy cascade and its seasonality, *arXiv*, doi:10.48550/ARXIV.2202.08637. 5.2.4

Barceló-Llull, B., P. Sangrà, E. Pallàs-Sanz, E. D. Barton, S. N. Estrada-Allis, A. Martínez-Marrero, B. Aguiar-González, D. Grisolía, C. Gordo, Ángel Rodríguez-Santana, Ángeles Marrero-Díaz, and J. Arístegui (2017), Anatomy of a subtropical intrathermocline eddy, *Deep Sea Research Part I: Oceanographic Research Papers*, *124*, 126 – 139, doi:https://doi.org/10.1016/j.dsr.2017.03.012. 2.6

Beldring, S., K. Engeland, L. A. Roald, N. R. Sælthun, and A. Voksø (2003), Estimation of parameters in a distributed precipitation-runoff model for Norway, *Hydrology and Earth System Sciences*, *7*(3), 304–316, doi:10.5194/hess-7-304-2003. 3.1.1

Belkin, I., and Y. Mikhailitchenko (1986), Thermohaline structure of the frontal zone of the Northwest Pacific Ocean at 160E (in Russian), *Okeanologiya*, *26*, 70–72. 2.6

Belkin, I., A. Foppert, T. Rossby, S. Fontana, and C. Kincaid (2020), A Double-Thermostad Warm-Core Ring of the Gulf Stream, *Journal of Physical Oceanography*, *0*(0), null, doi:10.1175/JPO-D-18-0275.1. 2.6

Belonenko, T., V. Travkin, A. Koldunov, and D. Volkov (2021), Topographic experiments over dynamical processes in the norwegian sea, *Russian Journal of Earth Sciences*, *21*, 1–15, doi:10.2205/2020ES000747. 2.7

Belonenko, T. V., I. L. Bashmachnikov, A. V. Koldunov, and P. A. Kuibin (2017), On the vertical velocity component in the mesoscale Lofoten vortex of the Norwegian Sea, *Izvestiya, Atmospheric and Oceanic Physics*, *53*(6), 641–649, doi: 10.1134/S0001433817060032. 2.7, 5.2.2

Bertsekas, D. P. (1996), *Constrained Optimization and Lagrange Multiplier Methods (Optimization and Neural Computation Series)*, 1 ed., Athena Scientific. 3.4

Biescas, B., V. Sallares, J. Pelegrí, F. Machín, R. Carbonell, G. G. Buffett, J. Danobeitia, and A. Calahorrano (2008), Imaging meddy finestructure using multichannel seismic reflection data, *Geophysical Research Letters*, *35*, 0–4, doi: 10.1029/2008GL033971. 5.2.3

Blindheim, J., and S. Østerhus (2005), The nordic seas, main oceanographic features, *Washington DC American Geophysical Union Geophysical Monograph Series*, *158*, doi:10.1029/158GM03. 2.3

Blumsack, S. L., and P. J. Gierasch (1972), Mars: The Effects of Topography on Baroclinic Instability, *Journal of the Atmospheric Sciences*, *29*(6), 1081–1089. 2.5

Bogdanov, K., V. Iliychev, V. Lobanov, and R. Medjitov (1985), Investigation of anticyclonic eddy in the northwest part of the Pacific Ocean (in Russian), *DOH. Acad. Sci. USSR*, *281*, 1210–1213. 2.6

Bosse, A., I. Fer, J. M. Lilly, and H. Søiland (2019), Dynamical controls on the longevity of a non-linear vortex : The case of the Lofoten Basin Eddy, *Scientific Reports, Nature*, *9*(13448), null, doi:10.1038/s41598-019-49599-8. 2.7

Bracco, A., and J. Pedlosky (2003), Vortex Generation by Topography in Locally Unstable Baroclinic Flows, *Journal of Physical Oceanography*, *33*(1), 207–219. 2.5

Bracco, A., J. Pedlosky, and R. S. Pickart (2008), Eddy Formation near the West Coast of Greenland, *Journal of Physical Oceanography*, *38*(9), 1992–2002. 2.5

Brandt, L., and K. Nomura (2007), The physics of vortex merger and the effects of ambient stable stratification, *Journal of Fluid Mechanics*, *592*, 413 – 446, doi:10.1017/S0022112007008671. 2.6, 2.6

Brandt, L. K., T. K. Cichocki, and K. K. Nomura (2010), Asymmetric vortex merger: mechanism and criterion, *Theoretical and Computational Fluid Dynamics*, *24*(1), 163–167. 2.6

Bretherton, F. (1966), Baroclinic instability and the short wavelength cutoff in terms of potential vorticity, *Quart. J. Roy. Meteor. Soc.*, *92*, 335–345. 3.3.3

Bretherton, F. P., and D. B. Haidvogel (1976), Two-dimensional turbulence above topography, *Journal of Fluid Mechanics*, *78*(1), 129–154, doi:10.1017/S002211207600236X. 2.7, 3.4, 3.4, 3.5, 3.4

Brundage, W. L., and J. P. Dugan (1986), Observations of an Anticyclonic Eddy of 18° C Water in the Sargasso Sea, *Journal of Physical Oceanography*, *16*(4), 717–727, doi:10.1175/1520-0485(1986)016<0717:OOAAEO>2.0.CO;2. 2.6

Carnevale, G., and J. Frederiksen (1987), Nonlinear stability and statistical mechanics of flow over topography, *Journal of Fluid Mechanics*, *175*, 157 – 181, doi:10.1017/S002211208700034X. 3.4, 5.2.1

Carton, X., G. Maze, and B. Legras (2002), A two-dimensional vortex merger in an external strain field, *Journal of Turbulence*, *3*, N45, doi:10.1088/1468-5248/3/1/045. 2.6

Carton, X., N. Daniault, J. Alves, L. Cherubin, and I. Ambar (2010), Meddy dynamics and interaction with neighboring eddies southwest of Portugal: Observations and modeling, *Journal of Geophysical Research: Oceans*, *115*(C6), doi:10.1029/2009JC005646. 2.6

Carton, X. J. (1992), On the merger of shielded vortices, *Europhysics Letters (EPL)*, *18*(8), 697–703, doi:10.1209/0295-5075/18/8/006. 2.6

Cerretelli, C., and C. H. K. Williamson (2003), The physical mechanism for vortex merging, *Journal of Fluid Mechanics*, *475*, 41–77, doi:10.1017/S0022112002002847. 2.6, 2.12

Chanut, J., B. Barnier, W. Large, L. Debreu, T. Penduff, J. M. Molines, and P. Mathiotc (2008), Mesoscale Eddies in the Labrador Sea and Their Contribution to Convection and Restratification, *Journal of Physical Oceanography*, *38*, 1617–1643. 2.5

Chao, S.-Y., and P.-T. Shaw (1996), Initialization, asymmetry, and spindown of arctic eddies, *Journal of Physical Oceanography*, *26*(10), 2076 – 2092, doi:10.1175/1520-0485(1996)026<2076:IAASOA>2.0.CO;2. 5.2.1

Charney, J. G. (1947), The Dynamics of Long Waves in a Baroclinic Westerly Current., *Journal of Atmospheric Sciences*, *4*, 136–162. 1, 2.1, 2.5, 3.3.4

Charney, J. G., and M. E. Stern (1962), On the stability of internal baroclinic jets in a rotating atmosphere, *Journal of Atmospheric Sciences*, *19*(2), 159 – 172, doi:10.1175/1520-0469(1962)019<0159:OTSOIB>2.0.CO;2. 3.3.4

Chelton, D. B., M. G. Schlax, R. M. Samelson, and R. A. de Szoeke (2007), Global observations of large oceanic eddies, *Geophysical Research Letters*, *34*(15). 1, 2.2, 2.4

Chelton, D. B., M. G. Schlax, and R. M. Samelson (2011), Global observations of nonlinear mesoscale eddies, *Progress in Oceanography*, *91*(2), 167–216, doi:https://doi.org/10.1016/j.pocean.2011.01.002. 1, 2.2, 2.4

Chiswell, S. M. (2005), Mean and variability in the wairarapa and hikurangi eddies, new zealand, *New Zealand Journal of Marine and Freshwater Research*, *39*(1), 121–134, doi:10.1080/00288330.2005.9517295. 2.7

Ciani, D., X. Carton, and J. Verron (2016), On the merger of subsurface isolated vortices, *Geophysical & Astrophysical Fluid Dynamics*, *110*(1), 23–49, doi:10.1080/03091929.2015.1135430. 5.2.1

Collins, M., R. Knutti, J. Arblaster, J.-L. Dufresne, T. Fichefet, P. Friedlingstein, X. Gao, W. Gutowski, T. Johns, G. Krinner, M. Shongwe, C. Tebaldi, A. Weaver, and M. Wehner (2013), Chapter 12 - long-term climate change: Projections, commitments and irreversibility, in *Climate Change 2013: The Physical Science Basis. IPCC Working Group I Contribution to AR5*, edited by IPCC, Cambridge University Press, Cambridge. 5.2.1

Corréard, S. M., and X. J. Carton (1999), Vertical alignment of geostrophic vortices, in *IUTAM Symposium on Simulation and Identification of Organized Structures in Flows*, edited by J. N. Sørensen, E. J. Hopfinger, and N. Aubry, pp. 191–200, Springer Netherlands, Dordrecht. 2.6

Cresswell, G. (1982), The Coalescence of Two East Australian Current Warm-Core Eddies, *Science (New York, N.Y.)*, *215*, 161–4, doi:10.1126/science.215.4529.161. 2.6

Cummins, P. F., and G. Holloway (1994), On eddy–topographic stress representation, *Journal of Physical Oceanography*, *24*(3), 700–706. 2.7

Delman, A., and T. Lee (2021), Global contributions of mesoscale dynamics to meridional heat transport, *Ocean Science*, *17*(4), 1031–1052, doi:10.5194/os-17-1031-2021. 2.2

Dmitrenko, I. A., S. A. Kirillov, V. V. Ivanov, and R. A. Woodgate (2008), Mesoscale Atlantic water eddy off the Laptev Sea continental slope carries the signature of upstream interaction, *Journal of Geophysical Research: Oceans*, *113*(C7), doi:10.1029/2007JC004491. 2.6

Dong, J., B. Fox-Kemper, H. Zhang, and C. Dong (2020), The seasonality of submesoscale energy production, content, and cascade, *Geophysical Research Letters*, *47*(6), e2020GL087,388, doi:https://doi.org/10.1029/2020GL087388. 5.2.4

Dosser, H. V., and M.-L. Timmermans (2018), Inferring circulation and lateral eddy fluxes in the arctic ocean's deep canada basin using an inverse method, *Journal of Physical Oceanography*, *48*(2), 245 – 260, doi:10.1175/JPO-D-17-0190.1. 5.2.1

Dritschel, D. (1995), A general theory for two-dimensional vortex interactions. j fluid mech, *Journal of Fluid Mechanics*, *293*, 269 – 303, doi:10.1017/S0022112095001716. 2.6

Dritschel, D. G. (1985), The stability and energetics of corotating uniform vortices, *Journal of Fluid Mechanics*, *157*, 95–134, doi:10.1017/S0022112085002324. 2.6

Dritschel, D. G. (2002), Vortex merger in rotating stratified flows, *Journal of Fluid Mechanics*, *455*(1), 83–101, doi:10.1017/S0022112001007364. 2.6

Dritschel, D. G., and D. W. Waugh (1992), Quantification of the inelastic interaction of unequal vortices in two-dimensional vortex dynamics, *Physics of Fluids A: Fluid Dynamics*, *4*(8), 1737–1744, doi:10.1063/1.858394. 2.6

Eady, E. T. (1949), Long waves and cyclone waves, *Tellus*, *1*(3), 33–52, doi:https://doi.org/10.1111/j.2153-3490.1949.tb01265.x. 1, 2.1, 1, 3.3.4

Eden, C., and C. Böning (2002), Sources of eddy kinetic energy in the Labrador Sea, *Journal of Physical Oceanography*, *32*, 3346–3363. 2.5

Eden, C., M. Jochum, and G. Danabasoglu (2009), Effects of different closures for thickness diffusivity, *Ocean Modelling*, *26*(1), 47–59, doi:https://doi.org/10.1016/j.ocemod.2008.08.004. 1

Ezat, M., T. Rasmussen, B. Hönisch, J. Groeneveld, and P. Demenocal (2017), Article episodic release of co 2 from the high-latitude north atlantic ocean during the last 135 kyr, *Nature Communications*, *8*, doi:10.1038/ncomms14498. 2.2

Farneti, R., T. Delworth, A. Rosati, S. Griffies, and F. Zeng (2010), The role of mesoscale eddies in the rectification of the southern ocean response to climate change, *Journal of Physical Oceanography - J PHYS OCEANOGR*, *40*, 1539–1557, doi:10.1175/2010JPO4353.1. 2.2

Fer, I., A. Bosse, B. Ferron, and P. Bouruet-Aubertot (2018), The Dissipation of Kinetic Energy in the Lofoten Basin Eddy, *Journal of Physical Oceanography*, *48*(6), 1299–1316, doi:10.1175/JPO-D-17-0244.1. 2.6, 2.6, 2.7, 5.2.2

Fjørtoft, R. (1953), On the changes in the spectral distribution of kinetic energy for twodimensional, nondivergent flow, *Tellus*, *5*(3), 225–230, doi:10.3402/tellusa.v5i3.8647. 2.2

Fossum, I. (2006), Analysis of instability and mesoscale motion off southern norway, *Journal of Geophysical Research: Oceans*, *111*(C8), doi:https://doi.org/10.1029/2005JC003228. 2.5

Garreau, P., F. Dumas, S. Louazel, A. Stegner, and B. Le Vu (2018), High-Resolution Observations and Tracking of a Dual-Core Anticyclonic Eddy in the Algerian Basin, *Journal of Geophysical Research: Oceans*, *123*(12), 9320–9339, doi:10.1029/2017JC013667. 2.6

Gelderloos, R., C. A. Katsman, and S. S. Drijfhout (2011), Assessing the Roles of Three Eddy Types in Restratifying the Labrador Sea after Deep Convection, *Journal of Physical Oceanography*, *41*(11), 2102–2119, doi:10.1175/JPO-D-11-054.1. 2.5

Gent, P. R., and J. C. Mcwilliams (1990), Isopycnal mixing in ocean circulation models, *Journal of Physical Oceanography*, *20*(1), 150 – 155, doi:10.1175/1520-0485(1990)020<0150:IMIOCM>2.0.CO;2. 2.7

Gill, A., J. Green, and A. Simmons (1974), Energy partition in the large-scale ocean circulation and the production of mid-ocean eddies, *Deep Sea Research and Oceanographic Abstracts*, *21*(7), 499–528. 2.4

Glover, D. M., S. C. Doney, W. K. Oestreich, and A. W. Tullo (2018), Geostatistical analysis of mesoscale spatial variability and error in seawifs and modis/aqua global ocean color data, *Journal of Geophysical Research: Oceans*, *123*(1), 22–39, doi:https://doi.org/10.1002/2017JC013023. 2.2

Golitsyn, G. (1970), A similarity approach to the general circulation of planetary atmospheres, *Icarus*, *13*(1), 1–24, doi:https://doi.org/10.1016/0019-1035(70)90112-0. 5.2.2

Griffies, S. (2004), *Fundamentals of Ocean Climate Models*, Princeton University Press. 2.2

Griffiths, R. W., and E. J. Hopfinger (1987), Coalescing of geostrophic vortices, *Journal of Fluid Mechanics*, *178*, 73–97, doi:10.1017/S0022112087001125. 2.6

Gula, J., T. M. Blacic, and R. E. Todd (2019), Submesoscale coherent vortices in the gulf stream, *Geophysical Research Letters*, *46*(5), 2704–2714, doi:https://doi.org/10.1029/2019GL081919. 5.2.3

Haidvogel, D., H. Arango, W. Budgell, B. Cornuelle, E. Curchitser, E. D. Lorenzo, K. Fennel, W. Geyer, A. Hermann, L. Lanerolle, J. Levin, J. McWilliams, A. Miller, A. Moore, T. Powell, A. Shchepetkin, C. Sherwood, R. Signell, J. Warner, and J. Wilkin (2008), Ocean forecasting in terrain-following coordinates: Formulation and skill assessment of the Regional Ocean Modeling System, *Journal of Computational Physics*, *227*(7), 3595 – 3624. 3.1

Halo, I., B. Backeberg, P. Penven, I. Ansorge, C. Reason, and J. Ullgren (2014), Eddy properties in the Mozambique Channel: A comparison between observations and two numerical ocean circulation models, *Deep Sea Research Part II: Topical Studies in Oceanography*, *100*(0), 38 – 53. 3.2

Hanzlick, D. J. (1983), Phd thesis, the west spitsbergen current: transport, forcing and variability, *University of Washington, USA*. 2.5

Hasselmann, K. (2010), *Seventy Years of Exploration in Oceanography: A Prolonged Weekend Discussion with Walter Munk*, Springer Berlin Heidelberg. 2.1

Haugan, P. M., G. Evensen, J. A. Johannessen, O. M. Johannessen, and L. H. Pettersson (1991), Modeled and observed mesoscale circulation and wavecurrent refraction during the 1988 norwegian continental shelf experiment, *Journal of Geophysical Research*, *96*, 10,487–10,506. 2.5

Helland-Hansen, B., and F. N. Hjalmar (1909), The norwegian sea; its physical oceanography based upon the norwegian researches 1900-1904, *Report on Norwegian fishery and marine-investigations*, *2*(2). 2.3

Hernández-Hernández, N., J. Arístegui, M. F. Montero, E. Velasco-Senovilla, F. Baltar, Marrero-Díaz, A. Martínez-Marrero, and Rodríguez-Santana (2020), Drivers of plankton distribution across mesoscale eddies at submesoscale range, *Frontiers in Marine Science*, *7*, doi:10.3389/fmars.2020.00667. 2.2

Holloway, G. (1992), Representing topographic stress for large-scale ocean models, *Journal of Physical Oceanography*, *22*(9), 1033 – 1046, doi:10.1175/1520-0485(1992)022<1033:RTSFLS>2.0.CO;2. 2.7, 2.7

Huang, M.-J. (2005), The physical mechanism of symmetric vortex merger: A new viewpoint, *Physics of Fluids*, *17*(7), 074,105, doi:10.1063/1.1949647. 2.6

Ikeda, M., J. A. Johannessen, K. Lygre, and S. Sandven (1989), A process study of mesoscale meanders and eddies in the norwegian coastal current, *Journal of Physical Oceanography*, *19*(1), 20 – 35, doi:10.1175/1520-0485(1989)019<0020:APSOMM>2.0.CO;2. 2.5

Isachsen, P. E. (2015), Baroclinic instability and the mesoscale eddy field around the Lofoten Basin, *Journal of Geophysical Research: Oceans*, *120*(4), 2884–2903. 2.5, 2.5

Isachsen, P. E., J. H. LaCasce, C. Mauritzen, and S. H. äkkinnen (2003), Wind-Driven Variability of the Large-Scale Recirculating Flow in the Nordic Seas and Arctic Ocean, *Journal of Physical Oceanography*, *33*, 2534–2550. 1, 2.5

Itoh, S., and I. Yasuda (2010), Water Mass Structure of Warm and Cold Anticyclonic Eddies in the Western Boundary Region of the Subarctic North Pacific, *Journal of Physical Oceanography*, *40*(12), 2624–2642, doi:10.1175/2010JPO4475.1. 2.6

Ivanov, V., and A. Korablev (1995), Formation and regeneration of the pycnocline lens in the Norwegian Sea., *Russian Meteorology and Hydrology*, (9), 62–69. 1, 5.2.2

Jakobsen, P. K., M. H. Ribergaard, D. Quadfasel, T. Schmith, and C. W. Hughes (2003), Near-surface circulation in the northern north atlantic as inferred from lagrangian drifters: Variability from the mesoscale to interannual, *Journal of Geophysical Research: Oceans*, *108*(C8), doi:https://doi.org/10.1029/2002JC001554. 2.5

Keating, S. (2014), Baroclinic instability, https://www.climatescience.org.au/sites/default/files/BaroclinicInstabilityKeating.pdf, online: accessed 2022-02-28. 3.4, 3.3.4

Klein, P., G. Lapeyre, L. Siegelman, B. Qiu, L.-L. Fu, H. Torres, Z. Su, D. Menemenlis, and S. Le Gentil (2019), Ocean-scale interactions from space, *Earth and Space Science*, *6*(5), 795–817, doi:https://doi.org/10.1029/2018EA000492. 5.2.4

Köhl, A. (2007), Generation and Stability of a Quasi-Permanent Vortex in the Lofoten Basin, *Journal of Physical Oceanography*, *37*(11), 2637–2651. 1, 2.5, 2.6, 2.7

Kraichnan, R. H. (1967), Inertial ranges in two-dimensional turbulence, *The Physics of Fluids*, *10*(7), 1417–1423, doi:10.1063/1.1762301. 2.2

Kyrchei, I. I. (2018), Cramer's rules for the system of two-sided matrix equations and of its special cases, in *Matrix Theory*, edited by H. A. Yasser, chap. 1, IntechOpen, Rijeka, doi:10.5772/intechopen.74105. 3

L. Vere, S. (1997), IAPSO PRESIDENT'S INVITED LECTURE, http://iugg.org/iapso/JointAssembly97/munk/munk.html, online; Accessed 2022-02-28. 2.1

LaCasce, J. H., O. A. Nøst, and P. E. Isachsen (2008), Asymmetry of free circulations in closed ocean gyres, *Journal of Physical Oceanography*, *38*(2), 517 – 526, doi:10.1175/2007JPO3789.1. 5.2.1

Lappa, M. (2012), *Rotating Thermal Flows in Natural and Industrial Processes*, Wiley, doi:10.1002/9781118342411. 3.3.3, 3.3.4

Large, W. G., J. C. McWilliams, and S. C. Doney (1994), Oceanic vertical mixing: A review and a model with a nonlocal boundary layer parameterization, *Reviews of Geophysics*, *32*(4), 363–403, doi:https://doi.org/10.1029/94RG01872. 3.1.2

Larichev, V. D., and I. M. Held (1995), Eddy amplitudes and fluxes in a homogeneous model of fully developed baroclinic instability, *Journal of Physical Oceanography*, *25*(10), 2285 – 2297, doi:10.1175/1520-0485(1995)025<2285:EAAFIA>2.0.CO;2. 2.2

Le Bras, I. A.-A., F. Straneo, J. Holte, and N. P. Holliday (2018), Seasonality of freshwater in the east greenland current system from 2014 to 2016, *Journal of Geophysical Research: Oceans*, *123*(12), 8828–8848, doi:https://doi.org/10.1029/2018JC014511. 2.3

Le Traon, P. Y. (2013), From satellite altimetry to Argo and operational oceanography: Three revolutions in oceanography, *Ocean Science*, *9*(5), 901–915. 2.1

Leweke, T., S. Le Dizès, and C. H. Williamson (2016), Dynamics and instabilities of vortex pairs, *Annual Review of Fluid Mechanics*, *48*(1), 507–541, doi:10.1146/annurev-fluid-122414-034558. 2.12

L'Her, A., M. Reinert, S. Prants, X. Carton, and M. Morvan (2021), Eddy formation in the bays of Kamchatka and fluxes to the open ocean, *Ocean Dynamics*, *71*(5), 601–612, doi:10.1007/s10236-021-01449-w. 2.7

Lilly, J. M., P. B. Rhines, F. Schott, K. Lavender, J. Lazier, U. Send, and E. DAsaro (2003), Observations of the Labrador Sea eddy field, *Progress in Oceanography*, *59*(1), 75–176. 2.5, 2.6

Lique, C., H. L. Johnson, and P. E. D. Davis (2015), On the interplay between the circulation in the surface and the intermediate layers of the arctic ocean, *Journal of Physical Oceanography*, *45*(5), 1393 – 1409, doi:10.1175/JPO-D-14-0183.1. 5.2.1

MacLachlan, C., A. Arribas, K. A. Peterson, A. Maidens, D. Fereday, A. A. Scaife, M. Gordon, M. Vellinga, A. Williams, R. E. Comer, J. Camp, P. Xavier, and G. Madec (2015), Global Seasonal forecast system version 5 (GloSea5): a high-resolution seasonal forecast system, *Quarterly Journal of the Royal Meteorological Society*, *141*(689), 1072–1084. 3.1.1

Manley, T. O., and K. L. Hunkins (1985), Mesoscale eddies of the arctic ocean, *Journal of Geophysical Research*, *90*, 4911–4930. 2.5, 5.2.1

Manucharyan, G. E., and A. F. Thompson (2022), Heavy footprints of upper-ocean eddies on weakened arctic sea ice inmarginal ice zones, *Nature Communications*, *13*(1), 2041–1723, doi:10.1038/s41467-022-29663-0. 5.2.1

Manucharyan, G. E., and M.-L. Timmermans (2013), Generation and Separation of Mesoscale Eddies from Surface Ocean Fronts, *Journal of Physical Oceanography*, *43*(12), 2545–2562, doi:10.1175/JPO-D-13-094.1. 5.2.2

Manucharyan, G. E., M. A. Spall, and A. F. Thompson (2016), A theory of the wind-driven beaufort gyre variability, *Journal of Physical Oceanography*, *46*(11), 3263 – 3278, doi:10.1175/JPO-D-16-0091.1. 5.2.1

Martinsen-Burrell, N., K. Julien, M. R. Petersen, and J. B. Weiss (2006), Merger and alignment in a reduced model for three-dimensional quasigeostrophic ellipsoidal vortices, *Physics of Fluids*, *18*(5), 057,101–057,101–14, doi:10.1063/1.2191887. 2.6

Mcphee, M., A. Proshutinsky, J. Morison, M. Steele, and M. Alkire (2009), Rapid change in freshwater content of the arctic ocean, *Geophysical Research Letters*, *36*, doi:10.1029/2009GL037525. 5.2.1

McWilliams, J. C. (1989), Statistical properties of decaying geostrophic turbulence, *Journal of Fluid Mechanics*, *198*, 199–230, doi:10.1017/S0022112089000108. 2.6

McWilliams, J. C. (2008), The Nature and Consequences of Oceanic Eddies, *Washington DC American Geophysical Union Geophysical Monograph Series*, *177*, 5–15, doi:10.1029/177GM03. 1, 2.2

Mechoso, C. R. (1980), Baroclinic instability of flows along sloping boundaries, *Journal of the Atmospheric Sciences*, *37*, 1393–1399. 2.5

Melander, M., N. Zabusky, and J. McWilliams (1987), Asymmetric vortex merger in two dimensions: Which vortex is "victorious"?, *Physics of Fluids - PHYS FLUIDS*, *30*, 2610–2612, doi:10.1063/1.866103. 2.6

Melander, M. V., N. J. Zabusky, and J. C. Mcwilliams (1988), Symmetric vortex merger in two dimensions: causes and conditions, *Journal of Fluid Mechanics*, *195*, 303–340, doi:10.1017/S0022112088002435. 2.6, 2.6

Meneghello, G., J. Marshall, C. Lique, P. E. Isachsen, E. Doddridge, J.-M. Campin, H. Regan, and C. Talandier (2021), Genesis and decay of mesoscale baroclinic eddies in the seasonally ice-covered interior arctic ocean, *Journal of Physical Oceanography*, *51*(1), 115 – 129, doi:10.1175/JPO-D-20-0054.1. 5.2.1, 5.2.2

Merryfield, W. J. (1998), Effects of stratification on quasi-geostrophic inviscid equilibria, *Journal of Fluid Mechanics*, *354*, 345–356, doi:10.1017/S0022112097007684. 2.7

Merryfield, W. J., and G. Holloway (1999), Eddy fluxes and topography in stratified quasi-geostrophic models, *Journal of Fluid Mechanics*, *380*, 59–80, doi:10.1017/S0022112098003656. 2.7

Merryfield, W. J., P. F. Cummins, and G. Holloway (2001), Equilibrium statistical mechanics of barotropic flow over finite topography, *J. Phys. Oceanogr.*, *31*, 1880–1890. 2.7

Meunier, P., and T. Leweke (2001), Three-dimensional instability during vortex merging, *Physics of Fluids*, *13*(10), 2747–2750, doi:10.1063/1.1399033. 2.6

Meunier, P., U. Ehrenstein, T. Leweke, and M. Rossi (2002), A merging criterion for two-dimensional co-rotating vortices, *Physics of Fluids*, *14*(8), 2757–2766, doi:10.1063/1.1489683. 2.6

MODE Group (1978), The mid-ocean dynamics experiment, *Deep Sea Research*, *25*(10), 859–910, doi:https://doi.org/10.1016/0146-6291(78)90632-X. 2.1, 2.1

Mysak, L. A., and F. Schott (1977), Evidence for baroclinic instability of the Norwegian Current, *Journal of Geophysical Research*, *82*(15), 2087–2095. 2.5

NASA (2020), Norwegian Sea, https://oceancolor.gsfc.nasa.gov/gallery/707/, online; Accessed 2021-05-03. 2.2

NASA/JPL/SwRI/MSSS/GeraldEichstädt/AlexisTranchandon/Solaris (2017), Citizens produce stunning images of jupiter from juno spacecraft, https://www.cbc.ca/news/multimedia/citizens-produce-stunning-images-of-jupiter-from-juno-spacecraft-1.4132653, online: accessed 2022-02-28. 5.4

Nof, D., and W. Dewar (1994), Alignment of lenses: laboratory and numerical experiments, *Deep Sea Research Part I: Oceanographic Research Papers*, *41*(8), 1207 – 1229, doi:https://doi.org/10.1016/0967-0637(94)90041-8. 2.6

Nøst, O. A., and P. E. Isachsen (2003), The large-scale time-mean ocean circulation in the Nordic Seas and Arctic Ocean estimated from simplified dynamics, *Journal of Marine Research*, *61*(2), 175–210. 1, 2.5

Nøst, O. A., J. Nilsson, and J. Nycander (2008), On the Asymmetry between Cyclonic and Anticyclonic Flow in Basins with Sloping Boundaries, *Journal of Physical Oceanography*, *38*(4), 771–787. 5.2.1

Nycander, J., and J. H. Lacasce (2004), Stable and unstable vortices attached to seamounts, *Journal of Fluid Mechanics*, *507*, 71–94, doi:10.1017/S0022112004008730. 2.7

Oceanic, N., and A. Administration (2021), Who first charted the gulf stream?s, https://oceanservice.noaa.gov/facts/bfranklin.html, online: accessed 2022-02-28. 2.1

Orlanski, I., and M. D. Cox (1973), Baroclinic instability in ocean currents, *Geophysical Fluid Dynamics*, *4*(4), 297–332, doi:10.1080/03091927208236102. 2.5

Orvik, K. A., and P. Niiler (2002), Major pathways of Atlantic water in the northern North Atlantic and Nordic Seas toward Arctic, *Geophysical Research Letters*, *29*(19), 2–1–2–4, doi:10.1029/2002GL015002. 1, 2.3

Ozugurlu, E., J. Reinaud, and D. Dritschel (2008), Interaction between two quasi-geostrophic vortices of unequal potential vorticity, *Journal of Fluid Mechanics*, *597*, 395 – 414, doi:10.1017/S0022112007000018. 2.6

Parisi, M., Y. Kaspi, E. Galanti, D. Durante, S. J. Bolton, S. M. Levin, D. R. Buccino, L. N. Fletcher, W. M. Folkner, T. Guillot, R. Helled, L. Iess, C. Li, K. Oudrhiri, and M. H. Wong (2021), The depth of jupiter’s great red spot constrained by juno gravity overflights, *Science*, *374*(6570), 964–968, doi:10.1126/science.abf1396. 5.2.2

Pedlosky, J. (1964), The stability of currents in the atmosphere and the ocean: Part i, *Journal of Atmospheric Sciences*, *21*(2), 201 – 219, doi:10.1175/1520-0469(1964)021<0201:TSOCIT>2.0.CO;2. 2.5, 3.3.4

Pedlosky, J. (1987), *Geophysical Fluid Dynamics*, second ed., Springer, Berlin, doi:https://doi.org/10.1007/978-1-4612-4650-3. 2.4

Penven, P., V. Echevin, J. Pasapera, F. Colas, and J. Tam (2005), Average circulation, seasonal cycle, and mesoscale dynamics of the Peru Current System: A modeling approach, *Journal of Geophysical Research C: Oceans*, *110*(10), 1–21. 3.2, 3.2

Perovich, D., W. Meier, M. Tschudi, S. Farrell, S. Hendricks, and S. Gerland (2019), The arctic sea ice cover in "state of the climate in 2018", *Bulletin of the American Meteorological Society*, *100*(9), 146–150. 5.2.1

Perrot, X., and X. Carton (2008), Vortex interaction in an unsteady large-scale shear/strain flow, in *Proceeding IUTAM Symposium on Hamiltonian dynamics, vortex structures turbulence*, edited by B. A.V., K. V.V., M. I.S., and S. M.A., pp. 373–383, Springer, iSBN 978-1-4020-6743-3. 2.6

Perrot, X., and X. Carton (2010), 2d vortex interaction in a non-uniform flow, *Theoretical and Computational Fluid Dynamics*, *24*(1), 1432–2250, doi:10.1007/s00162-009-0127-4. 2.6

Perrot, X., X. Carton, and A. Guillou (2010), Geostrophic vortex alignment in external shear or strain, in *IUTAM Symposium on Turbulence in the Atmosphere and Oceans*, edited by D. Dritschel, pp. 217–228, Springer Netherlands, Dordrecht. 2.6

Phillips, N. A. (1951), A simple three-dimensional model for the study of large-scale extratropical flow patterns, *Journal of Atmospheric Sciences*, *8*(6), 381 – 394, doi:10.1175/1520-0469(1951)008<0381:ASTDMF>2.0.CO;2. 3.3.4

Phillips, N. A. (1954), Energy transformations and meridional circulations associated with simple baroclinic waves in a two-level, quasi-geostrophic model1, *Tellus*, *6*(3), 273–286, doi:https://doi.org/10.1111/j.2153-3490.1954.tb01123.x. 1

Polvani, L. M. (1991), Two-layer geostrophic vortex dynamics. Part 2. Alignment and two-layer V-states, *Journal of Fluid Mechanics*, *225*, 241–270, doi:10.1017/S0022112091002045. 2.6

Prants, S. V., M. V. Budyansky, V. B. Lobanov, A. F. Sergeev, and M. Y. Uleysky (2020), Observation and lagrangian analysis of quasi-stationary kamchatka trench eddies, *Journal of Geophysical Research: Oceans*, *125*(6), e2020JC016,187, doi:https://doi.org/10.1029/2020JC016187. 2.7

Prater, M. D. (2002), Eddies in the Labrador Sea as observed by profiling RAFOS floats and remote sensing, *Journal of Physical Oceanography*, *32*(2), 411–427. 2.5

Prater, M. D., and T. B. Sanford (1994), A Meddy off Cape St. Vincent. Part I: Description, *Journal of Physical Oceanography*, *24*(7), 1572–1586. 2.6, 2.6

Raj, R., L. Chafik, J. Nilsen, T. Eldevik, and I. Halo (2015), The Lofoten Vortex of the Nordic Seas, *Deep Sea Research Part I: Oceanographic Research*, *96*, 1–14. 2.7

Reinaud, J. N., and X. Carton (2019), The alignment of two three-dimensional quasi-geostrophic vortices, *Geophysical & Astrophysical Fluid Dynamics*, *0*(0), 1–37, doi: 10.1080/03091929.2019.1653462. 2.6

Reinaud, J. N., and X. Carton (2020), The alignment of two three-dimensional quasi-geostrophic vortices, *Geophysical & Astrophysical Fluid Dynamics*, *114*(4-5), 524–560, doi:10.1080/03091929.2019.1653462. 2.6

Reinaud, J. N., and D. G. Dritschel (2002), The merger of vertically offset quasi-geostrophic vortices, *Journal of Fluid Mechanics*, *469*, 287–315, doi:10.1017/S0022112002001854. 2.6, 2.6

Rhines, P. B. (1979), Geostrophic turbulence, *Annual Review of Fluid Mechanics*, *11*(1), 401–441, doi:10.1146/annurev.fl.11.010179.002153. 3.4

Richardson, P., A. Bower, and W. Zenk (2000), A census of Meddies tracked by floats, *Progress in Oceanography - PROG OCEANOGR*, *45*, 209–250, doi:10.1016/S0079-6611(99)00053-1. 2.6

Robinson, I. S. (2010), *Discovering the Ocean from Space: The unique applications of satellite oceanography*, Springer Praxis Books, 1 ed., Springer-Verlag Berlin Heidelberg. 2.1, 2.2

Rodionov, V., J. Nihoul, and A. Kostianoy (2004), Physical Oceanography of Frontal Zones in the Subarctic Seas, *Gulf Professional Publishing*, p. 326. 2.3, 2.3, 2.5

Rogachev, K., N. Shlyk, and E. Carmack (2007), The shedding of mesoscale anticyclonic eddies from the Alaskan Stream and westward transport of warm water, *Deep Sea Research Part II: Topical Studies in Oceanography*, *54*(23), 2643 – 2656, doi: https://doi.org/10.1016/j.dsr2.2007.08.017. 2.6

Rossby, T., M. D. Prater, and H. Søiland (2009), Pathways of inflow and dispersion of warm waters in the Nordic seas, *Journal of Geophysical Research: Oceans*, *114*(C4). 2.5, 2.6

Salmon, R., G. Holloway, and M. C. Hendershott (1976), The equilibrium statistical mechanics of simple quasi-geostrophic models, *Journal of Fluid Mechanics*, *75*(4), 691–703, doi:10.1017/S0022112076000463. 2.7, 2.7, 3.4

Schultz Tokos, K. L., H.-H. Hinrichsen, and W. Zenk (1994), Merging and Migration of Two Meddies, *Journal of Physical Oceanography*, *24*(10), 2129–2141, doi:10.1175/1520-0485(1994)024<2129:MAMOTM>2.0.CO;2. 2.6

ScienceDaily (2013), Jupiter mystery solved: Why the giant planet's mysterious great red spot has not disappeared., www.sciencedaily.com/releases/2013/11/131114131929.htm, online: accessed 2022-02-28. 5.2.2

Scott, R. B., and B. K. Arbic (2007), Spectral energy fluxes in geostrophic turbulence: Implications for ocean energetics, *Journal of Physical Oceanography*, *37*(3), 673 – 688, doi:10.1175/JPO3027.1. 2.2

Scott, R. B., and F. Wang (2005), Direct evidence of an oceanic inverse kinetic energy cascade from satellite altimetry, *Journal of Physical Oceanography*, *35*(9), 1650 – 1666, doi:10.1175/JPO2771.1. 2.2, 5.2.4

Shchepetkin, A. F. (1995), Interaction of turbulent barotropic shallow-water flow with topography. 2.7

Shchepetkin, A. F., and J. C. McWilliams (2005), The regional oceanic modeling system (ROMS): a split-explicit, free-surface, topography-following-coordinate oceanic model, *Ocean Modelling*, *9*(4), 347 – 404. 3.1

Sherwin, T. J., M. O. Williams, W. R. Turrell, S. L. Hughes, and P. I. Miller (2006), A description and analysis of mesoscale variability in the F äroe-Shetland Channel, *Journal of Geophysical Research: Oceans*, *111*(3), 1–17. 2.5

Shi, X. B., and L. P. Røed (1999), Frontal instabilities in a two-layer, primitive equation ocean model, *Journal of Physical Oceanography*, *29*(5), 948 – 968, doi:10.1175/1520-0485(1999)029<0948:FIIATL>2.0.CO;2. 2.5

Shirah, G. (2020), Earth Day 2020: Gulf Stream ocean current pull out to Earth observing fleet, https://svs.gsfc.nasa.gov/4802, online; Accessed 2022-02-28. 2.1

Smith, K. S. (2007), The geography of linear baroclinic instability in Earth's oceans, *Journal of Marine Research*, *65*(5), 655–683. 2.4, 3.3, 3.3.2, 3.3.3

Smith, R. K. (2003), Potential vorticity, https://www.meteo.physik.uni-muenchen.de/~roger/Lectures/Adm_Lectures/PV.pdf, online: accessed 2022-01-20. 3.3, 3.3.3

Søiland, H., and T. Rossby (2013), On the structure of the Lofoten Basin Eddy, *Journal of Geophysical Research: Oceans*, *118*(9), 4201–4212, doi:10.1002/jgrc.20301. 2.6, 2.7

Søiland, H., L. Chafik, and T. Rossby (2016), On the long-term stability of the Lofoten Basin Eddy, *Journal of Geophysical Research: Oceans*, *121*(7), 4438–4449, doi:10.1002/2016JC011726. 2.7

Solodoch, A., A. L. Stewart, and J. McWilliams (2021), Formation of anticyclones above topographic depressions, *Journal of Physical Oceanography*, *51*, 207–228. 2.7

Solomon, A., C. Heuzé, B. Rabe, S. Bacon, L. Bertino, P. Heimbach, J. Inoue, D. Iovino, R. Mottram, X. Zhang, Y. Aksenov, R. McAdam, A. Nguyen, R. P. Raj, and H. Tang (2021), Freshwater in the arctic ocean 2010–2019, *Ocean Science*, *17*(4), 1081–1102, doi:10.5194/os-17-1081-2021. 5.2.1

Spall, M. A. (2011), On the role of eddies and surface forcing in the heat transport and overturning circulation in marginal seas, *Journal of Climate*, *24*(18), 4844–4858. 1

Spall, M. A. (2013), On the circulation of Atlantic Water in the Arctic Ocean, *Journal of Physical Oceanography*, *43*(11), 2352–2371. 5.2.1

Spall, M. A., R. S. Pickart, P. S. Fratantoni, and A. J. Plueddemann (2008), Western Arctic Shelfbreak Eddies: Formation and Transport, *Journal of Physical Oceanography*, *38*(8), 1644–1668. 5.2.1, 5.2.2

Stammer, D. (1997), Global characteristics of ocean variability estimated from regional topex/poseidon altimeter measurements, *Journal of Physical Oceanography*, *27*(8), 1743 – 1769, doi:10.1175/1520-0485(1997)027<1743:GCOOVE>2.0.CO;2. 2.2, 2.4

Straneo, C. G. R., and Fiammeta (2015), Observations of watermass transformation and eddies in the Lofoten Basin of the Nordic Seas, *Journal of Physical Oceanography*, *Ahead of p*. 2.7

Sutyrin, G., and I. Yushina (1989), Numerical Modelling of the Formation, Evolution, Interaction and Decay of Isolated Vortices, in *Mesoscale/Synoptic Coherent structures in Geophysical Turbulence*, *Elsevier Oceanography Series*, vol. 50, edited by J. Nihoul and B. Jamart, pp. 721 – 736, Elsevier, doi:https://doi.org/10.1016/S0422-9894(08)70217-4. 2.6

Sutyrin, G. G., J. C. McWilliams, and R. Saravanan (1998), Co-rotating stationary states and vertical alignment of geostrophic vortices with thin cores, *Journal of Fluid Mechanics*, *357*, 321–349, doi:10.1017/S0022112097008136. 2.6

Sánchez-Lavega, A., A. Anguiano-Arteaga, P. Iñurrigarro, E. Garcia-Melendo, J. Legarreta, R. Hueso, J. F. Sanz-Requena, S. Pérez-Hoyos, I. Mendikoa, M. Soria, J. F. Rojas, M. Andrés-Carcasona, A. Prat-Gasull, I. Ordoñez-Extebarria, J. H. Rogers, C. Foster, S. Mizumoto, A. Casely, C. J. Hansen, G. S. Orton, T. Momary, and G. Eichstädt (2021), Jupiter's great red spot: Strong interactions with incoming anticyclones in 2019, *Journal of Geophysical Research: Planets*, *126*(4), e2020JE006,686, doi:https://doi.org/10.1029/2020JE006686. 5.2.2

Teigen, S. H., F. Nilsen, and B. Gjevik (2010), Barotropic instability in the West Spitsbergen Current, *Journal of Geophysical Research: Oceans*, *115*(C07016). 2.5

Teigen, S. H., F. Nilsen, R. Skogseth, B. Gjevik, and A. Beszczynska-Möller (2011), Baroclinic instability in the west spitsbergen current, *Journal of Geophysical Research: Oceans*, *116*(C7), doi:https://doi.org/10.1029/2011JC006974. 2.5

Tesi, T., F. Muschitiello, G. Mollenhauer, S. Miserocchi, L. Langone, C. Ceccarelli, G. Panieri, J. Chiggiato, A. Nogarotto, J. Hefter, G. Ingrosso, F. Giglio, P. Giordano, and L. Capotondi (2021), Rapid atlantification along the fram strait at the beginning

of the 20th century, *Science Advances*, *7*(48), eabj2946, doi:10.1126/sciadv.abj2946. 5.2.1

Thomsen, S., C. Eden, and L. Czeschel (2014), Stability analysis of the Labrador Current, *Journal of Physical Oceanography*, *44*(2), 445–463. 2.5

Timmermans, M. L. (2008), Eddies in the Canada Basin, Arctic Ocean, Observed from Ice-Tethered Profilers, *Journal of Physical Oceanography*, *38*(1), 133–145, doi:10.1175/2007JPO3782.1. 5.2.2

Tulloch, R., J. Marshall, C. Hill, and K. S. Smith (2011), Scales, growth rates, and spectral fluxes of baroclinic instability in the ocean, *Journal of Physical Oceanography*, *41*(6), 1057 – 1076, doi:10.1175/2011JPO4404.1. 2.2, 2.4, 2.5, 3.3.4

Uchida, T., R. Abernathey, and S. Smith (2017), Seasonality of eddy kinetic energy in an eddy permitting global climate model, *Ocean Modelling*, *118*, doi:10.1016/j.ocemod.2017.08.006. 1

Umlauf, L., and H. Burchard (2003), A generic length-scale equation for geophysical turbulence models, *Journal of Marine Research*, *61*(2), 235–265. 3.1.1

Uppala, S. M., P. W. Kållberg, A. J. Simmons, U. Andrae, V. D. C. Bechtold, M. Fiorino, J. K. Gibson, J. Haseler, A. Hernandez, G. A. Kelly, X. Li, K. Onogi, S. Saarinen, N. Sokka, R. P. Allan, E. Andersson, K. Arpe, M. A. Balmaseda, A. C. M. Beljaars, L. V. D. Berg, J. Bidlot, N. Bormann, S. Caires, F. Chevallier, A. Dethof, M. Dragosavac, M. Fisher, M. Fuentes, S. Hagemann, E. Hólm, B. J. Hoskins, L. Isaksen, P. A. E. M. Janssen, R. Jenne, A. P. Mcnally, J.-F. Mahfouf, J.-J. Morcrette, N. A. Rayner, R. W. Saunders, P. Simon, A. Sterl, K. E. Trenberth, A. Untch, D. Vasiljevic, P. Viterbo, and J. Woollen (2005), The ERA-40 re-analysis, *Quarterly Journal of the Royal Meteorological Society*, *131*(612), 2961–3012. 3.1.1

Valcke, S., and J. Verron (1997), Interactions of Baroclinic Isolated Vortices: The Dominant Effect of Shielding, *Journal of Physical Oceanography*, *27*(4), 524–541, doi:10.1175/1520-0485(1997)027<0524:IOBIVT>2.0.CO;2. 5.2.1

Vallis, G. K. (2006), *Atmospheric and oceanic fluid dynamics: fundamentals and large-scale circulation*, 745 pp., Cambridge University Press. 2.1, 2.2, 2.2, 2.4, 3.3.1, 3.3.2

Velasco Fuentes, O. U., and F. A. Velázquez Muñoz (2003), Interaction of two equal vortices on a plane, *Physics of Fluids*, *15*(4), 1021–1032, doi:10.1063/1.1556293. 2.6

Venaille, A. (2012), Bottom-trapped currents as statistical equilibrium states above topographic anomalies, *Journal of Fluid Mechanics*, *699*, 500–510, doi:10.1017/jfm.2012.146. 2.16, 2.7

Vollmer, L., and K. Eden (2013), A global map of meso-scale eddy diffusivities based on linear stability analysis, *Ocean Modelling*, *72*, 198–209. 2.4

von Hardenberg, J., J. C. McWilliams, A. Provenzale, A. Shchepetkin, and J. B. Weiss (2000), Vortex merging in quasi-geostrophic flows, *Journal of Fluid Mechanics*, *412*, 331–353, doi:10.1017/S0022112000008442. 2.6

Waite, A., L. Stemmann, L. Guidi, P. Calil, A. Hogg, M. Feng, P. Thompson, M. Picheral, and G. Gorsky (2016), The wineglass effect shapes particle export to the deep ocean in mesoscale eddies, *Geophysical Research Letters*, *43*(18), 9791–9800, doi:10.1002/2015GL066463. 2.2

Walczowski, W. (2014), *Atlantic Water in the Nordic Seas*, Springer International Publishing, doi:10.1007/978-3-319-01279-7. 2.3

Wang, Q., N. V. Koldunov, S. Danilov, D. Sidorenko, C. Wekerle, P. Scholz, I. L. Bashmachnikov, and T. Jung (2020), Eddy kinetic energy in the arctic ocean from a global simulation with a 1-km arctic, *Geophysical Research Letters*, *47*(14), e2020GL088,550, doi:https://doi.org/10.1029/2020GL088550. 5.2.1

Warner, J. C., C. R. Sherwood, H. G. Arango, and R. P. Signell (2005), Performance of four turbulence closure models implemented using a generic length scale method, *Ocean Modelling*, *8*(1–2), 81 – 113. 3.1.1

Watanabe, E. (2011), Beaufort shelf break eddies and shelf-basin exchange of Pacific summer water in the western Arctic Ocean detected by satellite and modeling analyses, *Journal of Geophysical Research: Oceans*, *116*(8), doi:10.1029/2010JC006259. 5.2.2

Waugh, D. W. (1992), The efficiency of symmetric vortex merger, *Physics of Fluids A: Fluid Dynamics*, *4*(8), 1745–1758, doi:10.1063/1.858395. 2.6

Woodgate, R. A., K. Aagaard, R. D. Muench, J. Gunn, G. Björk, B. Rudels, A. Roach, and U. Schauer (2001), The arctic ocean boundary current along the eurasian slope and the adjacent lomonosov ridge: Water mass properties, transports and transformations from moored instruments, *Deep Sea Research Part I: Oceanographic Research Papers*, *48*(8), 1757–1792, doi:https://doi.org/10.1016/S0967-0637(00)00091-1. 5.2.1

Yang, S., H. Song, B. Coakley, K. Zhang, and W. Fan (2022), A mesoscale eddy with submesoscale spiral bands observed from seismic reflection sections in the northwind basin, arctic ocean, *Journal of Geophysical Research: Oceans*, *127*(3), e2021JC017,984, doi:https://doi.org/10.1029/2021JC017984. 5.2.3

Yasuda, I., and G. R. Flierl (1995), Two-dimensional asymmetric vortex merger: Contour dynamics experiment, *Journal of Oceanography*, *51*(2), 145–170, doi:10.1007/BF02236522. 2.6

Yu, L.-S., A. Bosse, I. Fer, K. A. Orvik, E. M. Bruvik, I. Hessevik, and K. Kvalsund (2017), The Lofoten Basin eddy: Three years of evolution as observed by Seagliders, *Journal of Geophysical Research: Oceans*, *122*(8), 6814–6834, doi:10.1002/2017JC012982. 2.6, 2.14, 2.7, 5.2.2

Yu, X., J. Callies, R. Barkan, K. Polzin, E. Frajka-Williams, C. Buckingham, and S. Griffies (2021), Kinetic energy transfers between mesoscale and submesoscale motions in the open ocean's upper layers, *Journal of Physical Oceanography*, *52*, doi:10.1175/JPO-D-21-0099.1. 5.2.4

Zhao, J., A. Bower, J. Yang, X. Lin, and C. Zhou (2018a), Structure and formation of anticyclonic eddies in the iceland basin, *Journal of Geophysical Research: Oceans*, *123*(8), 5341–5359, doi:https://doi.org/10.1029/2018JC013886. 2.7

Zhao, M., and M.-L. Timmermans (2015), Vertical scales and dynamics of eddies in the Arctic Ocean's Canada Basin, *Journal of Geophysical Research: Oceans*, *120*, n/a–n/a, doi:10.1002/2015JC011251. 2.6, 5.2.1

Zhao, M., M.-L. Timmermans, S. Cole, R. Krishfield, A. Proshutinsky, and J. Toole (2014), Characterizing the eddy field in the arctic ocean halocline, *Journal of Geophysical Research: Oceans*, *119*(12), 8800–8817, doi:10.1002/2014JC010488. 5.2.1, 5.2.2

Zhao, M., M.-L. Timmermans, R. Krishfield, and G. E. Manucharyan (2018b), Partitioning of kinetic energy in the arctic ocean's beaufort gyre, *J. Geophys. Res. Oceans*, *123*, 4806–4819. 5.2.2

Zou, J., and G. Holloway (1994), Entropy maximization tendency in topographic turbulence, *Journal of Fluid Mechanics*, *263*, 361–374, doi:10.1017/S0022112094004155. 2.7

Zou, Z., P. Bakhtiari Rad, L. Macelloni, and L. Zhang (2021), Temporal and spatial variations in three-dimensional seismic oceanography, *Ocean Science*, *17*(4), 1053–1066, doi:10.5194/os-2020-112. 5.2.3

# Part II

# Papers

# Paper I

## Topographic influence on baroclinic instability and the mesoscale eddy field in the northern North Atlantic Ocean and the Nordic Seas

**Trodahl, M.** and Isachsen, P. E.
Journal of Physical Oceanography, 2018

doi: 10.1175/JPO-D-17-0220.1

# Topographic Influence on Baroclinic Instability and the Mesoscale Eddy Field in the Northern North Atlantic Ocean and the Nordic Seas

MARTA TRODAHL

*University of Oslo, Oslo, Norway*

PÅL ERIK ISACHSEN

*University of Oslo, and Norwegian Meteorological Institute, Oslo, Norway*

(Manuscript received 24 October 2017, in final form 3 September 2018)

ABSTRACT

A weak planetary vorticity gradient and weak density stratification in the northern North Atlantic and Nordic seas lead to time-mean currents that are strongly guided by bottom topography. The topographic steering sets up distinct boundary currents with strong property fronts that are prone to both baroclinic and barotropic instability. These instability processes generate a macroturbulent eddy field that spreads buoyancy and other tracers out from the boundary currents and into the deep basins. In this paper we investigate the particular role played by baroclinic instability in generating the observed eddy field, comparing predictions from linear stability calculations with diagnostics from a nonlinear eddy-permitting ocean model hindcast. We also look into how the bottom topography impacts instability itself. The calculations suggest that baroclinic instability is a consistent source of the eddy field but that topographic potential vorticity gradients impact unstable growth significantly. We also observe systematic topographic effects on finite-amplitude eddy characteristics, including a general suppression of length scales over the continental slopes. Investigation of the vertical structure of unstable modes reveal that Eady theory, even when modified to account for a bottom slope, is unfit as a lowest-order model for the dynamics taking place in these ocean regions.

## 1. Introduction

The northwestern North Atlantic Ocean and Nordic seas are probably the places in the world where bottom topography has its biggest impact on the ambient potential vorticity (PV) gradients that govern large-scale ocean flows. The reason is a combination of a weak planetary vorticity gradient and a weak density stratification caused by persistent air–sea cooling. The planetary vorticity gradient in the Arctic Ocean is even weaker, but there the water column is more strongly stratified because of the large influx of river water and the distillation process caused by the seasonal cycle of sea ice freezing and melting. So it is in the northern North Atlantic and in the sub-Arctic that topographic effects are most dramatic.

The strong topographic steering in these regions can be seen in the top panel of Fig. 1. Shown are observed time-mean sea surface temperatures (SST) extracted from the Operational Sea Surface Temperature and Sea Ice Analysis (OSTIA) reanalysis (Donlon et al. 2012) as well as time-mean geostrophic surface currents estimated by differentiating the mean dynamic topography (MDT) distributed by AVISO. In the Nordic seas, observations like these have inspired lowest-order descriptions of the large-scale flow fields based on closed $f/H$ theory (Nøst and Isachsen 2003; Isachsen et al. 2003; Aaboe and Nøst 2008) where currents, at least at the bottom, are assumed to essentially follow $f/H$ contours ($f$ is the Coriolis parameter and $H$ is the bottom depth). Where such contours close on themselves, as they do in ocean basins where gradients in $H$ dominate over gradients in $f$, the theories predict circulation strengths from approximate balances between divergences in the top and bottom Ekman layers. Similar descriptions of large-scale balances in the Irminger and Labrador Seas of the northwestern North Atlantic are still missing, but Fig. 1 makes it evident that topography plays a lowest-order role there too. Currents also feel the bottom in the eastern North Atlantic but to a lesser degree because of a stronger vertical density stratification there.

*Corresponding author*: Marta Trodahl, marta.trodahl@geo.uio.no

DOI: 10.1175/JPO-D-17-0220.1

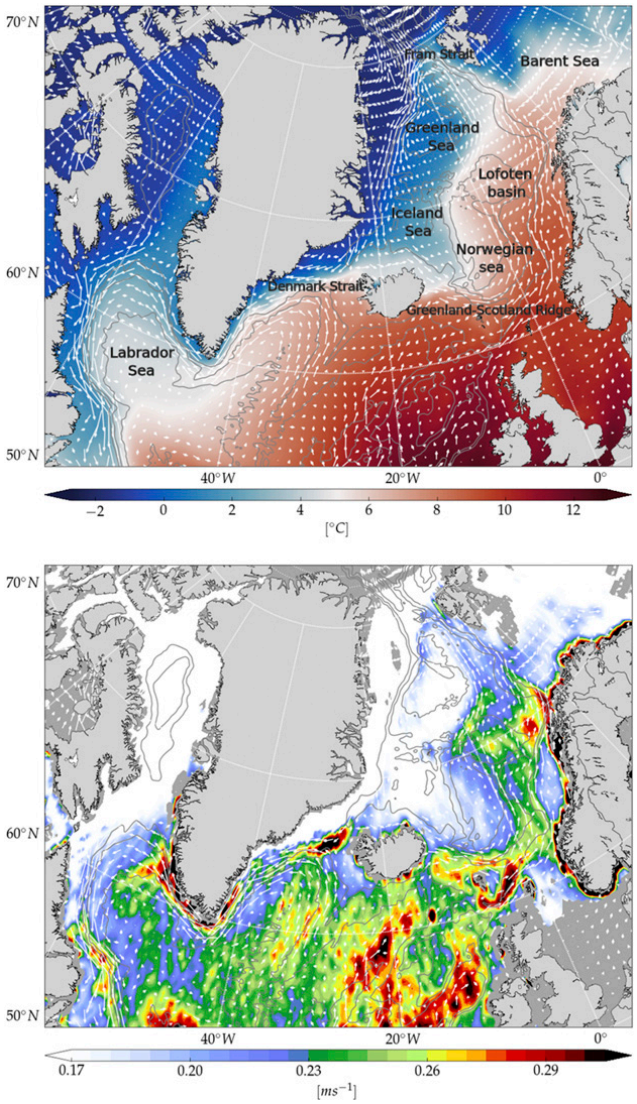


FIG. 1. (top) Time-mean sea surface temperatures (°C) from the OSTIA reanalysis and (bottom) square root of geostrophic EKE ($m\,s^{-1}$) obtained by differentiating along-track SSH anomalies provided by AVISO. Vectors show time-mean surface geostrophic currents (arbitrary scale), also provided by AVISO.

The strong topographic steering in the west and the north creates distinct property fronts, especially between poleward-flowing warm and salty Atlantic Water (AW) and southward-flowing cold and fresh Polar Water (PW). The sharpness of these fronts must somehow reflect a balance between alongfront advection by the time-mean currents and across-front stirring or ''mixing'' by mesoscale or submesoscale transients. And, unsurprisingly, most of the frontal zones are also associated with high flow variability, as illustrated by an estimate of surface eddy kinetic energy (EKE) given in the bottom panel of Fig. 1. So the large-scale currents clearly feel the topography, hence the sharp fronts. But to what extent is this also the case for the instability processes and mesoscale eddy field whose raison d'être is to wash out those same fronts?

Studies of the stability of large-scale currents and on mesoscale dynamics in the northwestern North Atlantic and Nordic seas have mostly focused on energetic hot spots like the Labrador Sea and the Lofoten Basin of the Nordic seas. Several studies have suggested that Labrador Sea eddies can be categorized into at least two groups: Irminger rings (IR) and boundary current eddies (BCEs) (Chanut et al. 2008; Gelderloos et al. 2011; Hátún et al. 2007). The IRs are long lived, primarily warm anticyclonic eddies formed in the region off Cape Desolation, whereas the smaller BCEs are fresh and form all along the boundary current. (Lilly et al. 2003; Gelderloos et al. 2011; de Jong et al. 2014; Hátún et al. 2007). The sources of these vortices have been studied both with primitive equation models of varying levels of realism (Eden and Böning 2002; Katsman et al. 2004; Chanut et al. 2008) and with idealized quasigeostrophic models (Bracco and Pedlosky 2003; Bracco et al. 2008). The more realistic model studies suggested that both baroclinic and barotropic, or even mixed instability, may be present whereas the idealized QG studies indicated that baroclinic instability alone was sufficient at explaining both the spatial distribution and scales of much of the observed eddy field. Topographic influence was predominant in all studies, and Bracco and Pedlosky (2003) and Bracco et al. (2008) found that baroclinic instability, in particular, is suppressed by the topographic PV gradient associated with the continental slope. But the same authors also found that the flow would get extremely unstable along a particularly steep part of the slope. This interesting result is in agreement with the observations in Fig. 1 that show enhanced mesoscale eddy activity off the steepest part of the southern Greenland slope.

In the Nordic seas, linear baroclinic instability of the Norwegian Atlantic Current (NwAC) as it skirts the Lofoten Basin off northern Norway was studied by Isachsen (2015). Quasigeostrophic (QG) vertical mode calculations carried out on the background state of a model with realistic bathymetry suggested that the flow there is also most unstable over the steepest part of the continental slope, in agreement with the findings from the Labrador Sea. This behavior is not obvious. In classical Eady theory (where the planetary vorticity gradient, relative vorticity, and variations in layer thickness are all neglected) instability forms by an interaction between top and bottom edge waves. Eady or two-layer Phillips theory can be modified to take a linear bottom slope into account (Blumsack and Gierasch 1972; Mechoso 1980; Isachsen 2011). The modified theory generally suggests *suppressed* growth

over an inclined bottom—relative to growth over a flat bottom. Stability is controlled by the slope parameter $\delta = \alpha/s$, where $\alpha$ is the bottom slope and $s$ is the isopycnal slope. In the boundary currents present in our study region, with buoyant surface currents flowing with the coast to their right, $\delta$ is negative. For such a setting, modified Eady theory predicts both lower growth rates and smaller scales compared to flat-bottom conditions. The following question then emerges: How does one reconcile this prediction with the indication in Fig. 1 that eddy activity is *enhanced* along the steeper parts of the continental slopes in both the Labrador Sea and Nordic seas?

Bracco and Pedlosky (2003) and Bracco et al. (2008) explained the faster growth along very steep continental slopes by considering the dynamics of a current stabilized by topography everywhere except for a small region that has infinite slope (i.e., a vertical wall). But Isachsen (2015) obtained the highest growth rates over the steepest part of the slope without resorting to such a limiting case. Inspection of the vertical structure of unstable waves instead revealed that Eady or two-layer Phillips instability is typically not at play. The bottom topography basically changes the near-bottom PV gradient to the extent that interaction between surface and bottom edge waves is prohibited. Instead, unstable growth in the QG model occurs by interactions between edge waves at either the top or bottom surfaces and interior ''Rossby'' or PV waves existing because of layer thickness gradients. Or, in some cases, instability is caused by interactions entirely between interior PV waves.

Regardless of the details, the isolated studies from both the Labrador Sea and the Lofoten Basin have suggested that bottom topography may have a lowest-order effect on baroclinic instability of the cyclonic boundary currents that characterize the large-scale flow in these ocean regions. The purpose of the present study is to extend the investigation of topographic effects on baroclinic instability to the entire northern North Atlantic and Nordic seas. We will repeat the QG modal analysis of Isachsen (2015) and look into the PV dynamics that impacts the most unstable waves in different regions. The questions we raise are, first, whether baroclinic instability may be the main source of the observed mesoscale eddy variability in the region; second, whether the Eady model gives a useful quantitative description of growth rates and length scales; and third, what more general QG dynamics can reveal about topographic control on unstable growth.

We will do the linear stability calculations using time-mean fields of an eddy-permitting regional ocean model rather than on gridded observed fields. The reason behind this choice is a strong sensitivity of growth to the alignment of background currents relative to topographic gradients. A proper alignment is hard to obtain from, say, gridded hydrography (for the thermal wind shear) combined with gridded altimeter fields (for surface reference-level velocities). Analyzing fields from an eddy-permitting model also allows for an assessment of the relevance of linear theory in explaining the geographic distribution of the fully developed mesoscale eddy field in the same model.

In the following we present the model dataset and give an overview of methods used for analysis. We then show the results, first by characterizing the strength and lateral scales of the eddy field in the nonlinear ocean model. Energy conversion rates that indicate where both baroclinic and barotropic instability take place are also presented. Then we present results from the linear stability calculations and compare growth rates and corresponding lateral scales to the eddy characteristics from the nonlinear field. A comparison with the standard Eady prediction is also made. Finally, the vertical structure of unstable waves and its relation to topographic effects and the background PV gradients are studied at a few key locations. The paper ends with a summary and discussion of our results.

## 2. Data and methods

### a. *Model simulations*

The ''data'' for our study comes from a 17-yr-long eddy-permitting ocean model simulation conducted with the Regional Ocean Modeling System (ROMS; Shchepetkin and McWilliams 2005; Haidvogel et al. 2008) coupled to a sea ice module. ROMS is a hydrostatic, primitive equation model formulated with a near-orthogonal staggered C-grid in the horizontal and a vertical s-coordinate system in which the layers are draped over the seabed terrain. The s-coordinate is a generalized sigma coordinate, amended to allow for a more flexible vertical distribution of the layers.

The model's lateral grid spacing is 4 km. This resolution is sufficient to support the presence of mesoscale eddies on the scale of the internal Rossby deformation radius throughout most of the domain except for over very shallow shelf regions. The vertical grid consists of 35 layers distributed to obtain a finer resolution near the surface. A fourth-order centered scheme is used for vertical advection and a third-order upwind scheme is used for horizontal tracer and momentum advection. No explicit horizontal eddy viscosity or diffusion is applied, but the upwind advection scheme includes some implicit biharmonic diffusion. The *k*–epsilon version of the general

length scale (GLS) scheme (Umlauf and Burchard 2003; Warner et al. 2005) is employed for small-scale vertical mixing. The open lateral boundaries are relaxed toward the Global Forecast Ocean Assimilation Model (FOAM; MacLachlan et al. 2015), and atmospheric forcing is attained from the ERA-Interim atmospheric reanalysis (Uppala et al. 2005).

For all the analysis below we use daily mean fields. Hence, tides and other motions excited by fast atmospheric forcing have been filtered out. Such filtering should be justified given the focus on ocean mesoscale processes that typically have time scales from a few days to several weeks or months. We analyze only the last 10 years of the model simulation (1999–2009) to ensure that the dynamics has spun up to be consistent with boundary conditions.

The model time-mean SST and surface flow field are shown in Fig. 2. The model contains finer structure than what is seen in the observations, reflecting a coarser effective resolution in the observational dataset. But the general structure of the two fields agree well, and the model captures all the major frontal zones. Some of the AW, which should have entered the Nordic seas via the Denmark Strait between Iceland and Greenland instead recirculates there and is then transported by the East Greenland Current (EGC) into the Labrador Sea. Recirculation also happens in reality but appears to be stronger in the model, resulting in a Labrador Sea that is slightly too warm. In the northeastern Nordic seas the shelf regions are also slightly too warm and the deep basins too cold. This might indicate that the model currents are too constrained by topography, an effect not uncommon in models with terrain-following vertical coordinate systems (Haney 1991).

The figure also shows the model time-mean surface EKE field averaged over the 10-yr diagnostics period. Here we have used the definition $\mathrm{EKE} = (\overline{u'^2} + \overline{v'^2})/2$, where $u$ and $v$ are surface velocity components, the overlines represent means over time scales from one day to three months, and the primes indicate anomalies from such means. For EKE too, the more refined structures in the model field reflect a higher resolution compared to the observations. Note that the altimeter data contain instrumental noise that produces artificially high EKE levels at high wavenumbers (Le Traon et al. 1990). This is likely responsible for a general higher EKE level in the observations compared to the model, as seen especially in relatively quiescent regions. But the main spatial patterns of variability are captured in the model, including the tongue extending from the steep region off Greenland's southwestern coast. Model EKE levels in the Lofoten Basin are lower than in observations whereas EKE over the main boundary current there is higher. This might again reflect an overly strong topographic steering in the model.

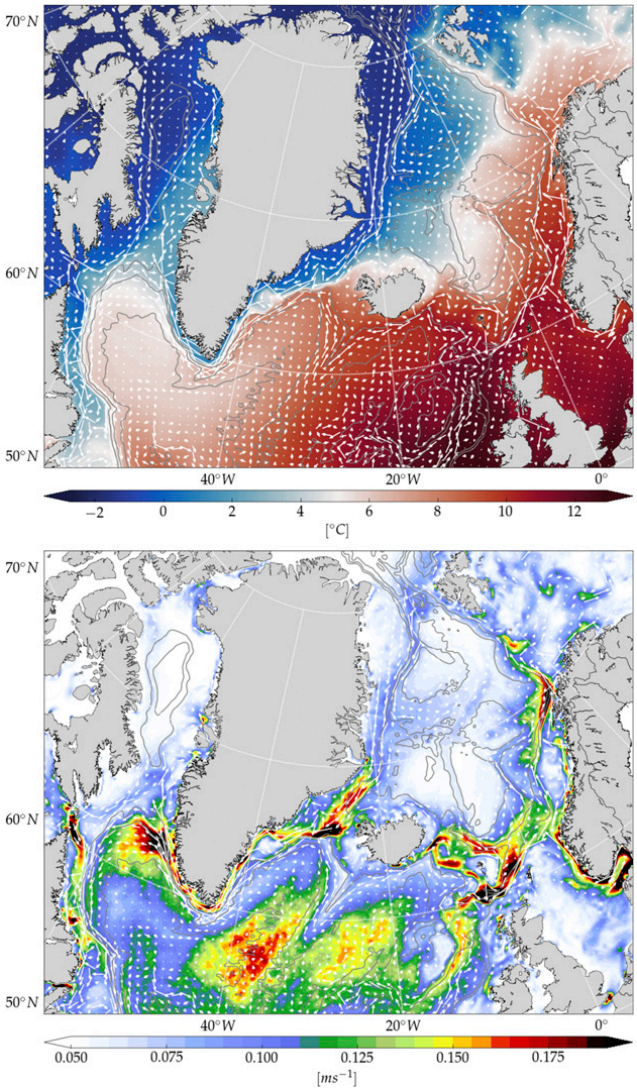


FIG. 2. (top) Model time-mean (1999–2009) SST (°C) and (bottom) square root of surface EKE (m s$^{-1}$).

### b. Eddy detection

Coherent mesoscale eddies were identified in the fully turbulent model run by the hybrid method of Penven et al. (2005). This involves locating closed contours of both SSH (streamlines for the surface geostrophic flow when the Rossby number is small) and the Okubo–Weiss (OW) parameter. The OW parameter is a measure of the relative strength of vorticity versus deformation, taking the following form:

$$\mathrm{OW} = S_n^2 + S_s^2 - \zeta^2,$$

where the normal strain $S_n = \partial_x u - \partial_y v$ and shear strain $S_s = \partial_x v + \partial_y u$ represent the total deformation while

relative vorticity $\zeta = \partial_x v - \partial_y u$ represents rotation. So, essentially, regions in the flow field having OW $\lesssim 0$ potentially indicate the core of coherent eddies (where rotation is expected to dominate over deformation). Although the OW parameter is originally designed to identify coherent structures in idealized 2D turbulent flows, it is also a commonly used tool for identifying vortices in real geophysical flows (Isern-Fontanet et al. 2003; Penven et al. 2005; Chelton et al. 2007).

For daily averaged model fields at 4-km horizontal resolution, we can expect both temporal and advective Rossby numbers (assuming flow speeds up to 0.5 m s$^{-1}$) to be well below one. So closed SSH contours are also good indicators of closed geostrophic streamlines. For each daily model field, local SSH extrema were thus identified and required to hold within a square of 24 neighboring grid points. This ensures a lower limit on the separation distance between two adjacent eddies, and overestimated eddy counts are more likely avoided as smaller variations in the SSH field are ignored. Within each such closed SSH region the OW parameter was then calculated from depth-averaged horizontal velocities. Where negative OW values were found, the edge of an eddy was defined by the OW = 0 contour.

For each detected eddy, a characteristic eddy kinetic energy and eddy effective radius were calculated from

$$\mathrm{EKE} = \frac{1}{A}\iint \frac{u'^2 + v'^2}{2}\, dA,$$

$$R = \sqrt{\frac{A}{\pi}},$$

where $A$ is the area of the eddy (the region within the OW = 0 contour). Finally, with the finite resolution of the model in mind, a minimum eddy effective radius was set to 8 km. Features smaller than this were rejected. Also, a maximum eddy radius was set to 200 km to prevent an entire ocean gyre to be identified as an eddy.

### c. *Linear stability calculations*

Linear baroclinic instability of the time-mean field in the model was studied using the algorithm proposed by Smith (2007). The basis for the analysis is the QG tendency equations for perturbation PV and buoyancy. The equations are linearized about a horizontally homogeneous mean state that consists of a background horizontal flow $\mathbf{U}(z) = U\hat{\mathbf{i}} + V\hat{\mathbf{j}}$ and vertical stratification $N^2(z) = -g/\rho_0 \partial_z \rho$ (where $g$ is the gravitational acceleration, $\rho$ is the background potential density field, and $\rho_0$ is a reference density). For small perturbations this gives

$$(\partial_t + \mathbf{U}\cdot\nabla)q + \mathbf{u}\cdot\nabla Q = 0, \quad -H < z < 0, \tag{1}$$

$$(\partial_t + \mathbf{U}\cdot\nabla)b + \mathbf{u}\cdot\nabla B = 0, \quad z = 0, \quad \text{and} \tag{2}$$

$$(\partial_t + \mathbf{U}\cdot\nabla)b + \mathbf{u}\cdot\nabla B + N^2\mathbf{u}\cdot\nabla h = 0, \quad z = -H, \tag{3}$$

where $Q$ and $B$ are the background potential vorticity and buoyancy, respectively; and $q$ and $b$ are the corresponding perturbations. The term $\mathbf{u}(z) = u\hat{\mathbf{i}} + v\hat{\mathbf{j}}$ is the perturbation horizontal velocity, and $h$ is the bottom topography variation, assumed to be small compared to total depth $H$. Note that $\nabla$ is the horizontal gradient operator.

In terms of the geostrophic streamfunction $\psi = p/(\rho_0 f)$ ($p$ is pressure and $f$ is the Coriolis parameter), the horizontal velocity is $\mathbf{u} = \hat{\mathbf{k}} \times \nabla\psi$, and the vertical component of relative vorticity is $\zeta = \nabla^2\psi$. Further we get that

$$Q = \nabla^2\Psi + \beta y + \Gamma\Psi,$$

$$q = \nabla^2\psi + \Gamma\psi,$$

$$B = f_0 \partial_z \Psi,$$

$$b = f_0 \partial_z \psi,$$

where upper- and lowercase letters denote mean and perturbation terms; $f_0$ and $\beta y$ are the constant and variable parts of the planetary vorticity, respectively; and $\Gamma = \partial_z[(f_0^2/N^2)\partial_z]$ is the so-called stretching operator that represents QG isopycnal layer thickness.

We assume a plane-wave solution, $\psi = \Re[\hat{\psi}(z)e^{i(kx+ly-\omega t)}]$, where $\hat{\psi}$ is the vertical structure of the perturbation, $\omega$ is the wave frequency, and $k$, $l$ are horizontal wavenumbers. Under the local approximation, in which we assume a horizontally slowly varying background field, we ignore the mean relative vorticity $\nabla^2\Psi$. Substitution into the evolution equations gives the following:

$$\omega(\Gamma - \kappa^2)\hat{\psi} = [\mathbf{K}\cdot(\hat{\mathbf{k}}\times\nabla Q) + \mathbf{K}\cdot\mathbf{U}(\Gamma - \kappa^2)]\hat{\psi}, \quad -H < z < 0, \tag{4}$$

$$(\mathbf{K}\cdot\mathbf{U} - \omega)\partial_z\hat{\psi} = \mathbf{K}\cdot\partial_z\mathbf{U}, \quad z = 0, \quad \text{and} \tag{5}$$

$$(\mathbf{K}\cdot\mathbf{U} - \omega)\partial_z\hat{\psi} = \mathbf{K}\cdot\Omega\hat{\psi}, \quad z = -H. \tag{6}$$

Here $\mathbf{K} = k\hat{\mathbf{i}} + l\hat{\mathbf{j}}$ is the horizontal wave vector, and $\kappa = \sqrt{k^2 + l^2}$ is its modulus. Finally, $\Omega = (\partial_z U - N^2/f_0\partial_y h)\hat{\mathbf{i}} + (\partial_z V + N^2/f_0\partial_x h)\hat{\mathbf{j}}$.

The analysis amounts to solving a generalized eigenvalue problem in discrete form is

$$\omega\mathbf{B}_{ij}\hat{\boldsymbol{\psi}}_j = \mathbf{A}_{ij}\hat{\boldsymbol{\psi}}_j. \tag{7}$$

Here **A** and **B** are tridiagonal, asymmetric $(35 \times 35)$ matrices containing the terms

$$\mathbf{B}_{ij} = \mathbf{\Gamma}_{ij} - K^2 \boldsymbol{\delta}_{ij}, \tag{8}$$

$$\mathbf{A}_{ij} = (k\mathbf{Q}_y^m - l\mathbf{Q}_x^m)\boldsymbol{\delta}_{ijm} + (k\mathbf{U}^m + l\mathbf{V}^m)\boldsymbol{\delta}_{inm}\mathbf{B}_{nj}, \tag{9}$$

where $i$, $j$ index the rows and columns. The $\delta$ symbols represent Kronecker tensors,

$$\boldsymbol{\delta} = \begin{cases} 0, & i \neq n \neq m \\ 1, & i = n = m \end{cases}, \tag{10}$$

with the value 1 on the diagonal elements, and otherwise zero. Hence the tensor products with $\boldsymbol{\delta}_{ijm}$, $\boldsymbol{\delta}_{inm}$, in $\mathbf{A}_{ij}$, leaves matrices with $(kQ_{y,i} - lQ_{x,i})$ and $(kU_i + lV_i)$ on the diagonals.

The eigenvalue problem is discretized on the staggered vertical model grid [see appendix B in Smith (2007)]. The discretized problem is solved at every horizontal model grid point for $200 \times 200$ wavenumbers. With Eady dynamics in mind, where the fastest-growing wave has a scale near the internal deformation radius, we calculated growth in the wavenumber range $0.1k_d < |k, l| < 10k_d$, where $k_d = 1/L_d$, and $L_d$ is the internal deformation radius, approximated by its WKB expression:

$$L_d = \frac{1}{f}\int_{-H}^{0} N\, dz. \tag{11}$$

Since the model has 35 vertical levels we get, at each location, 35 eigenvectors and their associated eigenvalues. The eigenvalues are complex ($\omega = \omega_r + i\omega_i$), and positive imaginary components give modes that grow exponentially in time.

In some cases, the waves selected by the above algorithm represent very small-scale surface or bottom intensified instabilities. Smith (2007) argues that such instabilities are likely of less significance in the extraction of available potential energy (APE) from the mean flow. Smith applied a filter in the selection process based on a measure of the waves' ability to extract mean-flow APE, in order to weed out the less important features. Here we instead followed the procedure of Vollmer and Eden (2013) and use a scale-selective horizontal diffusion operator, by adding $A_h\nabla^2 q$ to the right-hand side of Eq. (1) with $A_h = 10\,\mathrm{m^2\,s^{-1}}$, to filter out the smallest-scale perturbations. We are still not guaranteed the most energetically important perturbation by simply choosing the wave corresponding to the global maximum growth rate; however, we are now somewhat more liable to select a larger, possibly deeper, mode.

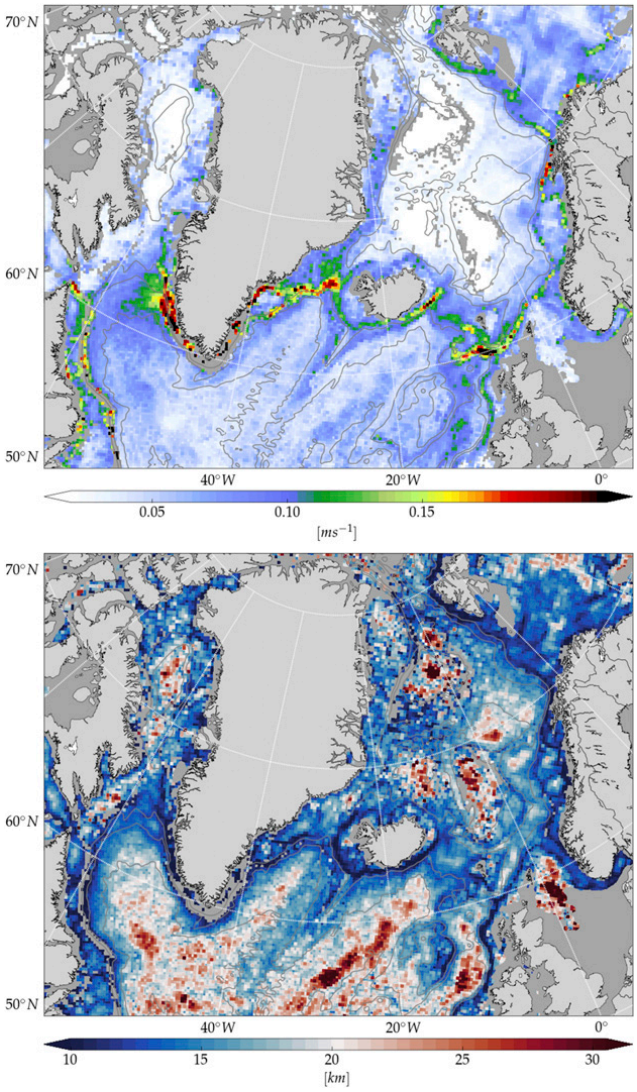


FIG. 3. Characteristics of detected coherent vortices: (top) square root of EKE ($\mathrm{m\,s^{-1}}$) and (bottom) effective radius (km). Gray regions indicate where no coherent eddies were detected or where the depth is shallower than 100 m.

## 3. Results

### a. Characteristics of the fully developed eddy field

Figures 1 and 2 show that the topographically guided boundary currents are also regions of high EKE, at least at the surface. But EKE estimates like these, made from a simple band passing of the velocity field, do not distinguish between macroturbulence created by instability and other types of variability reflecting, say, meandering of the currents or modulation of the current strengths. To start assessing whether the high EKE levels are indeed related to active instability processes, we will therefore look at actual eddies—coherent vortices—detected from the model field. The characteristic EKE and radius of the detected eddies are shown in Fig. 3.

The estimates have been averaged over the entire 10-yr run and over 20 km × 20 km boxes. A quantitative comparison with the Reynolds EKE in Fig. 2 would require a consideration of the eddy density (i.e., the frequency of vortex detections in each region). We do not pursue this but note that the overall vortex EKE pattern is in good general agreement with the Reynolds EKE. Some of the elevated Reynolds EKE levels over the deep basins of the northeastern North Atlantic do not have corresponding high vortex EKE. Presumably, variability there is instead reflecting variable wind forcing over this main storm-track corridor. But the comparison suggests that high EKE levels along all major frontal zones over continental slopes and underwater ridge systems reflects an abundance of coherent eddies and not just modulation of the strength and position of the currents.

There are regions in the model where absolutely no coherent eddies were found by the detection algorithm. In the Norwegian and Greenland basins as well as the Icelandic Plateau Reynolds EKE levels are extremely low (see also Figs. 1 and 2), so these are simply relatively quiescent regions. More conspicuous is an apparent lack of detected eddies along the southern tip of Greenland and along the continental slope of the southwestern Labrador Sea. The slope region off the southern tip of Greenland is otherwise characterized by high Reynolds EKE levels (see also Fig. 2), so this particular result is counter to expectations. But a probable explanation for the apparent lack of coherent vortices here is hinted at by our estimate of eddy effective radius shown in the bottom panel of Fig. 3. The estimate reveals that coherent eddies along the continental slope off southern Greenland are very small, near the vortex detection threshold, which we have set to 8 km.

The figure also shows a more interesting *general* tendency of reduced eddy length scales over nearly all the continental slopes. So the main frontal zones that contain the highest EKE levels are, at the same time, associated with smaller eddy scales. Suppressed length scales over topographic slopes may be associated with a halted inverse energy cascade caused by topographic Rossby wave radiation (Vallis and Maltrud 1994; LaCasce and Brink 2000). But, as mentioned in the introduction, suppressed scales over sloping bottoms is also consistent with the linearized baroclinic instability theory of Blumsack and Gierasch (1972).

The actual predictions of linearized theory in this region will be studied below. But before that we look briefly into the energetics of the fully developed macroturbulent field in the model. The conversion terms from mean flow energy to eddy available potential energy (EAPE) and to EKE are, respectively (Eden and Böning 2002),

$$T_2 = \int_{-H}^{0} -\rho_0 \overline{\mathbf{u}'b'} \cdot \frac{\nabla \overline{b}}{N^2}\, dz, \tag{12}$$

and

$$T_4 = \int_{-H}^{0} -\rho_0 \overline{\mathbf{u}'\mathbf{u}'} \cdot \nabla \overline{\mathbf{u}}\, dz. \tag{13}$$

In our diagnosis of these terms from model fields the overbars and primes represent the same time means and perturbations that we have earlier used to diagnose Reynolds EKE. Here $N^2$ is the horizontally local time-mean buoyancy frequency. Most other studies have used some form of globally averaged $N^2$ in their definition of APE and hence in estimating $T_2$ (e.g., Chen et al. 2014; Zhu et al. 2014; Eden and Böning 2002; Aiki et al. 2016; von Storch et al. 2012). But since there will always be an element of arbitrariness in the exact definition of APE, and since our discussion here will primarily be qualitative, we simply use the local value of $N^2$.

Our estimate of the "baroclinic production" term $T_2$ (related to baroclinic instability) shown in the top panel of Fig. 4, reveals positive values practically everywhere. In the energy framework of Lorenz (1955), this is consistent with the energy flow path of baroclinic instability. The production of EAPE primarily takes place along the major boundary currents and frontal zones, and this is much as expected. The agreement with model EKE (Figs. 2 and 3) is good but far from perfect. One reason for the discrepancy is that the connection between EAPE and EKE goes via a vertical Reynolds flux $\overline{w'b'}$. We do not show this term here, but it reveals the EAPE → EKE transfer, which is also enhanced over the boundary currents. More important is the fact that the equlilibrated EKE field reflects not only a balance between local production and dissipation but also the transport convergence of EKE by both the mean flow and the turbulent field itself. There are multiple indications of mean flow EKE advection that lead to enhanced EKE levels downstream of $T_2$ maxima (e.g., as seen both along the southwestern Greenland coast and north Norwegian coast). And enhanced EKE levels extending into the deep Labrador and Lofoten basins likely indicate that eddies act to spread EKE across the continental slopes. Finally, there are some instances of large positive $T_2$ values with little correspondence in elevated EKE values, most notably downstream of Denmark Strait. The elevated baroclinic production in that particular region actually takes place near the

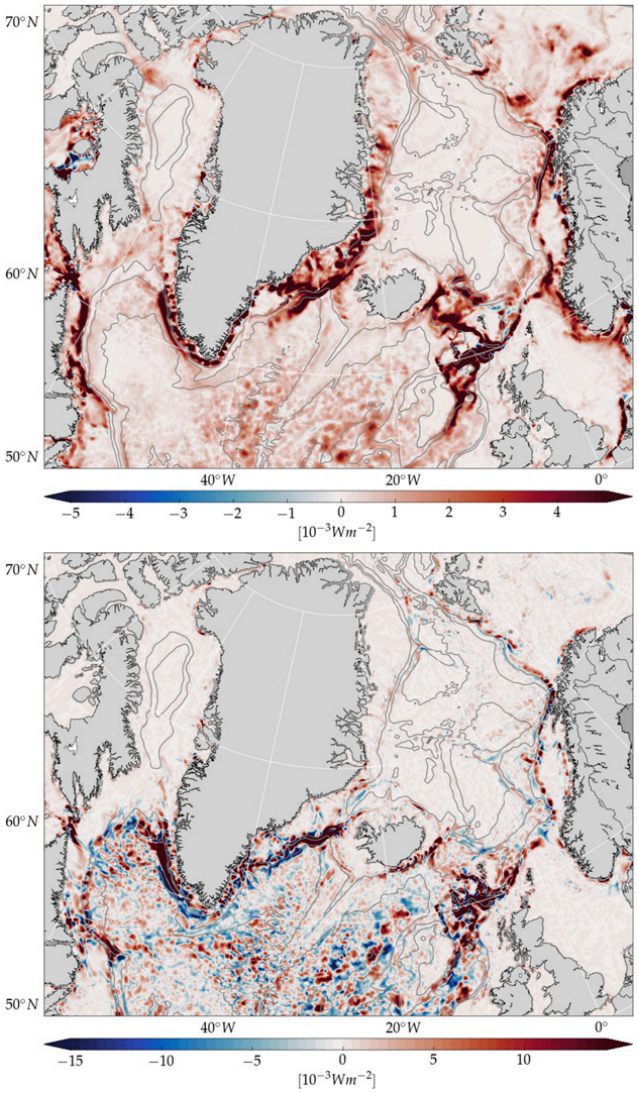


FIG. 4. (top) Depth-integrated MAPE-to-EAPE conversion $T_2$ and (bottom) MKE-to-EKE conversion $T_4$ ($10^{-3}\,\mathrm{W\,m^{-2}}$) from diagnosed model Reynolds fluxes.

bottom and involves dense waters that spill over the strait (Jungclaus et al. 2001; Mastropole et al. 2017). So whereas this process is not well captured by the surface EKE (Figs. 2 and 3), it does show up in bottom EKE densities (not shown).

The barotropic production term $T_4$, related to barotropic instability, is shown in the bottom panel of Fig. 4. This estimate is more noisy, displaying rapidly alternating regions of positive and negative values. But a first impression is that that barotropic instability ($T_4 > 0$) is also taking place along the boundary currents and may, in some places, dominate over baroclinic instability. This impression may partly be an artifact stemming from our choice of using a local rather than a globally averaged $N^2$ in the computation of $T_2$ (a globally averaged $N^2$, which also integrates over the weakly stratified interior basins, would be smaller than the local values over the highly stratified boundary currents). But a pronounced positive $T_4$ region off the southwest coast of Greenland is consistent with the claim by Eden and Böning (2002) that Irminger rings are formed by barotropic instability here. Positive $T_4$ along the Irminger rings formation site has also been reported by other studies (Zhu et al. 2014; Chen et al. 2014). So barotropic instability is likely also a ubiquitous process along the boundary currents in these regions, including the Nordic seas (Teigen et al. 2010; Ghaffari et al. 2018). But for the rest of this study we will examine the role of baroclinic instability and the effect the steep continental slopes have on this process.

### b. *The characteristics of linear baroclinic instability*

#### 1) OVERVIEW AND COMPARISON WITH EADY THEORY

The linear vertical mode problem was solved at each model grid point using time-mean currents and hydrography. Figure 5 shows the geographic distribution of the growth rate $\omega_i$ and corresponding wavelength $L_i = 2\pi/(k^2 + l^2)^{1/2}$ of the fastest-growing unstable modes. Overall, the boundary current regions and the frontal zone along the Greenland–Scotland ridge are the most unstable. Growth in the interior basins is slower, reflecting weaker baroclinic shears there. The agreement with the baroclinic production term $T_2$ diagnosed from the nonlinear model fields (Fig. 4) is surprisingly good given that this is an estimate based on the low-amplitude QG assumption.

The map of spatial scales of the fastest-growing waves is more noisy than that of growth rates, but some distinct patterns stand out. The stratified branches of the North Atlantic Current (NAC) in the northeastern Atlantic, as well as parts of the NwAC in the eastern Nordic seas and the EGC in the west, depict the largest length scales, reflecting highly stratified waters and large deformation radii there. Scales are smaller in the shallow North Sea and Barents Sea as well as in several of the deep but convective basins, likely reflecting smaller internal deformation radii there. The correspondence with the size of detected vortices (Fig. 3) is not nearly as clear as that between growth rates and baroclinic production $T_2$. But we note that the linear calculation does pick up the suppression of length scales along most continental slope regions, which is also seen in the fully developed turbulent field. We take this agreement as evidence that topographic slopes impact the mesoscale dynamics to the lowest order in these ocean regions—both for linear growth of baroclinic instability and for finite-amplitude eddies.

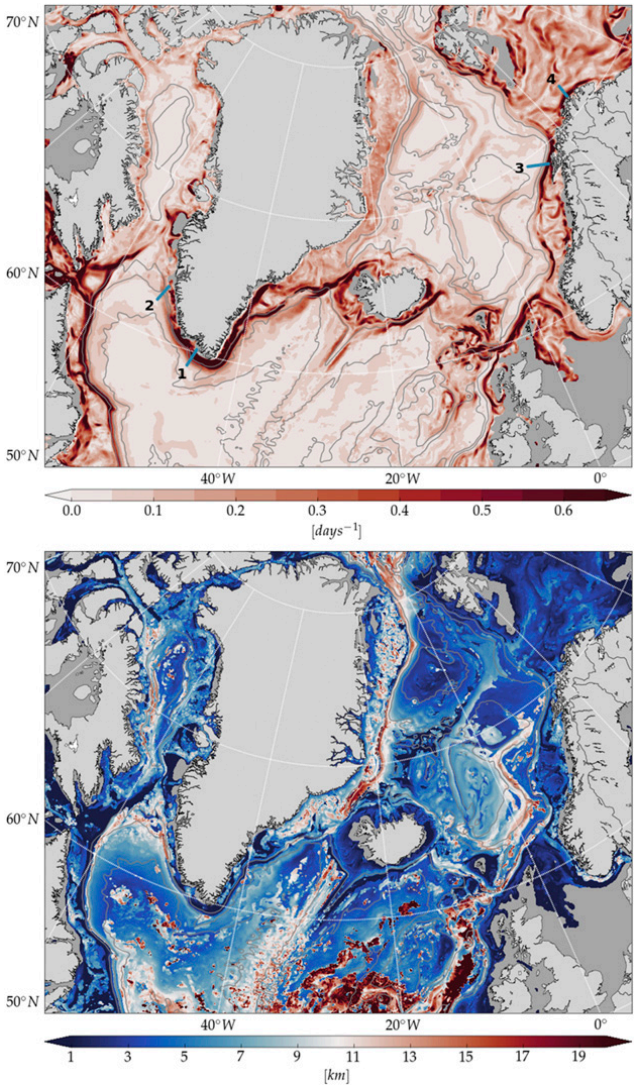


FIG. 5. (top) Growth rates (days$^{-1}$) and (bottom) wavelength (km) of the fastest-growing mode at each grid point. Areas shallower than 100 m have been masked out (in gray). In (a), we have also shown four transects discussed later in the text.

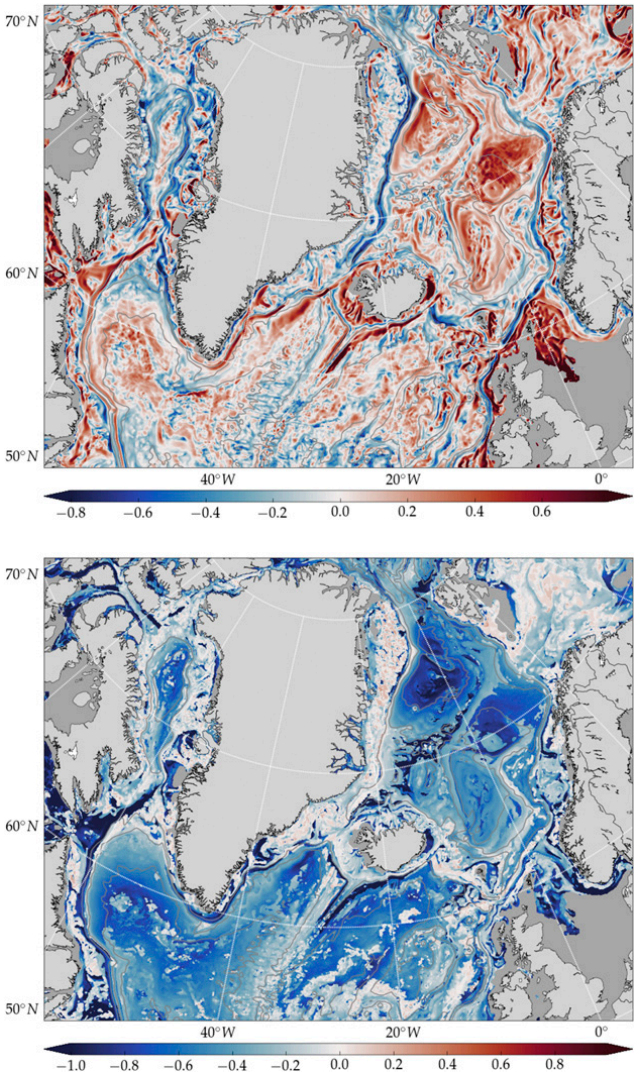


FIG. 6. (top) Growth rates and (bottom) wavelengths normalized by the corresponding values from Eady theory. Logarithmic color scales have been used, and areas shallower than 100 m have been masked out (in gray).

In summary, the linear growth calculations suggest the most intense mesoscale development to occur over the topographic slopes—in agreement with our diagnosis of the EAPE production term $T_2$. That the slope regions are the most unstable seems intuitive since density fronts are the sharpest there. But as also outlined above, Eady theory modified to include topography (Blumsack and Gierasch 1972; Mechoso 1980) predicts that unstable growth over the continental slope should be *reduced* relative to the corresponding values for flat-bottom conditions. To look for indication of such topographic suppression, growth rates and length scales normalized by the corresponding predictions from flat-bottom Eady theory have therefore been plotted in Fig. 6. We see that many slope regions are indeed characterized by lower normalized growth rates and shorter normalized length scales. The calculation, however, also shows regions with growth rates up to an order of magnitude higher than that of flat-bottom Eady dynamics, a result that is not predicted by the modified theory of Blumsack and Gierasch (1972). So modified Eady theory seems to account, qualitatively, for the observed growth at some locations but not all. Eady theory, whether it accounts for a bottom slope or not, is of course extremely limited in scope since it neglects the effects of internal PV gradients. The use of the full vertical QG modal equations, as done here, allows us a better chance of seeing how topography affects instability. The key to such understanding is the vertical structure of the PV gradient and specifically,

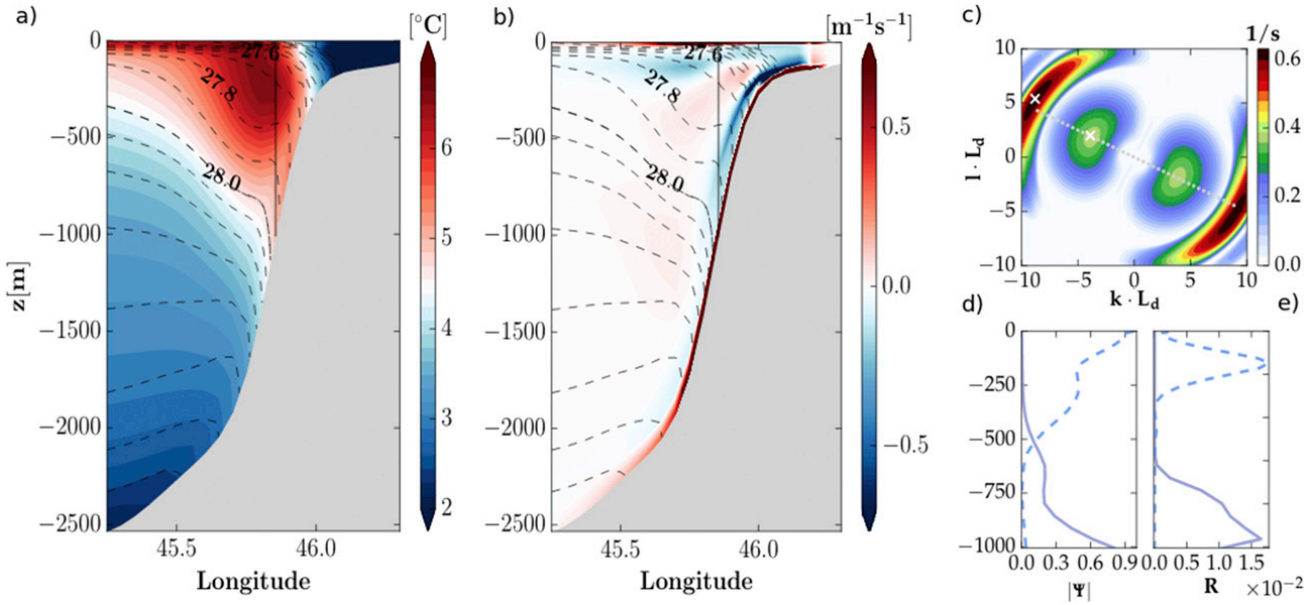


FIG. 7. Stability properties at a location off the southwestern coast of Greenland (location 1 in Fig. 5). Vertical sections of (a) time-mean temperature (°C) and (b) time-mean lateral PV gradient ($m^{-1}\,s^{-1}$), (c) growth rates ($days^{-1}$) as a function of nondimensional wavenumbers, and vertical profiles of (d) perturbation streamfunction amplitude ($m^2\,s^{-1}$) and (e) baroclinic energy conversion rate $R_{MAPE\to EAPE}$ ($10^{-3}\,W\,m^{-3}$) of the two most unstable waves (solid and dashed lines for the first and second modes, respectively).

as discussed below, the location of zero crossings in such gradients.

### 2) THE VERTICAL STRUCTURE OF UNSTABLE MODES

In this section we look in more detail at the vertical structure of background internal PV gradients and perturbation pressure of the fastest-growing waves at four locations (indicated by numbers in Fig. 5). The hope is to gain some understanding of the nature of instability and thereby check the extent to which Eady dynamics—with or without a bottom slope—offers a useful description of unstable growth.

We start by exploring a profile situated off the southern coast of Greenland, at 59.49°N, 45.59°W. Figure 7a shows a time-mean temperature transect through the site (line 1 in Fig. 5), taken perpendicular to the continental slope. The West Greenland Current (WGC), an extension of the EGC that resides on the shelf, carries cold and fresh surface water originating from the Arctic Ocean and from Greenland runoff. The Irminger Current (IC) is located farther offshore and carries recirculated warm, saline Atlantic water (Katsman et al. 2004). The juxtaposition of these water masses sets up a strong cross-shore density gradient resulting in inclined isopycnals with associated near-surface currents in thermal wind balance. Clearly, the tilted isopycnals reflect a large reservoir of APE that can be extracted by instability.

Isopycnal slopes at this location also steepen drastically near the bottom. This is likely the result of downslope bottom Ekman transport from the nortwestward-flowing currents. The flow in the EGC and WGC extends to all the way to the bottom, exporting dense deep waters produced north of the Greenland–Scotland Ridge. So the bottom flow is nonzero, and buoyant water from the shelf is likely advected down the slope in Ekman layers, raising APE. The process would ultimately be halted by convective overturning if isopycnals become vertical, but it can also be halted at an earlier stage by baroclinic instability. In fact, Brink (2016) suggests that such a balance between near-bottom Ekman transport and bolus transport by baroclinic instability may be an important source of small-scale eddies over continental shelves in general.

Figure 7b shows lateral PV gradient $\nabla(\beta y + \Gamma\Psi)$ along the transect. The gradient is taken in a rotated right-handed coordinate system with the $x$ axis aligned along the wave vector of the unstable wave, which for these cases translates to the horizontal direction of the thermal wind shear vector. Clearly, the PV gradient is not zero in the interior water column, as assumed by Eady theory. Over large parts of the slope the gradient changes sign twice in the vertical, suggesting that at least two distinct unstable modes may be present. Indeed, a plot of growth rates estimated halfway up the slope as a function of wavenumber (Fig. 7c) reveals at least two modes, both aligned with the top-to-bottom thermal wind shear. The fastest-growing mode has a horizontal length scale of approximately $L_d/8$ (cf. $L_d/1.6$ for flat-bottom Eady), and the vertical structure of the perturbation

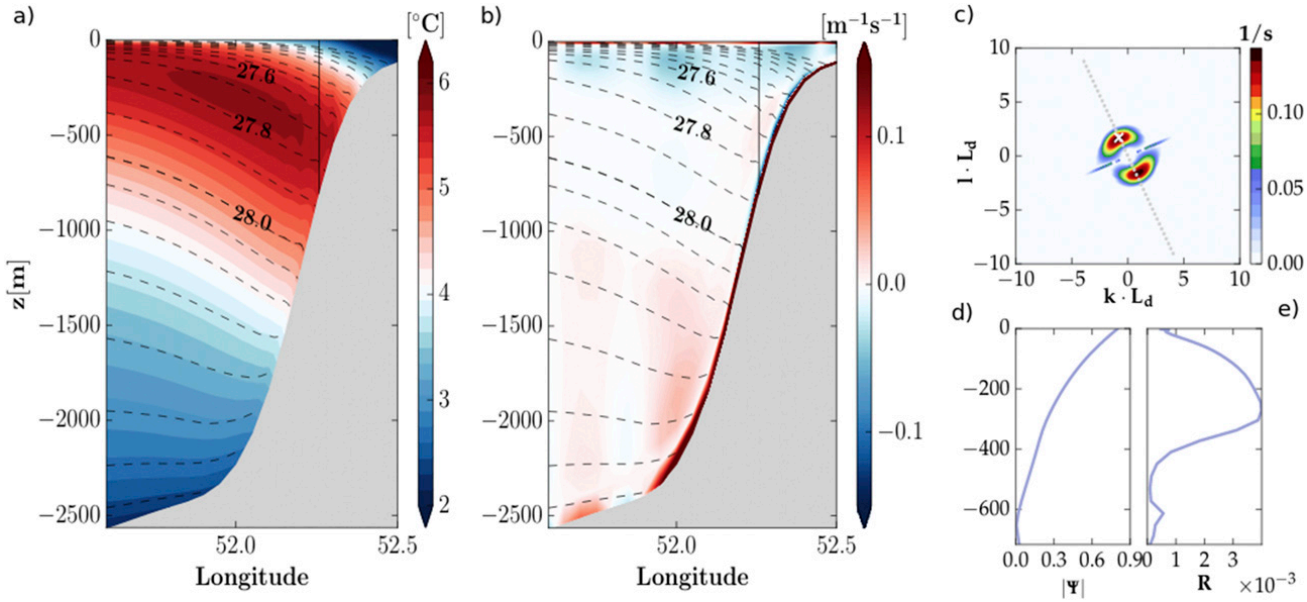


FIG. 8. As in Fig. 7, but for location 2 farther northwest along the south Greenland continental slope.

streamfunction (Fig. 7d) reveals that this mode is bottom intensified. The mode is associated with the lower of the two PV-gradient zero crossings and stems from an interaction between PV anomalies near the bottom and in the interior.

The EAPE production per unit volume (i.e., $T_2$ per unit depth) is

$$R_{\mathrm{MAPE}\to\mathrm{EAPE}} = -\rho_0 \overline{\mathbf{u}b} \cdot \frac{\nabla B}{N^2}, \tag{14}$$

where the overline here is the time mean, which has also been used to define the background field. In the QG formalism this becomes (Gill et al. 1974; Smith 2007)

$$R_{\mathrm{MAPE}\to\mathrm{EAPE}} = -\rho_0 \frac{f^2}{N^2} \overline{\nabla\psi \frac{\partial\psi}{\partial z}} \cdot \frac{\partial \mathbf{U}}{\partial z}. \tag{15}$$

Absolute extraction rates from any given mode depend on the unknown magnitude of the perturbation streamfunction (i.e., on the equilibrated EKE level). But the expression can tell us where in the water column MAPE is extracted. The result (Fig. 7e) shows maximum energy extraction near the bottom. The mode, apparently, works to flatten the very steep isopycnals near the bottom set up by the downslope bottom Ekman transport.

The second growing mode displays completely different vertical characteristics. It is surface intensified but with larger scales both in the vertical and horizontal (approximately $L_d/3$). The maximum energy conversion rate of this mode is found approximately where the background PV gradient changes sign at around 200 m and apparently works to flatten the density front separating WGC and IC waters.

The same two archetypal modes are commonly found along the entire southern coast of Greenland, where very fresh and buoyant water resides on the shelf slope. But farther west, where the continental slope widens and the isobaths start to turn southward, the hydrography, background PV gradient, and growth characteristics become different. An example from 62.94°N, 52.25°W is shown in Fig. 8 (line 2 in Fig. 5). Both waters associated with the WGC and IC are present here too, but lateral density gradients are weaker and, importantly, the steepening of isopycnals near the bottom is absent. The bottom flow is very weak here, and the result is a very weak downslope Ekman transport. As a consequence there is only one PV gradient reversal in the water column and only one unstable mode. This mode is surface intensified but deep, decaying very gradually to a value of zero at the bottom. Since the mode is deep, horizontal scales are larger than farther east, around $L_d/2$.

Although the unstable mode is deep, there is clear indication that Eady dynamics is not at play. The Eady model involves interacting edge waves and the perturbation streamfunction therefore attains its highest magnitude at the top and bottom boundary. But here, as for the surface mode at the location farther south, the unstable mode attains zero amplitude at the bottom. So a lower boundary edge wave is not at play. Instability might rather occur through an interaction between a surface edge wave and an internal PV wave or, alternatively, an interaction between two internal PV waves.

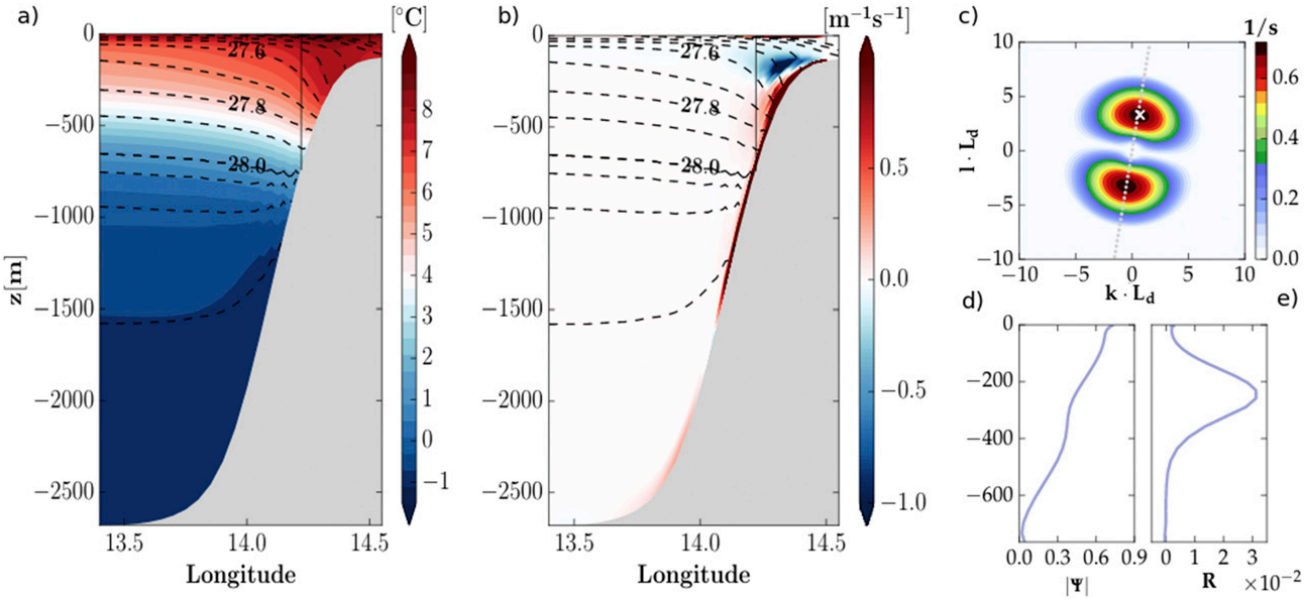


FIG. 9. As in Fig. 7, but for location 3 off the north Norwegian coast.

This situation (i.e., a growing mode that is deep but surface intensified, attaining zero amplitude at the bottom), is rather common along the continental slopes in our study region. Figure 9 shows another example from off the north Norwegian coast east of the Lofoten Basin (line 3 in Fig. 5). Here too the mode appears to involve interactions between a surface edge wave and an internal PV wave that act to flatten isopycnals over large parts of the water column while shutting off at the very bottom. It is worth noting that by attaining zero amplitude at depth the mode is essentially unaffected by the topographic PV gradient.

So over most of the continental slope, Eady theory seems not to apply. Bottom edge waves are for the most part not participating in the unstable interactions and internal Rossby waves, feeding on internal PV gradients, are instead needed. Evidence of pure Eady growth can only be found in a few places, notably where bottom slopes are weak. We include an example from a location in the Barents Sea at 72.47°N, 23.44°E (line 4 in Fig. 5). Figure 10 displays

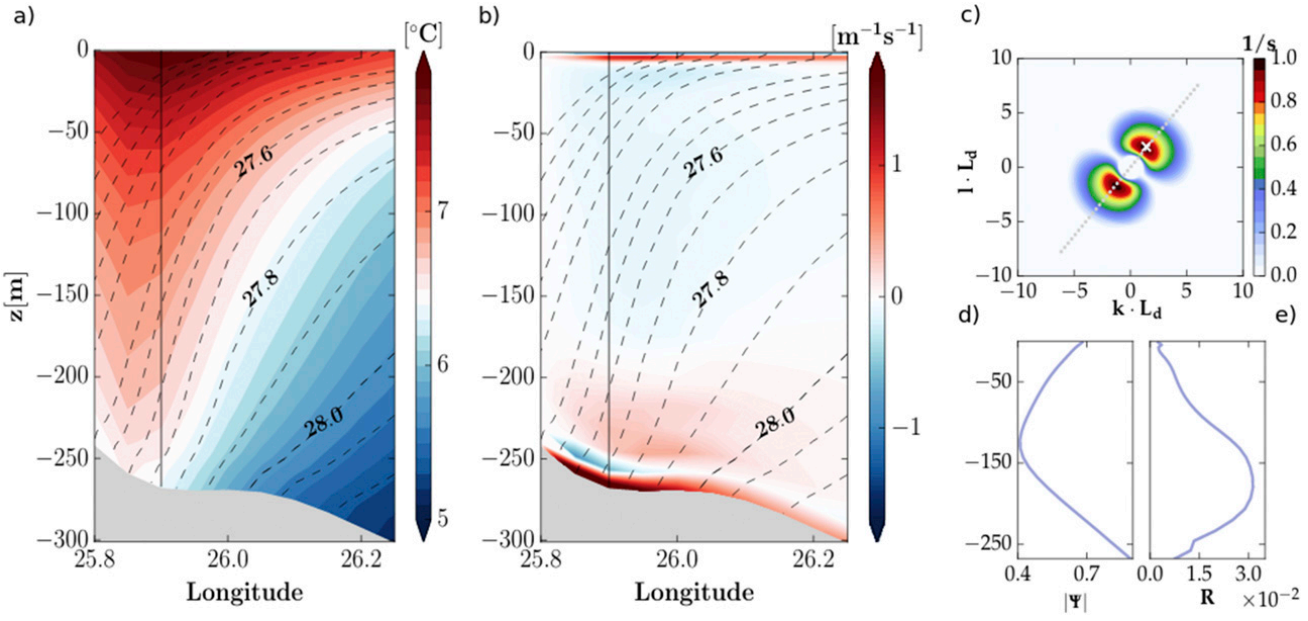


FIG. 10. As in Fig. 7, but for location 4 in the Barents Sea.

the hydrography and stability characteristics there. The largest growth rates occur at a scale of approximately $L_d/2.5$, and the wave is aligned with the thermal wind shear. Moreover, the perturbation pressure amplitude is minimum at middepths and increasing toward both boundaries, consistent with Eady dynamics. The perturbation pressure is also slightly larger at the bottom boundary than at the top, consistent with modified Eady theory with a negative slope parameter $\delta$ (see Fig. 6 of Isachsen 2015).

## 4. Summary and conclusions

The stability of currents in the northwestern North Atlantic and Nordic seas has been studied in isolated spots in the past. But here we looked at the overall geography of baroclinic instability and its relationship to the macroturbulent flow field in this region for the first time. Unsurprisingly, the calculations indicate that the currents are baroclinically unstable all along the continental slopes and also along underwater ridge systems. In a few locations, notably off the south Greenland coast, the fastest-growing waves are bottom intensified, acting to flatten steep isopycnals near the bottom. But for the most part instability works to release available potential energy associated with buoyant boundary currents residing at the surface.

We have seen that the steepest parts of the continental slopes generally have both the highest EKE levels and the fastest conversion of MAPE to EAPE. We also found that currents over the steep slopes are, for the most part, also the most baroclinically unstable—according to the linear QG vertical mode calculations conducted here. Of course the QG linear stability analysis has many limitations, the most severe of which are probably the small-slope assumption and the assumption of homogeneous conditions over the scale of the unstable waves. The validity of both assumptions become more questionable as the horizontal resolution of the analysis is increased. For example, the hydrographic and flow structure across the continental slopes in this region changes over a few tens of kilometers whereas the unstable waves we find have scales of a few kilometers. So the slowly changing background field assumption is not fulfilled in a strict sense. Furthermore, it is clear that the smallest scales predicted by the linear theory will not be resolved by the 4-km ROMS model or detected by our vortex detection algorithm with its detection threshold of 8 km. Finally, at scales of a few kilometers quasi geostrophy itself becomes questionable. A Rossby number cannot be estimated from the linear model results since these do not give a velocity scale. But if we assume that linear growth eventually leads to fully developed eddies of strength 10 cm $s^{-1}$ and scale 2 km, an effective Rossby number would be around 0.5. So one should be skeptical of the quantitative predictions of the linear growth estimates, particularly with respect to the smallest scales. Nevertheless, the impressive qualitative match between the obtained maps of baroclinic production $T_2$ and linear growth rate (Figs. 4 and 5) leads us to believe that there is ample qualitative information in these vertical mode QG calculations.

That unstable growth should be highest over the steepest continental slopes, as observed in most places here, is seemingly in contradiction with the modified Eady theory of Blumsack and Gierasch (1972) and Mechoso (1980). The theory predicts lower growth rates for nonflat topography—for the same thermal wind shear. Spall (2010) offers the explanation that in freely evolving flows the isopycnal slope of a boundary current adjusts continuously to the underlying bottom topography so that the slope parameter $\delta$ remains constant. So nondimensional growth rates will be constant regardless of the shape of the bottom underneath and steep slope regions will have higher *absolute* growth rates caused by a stronger thermal wind shear. This is essentially the ''baroclinic adjustment'' argument of Stone (1978) that macroturbulent transport is so effective that it keeps the criticality of the flow with respect to large-scale PV gradients (here being set by bottom topography) constant.

An alternative explanation has been proposed in relation to what takes place along the southwestern continental slope of Greenland. Here Bracco and Pedlosky (2003) and Bracco et al. (2008) suggested that a very steep slope basically acts as a vertical wall such that part of the mean flow really feels a flat bottom underneath. This notion was qualitatively supported in laboratory tank experiments by Wolfe and Cenedese (2006). They found the most important parameter in determining instability to be the width of the current relative to the width of the bottom slope region. Where the baroclinic current was narrower than the slope region underneath the flow was stabilized. But when the same current was made to flow over a very narrow slope—so that part of the current felt a flat bottom—it immediately became unstable.

Here we have pointed to an additional factor that may be at play. What we have seen is a general tendency for suppressed length scales over the continental slopes, a suppression that is related to a shortening of the vertical scale of instabilities. Around the southern tip of Greenland we have found bottom-trapped instabilities, but more generally we see instabilities that have zero amplitude at the bottom over steep slopes. This is clearly inconsistent with Eady dynamics, which relies on

interacting top and bottom edge waves. As discussed by Isachsen (2015), the flow field instead appears to organize itself so as to shelter the instability from the topographic PV gradients, which generally inhibits unstable growth. It is worth mentioning that de La Lama et al. (2016), in studying current meter records from all over the World Oceans, frequently found leading vertical empirical modes (EOFs) that have zero amplitude at the bottom. Motivated by this observational result LaCasce (2017) has argued that topographic slopes in the real oceans are nearly everywhere large enough to prevent the textbook flat-bottom baroclinic modes from existing. He instead advocates that steep-slope or ''rough bottom'' baroclinic modes are the orthogonal modes that should be used to characterize free waves. Our study here suggests that this result extends qualitatively over to baroclinically unstable waves as well, at least in the northern North Atlantic.

So at least three explanations have been proposed for why the boundary currents in the northern North Atlantic are generally more unstable over the steepest continental slopes. Untangling these explanations will require further effort, likely involving idealized modeling of freely evolving flows over a range topographic variations and forcing strengths (e.g., to examine the baroclinic adjustment hypothesis). An acceptable lowest-order theory must also be able to account for the few regions where unstable growth is *not* enhanced over the continental slope (e.g., as seen along northeastern Greenland in Fig. 5). Here we wish to emphasize that the surface-intensified (and in some cases bottom intensified) structure of unstable waves strongly suggest that instability be formed by interaction between surface edge waves and internal PV waves or entirely between internal PV waves, rather than between top and bottom edge waves. So the Eady model and two-layer Phillips models are clearly insufficient lowest-order descriptions whether they take a bottom slope into account or not. We believe that a three-layer model—with its ability to include an internal PV gradient reversal—is the minimal description required to get these processes right. This is not only important for our conceptual understanding but has implications for how eddy transport should be parameterization in coarse-grained climate models. The added complexity of one additional layer to the classical two-layer description seems daunting. But we believe it will be necessary if one wishes to obtain an adequate representation of topographic effects on mesoscale ocean dynamics and transport in these high-latitude regions.

*Acknowledgments.* The work was partially funded by Grant 221780 from the Research Council of Norway. The dynamic ocean topography fields used were produced by CLS Space Oceanography Division and distributed by AVISO, with support from CNES (http://www.aviso.altimetry.fr/).

## REFERENCES

Aaboe, S., and O. A. Nøst, 2008: A diagnostic model of the Nordic seas and Arctic Ocean circulation: Quantifying the effects of a variable bottom density along a sloping topography. *J. Phys. Oceanogr.*, **38**, 2685–2703, https://doi.org/10.1175/2008JPO3862.1.

Aiki, H., X. Zhai, and R. J. Greatbatch, 2016: Energetics of the global ocean: The role of mesoscale eddies. *Indo-Pacific Climate Variability and Predictability*, S. Behera and T. Yamagata, Eds., World Scientific Series on Asia-Pacific Weather and Climate, Vol. 7, World Scientific, 109–134, https://doi.org/10.1142/9789814696623_0004.

Blumsack, S. L., and P. J. Gierasch, 1972: Mars: The effects of topography on baroclinic instability. *J. Atmos. Sci.*, **29**, 1081–1089, https://doi.org/10.1175/1520-0469(1972)029<1081:MTEOTO>2.0.CO;2.

Bracco, A., and J. Pedlosky, 2003: Vortex generation by topography in locally unstable baroclinic flows. *J. Phys. Oceanogr.*, **33**, 207–219, https://doi.org/10.1175/1520-0485(2003)033<0207:VGBTIL>2.0.CO;2.

——, ——, and R. S. Pickart, 2008: Eddy formation near the west coast of Greenland. *J. Phys. Oceanogr.*, **38**, 1992–2002, https://doi.org/10.1175/2008JPO3669.1.

Brink, K. H., 2016: Continental shelf baroclinic instability. Part I: Relaxation from upwelling or downwelling. *J. Phys. Oceanogr.*, **46**, 551–568, https://doi.org/10.1175/JPO-D-15-0047.1.

Chanut, J., B. Barnier, W. Large, L. Debreu, T. Penduff, J. M. Molines, and P. Mathiotc, 2008: Mesoscale eddies in the Labrador Sea and their contribution to convection and restratification. *J. Phys. Oceanogr.*, **38**, 1617–1643, https://doi.org/10.1175/2008JPO3485.1.

Chelton, D. B., M. G. Schlax, R. M. Samelson, and R. A. de Szoeke, 2007: Global observations of large oceanic eddies. *Geophys. Res. Lett.*, **34**, L15606, https://doi.org/10.1029/2007GL030812.

Chen, R., G. R. Flierl, and C. Wunsch, 2014: A description of local and nonlocal eddy-mean flow interaction in a global eddy-permitting state estimate. *J. Phys. Oceanogr.*, **44**, 2336–2352, https://doi.org/10.1175/JPO-D-14-0009.1.

de Jong, M. F., A. S. Bower, and H. H. Furey, 2014: Two years of observations of warm-core anticyclones in the Labrador Sea and their seasonal cycle in heat and salt stratification. *J. Phys. Oceanogr.*, **44**, 427–444, https://doi.org/10.1175/JPO-D-13-070.1.

de La Lama, M. S., J. H. LaCasce, and H. K. Fuhr, 2016: The vertical structure of ocean eddies. *Dyn. Stat. Climate Syst.*, **1**, dzw001, https://doi.org/10.1093/climsys/dzw001.

Donlon, C. J., M. Martin, J. Stark, J. Roberts-Jones, E. Fiedler, and W. Wimmer, 2012: The Operational Sea Surface Temperature and Sea Ice Analysis (OSTIA) system. *Remote Sens. Environ.*, **116**, 140–158, https://doi.org/10.1016/j.rse.2010.10.017.

Eden, C., and C. Böning, 2002: Sources of eddy kinetic energy in the Labrador Sea. *J. Phys. Oceanogr.*, **32**, 3346–3363, https://doi.org/10.1175/1520-0485(2002)032<3346:SOEKEI>2.0.CO;2.

Gelderloos, R., C. A. Katsman, and S. S. Drijfhout, 2011: Assessing the roles of three eddy types in restratifying the Labrador Sea after deep convection. *J. Phys. Oceanogr.*, **41**, 2102–2119, https://doi.org/10.1175/JPO-D-11-054.1.

Ghaffari, P., P. E. Isachsen, O. A. Nøst, and J. E. Weber, 2018: The influence of topography on the stability of the Norwegian Atlantic Current off northern Norway. *J. Phys. Oceanogr.*, https://doi.org/10.1175/JPO-D-17-0235.1, in press

Gill, A., J. Green, and A. Simmons, 1974: Energy partition in the large-scale ocean circulation and the production of mid-ocean eddies. *Deep-Sea Res.*, **21**, 499–528, https://doi.org/10.1016/0011-7471(74)90010-2.

Haidvogel, D., and Coauthors, 2008: Ocean forecasting in terrain-following coordinates: Formulation and skill assessment of the Regional Ocean Modeling System. *J. Comput. Phys.*, **227**, 3595–3624, https://doi.org/10.1016/j.jcp.2007.06.016.

Haney, R. L., 1991: On the pressure gradient force over steep topography in sigma coordinate ocean models. *J. Phys. Oceanogr.*, **21**, 610–619, https://doi.org/10.1175/1520-0485(1991)021<0610:OTPGFO>2.0.CO;2.

Hátún, H., C. C. Eriksen, and P. B. Rhines, 2007: Buoyant eddies entering the Labrador Sea observed with gliders and altimetry. *J. Phys. Oceanogr.*, **37**, 2838–2854, https://doi.org/10.1175/2007JPO3567.1.

Isachsen, P. E., 2011: Baroclinic instability and eddy tracer transport across sloping bottom topography: How well does a modified Eady model do in primitive equation simulations? *Ocean Modell.*, **39**, 183–199, https://doi.org/10.1016/j.ocemod.2010.09.007.

——, 2015: Baroclinic instability and the mesoscale eddy field around the Lofoten Basin. *J. Geophys. Res. Oceans*, **120**, 2884–2903, https://doi.org/10.1002/2014JC010448.

——, J. H. LaCasce, C. Mauritzen, and S. Häkkinnen, 2003: Wind-driven variability of the large-scale recirculating flow in the Nordic seas and Arctic Ocean. *J. Phys. Oceanogr.*, **33**, 2534–2550, https://doi.org/10.1175/1520-0485(2003)033<2534:WVOTLR>2.0.CO;2.

Isern-Fontanet, J., E. García-Ladona, and J. Font, 2003: Identification of marine eddies from altimetric maps. *J. Atmos. Oceanic Technol.*, **20**, 772–778, https://doi.org/10.1175/1520-0426(2003)20<772:IOMEFA>2.0.CO;2.

Jungclaus, J. H., J. Hauser, and R. H. Käse, 2001: Cyclogenesis in the Denmark Strait overflow plume. *J. Phys. Oceanogr.*, **31**, 3214–3229, https://doi.org/10.1175/1520-0485(2001)031<3214:CITDSO>2.0.CO;2.

Katsman, C. A., M. A. Spall, and R. S. Pickart, 2004: Boundary current eddies and their role in the restratification of the Labrador Sea. *J. Phys. Oceanogr.*, **34**, 1967–1983, https://doi.org/10.1175/1520-0485(2004)034<1967:BCEATR>2.0.CO;2.

LaCasce, J. H., 2017: The prevalence of oceanic surface modes. *Geophys. Res. Lett.*, **44**, 11 097–11 105, https://doi.org/10.1002/2017GL075430.

——, and K. Brink, 2000: Geostrophic turbulence over a slope. *J. Phys. Oceanogr.*, **30**, 1305–1324, https://doi.org/10.1175/1520-0485(2000)030<1305:GTOAS>2.0.CO;2.

Le Traon, P. Y., M. C. Rouquet, and C. Boissier, 1990: Spatial scales of mesoscale variability in the North Atlantic as deduced from Geosat data. *J. Geophys. Res.*, **95**, 20 267–20 285, https://doi.org/10.1029/JC095iC11p20267.

Lilly, J. M., P. B. Rhines, F. Schott, K. Lavender, J. Lazier, U. Send, and E. D. Asaro, 2003: Observations of the Labrador Sea eddy field. *Prog. Oceanogr.*, **59**, 75–176, https://doi.org/10.1016/j.pocean.2003.08.013.

Lorenz, E. N., 1955: Available potential energy and the maintenance of the general circulation. *Tellus*, **7A**, 157–167, https://doi.org/10.1111/j.2153-3490.1955.tb01148.x.

MacLachlan, C., and Coauthors, 2015: Global Seasonal forecast system version 5 (GloSea5): A high-resolution seasonal forecast system. *Quart. J. Roy. Meteor. Soc.*, **141**, 1072–1084, https://doi.org/10.1002/qj.2396.

Mastropole, D., R. S. Pickart, H. Valdimarsson, K. Våge, K. Jochumsen, and J. Girton, 2017: On the hydrography of Denmark Strait. *J. Geophys. Res. Oceans*, **122**, 306–321, https://doi.org/10.1002/2016JC012007.

Mechoso, C. R., 1980: Baroclinic instability of flows along sloping boundaries. *J. Atmos. Sci.*, **37**, 1393–1399, https://doi.org/10.1175/1520-0469(1980)037<1393:BIOFAS>2.0.CO;2.

Nøst, O. A., and P. E. Isachsen, 2003: The large-scale time-mean ocean circulation in the Nordic seas and Arctic Ocean estimated from simplified dynamics. *J. Mar. Res.*, **61**, 175–210, https://doi.org/10.1357/002224003322005069.

Penven, P., V. Echevin, J. Pasapera, F. Colas, and J. Tam, 2005: Average circulation, seasonal cycle, and mesoscale dynamics of the Peru Current System: A modeling approach. *J. Geophys. Res.*, **110**, C10021, https://doi.org/10.1029/2005JC002945.

Shchepetkin, A. F., and J. C. McWilliams, 2005: The Regional Oceanic Modeling System (ROMS): A split-explicit, free-surface, topography-following-coordinate oceanic model. *Ocean Modell.*, **9**, 347–404, https://doi.org/10.1016/j.ocemod.2004.08.002.

Smith, K. S., 2007: The geography of linear baroclinic instability in Earth's oceans. *J. Mar. Res.*, **65**, 655–683, https://doi.org/10.1357/002224007783649484.

Spall, M. A., 2010: Non-local topographic influences on deep convection: An idealized model for the Nordic seas. *Ocean Modell.*, **32**, 72–85, https://doi.org/10.1016/j.ocemod.2009.10.009.

Stone, P. H., 1978: Baroclinic adjustment. *J. Atmos. Sci.*, **35**, 561–571, https://doi.org/10.1175/1520-0469(1978)035<0561:BA>2.0.CO;2.

Teigen, S. H., F. Nilsen, and B. Gjevik, 2010: Barotropic instability in the West Spitsbergen Current. *J. Geophys. Res.*, **115**, C07016, https://doi.org/10.1029/2009JC005996.

Umlauf, L., and H. Burchard, 2003: A generic length-scale equation for geophysical turbulence models. *J. Mar. Res.*, **61**, 235–265, https://doi.org/10.1357/002224003322005087.

Uppala, S. M., and Coauthors, 2005: The ERA-40 Re-Analysis. *Quart. J. Roy. Meteor. Soc.*, **131**, 2961–3012, https://doi.org/10.1256/qj.04.176.

Vallis, G. K., and M. E. Maltrud, 1994: Generation of mean flows and jets on a beta plane and over topography. *J. Phys. Oceanogr.*, **23**, 1346–1362, https://doi.org/10.1175/1520-0485(1993)023<1346:GOMFAJ>2.0.CO;2.

Vollmer, L., and K. Eden, 2013: A global map of meso-scale eddy diffusivities based on linear stability analysis. *Ocean Modell.*, **72**, 198–209, https://doi.org/10.1016/j.ocemod.2013.09.006.

von Storch, J.-S., C. Eden, I. Fast, H. Haak, D. Hernández-Deckers, E. Maier-Reimer, J. Marotzke, and D. Stammer, 2012: An estimate of the Lorenz energy cycle for the World Ocean based on the STORM/NCEP simulation. *J. Phys. Oceanogr.*, **42**, 2185–2205, https://doi.org/10.1175/JPO-D-12-079.1.

Warner, J. C., C. R. Sherwood, H. G. Arango, and R. P. Signell, 2005: Performance of four turbulence closure models implemented using a generic length scale method. *Ocean Modell.*, **8**, 81–113, https://doi.org/10.1016/j.ocemod.2003.12.003.

Wolfe, C. L., and C. Cenedese, 2006: Laboratory experiments of eddy generation by a buoyant coastal current flowing over variable bathymetry. *J. Phys. Oceanogr.*, **36**, 395–411, https://doi.org/10.1175/JPO2857.1.

Zhu, J. S., E. Demirov, Y. Zhang, and A. Polomska-Harlick, 2014: Model simulations of mesoscale eddies and deep convection in the Labrador Sea. *Adv. Atmos. Sci.*, **31**, 743–754, https://doi.org/10.1007/s00376-013-3107-y.

# Paper II

II

## The regeneration of the Lofoten Vortex through vertical alignment

**Trodahl, M.**, Isachsen, P. E, Lilly, J. M, Nilsson, J and Kristensen, N. M
Journal of Physical Oceanography, 2020
doi: 10.1175/JPO-D-20-0029.1

# The Regeneration of the Lofoten Vortex through Vertical Alignment

MARTA TRODAHL

*University of Oslo, Oslo, Norway*

PÅL ERIK ISACHSEN

*University of Oslo, and Norwegian Meteorological Institute, Oslo, Norway*

JONATHAN M. LILLY

*Theiss Research, La Jolla, California*

JOHAN NILSSON

*Stockholm University, Stockholm, Sweden*

NILS MELSOM KRISTENSEN

*Norwegian Meteorological Institute, Oslo, Norway*

(Manuscript received 13 February 2020, in final form 29 June 2020)

ABSTRACT

Observations from the past decades have promoted the idea of a long-lived anticyclonic vortex residing in the Lofoten Basin. Despite repeatedly recorded intense anticyclones, the observations cannot firmly decide whether the signature is of a single vortex or a succession of ephemeral vortices. A vortex persisting for decades requires some reinvigoration mechanism. Wintertime convection and vortex merging have been proposed candidates. We examine Lofoten Basin vortex dynamics using a high-resolution regional ocean model. The model is initialized from a coarser state with a weak eddy field. The slope current intensifies and sheds anticyclonic eddies that drift into the basin. After half a year, an anticyclone arrives at the center, providing the nucleus for a vortex that remains distinct throughout the simulation. Analyses show that this vortex is regenerated by repeated absorption and vertical stacking of lighter anticyclones. This compresses and—in concert with potential vorticity conservation—intensifies the combined vortex, which becomes more vertically stratified and also expels some fluid in the process. Wintertime convection serves mainly to vertically homogenize and densify the vortex, rather than intensifying it. Further, topographic guiding of anticyclones shed from the continental slope is vital for the existence and reinvigoration of the Lofoten vortex. These results offer a new perspective on the regeneration of oceanic anticyclones. In this scenario the Lofoten vortex is maintained through repeated merging events. Fluid remains gradually exchanged, although the vortex is identifiable as a persistent extremum in potential vorticity.

## 1. Introduction

The Lofoten Basin is distinct within the Nordic seas in that the region is exceptionally rich in mesoscale vortices. The vortex field is dominated by large, buoyant anticyclones originating from the unstable Norwegian Atlantic Current (NwAC) flowing along the Norwegian coast. The eddy shedding from the boundary current is responsible for spreading Atlantic Water (AW) away from the coast, making the basin also significantly warmer than the surrounding seas. The Lofoten Basin thus stands out as a hot spot in maps of both sea surface temperatures (SST) and eddy kinetic energy (EKE). The study area is indicated in Fig. 1. Shown are observed time-mean SSTs extracted from the Operational SST and Sea Ice Analysis (OSTIA) reanalysis (Donlon et al. 2012) as well as time-mean geostrophic surface currents estimated by differentiating the altimetric mean dynamic topography produced by AVISO. Warm, saline AW enters the Nordic Seas and is carried northward

*Corresponding author*: Marta Trodahl, marta.trodahl@geo.uio.no

DOI: 10.1175/JPO-D-20-0029.1

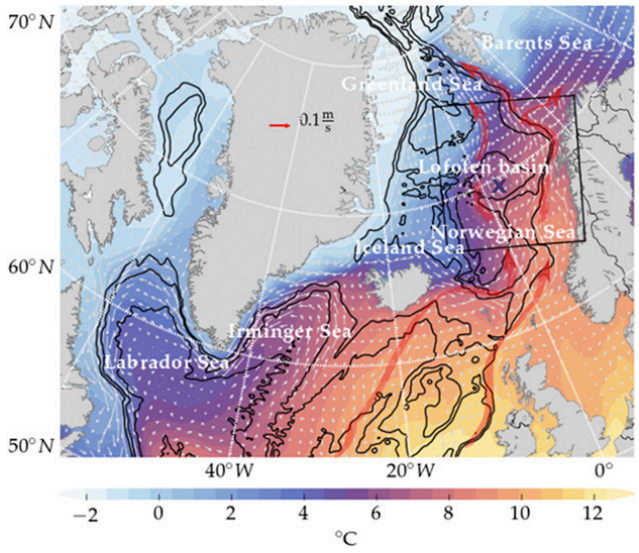


FIG. 1. Time-mean SSTs (°C) from the OSTIA reanalysis. Vectors show time-mean surface geostrophic currents, provided by AVISO. The study region is marked by the black box, and the observed Lofoten vortex time-mean position by the blue cross. Topography is shown in black contours for every 1000 m. The red lines show approximate paths taken by the NwAC.

toward the Arctic Ocean. On its journey the AW experiences heat loss to the atmosphere and progressively densifies (Mauritzen 1996). Through eddy activity the residence time of AW in these areas of major atmospheric heat loss is prolonged. The longest residence time of AW, about 1–3 years, is thought to occur in the Lofoten Basin (Gascard and Mork 2008).

In addition to being infused by transitory turbulent mesoscale features, the Lofoten Basin is home to a uniquely persistent anticyclonic vortex. Oceanographic observations gathered during the time span 1970–90 revealed the presence of a large, persistent high pressure perturbation in the central part of the basin (Ivanov and Korablev 1995a). Later studies have confirmed the presence of this high pressure feature which is commonly referred to as the Lofoten vortex (LV). What makes this one vortex remarkable compared with other vortices is that it somehow manages to sustain its coherence in a violent deformation field for long periods of time. Coherent mesoscale eddies in the ocean typically have lifetimes of days to months. The LV, however, leaves an imprint on decadal time-mean sea surface height (SSH) fields. This imprint suggests an exceptionally long-lived mesoscale vortex, observed perhaps nowhere else in the World Ocean. The dynamics providing such a resilience to vortex breakup presents a puzzle and has been the subject of considerable scientific attention over the last few decades. Søiland et al. (2016) speculate that the vortex lifetime may even extend beyond the five decades of available observational data.

Long-lived vortices are rare but have been observed elsewhere. A prevalence of large anticyclones is found on Jupiter and Saturn. Notably, the Great Red Spot in the Jovian atmosphere is an anticyclonic vortex that has survived for over 300 years (Nezlin et al. 1993). In the Argentine Basin, float trajectories and satellite altimetry have recorded a permanent, stationary anticyclone, the Zapiola Anticyclone (de Miranda et al. 1999). This vortex is, however, not analogous to the LV as it is driven by completely different dynamics. While the LV is situated in the deepest parts of a topographic depression, the Zapiola Anticyclone is a barotropic feature with a circulation forced to follow closed potential vorticity contours over a topographic rise (de Miranda et al. 1999). Another anticyclonic recirculation considered to be a quasi-permanent feature is the Mann Eddy, found along the path of the North Atlantic Current in the central Newfoundland Basin (Mann 1967; Meinen 2001). The persistence of the Mann Eddy is evidenced by its sea surface signature showing up in altimetry climatologies. Still, the dynamics of this vortex has not been meticulously examined up until the recent high-resolution (2.5 km) model study of Solodoch et al. (2020), the study also facilitates existing hydrographic and altimetry data to complement the model data. Unlike the LV, the Mann Eddy is surface intensified but similarly resides within a topographic depression in which it drifts. Mergers are found to assist in sustaining the vortex and its origins takes place within the depression. Perhaps more closely related to the LV, long-lived vortices have been observed as bulges within and below the thermocline in various regions of the World Ocean (Prater and Sanford 1994). These vortices are as a rule all anticyclones. A typical intrathermoclinic (ITV) or subthermoclinic vortex (STV) has a lens-like shape and an anomalous core with small vertical changes in water properties that stands out against the background stratification. The most well-known example of this type of vortices are Mediterranean water eddies (meddies). If they do not encounter a major seamount, meddies may dissipate slowly and stay intact for several years, some estimated from observations to last up to 5 years (Richardson et al. 2000). However, the same study estimated that about 90% out of 27 meddies analyzed, did collide with seamounts that led them to disintegrate. These collisions were found to occur on average 1.7 years after a meddy formation.

Observations show that the LV share similarities with subthermocline/intrathermocline anticyclonic vortices reported from other oceanic regions. The core consists

of a weakly stratified, fast-spinning water mass anomalous with respect to its surroundings.[1] The core depth is centered at about 700–900 m and the typical radius at which the maximum azimuthal velocity occurs is 15–30 km (Yu et al. 2017). The vortex commonly resides within the 3000-m isobath, near 3°E and 69.5°–70°N (Rossby et al. 2009; Søiland and Rossby 2013; Fer et al. 2018). The observed time-mean vortex position is indicated by a blue cross in Fig. 1.

Fer et al. (2018) report a maximum azimuthal speed of 0.8 m s$^{-1}$ at 950 m depth. The momentum balance of the core is highly nonlinear, with the relative vorticity estimated from the observed flow field typically around $-0.5f$ but reaching as low as $-0.9f$ ($f = 1.37 \times 10^{-4}$ being the Coriolis parameter at 70°N) near the eddy axis, which is close to the theoretical limit for anticyclones of $-f$ (Fer et al. 2018).

A continuous rejuvenation of the vortex is apparently needed to sustain such levels of intensity in an otherwise violent environment with high deformation rates as well as dissipation from e.g., bottom friction. Two hypotheses have been previously proposed for the maintenance of the vortex. Using observational data, Ivanov and Korablev (1995a,b) suggested that wintertime convection plays a key role. They postulate that convection events lead to a deepening of the isopycnals below the vortex core, causing the azimuthal velocity to intensify through the increased radial density gradient. However, in a later model study, Köhl (2007) suggested that anticyclonic eddies generated from the unstable boundary current propagate westward and are attracted to center of the basin by nonlinear drift under the topographic beta effect. The accumulation of anticyclones in the center of the relatively small Lofoten Basin encourages the mergers of like-signed vortices. Thus in this hypothesis, the slope eddies drift toward the Lofoten vortex and energize it through a merging process. In this study we will look closer at the merging hypothesis. We do not investigate meticulously the role played by convection, but recognize that it may affect the rejuvenation process.

Obtaining detailed observations of vortex mergers is an immense challenge. The process has limited predictability and happens on a very short time scale. Observations that have captured vortex interactions are few, and only sporadic accounts exist from in situ observations. Due to the challenges in obtaining sufficient amount of observational data, investigations of vortex mergers have more commonly been conducted in various numerical and theoretical settings. Many experiments consider idealized circumstances where the interacting vortices are studied in isolation with only some active processes. These idealized choices are imperative in order to assess how a merger is impacted by specific influences, such as external strain, stratification, and asymmetric vortex properties. The majority of theoretical works consider interactions of symmetric anticyclones that share the same strength and density, with cores situated on the same vertical level. But a much more realistic scenario is where the vortices are not necessarily similar in size, strength nor density.

One of the first records of a vortex coalescence was taken off the East Australian Current (Cresswell 1982). Two anticyclones at different depths coalesced by aligning vertically over the course of 20 days. Partly motivated by the observations of Cresswell (1982) and Nof and Dewar (1994) studied the interaction of two anticyclonic lenses having different densities. Using laboratory and numerical experiments, they found that the lenses are inclined to align vertically rather than undergoing a horizontal merger where a substantial amount of the two vortex cores melt together to form a single, larger vortex. When interacting, the lenses seek a final state where one is placed on top of the other. The lighter vortex slides on top of the denser vortex, resulting in a dual core vertical structure. The notion of vertical alignment was first presented by McWilliams (1990) in a study of decaying stratified 3D quasigeostrophic turbulence, where vortices in the end state largely appeared to be stacked on top of each other in elongated vertical structures. Sparked by these results, Polvani (1991) studied the process analytically in a quasigeostrophic two-layer system. He found that two vortices from different density classes coalesce by vertically aligning only if their radii are on the order of or larger than the Rossby deformation radius.

Over the years, an increasing observational record of dual core anticyclones emerged (Cresswell 1982; Bogdanov et al. 1985; Belkin and Mikhailitchenko 1986; Armi et al. 1989; Brundage and Dugan 1986; Prater and Sanford 1994; Schultz Tokos et al. 1994; Lilly et al. 2003; Rogachev et al. 2007; Dmitrenko et al. 2008; Itoh and Yasuda 2010; Carton et al. 2010; Baird and Ridgway 2012; Barceló-Llull et al. 2017; Garreau et al. 2018; Belkin et al. 2020). While the limited amount of data does not give direct evidence that these double cores arise from vertical alignment, several studies hypothesize that this could be the case. In an eddy census from the Labrador Sea, Lilly et al. (2003) found a strong dominance of anticyclonic vortices. The observed anticyclones were grouped into two categories, surface-intensified Irminger rings and middepth-intensified ''convective lens'' type eddies. Among both types of anticyclones, several exhibited vertically aligned cores. The hydrographic signature of the cores strongly suggested that they originated from

[1] Figure 7 shows time-mean profiles of the model simulated LV, which reproduces main observational features.

two initially separated eddies, rather than originating from, e.g., wintertime convection. The study concluded that the only tenable mechanism of joining the two cores was through vertical alignment.

Observations have also revealed that the Lofoten vortex core does at times have a dual core structure (Yu et al. 2017; Fer et al. 2018). In this paper, we study the mesoscale eddy field in the Lofoten Basin, with the focus on the regeneration mechanism of the LV. Specifically, we revisit the hypothesis of Köhl (2007) and investigate the role of vortex mergers. Benefiting from a model with unprecedentedly high temporal and spatial resolution, we bring new insights to this discussion by studying vortex interactions in detail. We investigate whether the observed occasional double-core structure of the LV may result from the kinds of vortex coalescence discussed by Nof and Dewar (1994). We find that vertical alignment episodes are indeed occurring, and moreover we find that these are common not only for the LV, but also for Lofoten Basin anticyclonic vortices in general. The vortices resident in the basin have generally been subject to different cooling and warming periods, and have originated in different seasons, and consequently reside at different vertical levels. We will give a high-resolution account of how merger events with the LV play out in a realistic setting with all complexity of the flow field present. The net result strongly supports the hypothesis that a vortex merger is the primary mechanism for the regeneration if the LV.

## 2. Data and methods

### a. Model

Our study employs a numerical simulation using the Regional Ocean Modeling System (ROMS; Shchepetkin and McWilliams 2005; Haidvogel et al. 2008). ROMS is a hydrostatic, primitive equation model formulated with a horizontal near-orthogonal staggered C grid and a vertical coordinate system, called the *s* coordinate (Shchepetkin and McWilliams 2005), in which the model layers follow the variations of the seabed terrain. The model domain is shown in Fig. 1.

The model's lateral grid spacing is 800 m. At this resolution, mesoscale eddies on the scale of the internal Rossby deformation radius of about 6–7 km would be well resolved throughout the domain, except on the very shallow parts of the continental shelf. The vertical grid consists of 60 layers distributed so as to obtain a finer resolution near the surface. The vertical spacing is at a minimum 0.3 m near the surface and up to 80 m in the bottom layers. A fourth-order centered scheme is used for vertical advection, and a third-order upwind scheme is used for horizontal advection. No explicit horizontal eddy viscosity or diffusion is applied, but the upwind advection scheme includes some implicit biharmonic diffusion. The $k$–$\varepsilon$ version of the general length scale (GLS) scheme is employed for small-scale vertical mixing (Umlauf and Burchard 2003; Warner et al. 2005). The open lateral boundaries are relaxed toward the global Forecast Ocean Assimilation Model (FOAM; MacLachlan et al. 2015) with a 15-day relaxation time scale, and atmospheric forcing is taken from the ERA-interim atmospheric reanalysis (Uppala et al. 2005). Runoff from major rivers are supplied by monthly climatologies from a river discharge model from the Norwegian Water Resources and Energy Directorate (Beldring et al. 2003).

The model is started in January 1993 and run for 10 years. The initial model state is given by FOAM, which has a resolution of 25 km. After two years of spinup, the last 8 years of the model simulation (1995–2003) are analyzed to ensure that the dynamics are consistent with the boundary conditions. Model output is stored every 6 h. For parts of the analysis we use daily mean fields, whereby tides and other motions excited by fast atmospheric forcing are mostly filtered out. Nevertheless, a high temporal resolution was found to be necessary to capture the details of the eddy interactions, so merging processes are studied with the 6-hourly model fields.

Figure 2 shows the time-mean SST and surface flow field extracted from observations [the Climatological Atlas of the Nordic Seas and Northern North Atlantic (1950–2012) (Korablev et al. 2014) and AVISO] and also the model. The model contains finer structures than the observations, reflecting the coarser effective resolution of the observational dataset. However, the general structure of the two fields agree well. The model captures the Mohn Ridge frontal zone as well as the warm water carried by the Norwegian Atlantic Current closer to the coast. A discrepancy between the observations and the model is seen north of the Lofoten Basin, around 5°–10°E and 72°N, where the model exhibits a tongue of cold water. This feature is seen in the wintertime observational data but is less prominent in the annual mean fields. The apparent lack of a cold tongue in the observations may plausibly be related to resolution or under sampling during winter. In the model, this feature seems to arise due to the steering of the time-mean current along the bottom topography. Alternatively, this might indicate that the model currents are too constrained by topography, an effect not uncommon in models with terrain-following vertical coordinate systems (Haney 1991).

Estimates of geostrophic surface EKE from satellite altimetry data (AVISO) and model are given in Figs. 2c

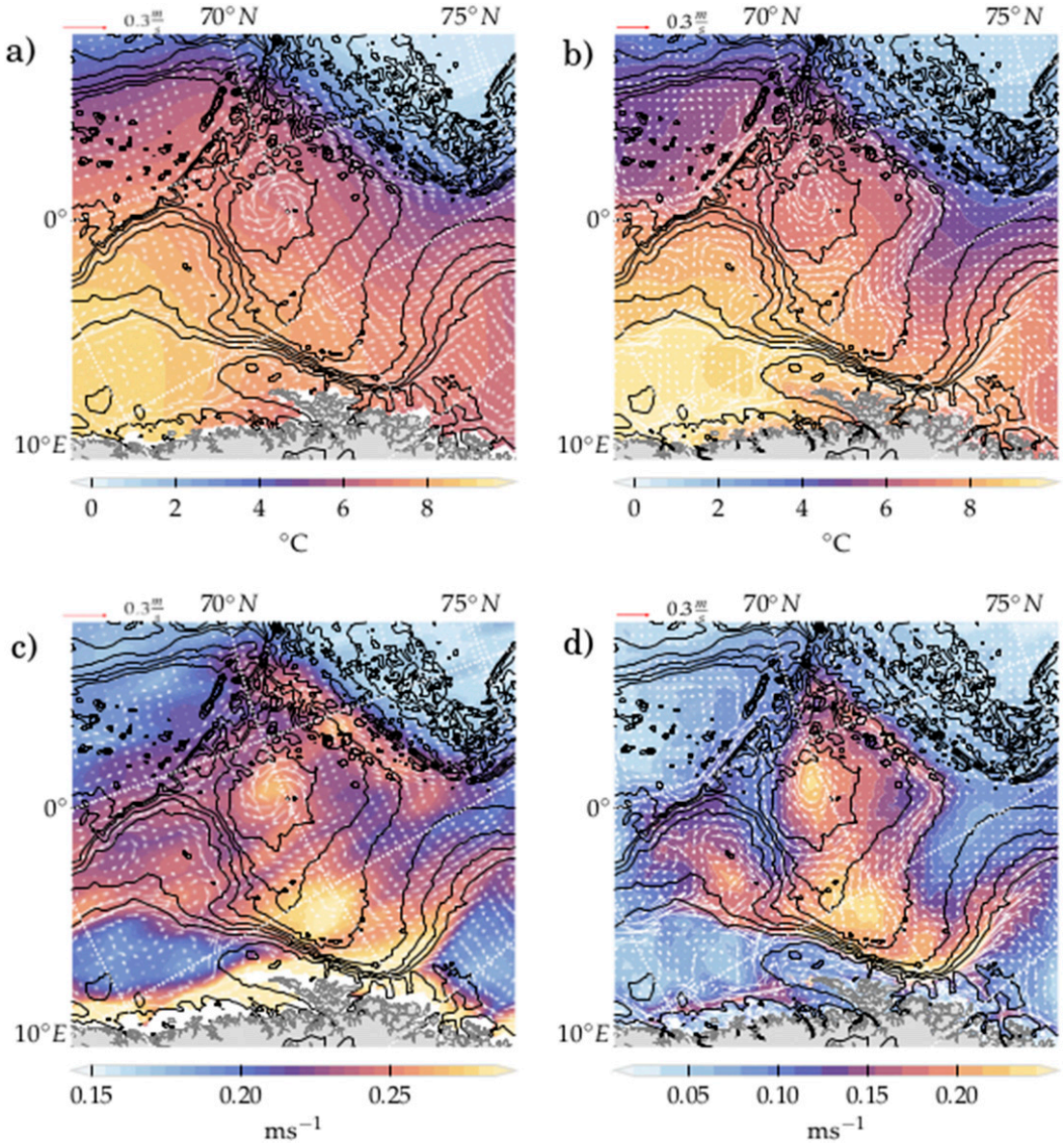


FIG. 2. Time-mean SSTs (°C) from (a) the Climatological Atlas of the Nordic Seas and Northern North Atlantic (1950–2012) and (b) model (1995–2002), together with square root of geostrophic EKE ($m\,s^{-1}$) obtained by differentiating along-track SSH anomalies provided by (c) AVISO and (d) the model. Vectors show time-mean surface geostrophic currents. Topography is shown with black contours in this and subsequent maps with 500-m increments, starting at the 200-m depth contour.

and 2d. The altimeter data contains instrumental noise, which produces artificially high EKE levels at high wavenumbers (Le Traon et al. 1990). This is likely responsible for a general higher EKE level in the observations compared to the model, as seen especially in relatively quiescent regions in the model. However, the main observed spatial patterns of variability are well captured by the model, including the EKE tongue extending from the steep slope region off the Lofoten Islands (around 10°–12°E and 68°N). Model EKE levels in the Lofoten Basin are close to those of the observations, giving us confidence in the eddy dynamics represented in the model.

### b. *Eddy detection*

We extract coherent mesoscale vortices from the model flow field using the eddy detection method of Penven et al. (2005) (for more details see the appendix). This method is based on the facts that a coherent vortex is a pressure perturbation with closed streamlines around its center and that the interior of a coherent vortex is characterized by strong relative vorticity. By

contrast, the boundary of the vortex, as well as the regions between separated vortices, are typically subject to large deformation rates. The method used is a hybrid scheme that involves locating closed contours of both SSH and of the Okubo–Weiss (OW) parameter (see Fig. 3). The OW parameter compares the strength of deformation to that of rotational motion taking the form

$$\mathrm{OW} = S_n^2 + S_s^2 - \zeta^2, \tag{1}$$

where the normal strain $S_n = \partial_x u - \partial_y v$ and shear strain $S_s = \partial_x v + \partial_y u$ measure the fluid deformation, while relative vorticity $\zeta = \partial_x v - \partial_y u$ represents rotation of the fluid about a vertical axis. Essentially, regions in the flow field where $\mathrm{OW} \lesssim 0$ are potentially coherent eddy cores. Although the OW parameter was originally designed to identify coherent structures in idealized 2D turbulent flows, it is also commonly applied to identify vortices in more realistic geophysical flows (Isern-Fontanet et al. 2003; Penven et al. 2005; Chelton et al. 2007). For detection purposes, we use the OW contour calculated from horizontal velocities at 100-m depth. We chose to do the detection a bit below the surface to avoid some noise in the OW parameter. Computing the OW directly at the surface produces more small-scale noise.

## 3. Results

### a. Model spinup

The model is initialized from FOAM fields interpolated to the model grid from lateral resolution of 25 km. The dynamical inconsistencies caused by the interpolation give rise to an initial shock creating some domain-wide gridscale noise. However, it takes less than a week before this shock has settled and the noise is smoothed out.

The deformation radius ($\int_{-H}^{0} N dz/f$), where $N$ is the square root of the buoyancy frequency computed using the ambient density field, in the area ranges from 2 to 8 km (as shown in Fig. 7a). Hence, the initial state drawn from a coarse model that has a weak mesoscale eddy field and no identifiable Lofoten vortex. Once the higher-resolution ROMS model begins running, the Norwegian Atlantic Slope Current (NwASC) off the Lofoten Islands quickly intensifies and via instabilities becomes a source of anticyclonic eddies that move into and energize the relatively quiescent initial model state in the Lofoten Basin. Figure 4 shows a snapshot of 1) model temperature and 2) at 400-m depth in the basin, one month into the simulation. No large anticyclones have reached the central Lofoten Basin at this point, the LV has not appeared yet. Originating from the slope, anticyclones shed from the NwAC trap and carry warm Atlantic water in their

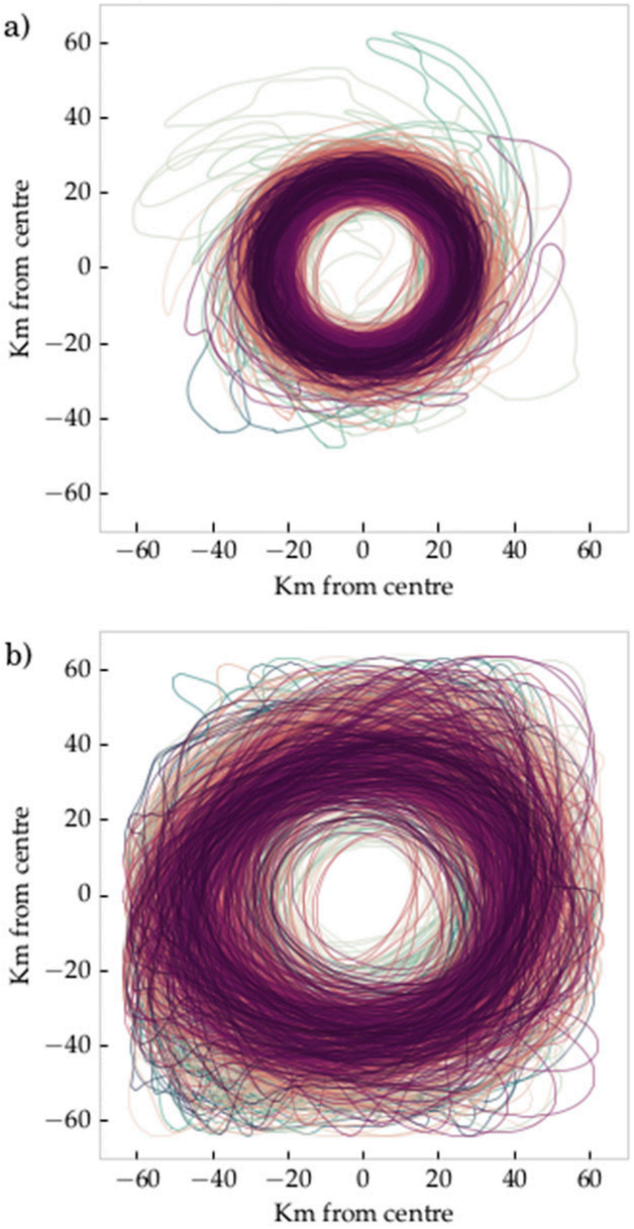


FIG. 3. (a) OW = 0 contours and (b) outermost SSH contour extracted daily around the LV center found each day during 1995–99, the first 4 years after the spinup period. Colors are arbitrary.

cores. The lateral westward spread of this water mass is readily seen in the figure.

As time proceeds, more slope anticyclones reach the central basin, which then accumulate there. At later stages in the simulation, the basin hydrography has undergone a substantial modification compared to the initial field. Figure 5a shows a vertical transect through the basin from the initial model state, the 15 January 1994. Figure 5b shows the same transect at the same date 8 years into the simulation. The fine resolution of the ROMS model produces sharper fronts and slender boundary currents. The initially broad NwAC is now

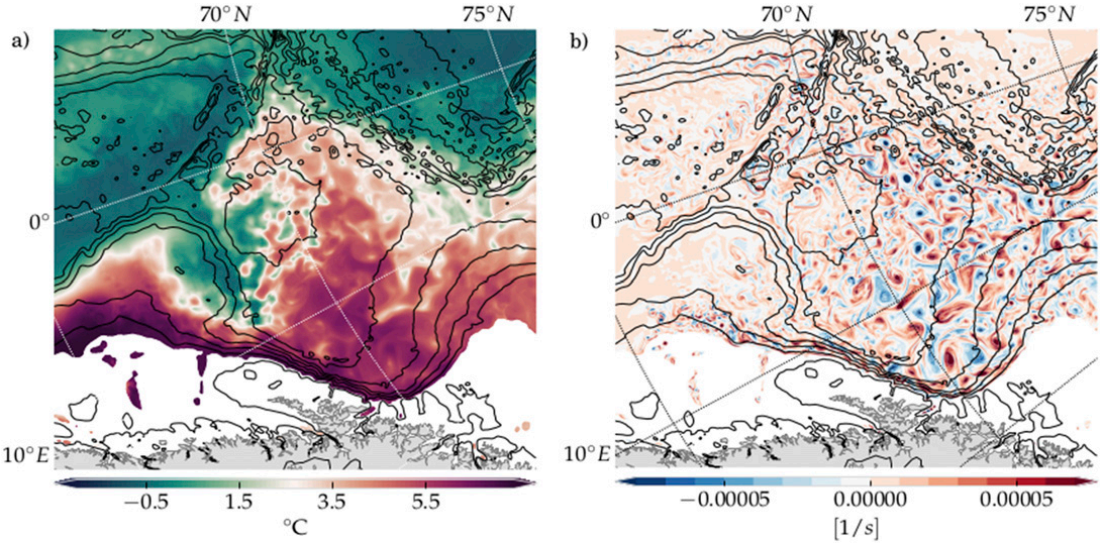


FIG. 4. Snapshot of (a) model temperature and (b) relative vorticity at 400-m depth on the 1 Feb 1994, one month after initialization. White areas are shallower than 400 m.

confined to the continental slope, in agreement with observations showing current width on the order of tens of kilometer (Orvik and Niiler 2002; Rodionov et al. 2004). The observed vertical extent of the AW typically lies between 500 and 700 m (Yu et al. 2017). The AW, with salinity above 35 psu and temperatures above 3°C, occupied the top 400 m at the start of the simulation, and later occupies the top 700 m. This indicates that when the high-resolution and eddy-rich simulation is initialized from the coarser model fields with a weaker eddy

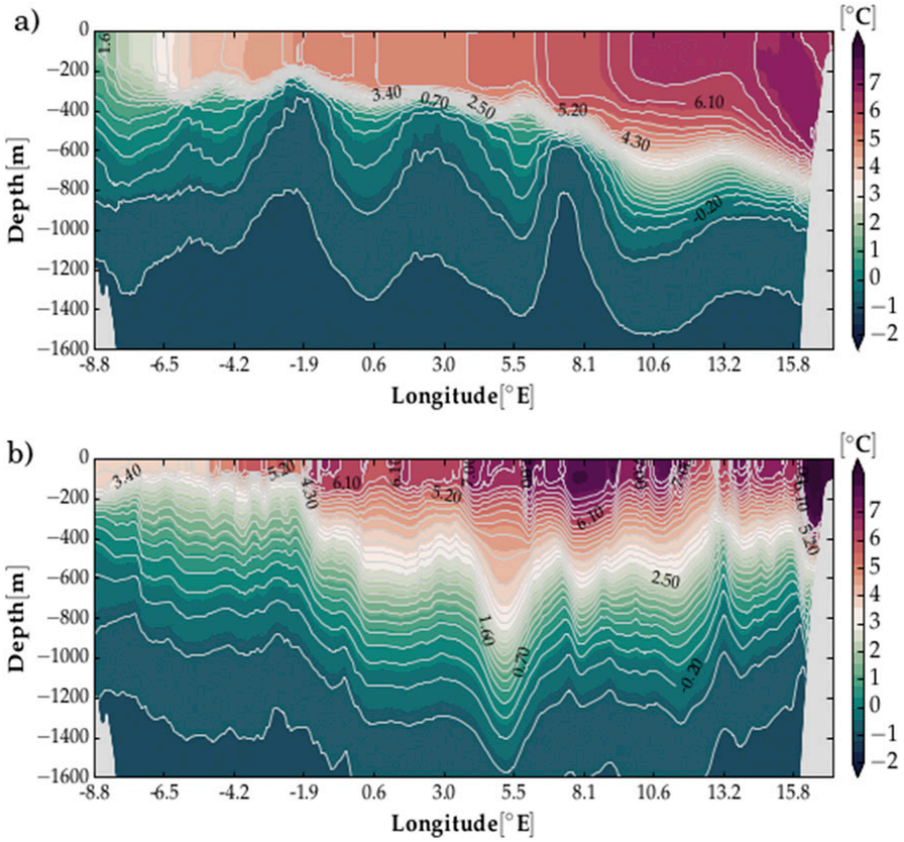


FIG. 5. Vertical transect through the basin at 70°N of model temperature taken from the initial field on (a) 15 Jan 1994 and (b) 15 Jan 2001. Temperature contours are shown in white.

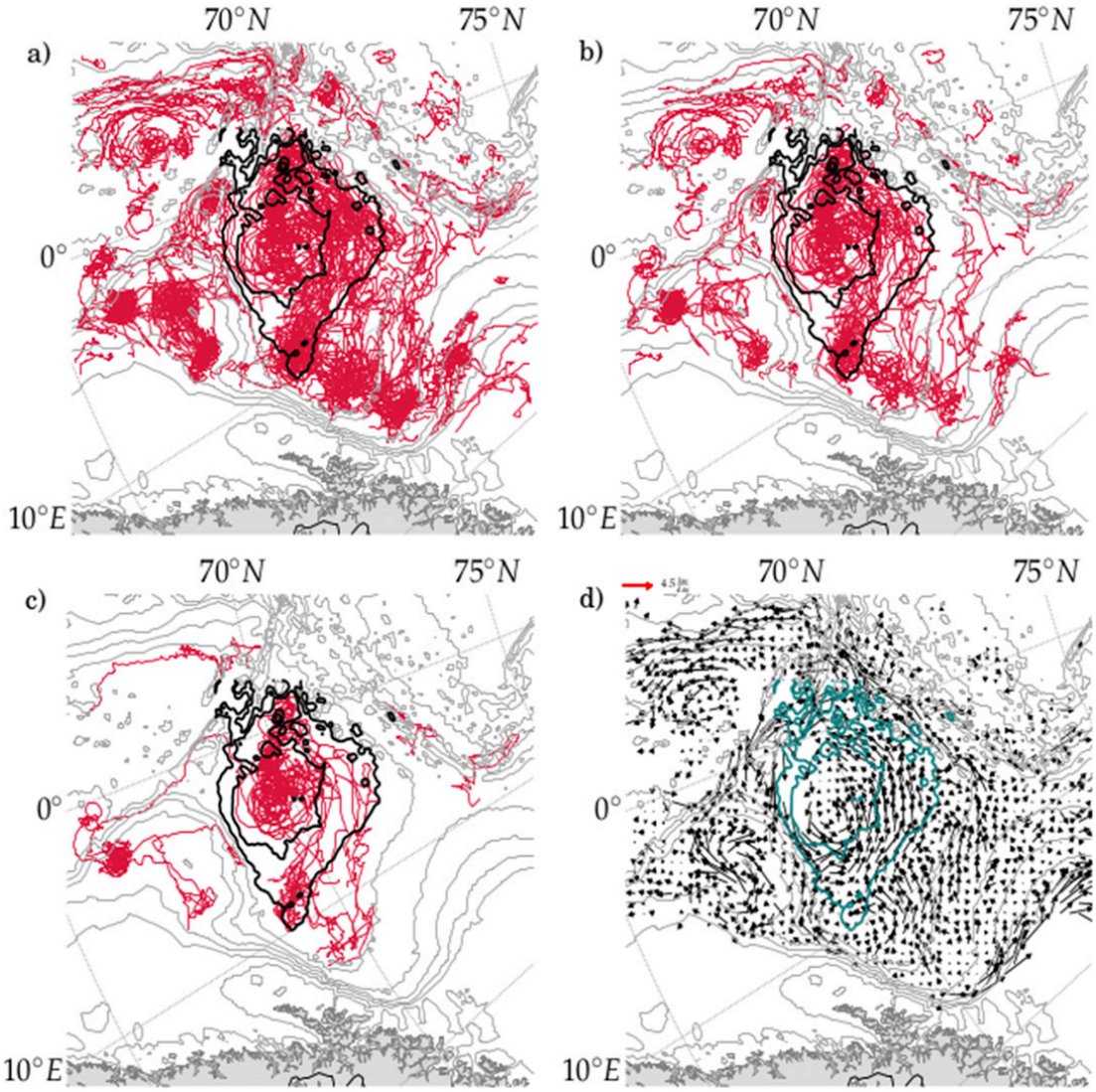


FIG. 6. (a) Anticyclonic vortex trajectories with durations longer than (a) 1, (b) 3, and (c) 7 months. (d) Binned (25 km × 25 km) vortex displacement vectors derived from these trajectories. Bins containing less than 8 counts were discarded. The 3000- and the 3200-m topographic contours surrounding the Lofoten Basin are highlighted in color. The blue box indicates a source region for anticyclonic vortex generation.

field ocean heat-flux divergence due to anticyclonic eddies propagating toward deeper waters, originating from the Lofoten continental slope, results in the general warming of upper Lofoten Basin.

Before discussing the life cycle of the Lofoten vortex in the model, we present a basin-wide census for all detected anticyclones.

### b. *Propagation and hydrography of Lofoten Basin anticyclones*

Figure 6 shows the trajectories of all detected anticyclonic vortex centers that we were able to trace for 1) 1 month or longer, 2) 3 months, and 3) 7 months after the initial 2-yr spinup period. The majority of the vortices originating from the boundary current have drifted westward along cyclonically arching routes into the central Lofoten Basin. In other words, the trajectories spiral in a counterclockwise sense toward the deepest part of the basin, where they typically terminate. Longer trajectories, lasting 3–6 months, can be traced back to the slope region associated with the elevated EKE values seen in Figs. 2c and 2d, indicating a source region, shown by the blue square. Three major areas of anticyclone generation and accumulation is seen off the slope, with the associated tracks following somewhat different paths into the basin. The southernmost tracks lie right off the 3200-m isobath. Some of these break off and follow a direct route into the central Lofoten Basin, while the rest move along a curved path and then turn cyclonically later. The tracks found farther north move

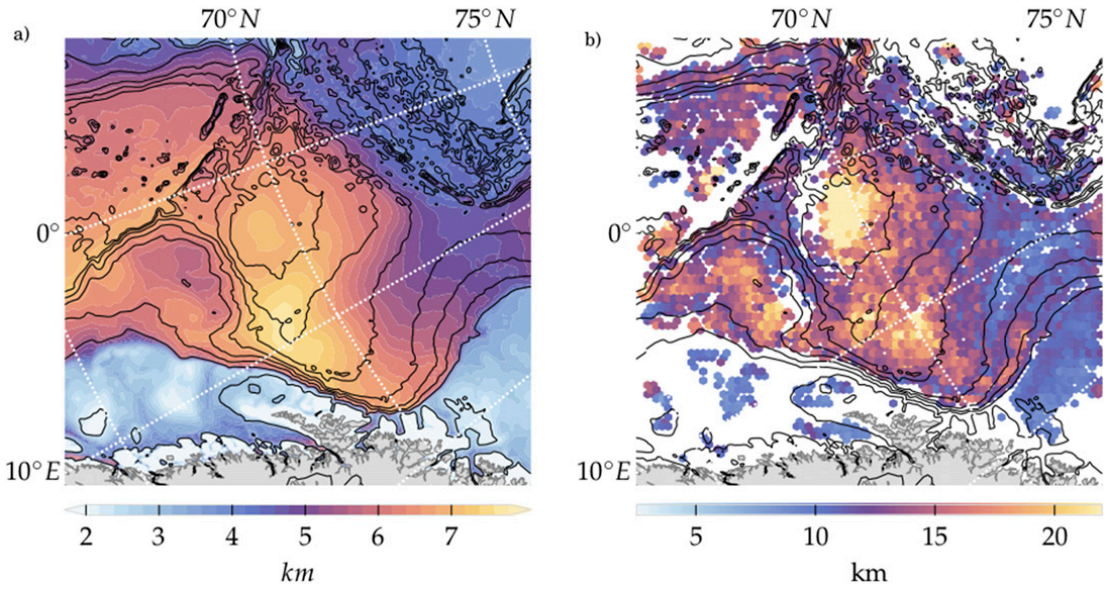


FIG. 7. (a) The first internal Rossby deformation radius ($\int_{H_0}^{0} N\,dz/f$) computed using the ambient density field and (b) vortex radii estimated from the mean distance between the eddy center and the OW contour of anticyclonic eddies. The white color indicates regions with no identified eddies.

along outer routes, tracing more or less out the 3000-m isobath. Their travel times are longer, which will likely alter their hydrographic structure. In the winter season, the vortices spending more time to reach the central basin are subject to longer cooling periods and would therefore be expected to be denser than the vortices taking the direct route from the boundary current.

Theoretical studies from the midlatitudes have shown that anticyclones tend to move southwest and cyclones to the northwest due to the planetary beta effect (McWilliams and Flierl 1979). Planetary beta effect is, however, very weak at the latitudes of the Lofoten Basin. Still, provided the slope is broad relative to the vortex length scales, the mechanism on the beta plane can be translated to vortex motion relative to topographic contours, the topographic beta effect. Taking the average magnitude of the slope within the area enclosed by the 2800-m isobath gives the following estimate of the topographic beta effect $\beta_T = f\nabla h/H \approx 2 \times 10^{-10}\,\mathrm{m^{-1}\,s^{-1}}$, which is more than an order of magnitude larger than the planetary beta effect $\beta \approx 6 \times 10^{-12}\,\mathrm{m^{-1}\,s^{-1}}$. Topographic beta causes anticyclones to propagate toward the center of a topographic depression while cyclones tend to move upslope, also moving in the pseudo-westward direction (Carnevale et al. 1991). Although their study considered barotropic vortices, we find a tendency for anticyclones to move downslope with shallow water to the right after they are released from the boundary current. The binned drift of anticyclonic tracks, shown in Fig. 6b, demonstrate a movement toward deeper regions.

The core radii of the tracked anticyclones are shown in Fig. 7b. The radii are estimated from the OW contours and radii values are bin averaged over 10 km × 10 km grid boxes. Earlier studies have shown that strong anticyclones with scales larger than the deformation radius can become very robust and have long lifetimes compared to their cyclonic counterparts. The internal Rossby radius, $L_d = \int_{-H}^{0} N\,dz/f$, computed from the model's time-mean hydrography where $N$ is square root of the ambient buoyancy frequency, is shown in Fig. 7a. Anticyclonic vortices are here indeed generally 2–4 times larger than $L_d$. We also note that the distribution of radii displays some resemblance to $L_d$, indicating a possible linkage to linear growth theory. However, the length scales share an even stronger resemblance with the EKE field shown in Fig. 2d. Such a similarity suggests that the equilibrated eddy scales are rather set by some form of Rhines scale arrest (Held 1999; Vallis 2006), which predicts an eddy length scale on the order of $\sqrt{U/\beta}$, where $U$ is the eddy velocity scale. If we take the topographic beta $\beta_T$ and $U \sim 0.2\,\mathrm{m\,s^{-1}}$, this Rhines scale is about 30 km.

### c. *Origin and characteristics of the Lofoten Basin vortex*

For the remainder of this study, we focus on the characteristics and history of the Lofoten vortex. We start by looking at a statistical description, and follow up with an investigation of the vortex life cycle.

Convection has been proposed as a generation mechanism of the LV (Ivanov and Korablev 1995b). However,

convection creates vertically aligned dipole vortices with cyclonic circulation in the upper ocean and anticyclonic circulation in the lower ocean (Send and Marshall 1995). Accordingly convection alone cannot create the LV, which has surface intensified anticyclonic circulation that extends to the bottom (see Fig. 9).

In our simulation, an anticyclonic vortex first appears in the center of the basin 170 days into the simulation during the spinup period. It is possible to trace this vortex back to the boundary current, in agreement with the hypothesis of Köhl (2007). On its way to the central basin, the initial LV is also subject to several mergers between smaller-scale vortices, by which it grows in size both laterally and vertically. The vertical thickness of the vortex in May is 800 m after experiencing a couple of months of winter. When it first appears near the continental slope in February–March, it is a shallow structure with a thickness of 300 m. From tracking other anticyclones throughout winter seasons, it seems doubtful that wintertime mixing alone can explain this rate of a deepening penetration of the vortex core, approximately 250 m per month. Instead, the process that allows the vortex to become a deep structure quite rapidly will be discussed in the next section.

The vortex signature grows stronger with time, following consecutive mergers after it settles in the central Lofoten Basin as the LV. From the beginning of the post spinup period, starting in 1995, a well-established anticyclonic vortex exists in the center of the basin. Close examination reveals that the LV remains coherent throughout the entire tracking period, i.e., for 8 years. The distribution of the LV positions during model years 1995–2002 are shown in Fig. 8. The time-mean position agrees well with observations (the observed location is indicated by the red cross in Fig. 1) (Fer et al. 2018). The vortex commonly resides near 2°–3°E and 69.5°–70°N, with occasional small geographical excursions. The excursions stay within the region bounded approximately by the 3200-m-depth contour. To a large extent, the shape of the distribution appears trace out the shape of the enclosing topographic contours.

Binned displacement vectors of the vortex center are also shown in Fig. 8 along with time-mean depth-averaged currents from the model. The average drift speed of the LV is about 1.7 km day$^{-1}$, which is close to the model-based estimate by Volkov et al. (2015) of 1.5 km day$^{-1}$. The vortex movement is weak with no distinct propagation direction in the deepest part of basin with the highest number of counts. This area has a fairly flat bottom topography. According to the topographic beta mechanism discussed earlier, a pseudo-westward movement is, however, evident farther out

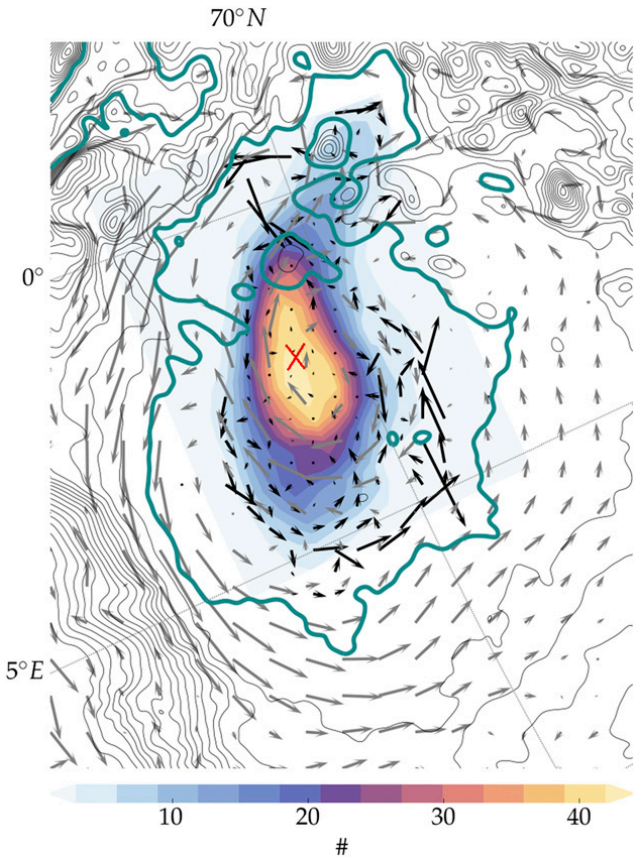


FIG. 8. Distribution of estimated LV center location (color shading) and the mean estimated center translation velocity in 15-km bins (black vectors), detected and tracked at 500-m depth over the years 1995–2003. Gray vectors show depth-average time-mean currents. Unlike earlier maps, topographic contours are drawn every 100 m in black, and the 3200-m isobath is indicated by thicker teal contours. The red cross indicates the time-mean position of the LV.

where the counts are lower. Here, the vortex might start to feel the effect of stronger topographic slopes and be forced to move cyclonically. The cyclonic drift has been mentioned in previous studies as possibly governed by the topographic beta effect (Raj et al. 2015; Søiland and Rossby 2013; Yu et al. 2017). Another possibility was suggested by Ivanov and Korablev (1995b), namely, that the LV is kept in place, within the 3000-m isobath, by its interaction with the time-mean cyclonic gyre circulation and that a cyclonic drift of the vortex center arises from the advection by the cyclonic time-mean current. The ambient depth averaged circulation simulated in the basin is indeed cyclonic, aligning with the vortex drift, and cannot be ruled out as a potential mechanism. But, importantly, the vortex drift typically exceeds the background currents, suggesting a combined effect of the topographic drift added to the advection by from the ambient circulation. The vortex detection was also carried out for cyclonic eddies (not shown here). In

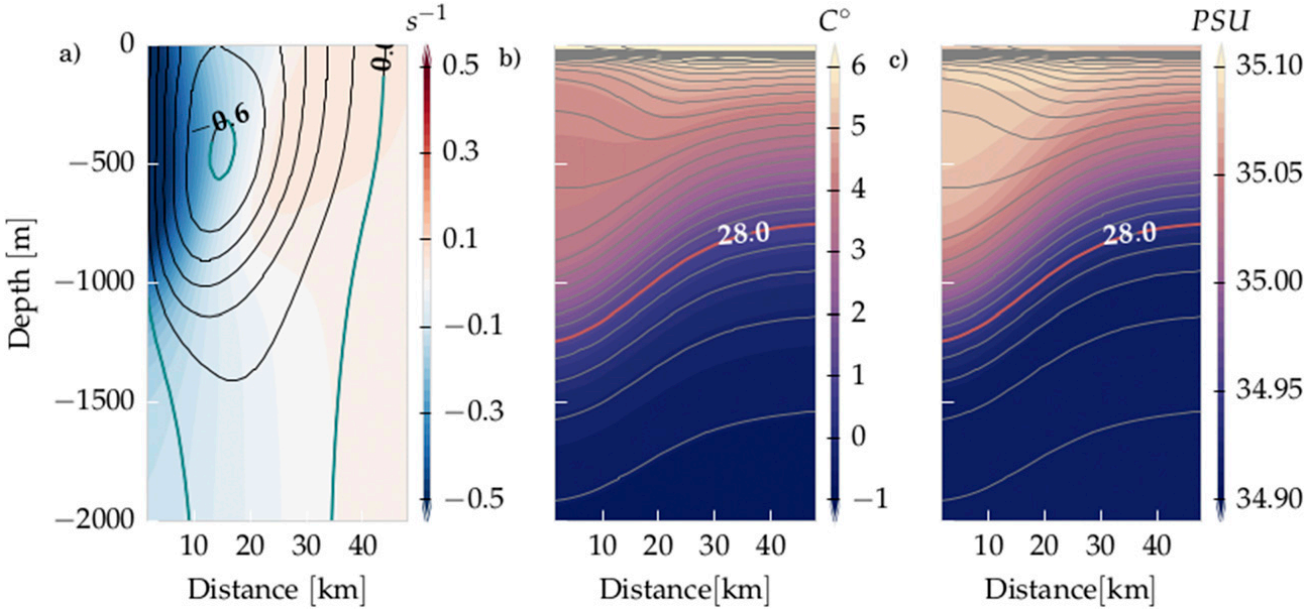


FIG. 9. Time-mean radial profiles of (a) vortex Rossby number $\zeta/f$ (color) and azimuthal velocity (black contours), with the velocity maxima and sign reversal highlighted (teal contours), (b) temperature, and (c) salinity in the Lofoten vortex core (color) together with isopycnals (gray contours). The 28.0 kg m$^{-3}$ isopycnal is shown in red.

agreement with Köhl (2007) and Volkov et al. (2015), we found frequent occurrences of cyclonic eddies in a band around the LV. In addition to the systematic westward drift relative to topographic contours, these cyclones and other neighboring vortices will likely contribute to a chaotic component in the LV movement. From model analysis, Köhl (2007) found the drift to occur in the opposite direction, anticyclonically, and attributed this drift to the interaction with surrounding cyclonic vortices.

Figure 9 displays the LV time-mean vertical structure of azimuthally averaged properties. The vortex Rossby number $\zeta/f$, where $\zeta = \mathbf{k} \cdot \nabla \times \mathbf{u}$ is relative vorticity, and azimuthal velocity are shown in Fig. 9a. At the center, the time-mean Rossby number reaches −0.7. The minimum instantaneous value reaches −0.94. For comparison, Yu et al. (2017) reported a minimum value of $\zeta_{\min} = -0.91\,f$ from their 3 years of Seaglider data. Similar values have been noted in other studies. With shipborne measurements, Søiland et al. (2016) estimated a minimum core vorticity of $-f$, and using 2 years of glider data Fer et al. (2018) found $\zeta_{\min} = -0.87 \pm 0.12f$. Thus our model reproduces LV core vorticity within the observed range.

The azimuthal velocity and the vorticity have pronounced subsurface maxima at a depth of about 500 m around 17 km from the center. The location roughly corresponds to the maximum isopycnal slope seen in the hydrography in Figs. 9b and 9c. The depth of the velocity maximum oscillates over time as the vortex evolves (not shown), mostly staying within the depth range of 400–900 m, and thus does at times reach the larger depth observed in other studies (Bosse et al. 2019). The maximum time-mean azimuthal velocity approaches 0.6 m s$^{-1}$ and its peak instantaneous value exceeds 0.9 m s$^{-1}$. Below 1500 m, the velocity stays nearly constant, with significant bottom velocities, stronger than 0.13 m s$^{-1}$ at 3000-m depth. Thus the vortex currents are expressed throughout the water column, and since the vortex is not isolated from the bottom, we can indeed expect bottom topography to assist in guiding the vortex movement.

### d. Mergers

We will now return to the question regarding the vortex's regeneration mechanism, focusing on a time span after its formation.

Since the LV is subject to cooling periods, its core will likely exhibit different hydrographic properties than most other vortices in the basin. Figure 10 display occurrences of the density in all anticyclonic vortices identified within the 3000-m depth contour during winter and summer, respectively. Core densities, computed from vertical profiles of temperature and salinity, are extracted from the position of maximum relative vorticity in the vortex centers. The seasonal mean density of the LV core is displayed by the dashed line. The peak in occurrences at or near the dashed line reflects the LV's presence in the collection of basin vortices. The LV, being a deep and moreover denser feature, encounters anticyclones with mostly lighter cores centered on various depths but on lighter isopycnals. A vertical alignment

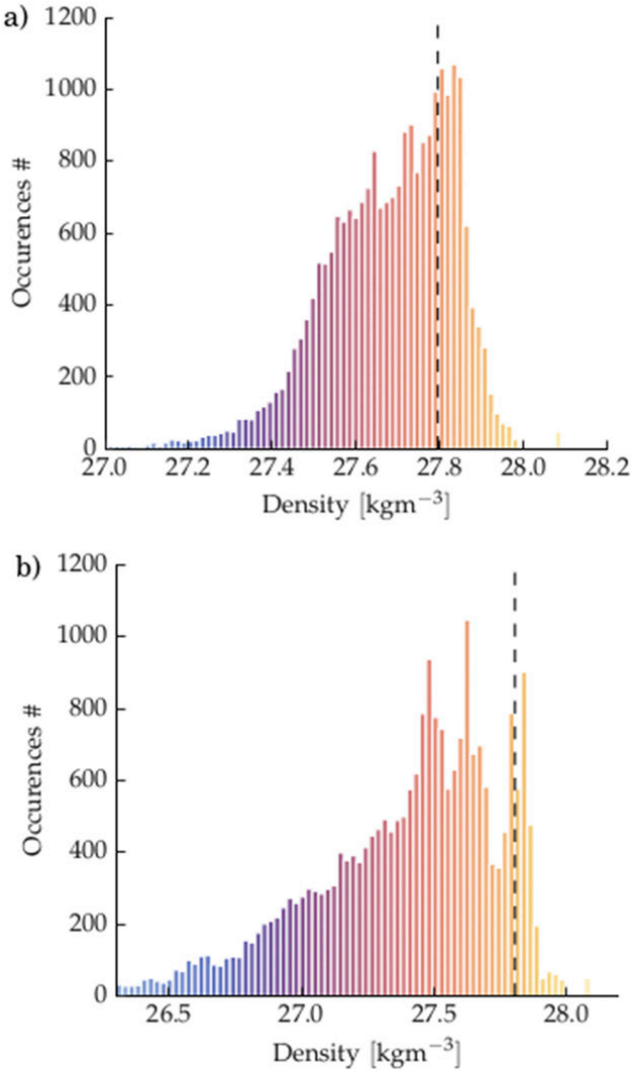


FIG. 10. Histogram of vortex core densities, extracted at depth of the maximum vorticity in the vortex center of all anticyclones identified in the central Lofoten Basin (within the 3000-m depth contour) during (a) winter and (b) summer. The dashed black lines show the time-mean density of the LV core at 400-m depth during the respective seasons.

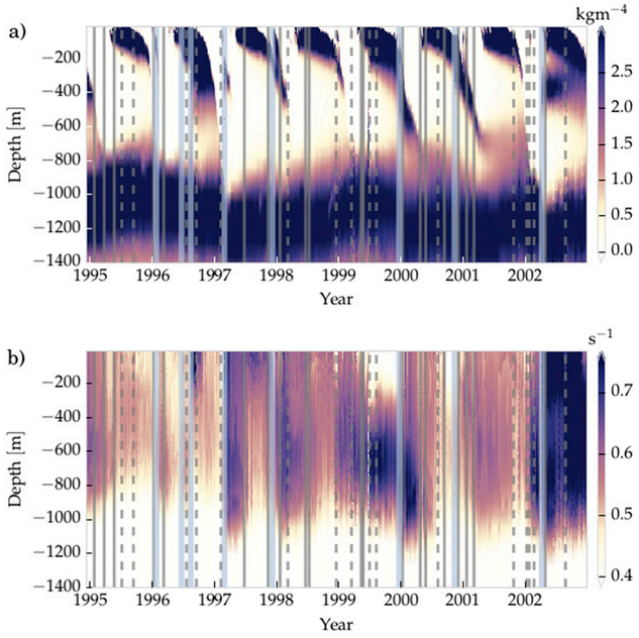


FIG. 11. Daily vertical profiles of (a) stratification and (b) absolute relative vorticity taken at the estimated LV core center. Solid gray lines mark complete merger events while dashed gray lines mark partial merger events. The translucent light blue bands denote vertical stacking events.

should then be a common outcome in the case when an encounter leads to a coalescence.

Daily vertical profiles of stratification and relative vorticity taken through the estimated center location of the LV core are shown in Fig. 11. The vertical density structure undergoes strong seasonal changes. During winter, the vortex has a well-mixed core that extends from the surface down to 800–1000 m. There is a sharp pycnocline below the core. This lower pycnocline is typically found around 1000–1200 m, in agreement with observations (Søiland et al. 2016). During summer, the LV has a lens-like signature in the density field (Fer et al. 2018). Upper and lower lobes of increased stratification create a lens-shaped subsurface structure. Starting in April/May the ocean surface experiences solar heating that puts a cap of restratified waters above the core, leading to an upper pycnocline. The surface warming extends down to approximately 200 m. When wintertime convection commences, the upper water column is again homogenized, the mixed layer grows, and the seasonal pycnocline gradually deepens. As a result of this deepening, the LV has two vertically stacked cores of weakly stratified water in early winter. In late winter, the surface undergoes strong cooling leading to vigorous vertical mixing which erodes all the way through the remains of the seasonal pycnocline, leading to the isopycnals outcropping at the surface, and the core reconnecting to atmospheric influences. The maximum depth of the summer-heated layer rarely exceeds 150–200 m, and its remnants are maintained through October/November before it deteriorates within a week due to vertical mixing.

Figure 11b show the corresponding relative vorticity profiles. These profiles do not show signs of distinct seasonal variations, but rather episodic burst of increased intensity. As there is little indication of a seasonal spinup, wintertime convection does not seem to be implicated in the main vortex regeneration. But we do not rule out a second-order impact convection might have. Next we will examine what effect merging events have on the intensity of the LV.

The conservation of potential vorticity is a key concept to consider as it is central to vortex dynamics.

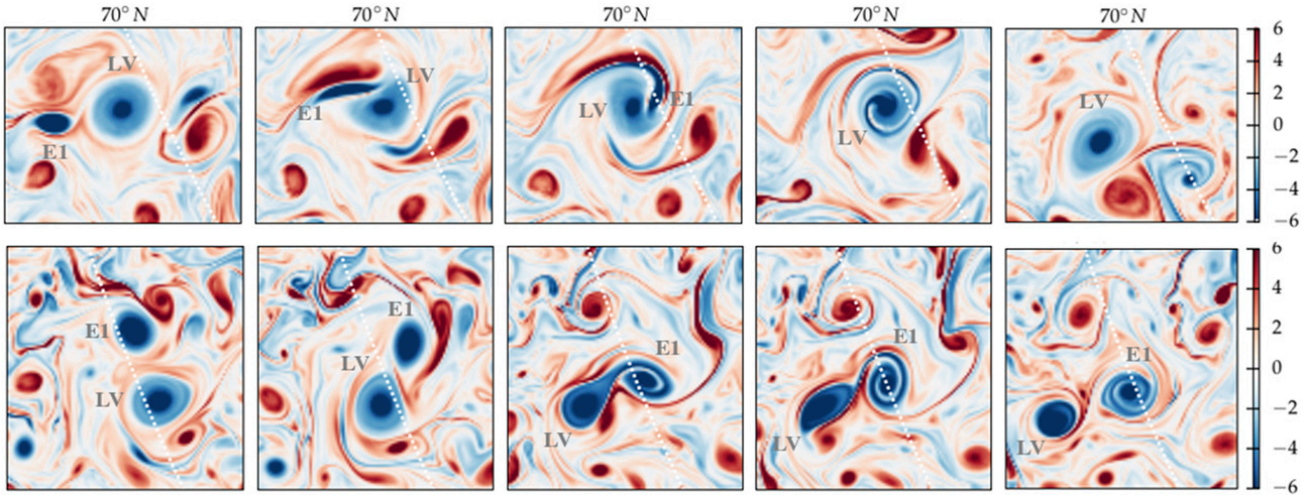


FIG. 12. Sequences of horizontal maps of relative vorticity at a 400-m depth displaying examples of (top) an asymmetric merger where the approaching vortex is smaller in size, but stronger than the LV, and (bottom) a partial merger event, where the LV is repelled from the approaching vortex after a brief interaction. The LV and the approaching vortex (E1) are labeled in all columns. The white dashed line shows 70°N.

Below, we will present the time evolution of the two main terms that constitute the quasigeostrophic potential vorticity (PV)—the stratification and the rate of spin—along the vortex trajectory. Following the vortex, in a Lagrangian framework, conservation of PV can be assumed as a first-order balance. In the absence of forcing and dissipation, the tendency equation for PV is

$$\frac{D}{Dt}q = 0,$$

$$q = \frac{\zeta + f}{\rho_0}\left(-\frac{\partial \rho}{\partial z}\right),$$

where $q$ is the vertical component of the Ertel PV (Vallis 2006). Here $\rho_0$ is a reference density and $-\partial\rho/\partial z$ is a measure of the strength of the stratification. Owing to the small geographical displacements in the LV position, variations in $f$ can be neglected. So, if the stratification increases, relative vorticity must become more negative, acting to intensify the current of an anticyclone. During violent events such as vortex mergers or in wintertime when the core is in contact with the atmosphere, we do not expect PV to be strictly conserved, but we will look for signs of correlation between two terms as we do expect to see a *tendency* toward such conservation.

Some examples of different types of mergers are shown in the horizontal vorticity maps at 500-m depth in Fig. 12. In the top row, the smaller vortex gets destroyed by LV, elongating strongly and eventually getting wrapped around it. The merger involves a neighboring cyclone that possibly assists in decreasing the separation distance between the two anticyclones. The cyclone forms a dipole with the smallest anticyclone which acts to propel it toward the LV through mutual advection. In addition to such complete merger events, the merger process is observed several times to be initiated but only partially completed. In a partial merger (PM), a filament of the weaker vortex is drained out and absorbed by the stronger vortex (Yasuda and Flierl 1995). An example of such an interaction is presented in the bottom row in Fig. 12. The southern vortex is the LV. A dipole approaches from the north, and as the separation distance between the anticyclones decrease, they start exchanging fluid. After a minor exchange, they separate. The cyclone is entrained in the interaction, and couples briefly to the LV, possibly leading to mutual advection away from the other anticyclone. It appears that the PM here leaves a more intense LV that has been reduced somewhat in size.

On average, three or four major merging events with other anticyclones are observed each year. Complete eddy merging events are marked by gray solid lines and partial merging events by gray dashed lines in Fig. 11. During some of the merging events, indicated by thicker gray bands, a double-core vertical structure suddenly appears. In such structures, two weakly stratified cores are separated by a layer of high stratification occurring at a variable depth. However, in contrast to early winter conditions, the intermediate pycnocline separating the two cores is not related to a deep seasonal pycnocline. The transition to a double-core structure is swift and is observed in all seasons, unlike the gradual, monthly transition into a double-core over the course of the winter season. This suggest a different mechanism at work. Importantly, the dividing layer is frequently deeper than the range of the seasonal pycnocline depth,

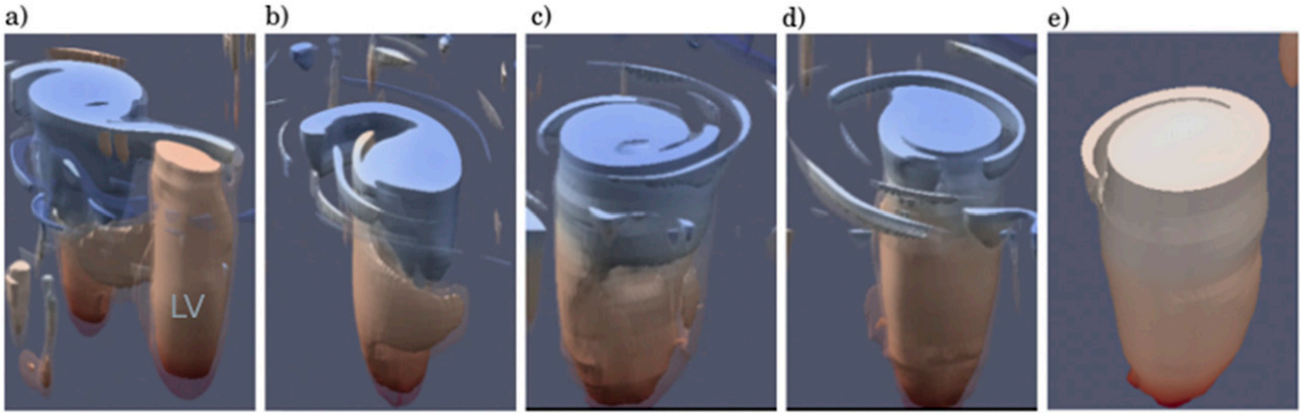


FIG. 13. (a)–(e) Isovolumes confined by the $2 \times 10^{-5}\,s^{-1}$ vorticity contour during the merger event in April/May 2002, with density shown in colors. The time from the previous plot is 12 h in (b) and (c), 10 days in (d), and 20 days in (e). The LV is labeled in (a).

situated well below 200 m. It typically persists for some months, before it erodes and the single-core structure is restored. The restoration into single vertical core happens substantially faster than when it occurs in other seasons. Occurrences of layers vertically separating two cores are evident in February 1997, December 1999, January 2000, and April 2002. Brief manifestations are also observed in January 1996 and December 1998, where initially the separation is situated around 200 m before it is shifted downward in time. Even more subtle incidents can be detected within the summer restratification caps by the staircases occurring in stratification. The most profound cases are seen in May 1996, June 1996, and October 2000. These abrupt downward shifts of stratification values are found on closer examination linked to the appearance of double cores.

The deep double-core structures arise from a vertical alignment of two anticyclones, in which one vortex slides on top of the other. Prior to the alignment the LV is 600–900 m deep. During the alignment, the core undergoes a massive vertical compression of typically 100 m or more, and from conservation of PV one would expect to see a response in relative vorticity as a result of this compression. As shown in Fig. 11b, the transitions are indeed connected to vigorous changes in relative vorticity. A rapid and substantial increase in negative vortex spin follows after a merger in all of the vertical alignment cases mentioned above. The spinup often shows a maximum increase in vorticity at around 600–700 m. However, in July 1996 only the upper part of the vortex strengthens significantly. Here, the vortex that slides on top of the LV experience greater squeezing than the LV core, while both upper and lower parts are squeezed and intensify after the January 1997 event and the April 2002 event.

Most of the partial mergers seem to have minor effects on the vortex rotation. But, there are some exceptions. Partial merger events in December 1998, June 1999 and June 2002 are all accompanied by a significant vorticity increase. The June 1999 event was illustrated in the horizontal transects in bottom panel of Fig. 12. In all cases, the cores interacting with the LV are situated on a shallower isopycnal. As they draw close to the LV, a vertical alignment is initiated but not completed. The process reaches the point at which the cores have started to compress, but no connection between the cores is established. The result is a brief interaction after which the cores detach and evolve as two separate entities, both intensified from the compression. In a fully turbulent field, it is difficult to determine what causes the vortices to separate instead of proceeding with the alignment. One speculation is that the cores may, for example, be too vertically offset, inhibiting the merger.

### *e. A three-dimensional view of vertical alignment*

Next we will take a closer three-dimensional look at one instance of the vertical alignment process. We examine the alignment event with the largest impact, the spring 2002 event. Figure 13 shows isovolumes of the LV and the approaching vortex (E1) confined by the $-2 \times 10^{-5}$ vorticity contour at different stages of the alignment process.

The LV is well mixed throughout the core as the two vortices meet. In Fig. 13a, the two vortices approach each other and have started to corotate. In Fig. 13b, both vortices develop tentacles that extend to the other vortex. These tentacles do not evolve on the same horizontal plane. The denser vortex rather extends its tentacle below the lighter vortex's arm. As these fast-moving handles advance, they curl around the opposite vortex body allowing the vortices to latch onto each other. The deepest tentacle, from the LV, then creates a bridge to the dense part of E1, and the LV begins to submerge. The LV makes a dive and merges with the

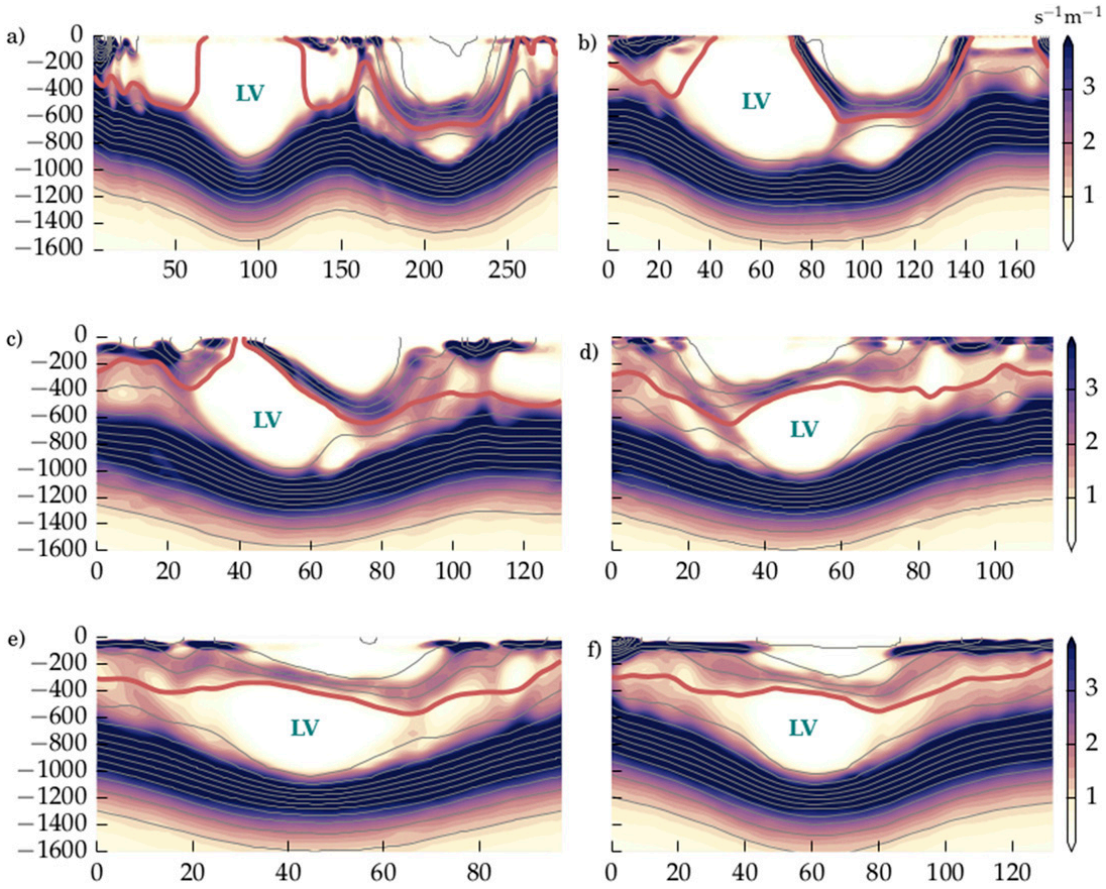


FIG. 14. Vertical transects of Ertel PV multiplied, for display purposes, by a factor of $10^{11}$, taken during the April/May 2002 merger event along a line connecting the center of both vortices. Isopycnals are shown in gray contours with the 1027.82 isopycnal marked in red. Shown are day (a) 0, (b) 6, (c) 8, (d) 14, (e) 19, and (f) 24. The LV is labeled in all panels.

lower part of E1. In Figs. 13c and 13d, an adjustment process follows where the two cores wobble back and forth until they finally align about the same vertical axis. One month after the merger is initiated, in Fig. 13e, the end product is an axisymmetric double-core vortex.

The vertical motion of the vortices during the alignment is more clearly depicted in vertical transects that cut through the centers of the vortex cores. Figure 14 shows Ertel PV along such transects through the two vortex cores at different stages of the merger. The transects rotate along with the two vortices as they orbit around a common mass center. A deep structure, the LV, meets a double-core vortex, E1, of comparable size and strength. E1 was shed from the boundary current a couple of months earlier and has a lighter upper core. Prior to the LV encounter, E1 has already undergone a vertical stacking, giving it two cores separated by an intermediate pycnocline. The lower core belongs to nearly the same density class as the LV and is the remains of a basin vortex that endured the winter season. The lightest isopycnal in the LV core is highlighted by a thicker red contour, and it connects to the upper boundary of the lower E1 core. In Fig. 14b, the vortices draw near and an intersecting layer composed of high values of PV shoals and tilts toward the surface, acting as a barrier between the LV and the upper E1 core. The LV then seems to slide adiabatically under the divide, shown in Figs. 14c–e, along the isopycnal connecting it to the lower E1 core. A subsequent adjustment toward an axisymmetric structure follows in the month ahead, see Fig. 14f.

The spring 2002 merger is not unique. The winter 1997 event is very similar, for example, in that the alignment leads to a reinvigorated vortex. The resemblance is evident in Figs. 15 and 16, showing radial plots of Ertel PV and relative vorticity averaged over a 5 day period before (panels a and c) and a 5 day period after (panels b and d) the mergers. Prior to the alignment, the core is subsurface intensified centered at approximately 600 m and with a total thickness of 1000 m. After the alignment, the LV is half this thickness, having experienced massive compression in the process. The two cores

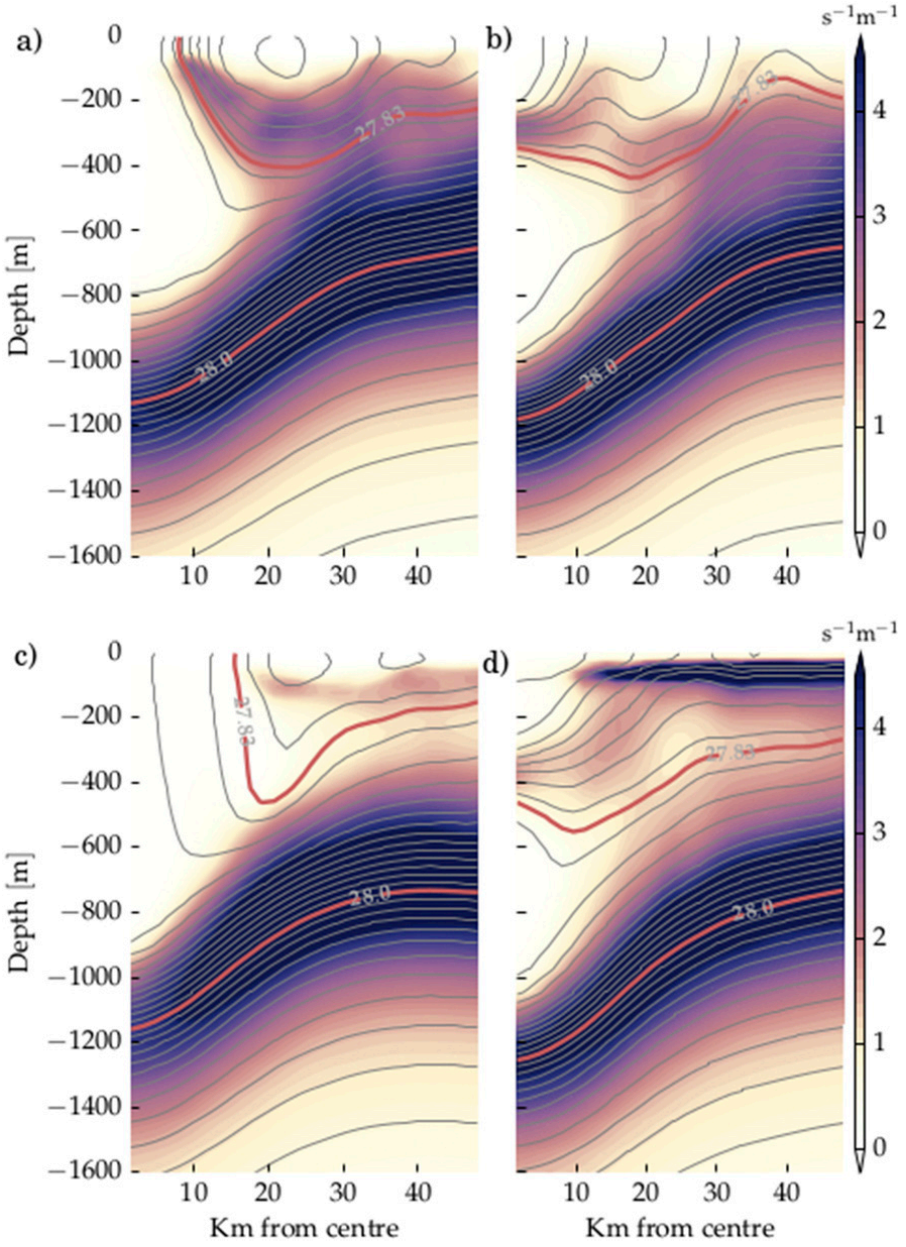


FIG. 15. Radial transects of azimuthally averaged LV Ertel PV multiplied by a factor of $10^{11}$. Shown is the time mean over 5 days, (a) before and (b) after the merger in winter 1997 and (c) before and (d) after the merger in spring 2002. Density is shown in gray contours with the 1027.82 isopycnal drawn in red.

of different strengths, separated by a high PV layer, create a structure with a greater vertical extent. The 28.0 kg m$^{-3}$ isopycnal below the initial core plunges down 100–200 m. Comparing initial and final conditions, the vorticity response is unmistakable: an upsurge in anticyclonic vortex rotation following the coalescence is clearly demonstrated.

Vertical alignment also occurs between two single-core structures. Nonetheless, the given examples serve as representative cases of the alignment process because the impact is the same even when two single cores join to share the same vertical axis. The cores are compressed and a spinup follows.

### *f. Integrated time series*

To sum up, we present an aggregated view of the vortex evolution. Figure 17a displays a time series of volume-integrated Rossby number, Ro = $\zeta/f$, computed from radial profiles of relative vorticity through the identified LV core. The volume of integration is bounded

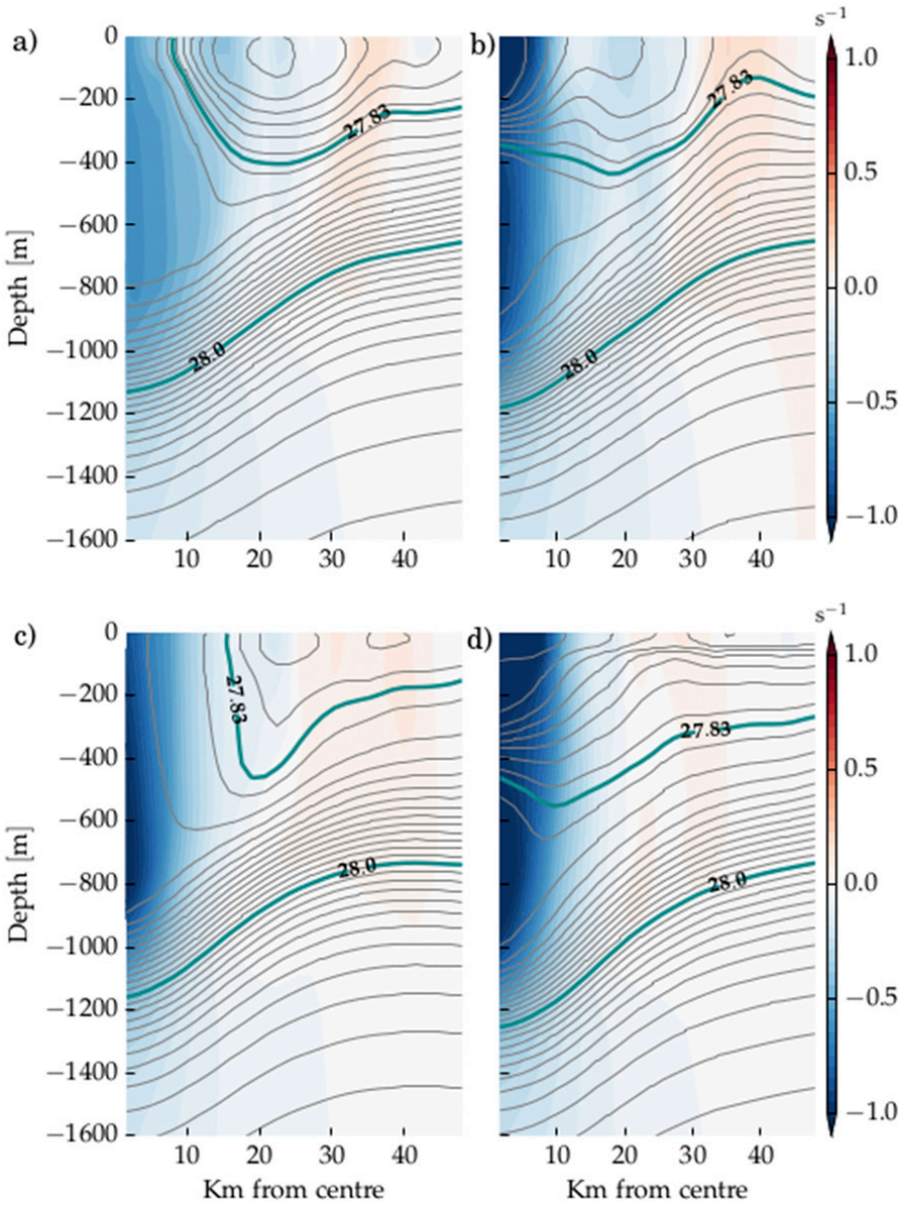


FIG. 16. Radial transects of azimuthally averaged LV relative vorticity multiplied by a factor of $10^4$, and averaged over 5 days. (a) Before and (b) after the merger in winter 1997 and (c) before and (d) after the merger in spring 2002 shown in Fig. 14. Density shown as gray contours with the 1027.82 isopycnal drawn in teal. Intensification is clearly seen, as is an increase in stratification.

laterally by the vorticity sign reversal at each model level and vertically by the thickness of the vortex core. The thickness of the core is defined by the vertical distance between the 1027.795 isopycnal and the 1027.895 isopycnal. The upper isopycnal outcrops in the winter seasons. Here, complete mergers are again denoted by solid lines and PM events by dashed lines. Vertical alignments are highlighted by teal bands.

The LV vorticity varies episodically through time as seen earlier in Fig. 17a. The variations show no clear seasonal cycle. Rather, sharp bursts of increased vortex intensity accompany each vertical alignment. Generally, the peaks in vorticity are followed by a steady decay period until another reinvigoration take place. The estimated slope of the decline is a decrease of 2%–4% per month, indicating a vortex decay time of 2–5 years. Belonenko et al. (2017) found a similar decay time of 2–3 years by evaluating the change in the LV rotation in between regeneration events. They suggested either baroclinic instability or a mixed baroclinic–barotropic instability as a likely cause of the gradual decay. Primitive equation calculations showed that perturbations developed

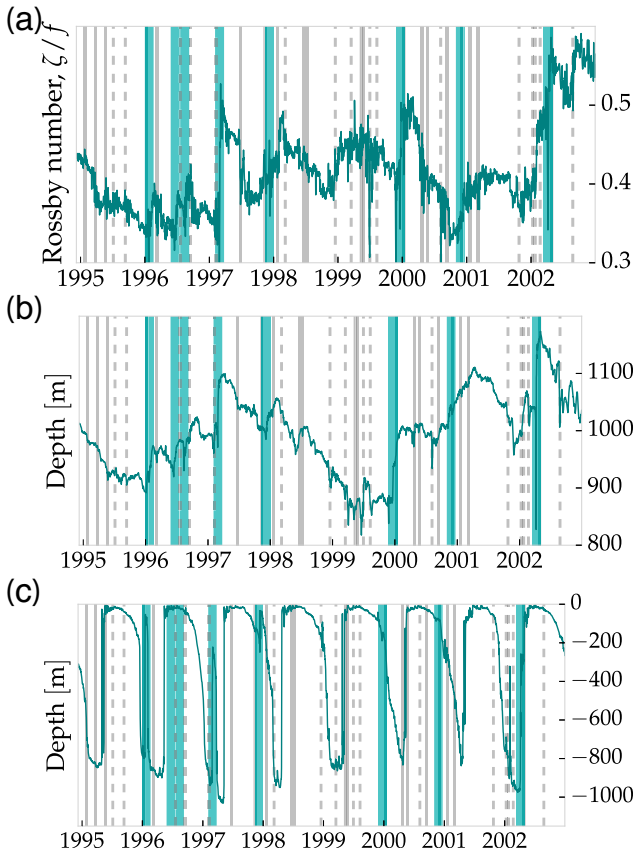


FIG. 17. Time series of (a) volume integrated Rossby number, (b) depth of the LV bottom isopycnal, and (c) LV mixed layer depth. Solid gray lines mark complete merger events, and dashed gray lines mark partial merger events. Teal bands indicate vertical alignment events.

on the rim of the vortex without penetrating deep into the core, giving rise to a decay time of 5–12 months. They noted that this time scale allowed for either eddy mergers or deep convection to interrupt further growth of the perturbations and to regenerate the LV. Finding most mergers during wintertime, they were not able to distinguish between the regeneration impact of the two mechanisms. Longer decay times have been reported in other studies considering the effect of small-scale turbulent diffusion (Søiland and Rossby 2013; Fer et al. 2018). Calculations from summertime observations suggested that the LV's total energy would be depleted in 14 years, whereas it would take 9 years for the kinetic energy to deplete (Fer et al. 2018). Our documentation of faster decay times suggests other processes are at work.

An overall gradual increase in LV Rossby number occurs during wintertime in 1998, 1999, and 2001. In 1998 and 2001, it could be linked to the vertical alignments, but there is no alignment in 1999. We are not sure why this slower, more gradual intensification occurs and we cannot exclude the possibility that convection has some impact here.

Time series of the depth of the 28.0 kg m$^{-3}$ isopycnal, representing the bottom of the LV, is displayed in Fig. 17b. Comparing this to Fig. 17a, we see that the depth variations of LV bottom boundary largely follow the evolution of relative vorticity. In particular, depressions of this lower LV isopycnal associated with vertical alignments typically occur contemporaneously with the increases in negative relative vorticity, as expected as a consequence of the vortex alignment process.

Figure 17c shows surface mixed layer depth recorded in the LV core. The mixed layer depth is taken as the depth where $\rho_{\mathrm{MLD}} = \rho_s + 0.03\,\mathrm{kg\,m^{-3}}$, where $\rho_s$ is the surface density at each time step. The depth of the mixed layer serves as a proxy for the strength of the wintertime convection. As discussed earlier, we do not see a clear seasonal signal in the vortex strength, as one would expect for a response to periods of convection. Specifically there is no systematic deepening of the lower vortex boundary during the winter seasons. Wintertime mixing appears commonly not to penetrate to the bottom of the vortex. Also, we note that the creation of an intermediate pycnocline through the vortex stacking act as a barrier to deep convective mixing. The role of wintertime convection thus seems mainly to act to vertically homogenize and densify the LV, rather than intensify it.

## 4. Discussion and conclusions

A particularly unique feature exists in the Lofoten Basin—a quasi-permanent anticyclonic vortex located in the deepest part of its topography depression. Extensive research in the area since the 1970s established the Lofoten vortex's existence and broad-scale features. However, several questions regarding the vortex's dynamics have remained outstanding. In this study we have examined in detail one of two mechanisms previously suggested for maintaining the vortex: vortex mergers (Köhl 2007). Using a model simulation with much higher resolution than previously utilized in this region has enabled us to study Lofoten vortex evolution in detail, both temporally and spatially.

The model was initialized from a coarser-resolution model simulation with fairly smooth hydrography and a weak eddy field that lacks a Lofoten Basin anticyclonic vortex. At the start of the simulation, the poleward flowing current of warm Atlantic Water along the Norwegian Continental Slope intensifies and begins to shed anticyclonic eddies that drift into the Lofoten Basin. The Lofoten vortex forms just 160–200 days into the simulation spinup, seeded by anticyclones that can

be traced back to the boundary current. The simulated vortex characteristics compare well with observations. The model's LV has a deep and well-mixed core with a strength in agreement with previous observational findings (Søiland and Rossby 2013; Yu et al. 2017; Fer et al. 2018). The velocity signal is found to be non-negligible at the bottom. In our model, the LV moves in a cyclonic sense at a faster rate than implied by the mean currents, suggesting topographic beta drift as an additional factor.

We found that anticyclones shed from the boundary current propagate westward and make their way into the deepest parts of the basin along generally cyclonic routes, in agreement with earlier studies (Volkov et al. 2013, 2015). Here, they interact with the LV, and some interactions lead to a coalescence. In our simulation, 3–4 merger events occur each year, with no clear seasonal bias. While there might still be favorable conditions for mergers during wintertime, we did not find this in our analysis. Köhl (2007) also found three to four yearly events. However, he observed slightly more mergers occurring during the period February–May, and none in November–December. Belonenko et al. (2017) identified one to two mergers per year with a distribution skewed toward wintertime. They analyzed the response of wintertime convection and mergers on the LV relative vorticity and energy budget. The fact that most mergers in their study happened in the same period as wintertime convection made it difficult to discern which mechanism was responsible for the vortex regeneration. They found that barotropic and baroclinic potential energy anomalies intensified during both processes, while relative vorticity did not always increase following a merger. In our analysis, the LV relative vorticity is also not affected by all mergers but importantly, it is strongly reinforced after vertical alignments. We conclude that it is these stacking events that have the strongest impact on the vortex spinup. The reinforcement take place according to the PV conservation tendency principle, through the substantial squeezing of the LV core when it is forced below a lighter core that slides on top of it. Such squeezing, on the order of hundreds of meters, was reported earlier by Cresswell (1982) in their description of the coalescence of two anticyclonic vortices in the Tasman Sea. After the alignment, the lower boundary of the lighter vortex was lifted up 230 m, while the boundary of the denser vortex was depressed by at least 100 m.

In our simulations, vertical alignment events produce a double-core structure that persists for weeks to months, depending on the season. The process we observed is well described by the experiments by Nof and Dewar (1994). A complex stacked vertical structure of the LV core has indeed been seen in observational studies (Yu et al. 2017; Fer et al. 2018). Figure 6a in Yu et al. (2017) show the radial distribution of buoyancy frequency in the LV core. The observed double core structure shown there is very similar to that found in the model following an alignment (see Figs. 15b,c). Bearing seasonal and year-to-year variations in mind, the general vertical structure of our modeled LV agrees well with the observed LV (see Figs. 3 and 4a in Fer et al. 2018). The region of strong stratification separating two cores has, however, been attributed to the remains of the seasonal pycnocline. We find that the seasonal pycnocline does not extend to a deep enough depth to explain the occasional deep occurrences of this feature, neither can it explain the sudden transition into a double-core structure.

We did not look closely into the cases where an interaction is prevented or interrupted. More studies are needed to identify criteria that allows an alignment to occur. In a study of the alignment of two three-dimensional QG vortices, Reinaud and Carton (2020) found that most vortex states are stable to vertical alignments. However, they note that alignments are indeed observed in more realistic settings, and that influences of external flow are needed for alignments to take place, because the vortices otherwise stay in stable corotating states. In our study, we saw quantitative implications of the effects of surrounding vortices during several vortex interaction events. External influences seemed to both contribute in bringing the vortices closer and, in some cases, disrupt the interaction. It seems likely that a coalescence could be interrupted by a cyclone locking onto one of the interacting anticyclones creating a dipole effect preventing further core attraction. This occurs in two of the partial merger events mentioned earlier. A dipole mechanism preventing mergers of anticyclones without a surrounding flow field was described by Ciani et al. (2016) and Valcke and Verron (1997). We were not able to observe this precise mechanism. However, we did observe a similar repulsive dipole mechanism, in the examples mentioned above, when a surrounding vortex field do exist. As pointed out by Reinaud and Carton (2020), vortex alignment in a weak internal strain field should be further addressed.

The increasing number of observations of double core oceanic eddies indicate that what has been referred to as an unusual eddy structure (Zhao and Timmermans 2015), might not be as uncommon than formerly though. Indeed, in the Labrador Sea, the number of double cores vortices observed suggested that they are more common to find than single cores in that region (Lilly et al. 2003). Among the observation sites, the most comparable region to the Lofoten Basin is possibly the Arctic Ocean. The Canada Basin, in particular, consists of closed topographic contours and is home to nearly exclusively

anticyclonic eddies. The bowl-shaped basin might have a similar impact as the one we see in the Lofoten Basin, where the anticyclones are attracted to the central parts. Thus, we might expect that there also exist a migration of anticyclones toward the center of the Canada Basin. In a recent study by Zhao and Timmermans (2015) 58 eddies, all anticyclones, were identified and analyzed with mooring instruments and CTD measurements. They classified three types of eddies: shallow, middepth, and deep eddies. The middepth eddies had two cores between 200 and 1000 m, and had two velocity maxima in the vertical. The two cores consisted of different water masses, the shallower core situated at the base of the halocline (≈200 m) consisted of Eurasian Water and the deeper core of Atlantic Water. The authors hypothesize that the entire eddy structure arise at the front separating Eurasian and Canadian water masses, and is then advected away from the front. While this may be an appropriate description, it is also possible, as shown in this paper, that distinct eddies that hold Eurasian and Canadian waters interact after their generation, and are forced to vertically align in a coalescence.

The LV is a special case due to its geographical stationarity and the continuous supply of anticyclones into the region. However, it is not dynamically unique in its response to an alignment. In our simulation, the dual-core structure is not only observed for the LV, but is also common for other basin anticyclones. Our results offer a clearly documented and efficient regeneration mechanism for oceanic anticyclones such as the Lofoten vortex, in which vertical alignment of a denser nucleus and a lighter satellite vortex energizes the vortex, with the two cores being subsequently fused through vertical convection.

The full picture of the Lofoten Basin vortex dynamics involves also cyclonic vortices. An extended vortex census will be presented in a follow-up study with the focus on the asymmetry between cyclones and anticyclones. The study will also present an overview of typical vertical scales and structures of the vortex field.

*Acknowledgments.* The Ssalto/Duacs altimeter products were produced and distributed by the Copernicus Marine and Environment Monitoring Service (CMEMS) (http://www.marine.copernicus.eu).

## APPENDIX

### Detection Routine

The detection routine consists of three steps. First, local extrema are identified in daily model SSH field. Each local extremum has to exceed the value of all neighboring grid points within a square box with edges 20 km from the extrema. This requirement ensures a lower limit on the separation distance between two adjacent eddies. Overestimated eddy counts will also occur less frequently since smaller-scale variations in the SSH field are ignored. Second, the largest closed SSH contour surrounding the extreme is located. Third, within the closed SSH region, we extract the OW = 0 contour. The eddy center is defined as the geographical mean position of all the points inside this OW = 0 contour. Finally, considering the finite resolution of the model, a minimum eddy effective radius is set to 2 km. Features smaller than this are rejected. A maximum eddy radius is also set to 100 km to prevent gyre-scale flows to be identified as eddies.

The effective radius of a detected vortex is estimated using the area of the OW = 0 contour, $R = \sqrt{A_{\mathrm{OW}}/\pi}$. This estimate is a conservative measure because the contour marks the extent of the inner vortex core, and will thus yield smaller vortex scales than the area of the SSH contour. Additionally, the SSH contour is often more disturbed by the nearby strain field and by the interaction with the external vortex or current field. These disturbances give rise to more variability in the size measure and stronger deformation of the contour. Laxenaire et al. (2020) shows that the contour associated with the maximum azimuthal speed, the ''speed radius,'' is a less noisy measure of the vortex radius than that of the outermost closed SSH contour. Similarly, we find less variability in the OW contours when compared to the SSH contours. Figure 3 displays the SSH and OW contours associated with the LV extracted around the LV center during the first 4 years of the simulation. The OW contours are more compact and less elliptical, with exceptions of occasional features containing tails of high vorticity.

To follow the detected eddies in time, we use the tracking algorithm developed by Penven et al. (2005). Eddies in two subsequent daily frames are linked by a similarity condition. Two eddies, e1 and e2, are considered the same if the generalized distance

$$X_{\mathrm{e1,e2}} = \sqrt{\frac{\delta D^2}{D_0} + \frac{\delta R^2}{R_0} + \frac{\delta \zeta^2}{\zeta_0}} \qquad \text{(A1)}$$

is minimal. The terms are the normalized differences in separation distance ($D_0$ = 25 km), radius ($R_0$ = 20 km), and vorticity ($\zeta_0 = 10^{-5}\,\mathrm{s}^{-1}$). To prevent a change in the vorticity signature, the normalization factor $X_{\mathrm{e1,e2}}$ is set to infinity if two eddies are of opposite polarity (Halo et al. 2014). Two eddies are not connected if the propagation distance between the

linked eddy positions is larger than twice the mean radius of the eddies.

During some interactions, eddies briefly share an outer SSH contour before they repel each other. In other interactions, either with the surrounding field or with other vortices, deformations cause a major distortion of the contours. The individual eddy identities are often lost during such processes. To accommodate this phenomenon, we therefore expanded the tracking routine to include a search for eddy linkages further back in time. An identified eddy is allowed to disappear for up to three days before it reappears, otherwise the track is terminated. We chose three days because by inspection this criterion showed to be stable and produce smooth trajectories, whereas for longer periods some tracks became unrealistic.

## REFERENCES


Armi, L., D. Hebert, N. Oakey, J. F. Price, P. L. Richardson, H. T. Rossby, and B. Ruddick, 1989: Two years in the life of a Mediterranean salt lens. *J. Phys. Oceanogr.*, **19**, 354–370, https://doi.org/10.1175/1520-0485(1989)019<0354:TYITLO>2.0.CO;2.

Baird, M. E., and K. R. Ridgway, 2012: The southward transport of sub-mesoscale lenses of Bass Strait Water in the Centre of anti-cyclonic mesoscale eddies. *Geophys. Res. Lett.*, **39**, L02603, https://doi.org/10.1029/2011GL050643.

Barceló-Llull, B., and Coauthors, 2017: Anatomy of a subtropical intrathermocline eddy. *Deep-Sea Res. I*, **124**, 126–139, https://doi.org/10.1016/j.dsr.2017.03.012.

Beldring, S., K. Engeland, L. A. Roald, N. R. Sælthun, and A. Voksø, 2003: Estimation of parameters in a distributed precipitation-runoff model for Norway. *Hydrol. Earth Syst. Sci.*, **7**, 304–316, https://doi.org/10.5194/hess-7-304-2003.

Belkin, I., and Y. Mikhailitchenko, 1986: Thermohaline structure of the frontal zone of the northwest Pacific Ocean at 160°E (in Russian). *Okeanologiya*, **26**, 70–72.

——, A. Foppert, T. Rossby, S. Fontana, and C. Kincaid, 2020: A double-thermostad warm-core ring of the Gulf stream. *J. Phys. Oceanogr.*, **50**, 489–507, https://doi.org/10.1175/JPO-D-18-0275.1.

Belonenko, T. V., I. L. Bashmachnikov, A. V. Koldunov, and P. A. Kuibin, 2017: On the vertical velocity component in the mesoscale Lofoten vortex of the Norwegian Sea. *Izv. Atmos. Ocean. Phys.*, **53**, 641–649, https://doi.org/10.1134/S0001433817060032.

Bogdanov, K. T., V. I. Iliychev, V. B. Lobanov, and R. D. Medjitov, 1985: Investigation of anticyclonic eddy in the northwest part of the Pacific Ocean (in Russian). *Dokl. Acad. Sci. USSR*, **281**, 1210–1213.

Bosse, A., I. Fer, J. M. Lilly, and H. Søiland, 2019: Dynamical controls on the longevity of a non-linear vortex: The case of the Lofoten Basin Eddy. *Sci. Rep.*, **9**, 13448, https://doi.org/10.1038/S41598-019-49599-8.

Brundage, W. L., and J. P. Dugan, 1986: Observations of an anticyclonic eddy of 18°C water in the Sargasso Sea. *J. Phys. Oceanogr.*, **16**, 717–727, https://doi.org/10.1175/1520-0485(1986)016<0717:OOAAEO>2.0.CO;2.

Carnevale, G. F., R. C. Kloosterziel, and G. J. F. Van Heijst, 1991: Propagation of barotropic vortices over topography in a rotating tank. *J. Fluid Mech.*, **233**, 119–139, https://doi.org/10.1017/S0022112091000411.

Carton, X., N. Daniault, J. Alves, L. Cherubin, and I. Ambar, 2010: Meddy dynamics and interaction with neighboring eddies southwest of Portugal: Observations and modeling. *J. Geophys. Res.*, **115**, C06017, https://doi.org/10.1029/2009JC005646.

Chelton, D. B., M. G. Schlax, R. M. Samelson, and R. A. de Szoeke, 2007: Global observations of large oceanic eddies. *Geophys. Res. Lett.*, **34**, L15606, https://doi.org/10.1029/2007GL030812.

Ciani, D., X. Carton, and J. Verron, 2016: On the merger of subsurface isolated vortices. *Geophys. Astrophys. Fluid Dyn.*, **110**, 23–49, https://doi.org/10.1080/03091929.2015.1135430.

Cresswell, G., 1982: The coalescence of two East Australian current warm-core eddies. *Science*, **215**, 161–164, https://doi.org/10.1126/science.215.4529.161.

de Miranda, A. P., B. Barnier, and W. K. Dewar, 1999: On the dynamics of the Zapiola anticyclone. *J. Geophys. Res.*, **104**, 21 137–21 149, https://doi.org/10.1029/1999JC900042.

Dmitrenko, I. A., S. A. Kirillov, V. V. Ivanov, and R. A. Woodgate, 2008: Mesoscale Atlantic water eddy off the Laptev Sea continental slope carries the signature of upstream interaction. *J. Geophys. Res.*, **113**, C07005, https://doi.org/10.1029/2007JC004491.

Donlon, C. J., M. Martin, J. Stark, J. Roberts-Jones, E. Fiedler, and W. Wimmer, 2012: The Operational Sea Surface Temperature and Sea Ice Analysis (OSTIA) system. *Remote Sens. Environ.*, **116**, 140–158, https://doi.org/10.1016/j.rse.2010.10.017.

Fer, I., A. Bosse, B. Ferron, and P. Bouruet-Aubertot, 2018: The dissipation of kinetic energy in the Lofoten Basin eddy. *J. Phys. Oceanogr.*, **48**, 1299–1316, https://doi.org/10.1175/JPO-D-17-0244.1.

Garreau, P., F. Dumas, S. Louazel, A. Stegner, and B. Le Vu, 2018: High-resolution observations and tracking of a dual-core anticyclonic eddy in the Algerian basin. *J. Geophys. Res. Oceans*, **123**, 9320–9339, https://doi.org/10.1029/2017JC013667.

Gascard, J.-C., and K. A. Mork, 2008: Climatic importance of large-scale and mesoscale circulation in the Lofoten Basin deduced from Lagrangian observations. *Arctic-Subarctic Ocean Fluxes*, R. R. Dickson, J. Meinke, and P. Rhines, Eds., Springer, 131–143, https://doi.org/10.1007/978-1-4020-6774-7_7.

Haidvogel, D., and Coauthors, 2008: Ocean forecasting in terrain-following coordinates: Formulation and skill assessment of the regional ocean modeling system. *J. Comput. Phys.*, **227**, 3595–3624, https://doi.org/10.1016/j.jcp.2007.06.016.

Halo, I., B. Backeberg, P. Penven, I. Ansorge, C. Reason, and J. Ullgren, 2014: Eddy properties in the Mozambique channel: A comparison between observations and two numerical ocean circulation models. *Deep-Sea Res. II*, **100**, 38–53, https://doi.org/10.1016/j.dsr2.2013.10.015.

Haney, R. L., 1991: On the pressure gradient force over steep topography in sigma coordinate ocean models. *J. Phys. Oceanogr.*, **21**, 610–619, https://doi.org/10.1175/1520-0485(1991)021<0610:OTPGFO>2.0.CO;2.

Held, I. M., 1999: The macro turbulence of the troposphere. *Tellus*, **51B**, 59–70, https://doi.org/10.3402/TELLUSB.V51I1.16260.

Isern-Fontanet, J., E. García-Ladona, and J. Font, 2003: Identification of marine eddies from altimetric maps. *J. Atmos. Oceanic Technol.*, **20**, 772–778, https://doi.org/10.1175/1520-0426(2003)20<772:IOMEFA>2.0.CO;2.

Itoh, S., and I. Yasuda, 2010: Water mass structure of warm and cold anticyclonic eddies in the western boundary region of the subarctic North Pacific. *J. Phys. Oceanogr.*, **40**, 2624–2642, https://doi.org/10.1175/2010JPO4475.1.

Ivanov, V., and A. Korablev, 1995a: Formation and regeneration of the pycnocline lens in the Norwegian Sea. *Russ. Meteor. Hydrol.*, **9**, 62–69.

——, and ——, 1995b: Interpycnocline lens dynamics in the Norwegian Sea. *Russ. Meteor. Hydrol.*, **10**, 32–37.

Köhl, A., 2007: Generation and stability of a quasi-permanent vortex in the Lofoten Basin. *J. Phys. Oceanogr.*, **37**, 2637–2651, https://doi.org/10.1175/2007JPO3694.1.

Korablev, A., A. Smirno, and O. K. Baranova, 2014: Climatological atlas of the Nordic Seas and northern North Atlantic. NOAA Atlas NESDIS 77, 116 pp., https://data.nodc.noaa.gov/woa/REGCLIM/NORDIC_SEAS/DOC/NESDIS77-lr.pdf.

Laxenaire, R., S. Speich, and A. Stegner, 2020: Evolution of the thermohaline structure of one Agulhas ring reconstructed from satellite altimetry and Argo floats. *J. Geophys. Res. Oceans*, **124**, 8969–9003, https://doi.org/10.1029/2018JC014426.

Le Traon, P. Y., M. C. Rouquet, and C. Boissier, 1990: Spatial scales of mesoscale variability in the North Atlantic as deduced from Geosat data. *J. Geophys. Res.*, **95**, 20 267–20 285, https://doi.org/10.1029/JC095iC11p20267.

Lilly, J. M., P. B. Rhines, F. Schott, K. Lavender, J. Lazier, U. Send, and E. D. Asaro, 2003: Observations of the Labrador Sea eddy field. *Prog. Oceanogr.*, **59**, 75–176, https://doi.org/10.1016/j.pocean.2003.08.013.

MacLachlan, C., and Coauthors, 2015: Global Seasonal forecast system version 5 (GloSea5): A high-resolution seasonal forecast system. *Quart. J. Roy. Meteor. Soc.*, **141**, 1072–1084, https://doi.org/10.1002/qj.2396.

Mann, C., 1967: The termination of the Gulf Stream and the beginning of the North Atlantic Current. *Deep-Sea Res. Oceanogr. Abstr.*, **14**, 337–359, https://doi.org/10.1016/0011-7471(67)90077-0.

Mauritzen, C., 1996: Production of dense overflow waters feeding the North Atlantic across the Greenland-Scotland Ridge. Part 1: Evidence for a revised circulation scheme. *Deep-Sea Res. I*, **43**, 769–806, https://doi.org/10.1016/0967-0637(96)00037-4.

McWilliams, J. C., 1990: The vortices of two-dimensional turbulence. *J. Fluid Mech.*, **219**, 361–385, https://doi.org/10.1017/S0022112090002981.

——, and G. R. Flierl, 1979: On the evolution of isolated, nonlinear vortices. *J. Phys. Oceanogr.*, **9**, 1155–1182, https://doi.org/10.1175/1520-0485(1979)009<1155:OTEOIN>2.0.CO;2.

Meinen, C., 2001: Structure of the North Atlantic current in stream-coordinates and the circulation in the newfoundland basin. *Deep-Sea Res. I*, **48**, 1553–1580, https://doi.org/10.1016/S0967-0637(00)00103-5.

Nezlin, M. V., E. N. Snezhkin, A. Dobroslavsky, and A. Pletnev, 1993: *Rossby Vortices, Spiral Structures, Solitons: Astrophysics and Plasma Physics in Shallow Water Experiments*. Springer, 88 pp.

Nof, D., and W. Dewar, 1994: Alignment of lenses: Laboratory and numerical experiments. *Deep-Sea Res. I*, **41**, 1207–1229, https://doi.org/10.1016/0967-0637(94)90041-8.

Orvik, K. A., and P. Niiler, 2002: Major pathways of Atlantic water in the northern North Atlantic and Nordic Seas toward Arctic. *Geophys. Res. Lett.*, **29**, 1896, https://doi.org/10.1029/2002GL015002.

Penven, P., V. Echevin, J. Pasapera, F. Colas, and J. Tam, 2005: Average circulation, seasonal cycle, and mesoscale dynamics of the Peru current system: A modeling approach. *J. Geophys. Res.*, **110**, C10021, https://doi.org/10.1029/2005JC002945.

Polvani, L. M., 1991: Two-layer geostrophic vortex dynamics. Part 2. Alignment and two-layer V-states. *J. Fluid Mech.*, **225**, 241–270, https://doi.org/10.1017/S0022112091002045.

Prater, M. D., and T. B. Sanford, 1994: A meddy off Cape St. Vincent. Part I: Description. *J. Phys. Oceanogr.*, **24**, 1572–1586, https://doi.org/10.1175/1520-0485(1994)024<1572:AMOCSV>2.0.CO;2.

Raj, R., L. Chafik, J. Nilsen, T. Eldevik, and I. Halo, 2015: The Lofoten vortex of the Nordic seas. *Deep-Sea Res. I*, **96**, 1–14, https://doi.org/10.1016/j.dsr.2014.10.011.

Reinaud, J. N., and X. Carton, 2020: The alignment of two three-dimensional quasi-geostrophic vortices. *Geophys. Astrophys. Fluid Dyn.*, https://doi.org/10.1080/03091929.2019.1653462, in press.

Richardson, P. L., A. S. Bower, and W. Zenk, 2000: A census of Meddies tracked by floats. *Prog. Oceanogr.*, **45**, 209–250, https://doi.org/10.1016/S0079-6611(99)00053-1.

Rodionov, V., J. Nihoul, and A. Kostianoy, 2004: *Physical Oceanography of Frontal Zones in the Subarctic Seas*. Gulf Professional Publishing, 326 pp.

Rogachev, K., N. Shlyk, and E. Carmack, 2007: The shedding of mesoscale anticyclonic eddies from the Alaskan Stream and westward transport of warm water. *Deep-Sea Res. II*, **54**, 2643–2656, https://doi.org/10.1016/j.dsr2.2007.08.017.

Rossby, T., M. D. Prater, and H. Søiland, 2009: Pathways of inflow and dispersion of warm waters in the Nordic seas. *J. Geophys. Res.*, **114**, C04011, https://doi.org/10.1029/2008JC005073.

Schultz Tokos, K. L., H.-H. Hinrichsen, and W. Zenk, 1994: Merging and migration of two meddies. *J. Phys. Oceanogr.*, **24**, 2129–2141, https://doi.org/10.1175/1520-0485(1994)024<2129:MAMOTM>2.0.CO;2.

Send, U., and J. Marshall, 1995: Integral effects of deep convection. *J. Phys. Oceanogr.*, **25**, 855–872, https://doi.org/10.1175/1520-0485(1995)025<0855:IEODC>2.0.CO;2.

Shchepetkin, A. F., and J. C. McWilliams, 2005: The Regional Oceanic Modeling System (ROMS): A split-explicit, free-surface, topography-following-coordinate oceanic model. *Ocean Modell.*, **9**, 347–404, https://doi.org/10.1016/j.ocemod.2004.08.002.

Søiland, H., and T. Rossby, 2013: On the structure of the Lofoten Basin eddy. *J. Geophys. Res. Oceans*, **118**, 4201–4212, https://doi.org/10.1002/jgrc.20301.

——, L. Chafik, and T. Rossby, 2016: On the long-term stability of the Lofoten Basin eddy. *J. Geophys. Res. Oceans*, **121**, 4438–4449, https://doi.org/10.1002/2016JC011726.

Solodoch, A., A. Stewart, and J. C. Mcwilliams, 2020: The Mann Eddy: Formation and interaction with the North Atlantic Current. *Ocean Science Meeting*, San Diego, CA, Amer. Geophys. Union, Abstract PL24C-2676, https://agu.confex.com/agu/osm20/meetingapp.cgi/Paper/639707.

Umlauf, L., and H. Burchard, 2003: A generic length-scale equation for geophysical turbulence models. *J. Mar. Res.*, **61**, 235–265, https://doi.org/10.1357/002224003322005087.

Uppala, S. M., and Coauthors, 2005: The ERA-40 Re-Analysis. *Quart. J. Roy. Meteor. Soc.*, **131**, 2961–3012, https://doi.org/10.1256/qj.04.176.

Valcke, S., and J. Verron, 1997: Interactions of baroclinic isolated vortices: The dominant effect of shielding. *J. Phys. Oceanogr.*, **27**, 524–541, https://doi.org/10.1175/1520-0485(1997)027<0524:IOBIVT>2.0.CO;2.

Vallis, G. K., 2006: *Atmospheric and Oceanic Fluid Dynamics: Fundamentals and Large-Scale Circulation*. Cambridge University Press, 745 pp.

Volkov, D. L., T. V. Belonenko, and V. R. Foux, 2013: Puzzling over the dynamics of the Lofoten basin—A sub-Arctic hot spot of ocean variability. *Geophys. Res. Lett.*, **40**, 738–743, https://doi.org/10.1002/grl.50126.

——, A. Kubryakov, and R. Lumpkin, 2015: Formation and variability of the Lofoten Basin vortex in a high-resolution ocean model. *Deep-Sea Res. I*, **105**, 142–157, https://doi.org/10.1016/j.dsr.2015.09.001.

Warner, J. C., C. R. Sherwood, H. G. Arango, and R. P. Signell, 2005: Performance of four turbulence closure models implemented using a generic length scale method. *Ocean Modell.*, **8**, 81–113, https://doi.org/10.1016/j.ocemod.2003.12.003.

Yasuda, I., and G. R. Flierl, 1995: Two-dimensional asymmetric vortex merger: Contour dynamics experiment. *J. Oceanogr.*, **51**, 145–170, https://doi.org/10.1007/BF02236522.

Yu, L.-S., A. Bosse, I. Fer, K. A. Orvik, E. M. Bruvik, I. Hessevik, and K. Kvalsund, 2017: The Lofoten Basin eddy: Three years of evolution as observed by Seagliders. *J. Geophys. Res. Oceans*, **122**, 6814–6834, https://doi.org/10.1002/2017JC012982.

Zhao, M., and M.-L. Timmermans, 2015: Vertical scales and dynamics of eddies in the Arctic Ocean's Canada Basin. *J. Geophys. Res. Oceans*, **120**, 8195–8209, https://doi.org/10.1002/2015JC011251.